

AD-A140 584

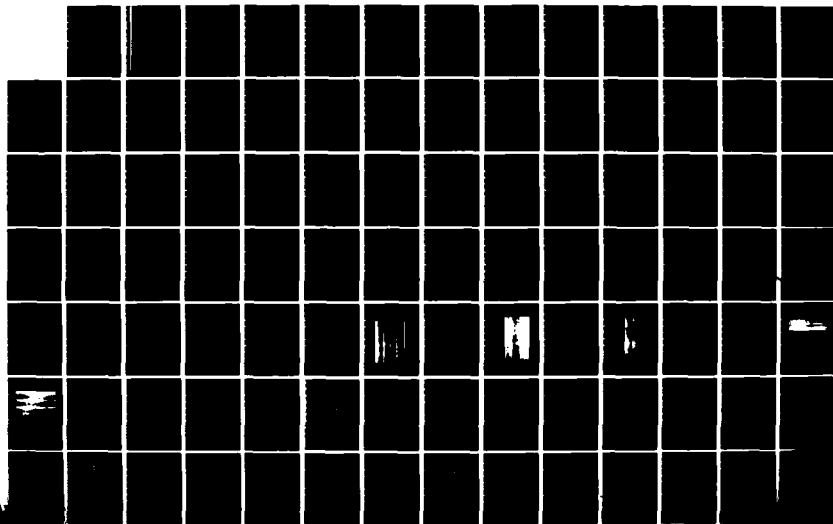
ANALYSIS OF SEASAT SAR IMAGERY COLLECTED DURING THE
JASIN EXPERIMENT(U) ENVIRONMENTAL RESEARCH INST OF
MICHIGAN ANN ARBOR E S KASISCHKE ET AL. MAY 83
ERIM-155900-16-T N00014-81-C-0692

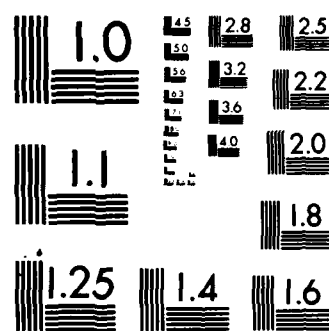
1/3

UNCLASSIFIED

F/G 8/3

NL





MICROCOPY RESOLUTION TEST CHART
NATIONAL BUREAU OF STANDARDS-1963-A

155900-16-T

AD-A140 584

DTIC FILE COPY

Topic Report

ANALYSIS OF SEASAT SAR IMAGERY COLLECTED DURING THE JASIN EXPERIMENT

MAY 1983

E.S. KASISCHKE
R.A. SHUCHMAN
J.D. LYDEN
Y.C. TSENG

Radar Division

Ocean Sciences Division
Office of Naval Research
Arlington, Virginia 22217

Contract No. N00014-81-C-0692

Technical Monitors: Hans Dolezalek
Commander Robert Kirk

ENVIRONMENTAL
RESEARCH INSTITUTE OF MICHIGAN
BOX 8618 • ANN ARBOR • MICHIGAN 48107

DTIC

APR 27 1984

84 04 26 031

UNCLASSIFIED

SECURITY CLASSIFICATION OF THIS PAGE (When Data Entered)

REPORT DOCUMENTATION PAGE		READ INSTRUCTIONS BEFORE COMPLETING FORM
1. REPORT NUMBER	2. GOVT ACCESSION NO.	3. RECIPIENT'S CATALOG NUMBER
AD-A140584		
4. TITLE (and Subtitle) ANALYSIS OF SEASAT SAR IMAGERY COLLECTED DURING THE JASIN EXPERIMENT		5. TYPE OF REPORT & PERIOD COVERED Topic Report Aug. 1981 - May 1983
		6. PERFORMING ORG REPORT NUMBER 155900-16-T
7. AUTHOR(s) E.S. Kasischke, R.A. Shuchman, J.D. Lyden and Y.C. Tseng		8. CONTRACT OR GRANT NUMBER (s) N00014-81-C-0692
9. PERFORMING ORGANIZATION NAME AND ADDRESS Radar Division, Environmental Research Institute of Michigan, P.O. Box 8618, Ann Arbor, Michigan 48107		10. PROGRAM ELEMENT, PROJECT, TASK AREA & WORK UNIT NUMBERS
11. CONTROLLING OFFICE NAME AND ADDRESS Ocean Science Division, Office of Naval Research, Arlington, Virginia 22217		12. REPORT DATE May 1983
		13. NUMBER OF PAGES 202
14. MONITORING AGENCY NAME AND ADDRESS (if different from Controlling Office)		15. SECURITY CLASS. (of this report) Unclassified
		15a. DECLASSIFICATION/DOWNGRADING SCHEDULE
16. DISTRIBUTION STATEMENT (of this Report) Approved for public release; distribution unlimited.		
17. DISTRIBUTION STATEMENT (of the abstract entered in Block 20, if different from Report)		
18. SUPPLEMENTARY NOTES The Technical Monitors for this report were Mr. Hans Dolezalek and Commander Robert Kirk.		
19. KEY WORDS (Continue on reverse side if necessary and identify by block number) Synthetic Aperture Radar Internal Waves Seasat Ocean Fronts JASIN Wave Focusing Gravity Waves		
20. ABSTRACT (Continue on reverse side if necessary and identify by block number) This report summarizes the analysis of Seasat SAR imagery collected during the JASIN experiment. Studies performed on this data set include comparison of SAR-derived estimates of wavelength and direction versus surface measured values, evaluation of SAR/wave focusing algorithms and study of deep-water internal wave and frontal boundary patterns on the SAR imagery.		

UNCLASSIFIED

SECURITY CLASSIFICATION OF THIS PAGE (When Data Entered)

PREFACE

The work described in this report was conducted by personnel in the Radar Division of the Environmental Research Institute of Michigan. This work was supported by the Office of Naval Research, Coastal Sciences (Code 422CS) under Contract No. N00014-81-C-0692. The Technical Monitors for this work were Mr. Hans Dolezalek and Commander Robert Kirk.

The principal investigator for the ONR contract is Robert A. Shuchman. The work reported in this report was performed under the direction of Eric S. Kasischke. He was assisted by James D. Lyden in the gravity wave analysis and Y.C. Tseng in the analysis of meso-scale features.

The analysis of the JASIN Seasat wave data was performed in collaboration with J. Vesecky and H. Assal of Stanford University and R. Stewart of Scripps Institute of Oceanography. The analysis of deep water mesoscale features on the JASIN Seasat imagery was performed in collaboration with A. Liu and Steve Borschardt of Dynamics Technology, Incorporated.



AI

ACKNOWLEDGMENTS

This study would not have been possible without the cooperation and assistance of many people. It is a pleasure to acknowledge the help of the following individuals: A. Klooster, J. Losee, and R. Roumaya of ERIM processed SAR data for the study; B. Holt of the Jet Propulsion Laboratory provided copies of Seasat SAR data; D. Lodge of the Royal Air Force Establishment and the European Space Agency provided the use of Seasat SAR signal films collected at the Oak Hanger receiving station; J. Vesecky of Stanford University, and R. Stewart of Scripps Institute of Oceanography provided sea-truth information collected during JASIN; and G. Meadows of the University of Michigan provided oceanographic expertise.

It should be noted that the wave focusing analysis described in this report was partially supported by funding under the Seasat Announcement of Opportunity. The contract number is MO-A01-78-00-4339 and is monitored by Messrs. J. W. Sherman, III and P. Deleonibus. The analysis of deep water mesoscale features was partially supported by funding provided by the Naval Research Laboratory (NRL). The NRL Contract Numbers are N00014-81-C-2254 and N00014-82-C-2308 and are monitored by Mr. P. A. Mitchell.

TABLE OF CONTENTS

PREFACE.....	iii
ACKNOWLEDGMENTS.....	iv
1. INTRODUCTION.....	1
2. BACKGROUND.....	3
2.1 The Joint Air-Sea Interaction Experiment.....	3
2.2 The Seasat Synthetic Aperture Radar.....	5
3. JASIN/SEASAT WAVE ANALYSIS.....	9
3.1 Fast Fourier Transform Analysis.....	9
3.1.1 Methods.....	10
3.1.2 Results.....	14
3.2 SAR Detection of Gravity Waves.....	17
3.2.1 Methods.....	17
3.2.2 Results.....	20
3.3 SAR Motion Corrections.....	22
3.3.1 Methods.....	26
3.3.2 Results.....	30
3.4 Wave Height Determination Using Digitally Processed Seasat SAR Imagery.....	35
3.4.1 Theoretical Development.....	35
3.4.2 Results.....	41
4. DETECTION OF MESOSCALE FEATURES.....	47
4.1 The JASIN Test Area.....	47
4.2 Occurrence of Mesoscale Features.....	50
4.3 Analysis of Internal Wave and Frontal Boundary Patterns..	70
4.3.1 Internal Wave Signatures.....	70
4.3.2 Frontal Boundaries.....	84
5. SUMMARY.....	89
APPENDIX A. SEASAT/JASIN PASSES.....	91
APPENDIX B. DIGITAL FOURIER TRANSFORMS OF JASIN SEASAT SAR DATA..	111
APPENDIX C. "THE ESTIMATION OF WAVE HEIGHT FROM DIGITALLY PROCESSED SAR IMAGERY".....	119
APPENDIX D. PAPERS PUBLISHED ON JASIN USING RESULTS OF ONR- SPONSORED RESEARCH.....	127
REFERENCES.....	199

LIST OF FIGURES

Figure 1.	Joint Air-Sea Interaction (JASIN) Experiment Area Showing Typical Seasat SAR Image Swaths and Sections of Images Used for Wave Analysis.....	4
Figure 2.	Example of Two-Dimensional FFT and Resultant One-Dimensional Wave Direction and Wave Number Spectra.....	12
Figure 3.	Sea Truth Versus SAR Derived Estimates of Dominant Wavelength and Direction of Propagation for JASIN Data.....	16
Figure 4.	Peak-to-Background Ratio Versus Telerotation Adjustment.....	31
Figure 5.	Two-Dimensional Fast Fourier Transforms and One-Dimensional Wave Direction and Wave Number Spectra Versus Telerotation Adjustments for Seasat Rev. 762 Data.....	34
Figure 6.	Peak-to-Background Ratio Versus Azimuth Focus Shift....	35
Figure 7.	Two-Dimensional Fast Fourier Transforms and One-Dimensional Wave Direction and Wave Number Spectra Versus Telerotation Adjustments for Seasat Rev. 1087 Data.....	37
Figure 8.	Comparison of Measured and Theoretical Cross-Sections of The Oceans for a Radar Frequency of 428 MHz, Horizontal Polarization.....	40
Figure 9.	Location of Major Bottom Topographic Features in Northeast Atlantic.....	48
Figure 10.	Coverage of Northeast Atlantic Ocean by the Seasat SAR From Overflights Made During the Jasin Experiment.....	51
Figure 11.	Locations of Jasin Test Area and Areas Examined During Deep Water Survey.....	52
Figure 12.	Seasat SAR Imagery Collected Over the Wyville-Thomson Ridge During Rev. 599.....	54

LIST OF FIGURES (CONTINUED)

Figure 13.	Ground Coverage Corresponding to Seasat SAR Rev. 599...	55
Figure 14.	Seasat SAR Image Collected Over Anton Dohrn Seamount During Rev. 791.....	56
Figure 15.	Ground Coverage of Rev. 791 Over Anton Dohrn Seamount..	57
Figure 16.	Seasat SAR Image of a Frontal Boundary Collected over Faeroe Bank Channel and Faeroe Ridge, Rev. 762.....	58
Figure 17.	Ground Coverage of Seasat SAR Rev. 762 Over Wyville- Thomson Ridge.....	59
Figure 18.	Wind Rows Imaged During Rev. 642.....	61
Figure 19.	Area of Low Radar Return Imaged During Rev. 547.....	62
Figure 20.	Location of Internal Wave-Like Signatures Identified on Seasat SAR Images Collected Over the JASIN area....	67
Figure 21.	Location of Frontal Boundaries Identified on Seasat SAR Images Collected Over the JASIN Area.....	69
Figure 22.	Seasat SAR Imagery of Deep Water Features Over the Wyville-Thomson Ridge; Rev. 762,.....	77
Figure 23.	Line Drawing of Internal Waves and a Frontal Boundary Observed in Figure 22 Superimposed on the Hydrographic Chart of the Northeast Atlantic Ocean.....	78
Figure 24.	Longitudinal and Transverse Bathymetric Profiles Across Ridge, with a Saddle-Like Valley at 0.....	79
Figure 25.	Schematic Diagram Summarizing the Generation and Evolution of an Internal Wave Packet over the Wyville- Thomson Ridge.....	81
Figure 26.	Profiles of Potential Temperature, Salinity, and Sigma Theta From Data Collected Over the Icelandic-Faeroe Rise Illustrating Deep Water Upwelling.....	83
Figure 27.	Cross-Section Diagram of Bottom Topography of the Wyville-Thomson Ridge.....	86
Figure 28.	Schematic Diagram Illustrating Deep Water Upwelling Over the Faeroe Bank Channel.....	87

LIST OF TABLES

Table 1.	Radar Parameters of the Seasat Synthetic Aperture Radar...	8
Table 2.	Sea Truth and Seasat Satellite Parameters for JASIN Data.....	15
Table 3.	Summary of Wavelength, Height, and Direction Data for JASIN Data.....	21
Table 4.	Derived Sea Truth Parameters for JASIN Experiment.....	23
Table 5.	Linear Correlations Between Wave Contrast and Environmental Parameters for JASIN Seasat Data.....	24
Table 6.	Multiple Linear Correlation Coefficients.....	25
Table 7.	Peak-to-Background Ratio Versus Telerotational Adjustment and Azimuth Focus Shift.....	32
Table 8.	Fast Fourier Transform Estimates of Dominant Wavelength and Direction as a Function of Range Telerotation Adjustments for Seasat Rev. 762.....	33
Table 9.	Fast Fourier Transform Estimates of Dominant Wavelength and Direction as a Function of Azimuth Focus Shift for Seasat Rev. 1087.....	38
Table 10.	Wave Height Calculations.....	44
Table 11.	Bottom Topographic Features in the Northeastern Atlantic.....	48
Table 12.	Summary of Occurrences of Bottom-Related Surface Patterns on Seasat SAR Imagery.....	64
Table 13.	Summary of Detections of Deep Water Topographic Features by Seasat SAR Imagery Using Data Collected During the JASIN Study.....	68
Table 14.	Summary of the Occurrence of Wind Rows and Areas of Low Radar Return.....	71
Table 15.	Comparison of Internal Wave Detection Groups to Environmental Parameters.....	73
Table 16.	Orientation of Internal Waves Observed on Seasat SAR Imagery Collected Over the JASIN Area.....	75

ANALYSIS OF SEASAT SAR IMAGERY COLLECTED
DURING THE JASIN EXPERIMENT1
INTRODUCTION

This report presents results from a continuing study for the Office of Naval Research of synthetic aperture radar imagery collected by the Seasat satellite (see Kasischke, 1980; Kasischke and Shuchman, 1981; Vesecky, et al., 1982, 1982a). This study investigated in detail Seasat SAR imagery collected over the North Atlantic Ocean during the Joint Air-Sea Interaction (JASIN) experiment during the summer/fall of 1978. The results of an associated JASIN/Seasat study, an investigation of the use of Seasat SAR data to estimate surface wind speed, are presented in a separate document (see Lyden, et al., 1983).

This study considered the Seasat SAR's ability to detect and measure ocean gravity waves and its potential for imaging large, mesoscale surface features such as internal waves, frontal boundaries and weather related patterns. This report, which discusses the various analyses performed during the study, is organized into five chapters, including this introduction, plus four appendices.

Chapter 2 discusses the background of the JASIN experiment and briefly reviews the Seasat SAR system. Chapter 3 discusses the additional analyses performed on the Seasat SAR wave imagery beyond those conducted during the initial study reported by Kasischke (1980). This chapter includes sections on correlations between sea truth and occasions when the Seasat SAR imaged gravity waves, the testing of SAR image enhancement routines on Seasat data, and assessment of a technique to extract wave height information from SAR imagery. Chapter 4 discusses the Seasat SAR's ability to detect three mesoscale surface features present in the JASIN test area: internal waves,

frontal boundaries, and surface features associated with meteorological phenomena. Finally, Chapter 5 presents a summary of this investigation.

Appendix A to this report presents diagrams outlining the location of each Seasat SAR pass used during this study. Each diagram also summarizes the wind and wave conditions present on that date. Appendix B presents the fast Fourier transforms which were generated from the JASIN Seasat SAR imagery. Appendix C presents a paper by Thomas (1982) which proposes a technique to extract wave height information from Seasat SAR data. This technique is evaluated in Chapter 3. Appendix D to this report contains copies of articles which resulted from the ONR-sponsored research of the Seasat SAR data collected during JASIN.

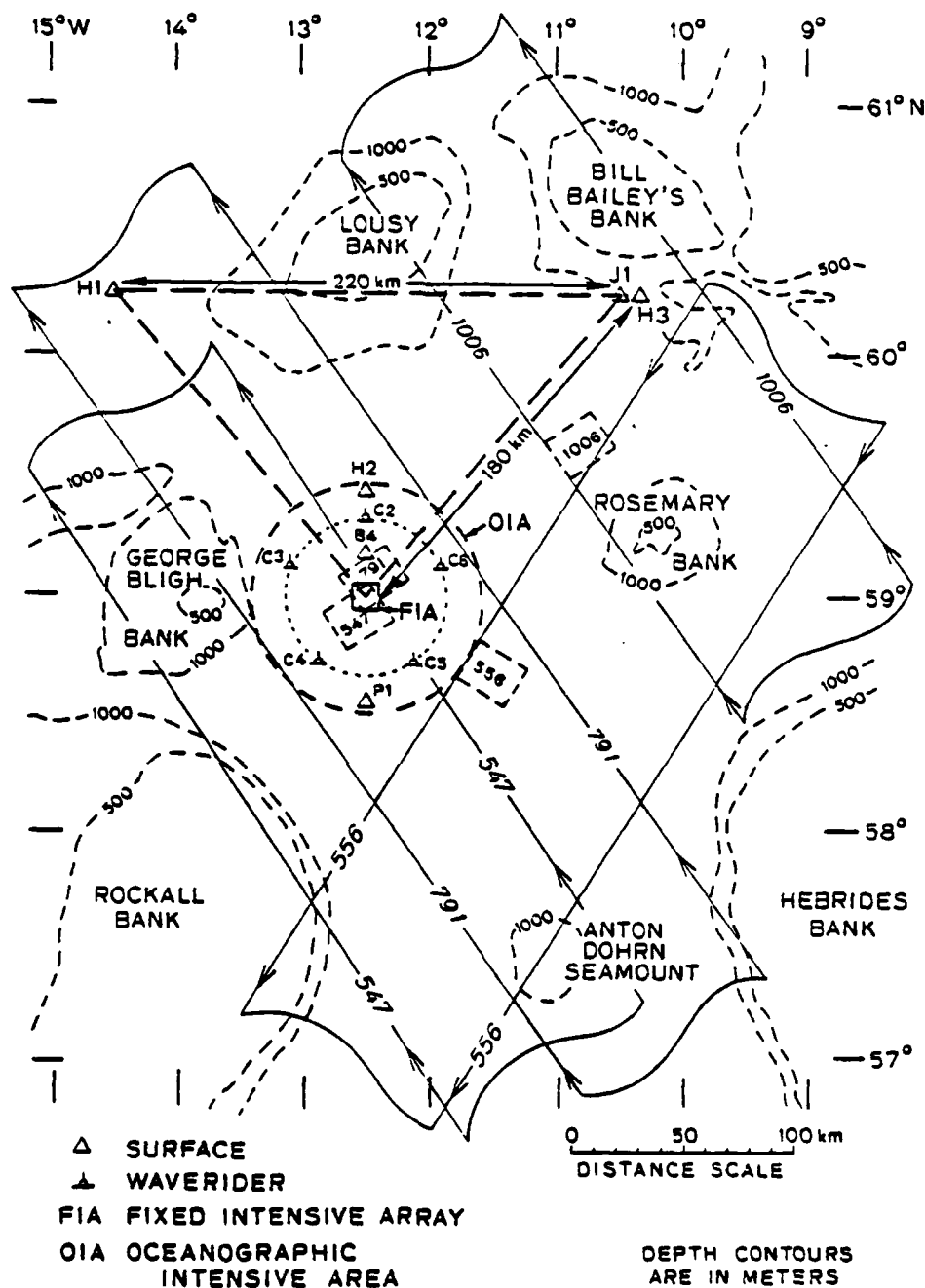


FIGURE 1. JOINT AIR-SEA INTERACTION (JASIN) EXPERIMENT AREA SHOWING TYPICAL SEASAT SAR IMAGE SWATHS AND SECTIONS OF IMAGES USED FOR WAVE ANALYSIS. (The Permanently Anchored Waverider Buoys Are Denoted C2 through C6. The Ship Deployed Pitch and Roll Buoys Were Typically Set in the FIA Area. After Vesecky, et. al., 1982.)

2 BACKGROUND

This chapter briefly reviews the Joint Air-Sea Interaction experiment and the synthetic aperture radar onboard the Seasat satellite. For a more in-depth discussion of the JASIN experiment, see Allan and Guymer (1980). For a review of the Seasat SAR's capabilities to image oceanographic phenomena, see Beal, et al. (1981), Shuchman, et al. (1981) or Fu and Holt (1982).

2.1 THE JOINT AIR-SEA INTERACTION EXPERIMENT

Data used in this study were collected during the Joint Air-Sea Interaction (JASIN) experiment. The JASIN experiment was proposed in 1966 as part of the Global Atmospheric Research Project and was sponsored and organized by the Royal Society of the United Kingdom. The primary aims of the JASIN experiment were to "observe and distinguish between the physical processes causing mixing in the atmospheric and oceanic boundary layers and relate them to mean properties of the layers; and to examine and quantify aspects of the momentum and heat budgets in the atmospheric and oceanic boundary layers and fluxes across and between them" (Royal Society, 1979). To this end, fifty principal investigators from nine countries collaborated on an intensive experiment from mid-July to mid-September, 1978. Fourteen oceanographic research vessels were on site at one time or another during this period. The JASIN experiment took place in the North Atlantic, in an area just west of Scotland, as is shown in Figure 1. Most of the meteorologic and oceanographic observations were made within the Oceanographic Intensive Area (OIA) (the large, "dashed-line" circle in Figure 1), but ships operating in the large triangular region made observations as well. Wave data were obtained from visual observations from these ships, from wave recorders mounted on the ships, from wave buoys deployed by the ships, and from

the returned echoes are processed to determine the distance to the scene and to obtain the measure of relative strength of the return (σ_0). In real-aperture systems, the resolution in azimuth is limited by the beamwidth (i.e., the physical length) of the antenna. Since resolution decreases with range for such systems, operation at spacecraft altitudes is not possible with real-aperture radars.

Synthetic aperture radar is a coherent radar that uses the motion of a moderately broad physical antenna beam to synthesize a very narrow beam, thus providing fine azimuthal (along-track) resolution (Brown and Porcello, 1969; Harger, 1970). Fine range (cross-track) resolution is achieved by transmitting either very short pulses or longer coded pulses which are compressed by matched-filtering techniques into equivalent short pulses. Usually, the coded pulse is a waveform linearly modulated in frequency.

Historically, in SAR systems, the phase history of a scattering point in the scene is recorded on photographic film as an anamorphic (astigmatic) Fresnel zone plate. The parameters of the zone plate are set in the azimuth direction by the Doppler frequencies produced by the relative motion between the sensor and the point scatterer, and in the range direction by the structure of the transmitted pulses. The film image is a collection of superimposed zone plates representing the collection of point scatterers in the scene. This film is used by a coherent optical processor (a set of spherical and cylindrical Fourier transform lenses) which focuses the anamorphic zone plates into the points which produced the microwave scatter of the scene (Kozma, et al., 1972).

Recently, SAR systems have employed digital techniques to both record and process the data. Digital processing typically uses matched filtering techniques to "dechirp" the signal in range, while Fast Fourier Transform (FFT) techniques achieve the required azimuthal compression of the SAR Doppler history (Ausherman, 1980).

permanently anchored wave rider buoys. The wave rider buoys were anchored within the OIA.

Seasat, launched just prior to the JASIN experiment, offered investigators a unique opportunity to collect satellite data over a well instrumented test site. A Seasat SAR receiving station had been set up at Oakhangar, England for the European Space Agency and radar data were collected on twenty different occasions when Seasat passed over or near the JASIN study area. The geographical relationship (to the JASIN area) of the eighteen Seasat passes examined for the JASIN study are presented in Appendix A of this report. Data from the other two passes were of too poor quality to process.

2.2 THE SEASAT SYNTHETIC APERTURE RADAR

The data presented in this report were collected by the Seasat satellite. Among the instrumentation carried by Seasat, which was launched during June of 1978, was a synthetic aperture radar (SAR). This satellite collected over 500 passes of SAR data before suffering a catastrophic power loss in October of 1978. The SAR on board Seasat was an L-band (23.5 cm wavelength) radar. It collected 25 x 25 meter resolution imagery with a ground swath-width of 100 km and a swath-length of up to 4000 km, and viewed the surface of the earth with an average incidence angle of 20°.

An imaging radar such as the Seasat SAR is an active device that senses the environment with short wavelength electromagnetic waves. As an active sensor, the Seasat SAR provided its own illumination in the microwave region of the electromagnetic spectrum and thus was not affected by diurnal changes in emitted or reflected radiation from the earth's surface.

Side-looking radars such as the Seasat SAR use pulse ranging, whereby the radar antenna attached to a moving platform illuminates a section of the ground and the amplitude, phase and polarization of

TABLE 1
RADAR PARAMETERS OF THE SEASAT SYNTHETIC APERTURE RADAR (SAR)

Frequency	1274.8 MHz
Wavelength	23.5 cm (L-band)
Transmitted Bandwidth	19 MHz
Pulse Duration	33.8 μ sec
Pulse Time-Bandwidth Product	642
Transmitter RF Power	800 W Peak - 46 W Average
Transmitter Type	Solid-State Bipolar Transmitter
PRF	1647
Satellite Altitude	~800 km
Nominal Range (20°)	~850 km
Antenna Beamwidth, Elevation	6°
Antenna Beamwidth, Azimuth	1°
Antenna Pointing Angle	19-25° off nadir, right side
Surface Resolution	25 m x 25 m (4 look data)
Slant Range Resolution	8 m
Azimuth Resolution (one look)	6.25 m
Integration Time:	0.5 to 2.5 sec depending on resolution
Image Swath Width	100 km
Image Length	250 to 4000 km
Sensor Power	60 W, nominal operation
Satellite Velocity	~7800 m/sec
Satellite Altitude	~800 km
Nominal Range (20°)	~850 km

After appropriate system corrections, digital data have better geometric and radiometric fidelity than optical data and are subject to fewer image processing artifacts such as noise streaks. Additionally, digital data recorded in square root mode can store 40 dB worth of information. In contrast, an optical SAR image has only an 18 dB dynamic range. A disadvantage of digital SAR data is that processing algorithms are quite slow, particularly when one-look (full resolution) data are required. Due to long processing times (i.e., 8 hours for a 100 x 100 km Seasat scene), a limited amount of digital Seasat SAR data exists. The optical processing time for a 100 x 100 km scene is approximately one minute, excluding set-up or film development.

Specific parameters of the Seasat SAR system are presented in Table 1. The wavelength at which the Seasat SAR system operates, 23.5 cm, does not penetrate more than a few centimeters into the water surface. Therefore, the recorded signal is primarily reflected from the water's surface and is a function of the surface roughness, slope, and motion of the scatterers. The 23.5 cm wavelength will also determine the ocean wavelength (Bragg wave) to which the SAR is most sensitive. The Bragg ocean wavelength for resonance for the Seasat SAR parameters is approximately 36 cm. The bandwidth and incidence angle, given in Table 1, determine the ground range resolution. The range to target, velocity, azimuth resolution and antenna dimensions are information that can be utilized to determine the synthetic aperture length. This information indicates an azimuth resolution of 6.25 m on the ground requires a synthetic aperture length of approximately 140 m. Seasat traveling at 800 km altitude had an orbital speed of 7.9 m/s, and therefore required about two seconds to synthesize the required aperture.

3 JASIN/SEASAT WAVE ANALYSIS

The initial analysis of the Seasat SAR imagery collected during the JASIN experiment focused on two areas (see Kasischke, 1980; Kasischke and Shuchman, 1981; Vesecky, et al., 1982, 1982a): (1) comparison of dominant wavelength and direction of gravity waves derived from SAR data to those obtained from surface measurement devices; and (2) analysis of the conditions under which the Seasat SAR imaged surface gravity waves, using a wave contrast measurement (peak-to-background ratio or PBR).

Since then, additional analyses have been performed on the JASIN Seasat SAR wave data:

1. Generation of digital fast Fourier transforms from all 18 JASIN passes,
2. Updating of surface truth information and further analysis of the wave contrast measurements,
3. Testing of motion compensation algorithms on Seasat SAR images of gravity waves, and
4. Evaluation of a technique published by Thomas (1982) to extract wave height estimates from Seasat SAR data.

This chapter discusses these activities.

3.1 FAST FOURIER TRANSFORM ANALYSIS

Previous comparisons of dominant wavelengths and directions of gravity waves derived from Seasat SAR data to surface truth estimates were based largely on the use of large area optical Fourier transforms (OFTs). Although it was demonstrated during these earlier studies that OFT estimates of dominant wavelength and direction compare favorably to surface measured estimates, there are several

shortcomings in this technique. First, using OFTs requires manual measurement of the distance to the center of the OFT spectrum and the spectrum orientation. Thus, this technique introduces the variability of the human interpreter. Next, to generate the OFTs from the JASIN Seasat data, very large apertures were used (25 by 25 km). In areas where waves are undergoing transformations, such as refraction (in shoaling water) or diffraction (around islands), it is not always practical to use such large apertures. Finally, in the near future, nearly all SAR data will be digitally processed. To produce OFTs, it will be necessary to first generate an image from the digital data, adding an additional step to the analysis.

The purpose of this portion of the study was to generate fast Fourier transforms of the Seasat SAR data collected during the JASIN experiment.

3.1.1 METHODS

All digital data discussed in this report were generated by ERIM's hybrid optical-digital processor (Ausherman, et al., 1975). The SAR image films (optically processed at ERIM) of ocean gravity waves from the JASIN Seasat passes were digitized using a 12.5 meter by 12.5 meter pixel aperture. A 1024 by 1024 line-by-point area was generated and the data recorded on a computer compatible tape (CCT). The area selected for digitization was the portion of the pass which was closest to the position where the concurrent surface gravity wave measurements were collected (see Appendix A).

The digital SAR ocean wave imagery was then analyzed using a standard computer package developed by ERIM under sponsorship of the Office of Naval Research (see Shuchman, et al., 1979). Using this routine, a 512 by 512 pixel subset of the digital data is extracted from the CCT. Usually the SAR data are geometrically rectified, but since the ERIM data had been previously geometrically corrected when

the data were optically correlated, this step was not necessary. The data are then corrected for long-period variations (such as power loss or antenna gain) to remove D.C. bias, smoothed using a $(\sin x)/x$ filter to reduce radar speckle and resampled to 256 by 256 pixels. This resampling results in a pixel size of 25 by 25 meters. These data are then inputted to a fast Fourier transform program to generate spectral estimates from the SAR data.

When the digital SAR data are fast Fourier transformed, the results are typically displayed as two-dimensional contour plots. Presented in Figure 2 is a typical two-dimensional contour plot produced from an FFT of SAR ocean wave data and one-dimensional spectra derived from it. Each of the three contour levels in Figure 2a represents 3 dB of energy from the SAR image. These three contour levels range from -3 dB to -9 dB (i.e., one-half to one-eighth of the peak value). Although this FFT produces no wave height information, the two-dimensional contour plot does portray wave number and wave direction information. The x-axis of the plot represents azimuth direction and the y-axis the range direction, with the units on the axes being wave number (k). By finding the center of the highest contour level in the spectrum, and measuring k_{range} and k_{azimuth} , an estimate of the dominant wave number (and hence wavelength) can be calculated, as can an estimate of the wave's orientation. If the SAR platform's direction is known, an estimate of the dominant wave direction can be calculated. Note, there is still a 180° ambiguity in the wave direction data.

The information in the two-dimensional FFT spectrum can be more rigorously analyzed. To do so, one-half of the plot in Figure 2a is summed digitally over specified wave number ranges to produce a one-dimensional wave number spectrum, as is shown in Figure 2b. Finally, a one-dimensional wave direction spectrum (usually at the peak wave number) can be plotted, as is presented in Figure 2c. The digital output from these plots can be consulted to extract exact estimates of dominant wavelength and direction.

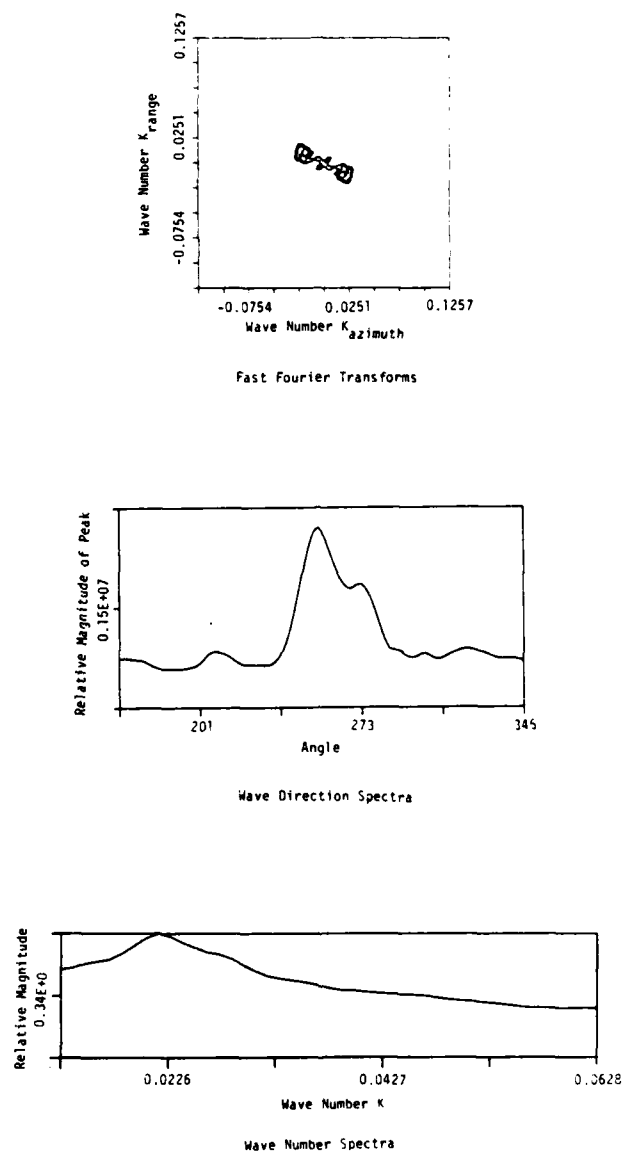


FIGURE 2. EXAMPLE OF TWO-DIMENSIONAL FFT AND RESULTANT ONE-DIMENSIONAL WAVE DIRECTION AND WAVE NUMBER SPECTRA. (Seasat Rev. 1087 Data.)

During the JASIN experiment, surface truth (wave data) were collected by a variety of different instruments. This instrumentation included pitch and roll buoys (Stewart, 1977) deployed from the R/V Atlantis II and R/V Discovery, a set of moored wave rider buoys which were within the Oceanographic Intensive Area, wave recorders onboard the R/V John Murray and R/V Discovery and visual readings made from the R/V John Murray. The exact location of the research vessels varied day to day depending on what experiments they were participating in, but all obtained wave data at the time of the Seasat overpass, or at worst, within an hour or two of it. The wave rider buoys were all located within the Oceanographic Intensive Area (their exact locations are marked by Figure 1) and the data from these were collected at the times of the Seasat overpasses.

Wave data and sea-truth estimates were processed using standard oceanographic techniques at the Scripps Institute of Oceanography. Included in this sea-truth data set were estimates of dominant wavelength and direction, wave height ($H_{1/3}$) and surface wind speed and direction. The two-dimensional ocean wave frequency spectra, $F(\theta, \omega)$ obtained from the buoys and wave recorders were converted to wave number spectra using the Jacobian approximation (g^2/ω^3 , where g is the gravitational acceleration and ω is the wave frequency) appropriate to deep water waves (Vesecky, et al., 1981).

Because several of the test dates had more than one available set of sea-truth, it was necessary to decide which value to use to compare to the FFT value. Available sea-truth was therefore ranked according to the desirability of the data source, as follows:

- | | |
|-------|--|
| BEST | 1. <u>Atlantis II</u> Pitch and Roll Buoy or <u>Discovery</u> Pitch and Roll Buoy. |
| ↓ | 2. Moored OIA Wave Rider Buoy. |
| ↓ | 3. <u>John Murray</u> Wave Recorder or <u>Discovery</u> Wave Recorder. |
| WORST | 4. <u>John Murray</u> Visual Readings. |

If no sea-truth data were available using the most desirable category, then the next highest category which contained the desired sea-truth data was used.

3.1.2 RESULTS

The two-dimensional fast Fourier transforms and their resultant one-dimensional wave-number and wave direction spectra (when appropriate) are presented in Appendix B to this report.

Table 2 summarizes the coincident surface measured wave and wind data along with the SAR-derived estimates of dominant wavelength and direction and wave contrast for the eighteen SAR overpasses made during the JASIN experiment. Included in Table 2 are the Seasat pass number, the date and time the SAR data were collected, the source of the sea truth used to compare to the SAR data, the distance between the SAR and surface observations, the surface measured values for dominant wave direction (θ_T), dominant wavelength (λ), significant wave height ($H_{1/3}$), wind speed (U) and wind direction (α_T) and SAR derived estimates of wave direction (θ_T -OFT and θ_T -FFT), wavelength (λ -OFT and λ -FFT) and wave contrast (PBR). (See Kasischke, 1980 for a discussion on wave contrast.)

From Table 2, we can see that estimates of dominant wavelength and direction were obtained from Seasat SAR data from thirteen passes using OFTs, and from seven passes using FFTs. Figure 3 plots the SAR derived (FFT) estimates of wavelength and direction versus the surface measured values.

For wavelength, it can be seen that both the estimates derived from FFTs and OFTs tend to be longer than the sea truth values, with the FFT values being somewhat longer. There are two cases where the OFT derived value varies significantly from the surface measured value of direction of wave propagation. Other than these two cases, there is very little variation. From Table 2 and Figure 3, it can be seen that the FFTs and OFTs give essentially the same result.

TABLE 2
SEA TRUTH AND SEASAT SATELLITE PARAMETERS FOR JASIN DATA

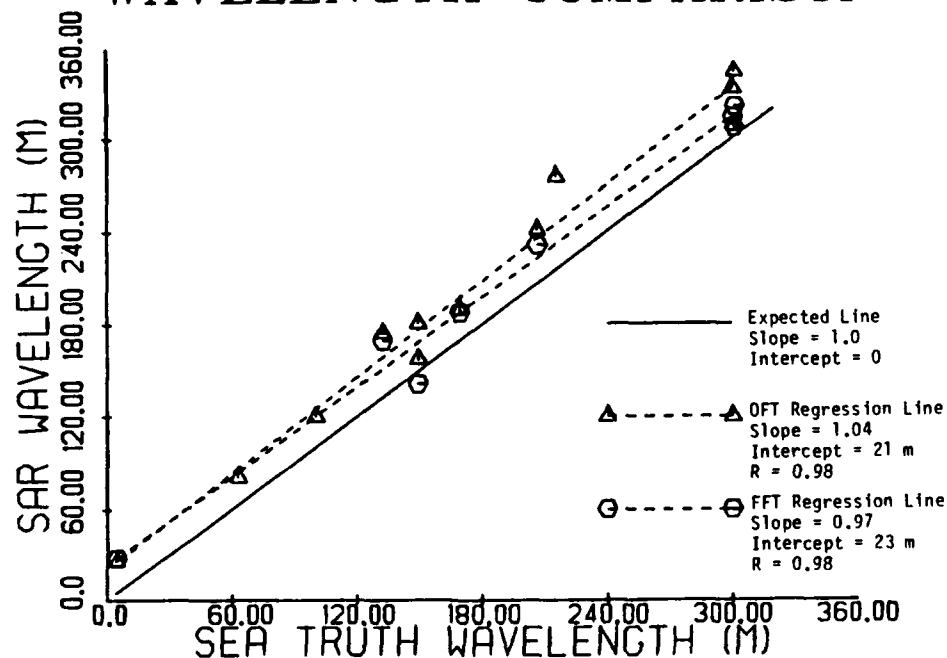
Pass	Satellite Data		Sea Truth Data			SAR-Derived Estimated									
	Date	Time (GMT)	Satellite Heading	SIS*	Distance Between Sea Truth and SAR (km)	θ_T (°)	λ (m)	$H_{1/3}$ (m)	U (m/s)	σ_T (°)	σ_T (°)	θ_T (°)	λ (m)	λ (m)	PBR
547	4 Aug. 78	0615	321	a	10	263	169	1.7	4.5	8	260	261	189	187	1.45
556	4 Aug. 78	2135	216	a	65	280	149	1.5	3.5	20	274	273	157	141	1.15
590	7 Aug. 78	0622	323	a	15	229	222	1.3	7.2	356	***	***	***	***	1.00
599	7 Aug. 78	2143	215	b/f	145	20	71	1.1	6.9	356	***	***	***	***	1.00
633	10 Aug. 78	0629	323	a	58	220	89	1.1	9.2	145	***	***	***	***	1.00
642	10 Aug. 78	2150	214	a	210	199	169	2.9	12.9	150	***	***	***	***	1.00
714	15 Aug. 78	2235	217	---	---	---	---	---	---	---	276	***	182	***	1.08
719	16 Aug. 78	0643	323	---	---	---	---	---	7.6	304	248	***	164	***	1.16
757	18 Aug. 78	2240	215	b	10	240**	215	4.9	15.2	186	253	***	275	***	1.21
762	19 Aug. 78	0641	324	d/f	45	240	206	4.3	12.0	186	234	227	241	231	2.17
791	21 Aug. 78	0724	325	b/f	35	230	132	3.3	13.0	235	252	252	174	169	1.81
834	24 Aug. 78	0730	324	a	55	295	149	2.8	10.2	272	271	***	180	***	1.16
958	1 Sept. 78	2354	215	c/b	32	354	100	1.3	7.2	255	296	***	120	***	1.00
1001	5 Sept. 78	0006	219	a	30	146	63	2.5	12.6	114	125	***	81	***	1.47
1006	5 Sept. 78	0815	322	a	70	83	107	3.6	6.6	91	***	***	***	***	1.00
1044	8 Sept. 78	0018	220	c/e	30	264**	301	3.5	11.5	195	257	264	344	321	2.56
1049	8 Sept. 78	0827	323	c/e	30	264	301	3.5	6.3	263	246	254	308	307	2.22
1087	11 Sept. 78	0030	221	---	---	---	---	---	13.2	046	253	253	299	289	1.88

* a. Atlantis II, Pitch and roll buoy.
b. Moored OIA, wave rider buoy.
c. Discovery, pitch and roll buoy.
d. John Murray, wave recorder.
e. Discovery, wave recorder.
f. John Murray, visual readings.

** Estimate.

*** IfT of SAR data did not produce a spectra which could be interpreted.

WAVELENGTH COMPARISON



DIRECTION OF WAVE PROPAGATION COMPARISON

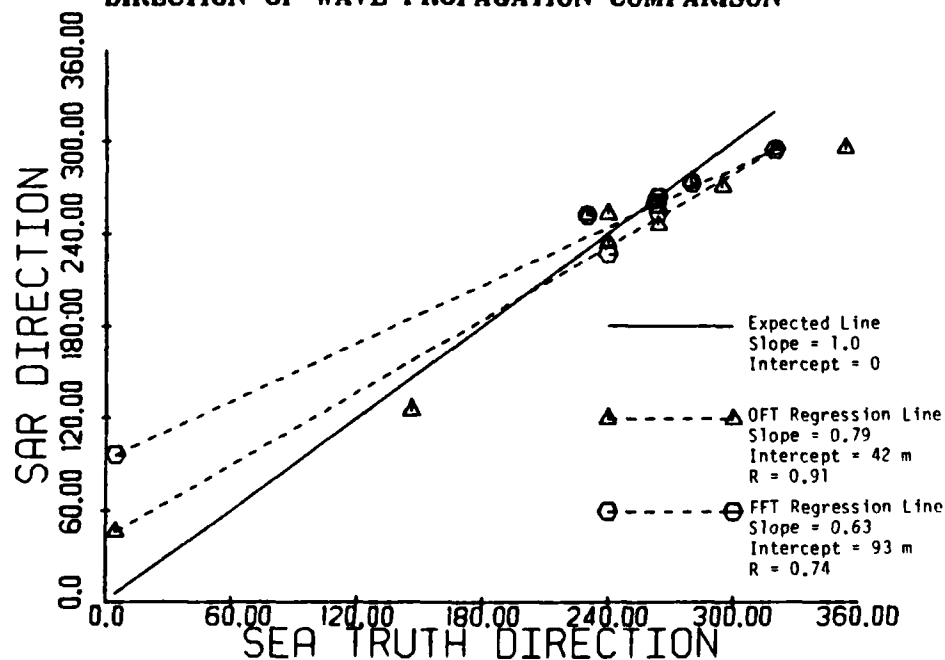


FIGURE 3. SEA TRUTH VERSUS SAR DERIVED ESTIMATES OF DOMINANT WAVELENGTH AND DIRECTION OF PROPAGATION FOR JASIN DATA.

It is interesting to note that the OFT technique provided spectral wave estimates on data for which the FFT technique showed no dominant wave. Recall that an aperture of 25 by 25 kilometers was used for each OFT, while an aperture of 6.4 by 6.4 kilometers was used for each FFT. Thus, the aperture for the OFTs was over 15 times as large as the aperture for FFTs. Hence, the OFTs has a better spectral resolution than the FFTs and therefore could in some cases resolve wave spectra features (dominant wavelength) and direction where the FFT could not. This large of an aperture can be used in areas where little change in wavelength and direction are occurring, but would probably result in very diffuse spectra in areas of wave refraction or diffraction. Also, because of the computation time involved, most FFT routines used today are limited to areas of 256 by 256 pixels.

3.2 SAR DETECTION OF GRAVITY WAVES

In determining whether a spaceborne SAR system will be an effective tool for gathering wave data, an area of important consideration is understanding the conditions under which a SAR will and will not image gravity waves. The JASIN data set provides a valuable opportunity to examine this question because, not only were a wide variety of surface measurements made which can be compared to the SAR data, but also because a wide spectrum of environmental conditions were encountered during the time span of the JASIN study.

3.2.1 METHODS

Both qualitative and quantitative techniques were applied to look for correlations between SAR imaging of gravity waves and environmental parameters. These parameters were either directly measured as part of the surface truth, or derived from the surface truth using theoretical relationships.

As mentioned in the previous section, wave measuring instruments collected wave period and directional data at or near the areas where SAR data were collected. From these wave data, significant wave heights ($H_{1/3}$) were also calculated. Other surface measurements of potential interest are surface wind speed (U) and direction (α).

When examining directional data (wind or wave), it is important to know how the waves (or wind) are traveling with respect to the radar look direction. The following directional variables were calculated:

1. θ_A : Normalized wave direction. When $\theta_A = 0^\circ$, the waves are traveling in the same direction as the SAR platform; when $\theta_A = 180^\circ$, the opposite direction
2. θ_{AC} : Wave direction normalized to a 0° to 90° range (where 0° is an azimuth traveling wave and 90° is a range traveling wave)
3. α_S : Wind direction relative to the radar look direction (normalized to a 0° to 90° range, where 90° would be a wind blowing perpendicular to the SAR look direction)
4. α_W : Wind direction relative to wave direction (normalized to a 0° to 90° range, where 90° would be a wind blowing perpendicular to the wave direction of travel).

It has been theorized that factors which might affect SAR imaging of gravity waves include the local tilt of the water surface (Elachi and Brown, 1977) and the orbital velocity of the gravity waves which causes a bunching of the smaller capillary and ultra-gravity waves (Alpers and Rufenach, 1979; Phillips, 1981).

Wave slope (S) can be defined as:

$$S = H_{1/3}/\lambda \quad (1)$$

where λ = the dominant wavelength.

Kinsman (1965) defines the orbital velocity of a gravity wave (v_o) as:

$$v_o = \frac{\omega H^{1/3}}{4} \quad (2)$$

where ω = wave frequency $(2\pi g/\lambda)^{1/2}$.

A normalized orbital velocity (v_n), defined as the orbital velocity in the direction of radar line-of-sight, can be calculated as:

$$v_n = v_o \sin \theta_{AC} \quad (3)$$

The surface measurements and derived variables were compared to the Seasat SAR data in both a qualitative and quantitative manner. For the qualitative comparison, the SAR data were subjectively divided into three visibility categories, and common denominators within these categories for surface measurements were determined. For the quantitative analysis, a wave crest-to-trough contrast measurement was used as a numerical indicator of visibility of waves on SAR imagery and statistically correlated to the various surface measurements and derived variables.

The SAR imagery collected over the JASIN area was visually examined and classified as having waves in one of three categories: (1) GOOD imagery, where gravity waves are clearly visible on the SAR image; (2) POOR imagery, where gravity waves are present, but detected only upon close inspection; and (3) NONE imagery, where no gravity wavelike patterns are visible on the SAR image. Upon categorizing the imagery, the surface measurements and derived data for each category were examined to determine if a trend could be detected.

The data set was then more rigorously analyzed by statistically comparing the surface measurements and derived variables to a recently developed wave crest-to-trough contrast measurement known as a

peak-to-background ratio (Kasischke, 1980; Kasischke and Shuchman, 1981). The peak-to-background ratio (PBR) is measured as follows: First, the peak intensity of the Fourier transform spectrum is extracted (either measured from an optical Fourier transform or digitally derived from a fast Fourier transform). Next, a minimum intensity from the same k-space as the peak intensity is extracted. The ratio of these two intensities (i.e., peak/minimum) is defined as the peak-to-background ratio. For this portion of the study, the peak and minimum intensities were measured as film densities of the photographic negative of the spectrum obtained from an optical Fourier transform of the wave data.

The peak-to-background ratios for the eighteen JASIN SAR overpasses were linearly correlated (Draper and Smith, 1966) to the various surface measurements and derived variables (such as wave slope, orbital velocity and normalized orbital velocity) to determine where a relationship might exist. It should be noted that a linear correlation does not imply that a cause/effect relationship exists between two variables in an a posteriori examination of the data such as is presented here; it only suggests where such a relationship might exist.

3.2.2 RESULTS

Table 3 lists wavelength (λ), wave height ($H_{1/3}$) and radar look direction normalized to the direction of wave travel (θ_{AC}) for the three classes of SAR wave imagery (i.e., GOOD, POOR and NONE). For θ_{AC} , a 0° reading means the waves are traveling parallel to the radar line-of-sight and a 90° reading indicates the waves are traveling perpendicular to the radar line-of-sight. An examination of Table 3 reveals that one of two conditions existed when waves were not visible on the SAR imagery: (1) the wave height ($H_{1/3}$) was less than 1.3 meters; or (2) the waves were traveling nearly parallel to the radar line-of-sight ($\theta_{AC} < 35^\circ$). For the POOR

TABLE 3
SUMMARY OF WAVELENGTH, HEIGHT, AND DIRECTION
DATA FOR JASIN DATA*

<u>Revolution</u>	<u>λ</u>	<u>$H_{1/3}$</u>	<u>θ_{AC}</u>
<u>None</u>			
590	89-222	1.3	84°-6°
599	71	1.1	15°
633	89	1.1	77°
642	169	2.9	15°
1006	105	3.6	33°
<u>Poor</u>			
556	149	1.5	64°
714	182*	---	59°*
719	164*	---	75°*
834	149	2.8	29°
958	100	1.3	41°
<u>Good</u>			
547	169	1.7	58°
757	215	4.9	25°
762	206	4.3	90°
791	132	3.3	85°
1001	63	2.5	73°
1044	301*	3.5	44°
1049	301	3.5	59°
1087	299*	---	32°

All data use sea truth estimates except for those denoted with an (), where SAR estimates were used.

wave imagery, we can also see that one of the above limits was being approached on three out of the five cases.

Table 4 summarizes the derived variables which were calculated to supplement the surface measured data. Included in this table is wave slope, orbital velocity (v_o), normalized orbital velocity (v_n), two estimates of wave direction relative to the SAR look direction (θ_A -sea truth and θ_A -OFT), wave direction normalized to radar look direction (θ_{AC} -sea truth and θ_{AC} -OFT) and two normalized wind directions (α_{SAR} and α_{WV}). The surface measured and derived variables were then linearly correlated to the wave contrast peak-to-background ratio (PBR).

Table 5 summarizes the linear correlations between the peak-to-background ratio and the various surface measurements and derived variables. Significant ($p < 0.05$) linear correlations existed between the wave contrast measurement and wavelength (both λ -sea truth and λ -OFT), and wave height ($H_{1/3}$). Table 6 summarizes multiple linear regression coefficients calculated between combinations of λ , $H_{1/3}$ and $\sin \theta_{AC} v_o$. Again, these coefficients are all significant ($p < 0.05$).

From the analysis of the sea and wind conditions during the JASIN study, there appears to be a positive correlation between wave detectability on SAR imagery and both wave height and wavelength of gravity waves. In other words, the longer the wavelength and the higher the wave, the greater the chance of detecting that wave on imagery collected by a Seasat type SAR.

3.3 SAR MOTION CORRECTIONS

Because the imaging mechanism employed by the synthetic aperture radar is dependent upon the phase history of the target being imaged, any motion in that target may result in a degraded SAR image. This phenomena was first reported on by Raney (1971) and more recently

TABLE 4
DERIVED SEA TRUTH PARAMETERS FOR JASIN EXPERIMENT

Pass	Wave Slope	V_o	$\sin \theta_{AC} V_o$	θ_A Sea Truth	θ_A OFT	θ_{AC} Sea Truth	θ_{AC} OFT	α_{SAR}	α_{wv}
547	0.009	0.20	0.22	122	119	48	61	43	75
556	0.010	0.24	0.22	64	58	64	58	74	80
590	0.054	0.17	0.17	84	---	84	---	57	47
	0.013	0.23	0.18	6	---	6	---	---	---
599	0.015	0.27	0.07	165	---	15	---	26	24
633	0.012	0.23	0.22	77	---	77	---	88	75
642	0.016	0.44	0.11	165	---	15	---	26	34
713	---	---	---	---	59	---	59	---	---
719	---	---	---	---	105	---	75	19	56
757	0.019	0.66	0.28	25	33	25	33	61	54
762	0.026	0.59	0.58	96	90	84	90	48	54
791	0.021	0.56	0.56	85	107	85	73	1	5
834	0.019	0.45	0.22	151	127	29	53	38	23
958	0.013	0.26	0.17	139	81	41	81	50	81
1001	0.037	0.62	0.59	107	86	73	86	15	32
1006	0.034	0.68	0.59	121	---	59	---	49	8
1044	0.023	0.40	0.27	44	37	44	37	65	69
1049	0.020	0.39	0.34	121	103	59	77	30	1
1087	---	---	---	---	32	---	32	84	27

TABLE 5
LINEAR CORRELATIONS BETWEEN WAVE CONTRAST (PBR) AND
ENVIRONMENTAL PARAMETERS FOR JASIN SEASAT DATA

<u>Parameter</u>	<u>Linear Correlation</u>
Wave Height	0.53**
Wavelength (Sea Truth)	0.67**
Wavelength (OFT)	0.71*
Wave Slope	-0.02
Wave Direction Relative to Radar Look Direction (Sea Truth)	0.28
Wave Direction Relative to Radar Look Direction (OFT)	-0.05
Normalized Orbital Velocity	0.43
Wind Direction Relative to SAR Look Direction	-0.06
Wind Direction Relative to Wave Direction	-0.10
Wind Speed	0.30

*Significant at $p < 0.01$

**Significant at $p < 0.05$

TABLE 6
MULTIPLE LINEAR CORRELATION COEFFICIENTS

<u>Parameter</u>	<u>PBR</u>
$H_{1/3}, \lambda$	0.71*
$\lambda, \sin \theta_{AC} v_0$	0.82*
$\lambda, \sin \theta_{AC} v_0, H_{1/3}$	0.83*

*Significant at $p < 0.01$

Shuchman and Zelenka (1978) and Shuchman (1981). Shuchman (1981) produced a set of equations which can be used to calculate the adjustments necessary to compensate for these motion distortions when processing the SAR signal histories.

Studies using aircraft SAR data have shown that the visibility or detectability of gravity waves is often sensitive to motion compensation adjustments made during the processing of the SAR signal histories (Kasischke, et al., 1979; Kasischke and Shuchman, 1981; Shuchman, et al., 1982). Because these motion compensation adjustments are inversely proportional to the velocity of the SAR platform, it was theoretically determined by early Seasat investigators that the motion adjustments may be necessary for optimum contrast wave imagery if the SAR data are processed to full resolution. Furthermore, it was determined by Shuchman and Zelenka (1978) that the adjustment, if necessary, would be quite small and the effect on the SAR wave imagery quite subtle.

3.3.1 METHODS

The purpose of the present investigation was to determine the degree of sensitivity of Seasat SAR data to motion compensation adjustments. This was accomplished in two separate experiments. First, wave detectability or contrast was measured as a function of both the range telerotation adjustment and azimuth teleshift adjustment. Next, SAR imagery with various telerotation and teleshift adjustments were digitized and fast Fourier transformed to determine if the spectral estimates varied.

A target velocity in the range (line-of-sight) direction affects the SAR imaging process in several ways. One effect is an azimuthal displacement of the moving target's image relative to a stationary target's image. When a target is accelerating in the range direction, this azimuth displacement changes during the imaging time,

resulting in a smearing in the azimuthal direction. Neither of these effects is correctable during processing.

A range velocity component will also cause a smearing or defocusing in the range direction due to a rotation of the phase history of the target. This effect can be corrected for during correlation of the data by rotating the lenses in the optical processor as described below.

Motion of a SAR imaged target in the along track direction results in a defocusing of the image in the azimuth direction. This defocusing can be compensated for during processing by adjusting the focal length of the azimuthal lens. For a more detailed discussion of the problems associated with imaging moving targets with a SAR, the reader is referred to articles by Shuchman (1981) or Shuchman, et al. (1981).

Shuchman (1981) presented equations to calculate adjustments to use during processing of the signal histories for the range and azimuth velocity components present in gravity waves. These velocity adjustments are directly proportional to the velocity of the SAR platform. The motion compensation adjustments are of two types: telerotation adjustments which compensate for motion in the range (line-of-sight) direction and teleshifts which compensate for motion in the azimuth direction.

The telerotation adjustment (Shuchman, 1981) is:

$$\phi = \frac{v_r P}{v_{AC} Q} \quad (4)$$

where v_r is the line-of-sight velocity of the target,
 v_{AC} is the SAR platform velocity, and
 P and Q are SAR processing parameters.

In a similar fashion, an adjustment can also be made to compensate for azimuth velocity distortions in the SAR data. As derived

by Shuchman and Zelenka (1978), the focal length (F_0) for SAR processing is defined as:

$$F_0 = \frac{R\lambda}{2M^2\lambda_0} \left(\frac{v_f}{v_{AC}} \right)^2 \quad (5)$$

where R is the slant range to the target,
 λ is the radar wavelength,
 λ_0 is the optical processor wavelength,
 M is azimuth demagnification of the optical processor, and
 v_f is the film velocity.

Using the focal length (F_0) calculated in Eq. (5), the shift in focal length (δF) produced by a moving target is defined as

$$\delta F = 2F_0 \frac{v_A}{v_{AC}} \quad (6)$$

where v_A is the target velocity parallel to the SAR platform direction.

It can be seen that both adjustments are inversely proportional to the velocity of the SAR platform. For the velocity of the Seasat satellite (~ 7800 m/s), the adjustments needed to correct for the phase velocity of the gravity waves are very much smaller than those needed for an aircraft SAR ($v_{AC} \approx 150$ m/s).

Telerotation adjustments were made on Seasat SAR data from Revolution 762. Surface measurements indicated the dominant wavelength at this time was 210 meters (phase velocity = $C = 18.1$ m/s) and the SAR data indicated a 241 meter ($C = 19.4$ m/s) dominant wave was present. The telerotation adjustment (ϕ) calculated for the Revolution 762 SAR data assumed a 19.4 m/s dominant wave was present. SAR imagery of waves from Revolution 762 were processed using the following telerotation adjustments: -9ϕ , -7ϕ , -5ϕ , -3ϕ , -2ϕ , $-\phi$, $0 + \phi$, $+2\phi$, $+3\phi$, $+5\phi$, $+7\phi$, and $+9\phi$. A negative ($-$) telerotation assumes

the waves are moving away from the SAR and a positive (+) telerotation assumes the waves are moving towards the SAR. During Rev. 762, the waves were moving towards the SAR.

Seasat SAR imagery from Revolution 1087 was optically processed using a variety of different azimuth focus shifts. No sea-truth was collected for this pass, but it was clear from an examination of the SAR imagery that the waves are nearly azimuth traveling. The optical Fourier transform of the SAR data indicates a 299 meter dominant wave is present ($C = 21.2$ m/sec), with an orientation of 34° relative to the satellite ground track. A teleshift, P , was calculated assuming the waves had a phase speed of 21.2 m/sec. Revolution 1087 data were processed using the following teleshifts: $-4P$, $-3P$, $-2P$, $-P$, 0 , P , $2P$, $3P$, $4P$. A negative ($-$) focus shift assumes the waves are moving in the same direction as the SAR platform while a positive (+) correction assumes the waves are moving in the opposite direction. Since no sea truth was available, the assumption was made that the waves were propagating towards the Scottish Coast, therefore opposite the SAR platform direction.

To explore the question of whether or not the telerotation and teleshift adjustments significantly alter the SAR derived estimates of wavelength and direction, digital analysis techniques were employed. SAR imagery from both Revolutions 762 and 1087 were digitized using ERIM's Optical Hybrid Digitizing Facility (see Ausherman, et al., 1975). For Revolution 762, imagery from the -2ϕ , $-\phi$, 0 , $+\phi$ and $+2\phi$ telerotation settings were digitized. For Revolution 1087, imagery from the $-2P$, $-P$, 0 , $+P$ and $+2P$ azimuth teleshifts were digitized. These digital data were then fast Fourier transformed and the resultant one-dimensional wave number and wave direction plots examined.

3.3.2 RESULTS

Figure 4 and Table 7 summarize the results of the wave contrast versus telerotation measurements. Note on Figure 4 that a positive telerotation is compensating for wave motion away from the radar while a negative telerotation adjusts for motion towards the radar. Each point on the curve represents an average of five separate measurements.

The trend in Figure 4 is clear. Telerotation adjustments do not appear to appreciably degrade Seasat SAR imagery within $\pm 3^\circ$ of the stationary focus setting. Studies of aircraft SAR data have shown that waves become undetectable on SAR imagery when a telerotation of $\pm 2^\circ$ from the optimum setting is used (see Kasischke, et al., 1979; Kasischke and Shuchman, 1981).

Figure 5 illustrates the two-dimensional spectra generated by a fast Fourier transform of the digitized SAR data from Revolution 762, for three telerotation adjustments (-2° , 0 , $+2^\circ$). Figure 5 also presents the one-dimensional wave direction and wave number spectra generated from the fast Fourier transform. Table 8 summarizes the dominant wavelength and direction of propagation for the various adjustments. We can see that the spectral estimates do not change when a non-zero range telerotation is used.

Table 7 and Figure 6 summarize the results of the wave contrast versus the azimuth teleshift adjustments. Again, each point represents an average of five points. It can be seen that the highest wave contrast was obtained when a land (0) teleshift setting was used. With the azimuth teleshifts, it appears that the Seasat SAR wave imagery was not significantly degraded until a focus shift greater than $\pm 2P$ was used.

Figure 7 illustrates the two-dimensional spectra generated from the Revolution 1087 data. For the three azimuth focus settings ($-2P$, 0 , $+2P$), Figure 7 also presents the one-dimensional wave direction

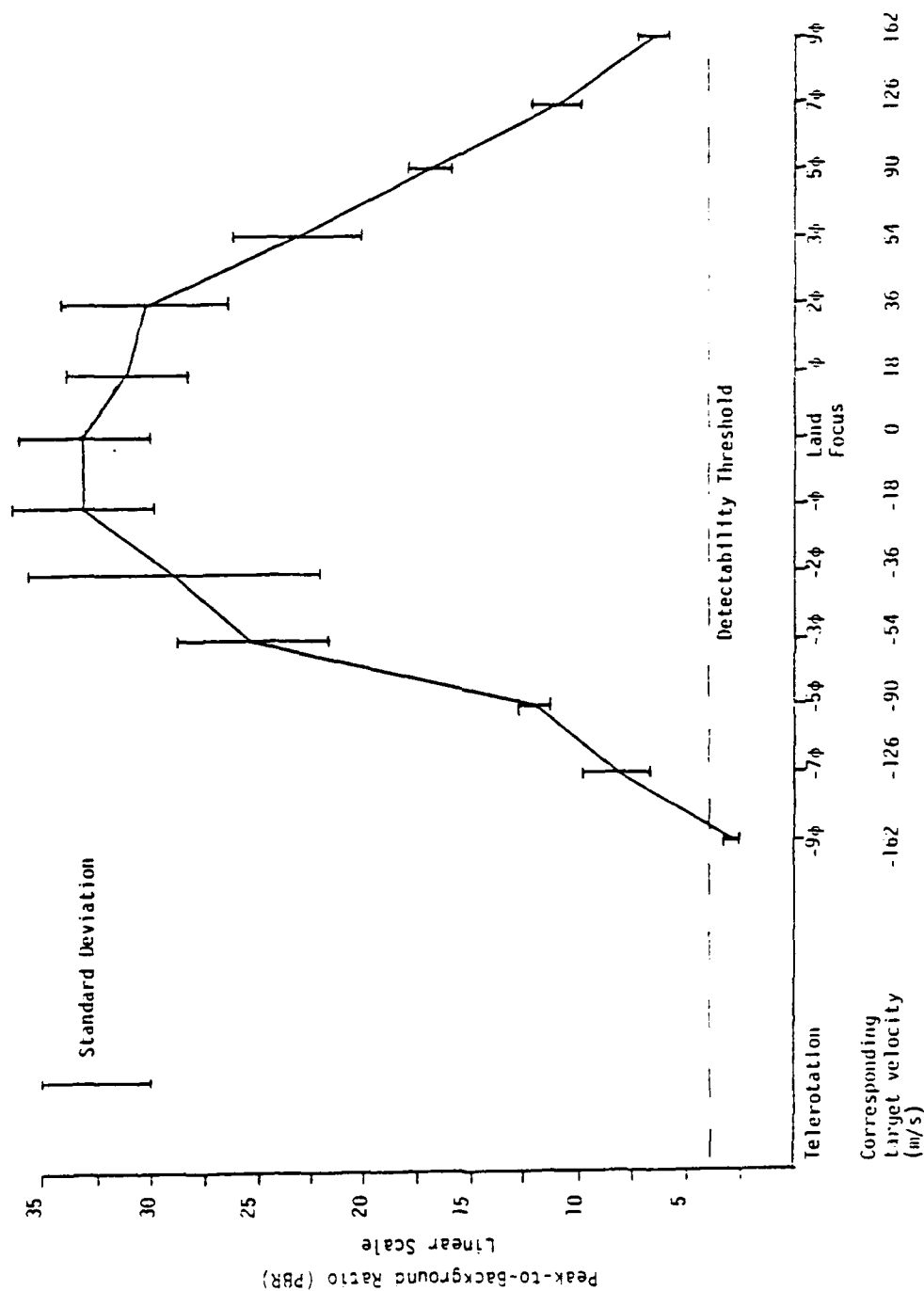


FIGURE 4. PEAK-TO-BACKGROUND RATIO VERSUS TELEROTATION ADJUSTMENT. (Seasat Rev. 762.)

TABLE 7
PEAK-TO-BACKGROUND (PBR) RATIO VERSUS TELEROTATIONAL
ADJUSTMENT AND AZIMUTH FOCUS SHIFT
(Seasat SAR Revs. 762 and 1087, respectively)

<u>Telerotation Setting</u>	<u>PBR</u>	<u>S.D.*</u>
+9 ϕ	6.7	0.6
+7 ϕ	11.1	1.1
+5 ϕ	17.1	1.0
+3 ϕ	23.3	3.0
+2 ϕ	30.4	3.9
+ ϕ	31.2	2.3
0 (Stationary Target)	33.3	3.0
- ϕ	33.3	3.2
-2 ϕ	28.9	6.7
-3 ϕ	25.3	3.5
-5 ϕ	12.1	0.7
-7 ϕ	8.2	1.6
-9 ϕ	2.9	0.2

<u>Focus Shift</u>	<u>PBR</u>	<u>S.D.*</u>
+4P	5.9	1.3
+3P	10.2	1.4
+2P	12.7	2.3
+P	11.8	0.8
0 (Stationary Target)	18.4	2.6
-P	14.7	2.8
-2P	13.5	1.8
-3P	8.3	0.9
-4P	6.0	0.9

*Standard Deviation

TABLE 8
FAST FOURIER TRANSFORM ESTIMATES OF DOMINANT
WAVELENGTH AND DIRECTION AS A FUNCTION OF
RANGE TELEROTATION ADJUSTMENTS FOR
SEASAT REV. 762

<u>Telerotation Setting</u>	<u>Dominant Wavelength</u>	<u>Dominant Direction</u>
-2 ϕ	259 m	227°
- ϕ	259 m	227°
0 (Stationary Focus)	259 m	227°
+ ϕ	259 m	227°
+2 ϕ	259 m	227°

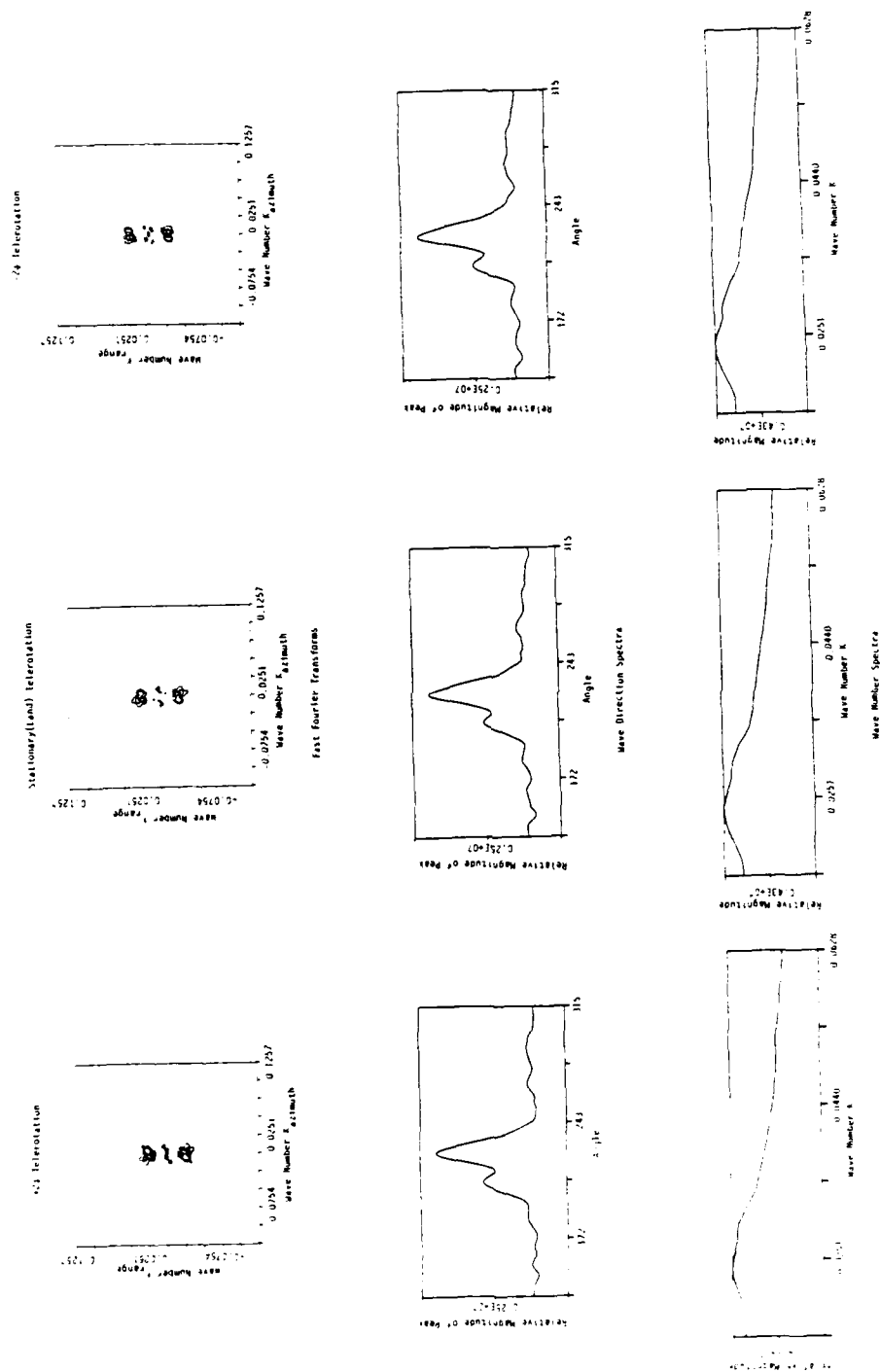


FIGURE 5. TWO-DIMENSIONAL FAST FOURIER TRANSFORMS AND ONE-DIMENSIONAL WAVE DIRECTION AND WAVE NUMBER SPECTRA VERSUS TELEROATION ADJUSTMENTS FOR SEASAT REV. 762 DATA

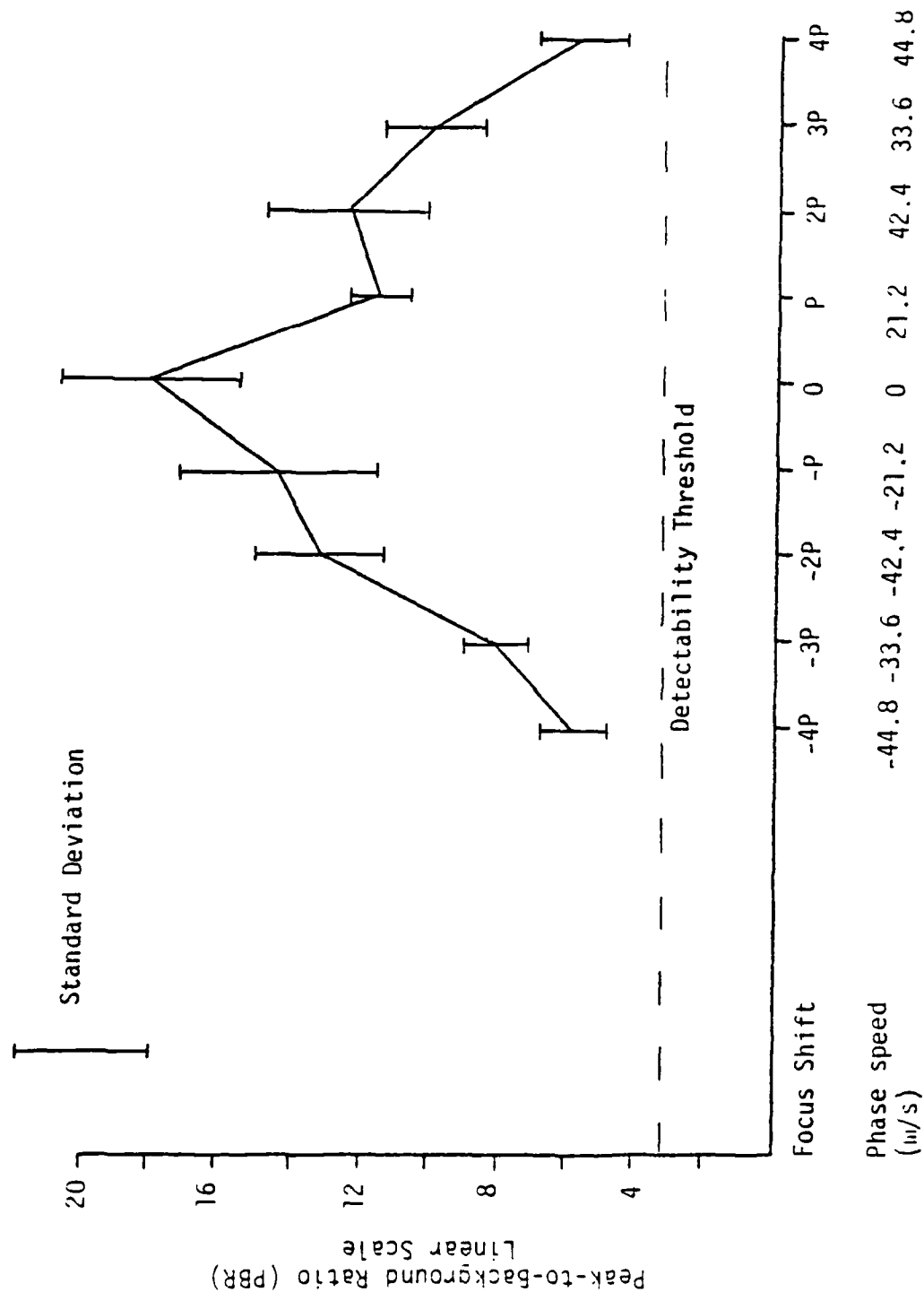


FIGURE 6. PEAK-TO-BACKGROUND RATIO VERSUS AZIMUTH FOCUS SHIFT. (Seasat Rev. 1087.)

and wave number spectra from these data. Table 9 summarizes the dominant wavelength and direction of propagation for the various teleshift adjustments. From Figure 7 and Table 9, we can see that the spectral estimates generated using different azimuth focus settings change very little when non-stationary settings are used.

It appears that for the wave conditions present during Revolutions 762 and 1087, motion compensation adjustments do not appreciably improve the detectability of waves on the Seasat SAR imagery. This insensitivity to motion effects is true in terms of both detectability of waves on SAR imagery and the estimates of dominant wavelength and direction obtained from the SAR data. This is not always the case when processing data from aircraft-mounted SARs (see Kasischke, et al., 1979; Kasischke and Shuchman, 1981; or Shuchman, et al., 1982) and may not be the case for all ocean waves imaged by Seasat.

3.4 WAVE HEIGHT DETERMINATION USING DIGITALLY PROCESSED SEASAT SAR IMAGERY

This section of the report examines a technique proposed by Thomas (1982) for the extraction of wave height information from digitally processed Seasat SAR imagery of ocean waves. A copy of Thomas' paper is included as Appendix C. The discussion presented below will include a brief review of the theory, measurements and results presented by Thomas, as well as some measurements made at ERIM which tend to confirm his results. Finally, a brief discussion of the limitations and possible errors associated with this approach is presented.

3.4.1 THEORETICAL DEVELOPMENT

The three basic assumptions in Thomas' method include: (1) that any wave modulation in the SAR imagery is caused by tilt modulation effects, (2) that all image intensity variations in a wave image are

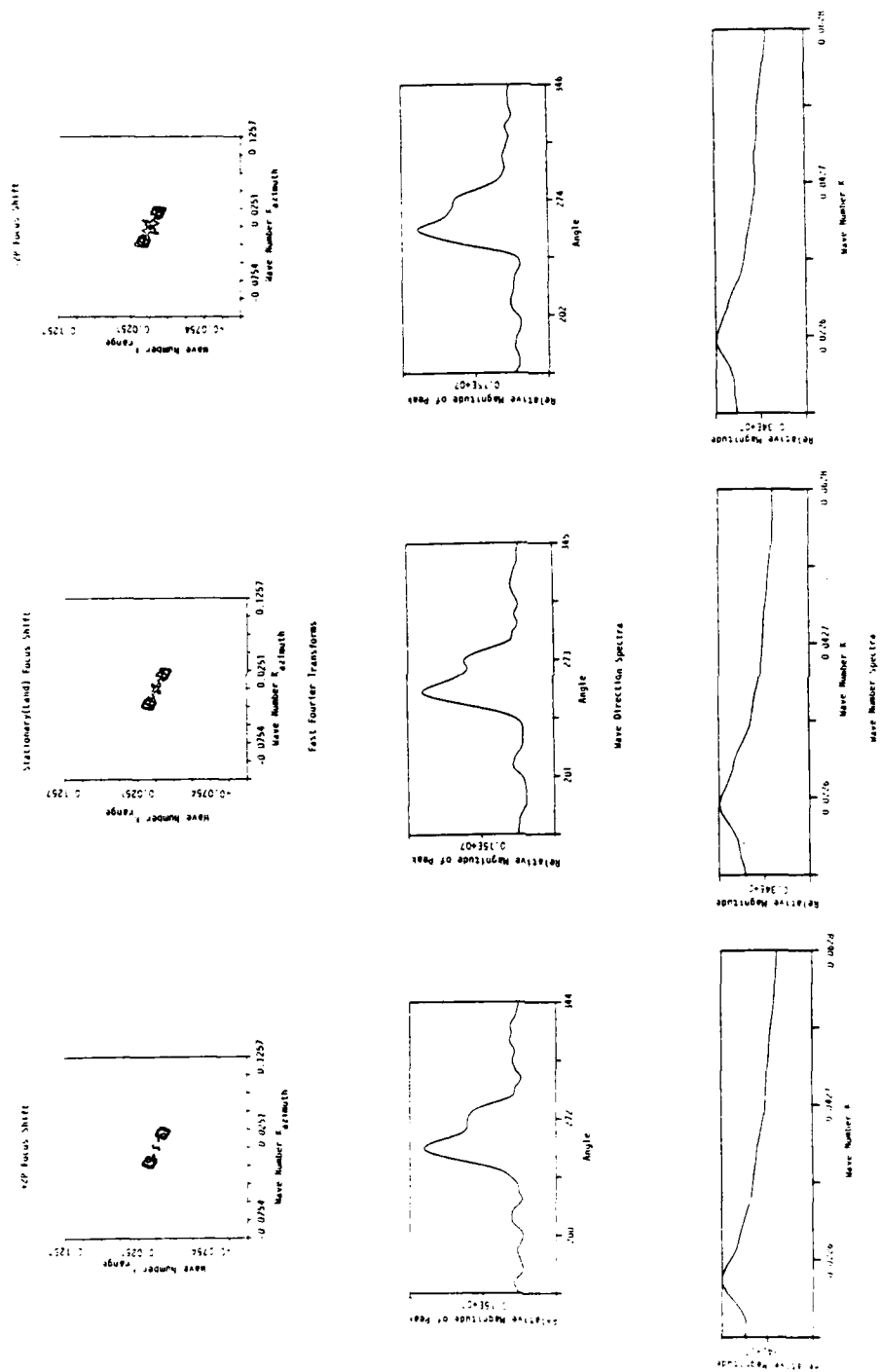


FIGURE 7. TWO-DIMENSIONAL FAST FOURIER TRANSFORMS AND ONE-DIMENSIONAL WAVE DIRECTION AND WAVE NUMBER SPECTRA VERSUS TELEROTATION ADJUSTMENTS FOR SEASAT REV. 1087 DATA

TABLE 9
FAST FOURIER TRANSFORM ESTIMATES OF DOMINANT
WAVELENGTH AND DIRECTION AS A FUNCTION OF
AZIMUTH FOCUS SHIFT FOR
SEASAT REV. 1087

<u>Azimuth Focus Setting</u>	<u>Wavelength</u>	<u>Direction</u>
-2P	289 m	254°
-P	289 m	253°
0 (Stationary Focus)	289 m	253°
+P	306 m	252°
+2P	306 m	250°

the result of the imaged gravity waves (due to tilt modulation) or speckle, and (3) that the speckle characteristics of a digitally processed SAR image are known. Each of these assumptions will be addressed briefly in Section 3.4.2. The method of Thomas relates the contrast in a digitally processed SAR wave image to a change in local incidence angle (slope) using a theoretical scattering model. By combining this slope measurement with wavelength (easily obtained by FFT analysis), an estimate for wave height can be calculated. Presented below is a review of this process adopting Thomas' nomenclature.

Denoting the ocean surface displacement from the mean level by $f(r, t)$, the significant wave height, H_s , can be expressed as

$$H_s = 4 \sqrt{\langle f^2 \rangle}, \quad (7)$$

where the brackets indicate a mean value. For a narrow-band swell-wave spectrum centered on wave number k_0 , the r.m.s. slope of the sea surface is given by

$$\tan \theta_r = \frac{k_0 H_s}{4} = \frac{\pi H_s}{2\lambda_0}, \quad (8)$$

where λ_0 is the swell wavelength. Therefore, H_s can be determined if $\tan \theta_r$ and λ_0 are known. Determination of λ_0 is easily accomplished by taking a Fast Fourier Transform (FFT). The r.m.s. slope ($\tan \theta_r$) of the ocean surface is obtained by comparing the variation of the radar cross-section attributed to waves with a theoretical scattering model which gives the variation of radar cross-section as a function of incidence angle. The theoretical variation of radar cross-section as a function of incidence angle was calculated by Valenzuela (1978), and is shown in Figure 8. Although the data in Figure 8 are for 428 MHz and Seasat operated at 1.275 GHz (L-band), theory predicts similar results for these two

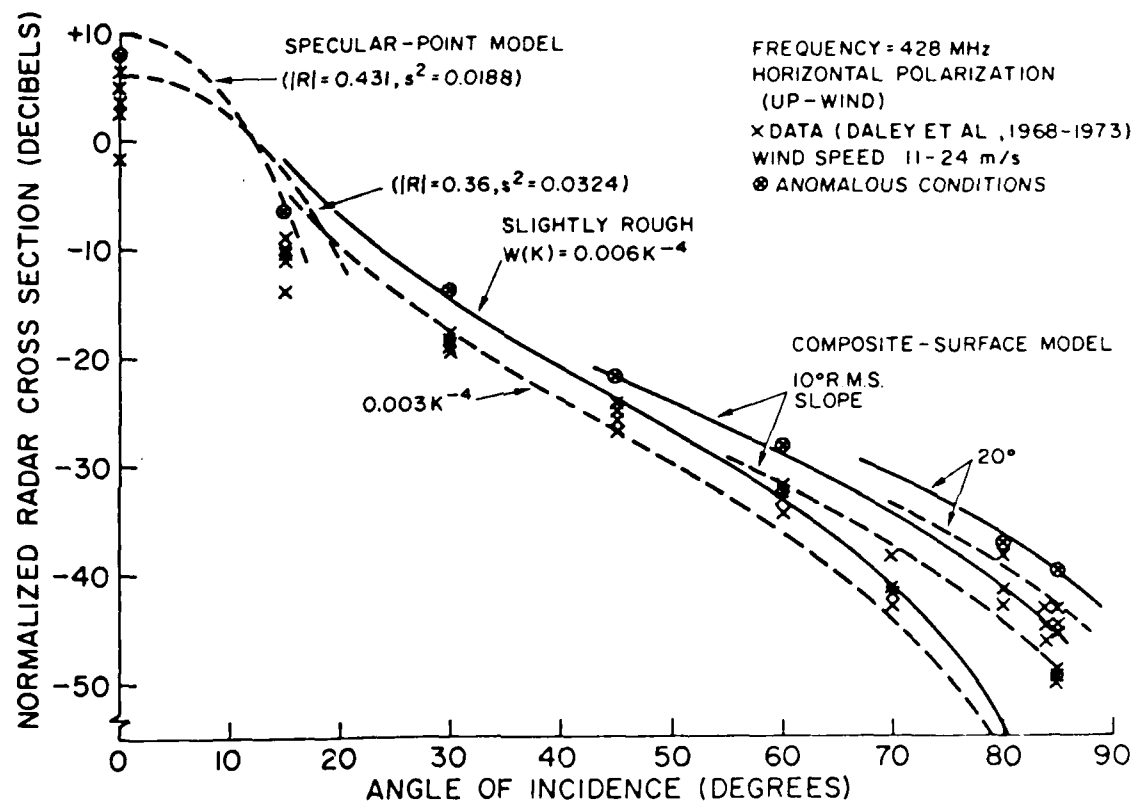


FIGURE 8. COMPARISON OF MEASURED AND THEORETICAL CROSS-SECTIONS OF THE OCEANS FOR A RADAR FREQUENCY OF 428 MHz, HORIZONTAL POLARIZATION. (After Valenzuela, 1978.)

frequencies. The variation in radar cross-section attributed to waves can be related to a change in local incidence angle (r.m.s. slope) by using the slope of the curve in Figure 8 at that particular incidence angle.

A SAR image contains intensity variations due to both speckle and natural reflectivity changes. Speckle is a characteristic of coherent imaging systems and is described by Porcello, et al. (1976).

Thomas presents a somewhat confusing argument where he refers to the term I_s , or the speckle intensity. An alternative way of deriving his results is to describe the effects of speckle by a multiplicative model (Wu, 1980; Lee, 1981) which may be written as

$$I = \bar{I}S \quad (9)$$

where I is the intensity at a given point, \bar{I} is the mean intensity in the neighborhood of that point, and S is a random variable with mean 1.0 and standard deviation

$$\sigma_s = \frac{1}{\sqrt{N}} \quad (10)$$

where N is the number of independent looks in the processor (Porcello, et al., 1976). We may also view \bar{I} as the "true" signal, uncontaminated by speckle. For the case in point, the true signal is due to waves on the surface, so we change notation and replace \bar{I} with I_w (the subscript referring to waves). We also replace I with I_t to avoid confusion. Equation (9) then becomes

$$I_t = I_w S, \quad (11)$$

from which we also have

$$I_t^2 = I_w^2 S^2. \quad (12)$$

We now invoke a theorem from probability theory which states that the mean value of the product of two uncorrelated variables is equal

to the product of the mean values of those variables. Applying this to Eqs. (11) and (12), we have

$$\langle I_t \rangle = \langle I_w \rangle \langle S \rangle \quad (13)$$

and

$$\langle I_t^2 \rangle = \langle I_w^2 \rangle \langle S^2 \rangle . \quad (14)$$

Using the definition of the variance, we have

$$\langle I_t \rangle^2 = \sigma_t^2 + \langle I_t \rangle^2 \quad (15)$$

and similarly for σ_w^2 and σ_s^2 . Substituting these into Eq. (14) and dividing by the square of Eq. (13) results in

$$\left[\frac{\sigma_t^2}{\langle I_t \rangle^2} + 1 \right] = \left[\frac{\sigma_w^2}{\langle I_w \rangle^2} + 1 \right] \left[\frac{\sigma_s^2}{\langle S \rangle^2} + 1 \right] , \quad (16)$$

which is the same as Thomas' Eq. (11). From Eq. (12) and $\langle S \rangle = 1$, the last quantity in brackets is equal to $(1 + 1/N)$, where N is the number of looks. Since the JPL and DFVLR digital images are processed to four looks, Eq. (16) becomes

$$\left[\frac{\sigma_t^2}{\langle I_t \rangle^2} + 1 \right] = 1.25 \left[\frac{\sigma_w^2}{\langle I_w \rangle^2} + 1 \right] , \quad (17)$$

which is Eq. (4) in Thomas (1982).

The terms σ_t^2 and $\langle I_t \rangle^2$ can be obtained easily from the digital image, and $\sigma_w / \langle I_w \rangle$ can then be calculated from Eq. (17). To relate this to Valenzuela's curve (Figure 8), the quantity $V = 10 \log_{10} [(\langle I_w \rangle + \sigma_w) / (\langle I_w \rangle - \sigma_w)]$ is calculated. This allows the determination of $\tan \theta_r$ which leads to the significant wave height.

3.4.2 RESULTS

Presented in Table 10 are the results of Thomas' two test cases and three additional measurements made at ERIM following the methods of Thomas. In general, the wave height estimates agree relatively well with those reported from sea truth measurements. Thomas does not elaborate on his actual image measurement technique. For the analysis presented here, image statistics from JPL digitally processed SAR data for areas of 100 x 100 pixels ($\sim 1.6 \times 1.6$ km) were generated. The size of the area selected to implement Thomas' algorithm could affect the results. If the area chosen is too small to accurately characterize the contrast in the SAR wave scene, the wave height estimate will be in error. An example would be if only a portion of a wavelength was studied. In this case, the contrast and resultant wave height estimate would both be low. Also, if there were not a sufficient number of points to "average" out a few outliers, the contrast measurement and resultant wave height estimate would be too high. On the other hand, if the area for statistics generation is too large, the incidence angle range it would subtend would not allow Valenzuela's curve to be used in the manner presented in Section 3.4.1.

Thomas makes the assumption that all wave modulation in the SAR wave scene is due to tilt modulation. This (as he agrees) is both a powerful and limiting assumption for his technique. Any modulation in the wave scene other than tilt modulation would decrease the estimated wave height. For waves not purely range-travelling, the combined effect of tilt modulation, straining and velocity bunching is poorly understood and it is doubtful whether the effect of tilt modulation (and thus, wave height) could be sorted out. Kasischke (1980) showed that wave contrast was more closely correlated to wave height than to wave slope for a variety of wave conditions and radar look angles. Perhaps one does not have to assume solely tilt modulation and use Valenzuela's curves to recover wave height information from image contrast measurements.

TABLE 10
WAVE HEIGHT CALCULATIONS

Orbit	Data Source	$\frac{\sigma_t}{\langle I_t \rangle}$	$\frac{\sigma_w}{\langle I_w \rangle}$	V (dB)	$\tan \theta_r$	λ_o (m)	H_s (m)	Sea Truth H_s (m)
762*	DFVLR	0.798	0.556	5.45	0.0492	217	6.8	5.5
791*	DFVLR	0.753	0.503	4.81	0.0434	132	3.7	2.95, 3.25
762**	JPL	0.73	0.48	4.53	0.0409	235	6.1	5.5
979**	JPL	0.58	0.26	1.88	0.0168	180	1.9	1.2
1049**	JPL	0.73	0.48	4.53	0.0409	244	6.4	5.0

*Thomas

**ERIM

Thomas also makes the assumption that any variability in image intensity over the areas studied was due to either ocean waves or speckle. This assumption could be violated due to local wind variations, extreme wave slopes causing specular reflections or breaking waves. He also makes the assumption that the speckle characteristics of the scene are known; this is probably valid but should be shown experimentally.

In summary, the approach of Thomas offers a possible means of extracting ocean wave height information from digitally processed Seasat SAR imagery for the case of range-traveling waves. Clearly, more work is necessary to fully evaluate its usefulness and limitations. Further tests should include: (1) varying the size of the area where statistics are generated to determine the sensitivity of the wave contrast (height) measures on this parameter; (2) applying the algorithm to a wider range of wave conditions and radar look directions to determine whether wave contrast can be related to wave height for waves not purely range-traveling; and (3) studying the speckle characteristics of digitally processed Seasat SAR data to determine its characteristics experimentally.

DETECTION OF MESOSCALE FEATURES

During the early examination of Seasat SAR imagery, it became evident that a variety of patterns were present on the oceans' surface which were being detected by the Seasat SAR. Because of the variety of surface and subsurface measurements which were made at the times of the Seasat overpasses during the JASIN experiment, this data set offers an opportunity to gain a better understanding of why many of the mesoscale features occurred and were detected by the Seasat SAR. Because many of the surface and subsurface measurements are just now being prepared for publication, the present study concentrated on investigating the spatial and temporal distribution of the mesoscale patterns. Linking the Seasat SAR imagery with the "sea-truth" measurements is a task which requires further efforts.

4.1 THE JASIN TEST AREA

During the previous gravity wave analysis, we were primarily concerned with the area in and around the Oceanographic Intensive Array (see Figure 1). During the analysis of mesoscale features, we studied Seasat SAR imagery collected over the Northeast Atlantic Ocean, in an area bounded by the United Kingdom and the Faeroe Islands on the east, 18° W longitude on the west, 54° N latitude on the south and 64° N latitude on the north. This area is presented in Figure 9, which was reproduced from the Institute of Oceanographic Sciences Chart Number C6567 (for a description of this chart, see Roberts, et al., 1979). In conjunction with the JASIN experiment, extensive hydrographic surveys of this portion of the Atlantic were made, resulting in a bathymetric chart which is unusually accurate for a deep water area.

There are 17 distinct bottom topographic features present in this area. These features are listed in Table 11, along with the shallowest contour interval charted for that feature, the estimated depth

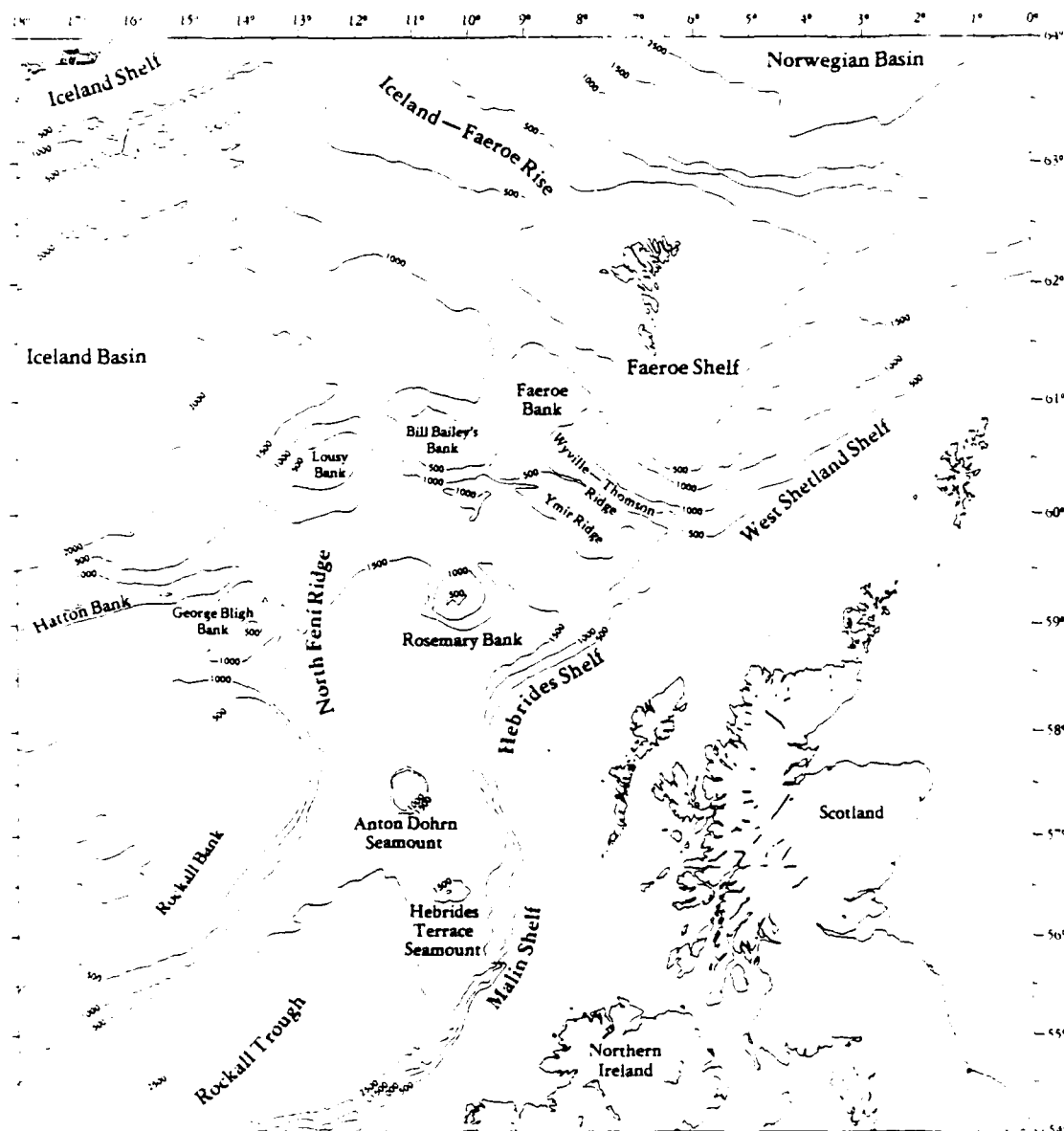


FIGURE 9. LOCATION OF MAJOR BOTTOM TOPOGRAPHIC FEATURES IN NORTHEAST ATLANTIC.

TABLE 11
BOTTOM TOPOGRAPHIC FEATURES IN THE NORTHEASTERN ATLANTIC

<u>Bottom Feature</u>	<u>Shallowest Point (m)</u>	<u>Depth of Adjacent DW (m)</u>	<u>Slope (Degrees)</u>
Iceland-Faeroe Rise	300	1000	5
Bill Bailey's Bank	100	1200	13
Lousy Bank	300	1500	28
Hatton Bank	500	2000	18
George Bligh Bank	500	1100	11
Faeroe Bank	100	1000	8
Faeroe Shelf	300	1000	7
Wyville-Thomson Ridge	400	1200	17
Ymir Ridge	600	1500	31
North Feni Ridge	1200	2000	5
Rosemary Bank	500	2000	23
Rockall Bank	300	2300	20
Anton Dohrn Seamount	600	2100	28
West Shetland Shelf	300	1000	11
Malin Shelf	200	2000	31
Hebrides Terrace Seamount	1000	2400	27
Hebrides Shelf	200	1500	28

of the adjacent deep water area, and the calculated slope for the feature. As will be discussed later, the interaction between these bottom features and ocean currents results in internal waves and frontal boundaries in this area.

In order to study the relationship between surface patterns and Seasat SAR imagery and these bottom features, the following procedure was used: First, the location of the ground coverage of the Seasat SAR was obtained by consulting the satellite data record (SDR) for each pass. (The SDR contains a series of ground latitude and longitude coordinates for specific times during the Seasat pass. Since most of Seasat SAR images contained annotations of the time the data were collected, the location of a particular surface pattern could be identified by noting the time when the pattern occurred during that orbit.) Next, the ground coverage of each pass was marked on an overlay placed on the chart. Finally, the locations of all internal waves, frontal boundaries and weather patterns were noted and then marked on the overlay.

Imagery from 15 of the 18 JASIN Seasat passes was studied. The imagery from three of the passes did not have accurate time annotations and contained no land; therefore, they could not be accurately located. Figure 10 shows the total SAR coverage of the Northeast Atlantic by the 15 passes.

4.2 OCCURRENCE OF MESOSCALE FEATURES

Four distinct mesoscale features were present on the JASIN/Seasat SAR imagery: internal waves, frontal boundaries, areas of low radar backscatter believed to be weather patterns, and windrows. In this section we will first present examples of these surface patterns and then discuss their spatial and temporal distribution on the JASIN/Seasat imagery. The locations of the five examples of SAR images presented in this chapter are shown in Figure 11.

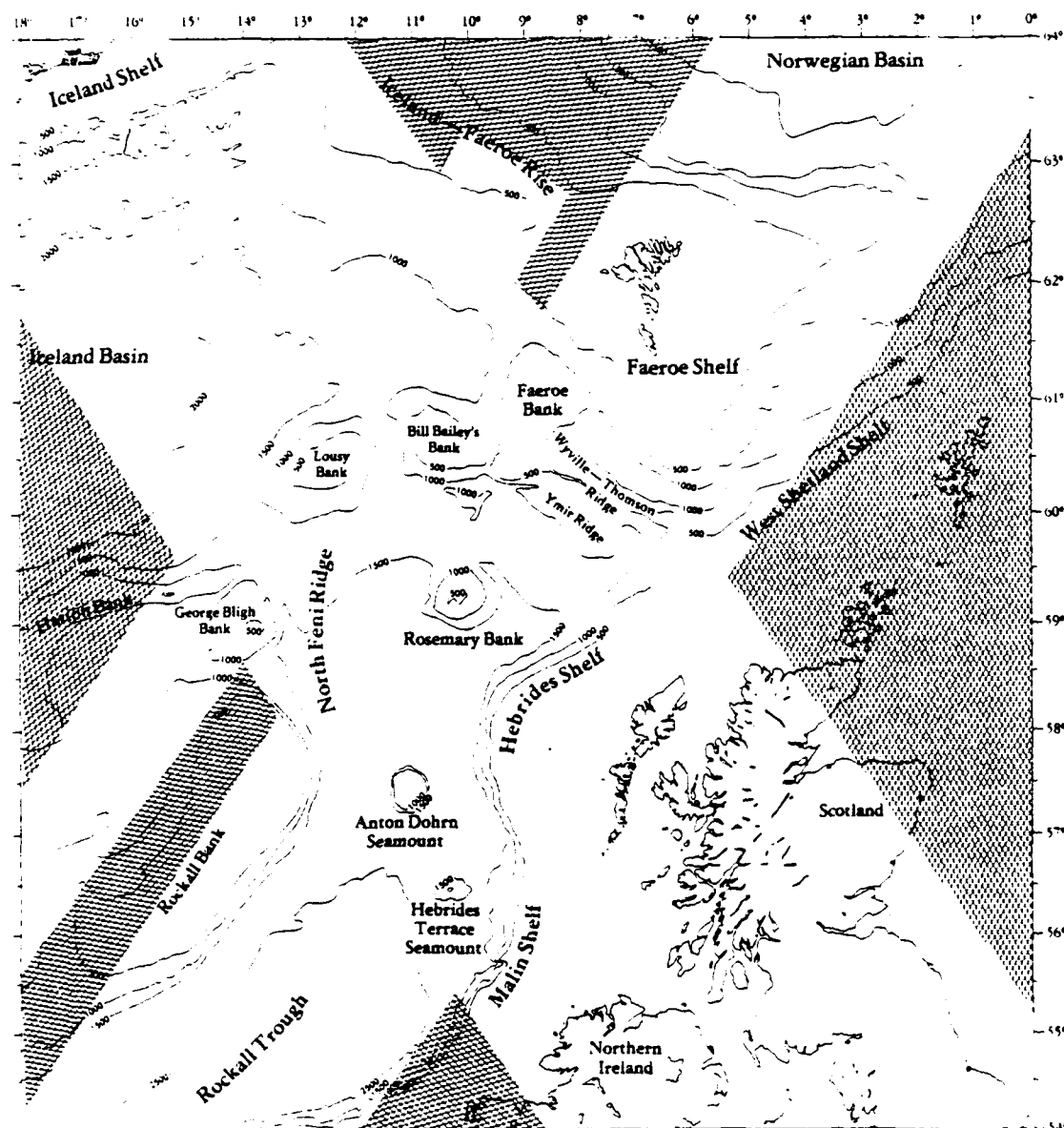


FIGURE 10. COVERAGE OF NORTHEAST ATLANTIC OCEAN BY THE SEASAT SAR FROM OVERFLIGHTS MADE DURING THE JASIN EXPERIMENT. (Depth in Meters.)

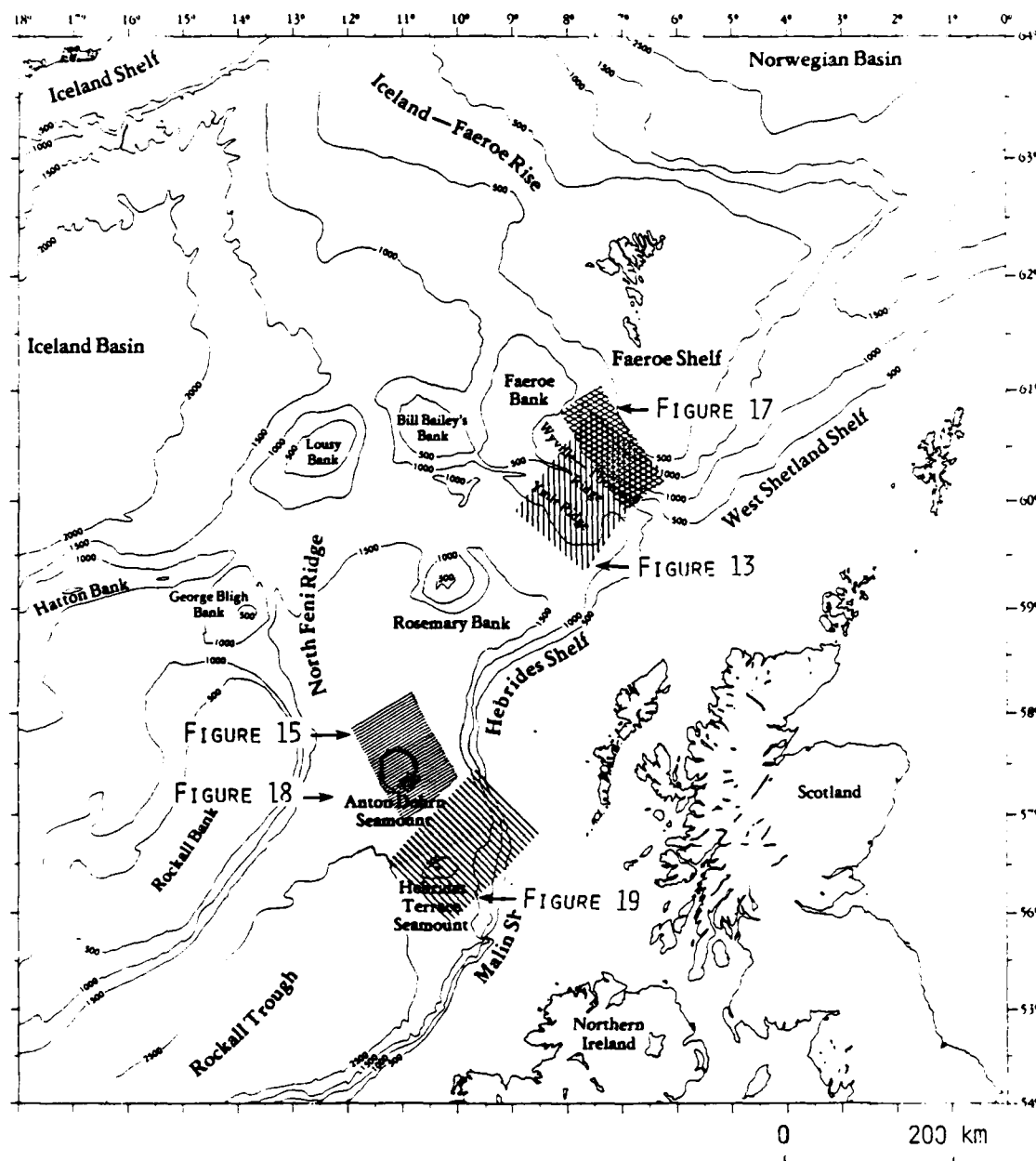


FIGURE 11. LOCATIONS OF JASIN TEST AREA AND AREAS EXAMINED DURING DEEP WATER SURVEY. (AFTER INSTITUTE OF OCEANIC SCIENCES CHART No. C6567, DEPTH IN METERS)

The JPL-optically processed imagery presented in Figure 12 was collected during Rev. 599 (7 August 1978) as Seasat passed over the Wyville-Thomson Ridge. The corresponding bathymetric chart for this coverage is presented in Figure 13. From Figure 12, it can be observed that there are numerous internal wave signatures. Note on the SAR image that the internal waves are both range (e.g., C/D1 to C/D2) and azimuth (e.g., A9 to D9) traveling. The internal waves in the lower left corner of the SAR image appear to occur over the Ymir Ridge; the internal waves in the middle of the image appear over the Wyville-Thomson Ridge; and those at the top of the image occur over the Faeroe Bank Channel.

Surface measurements collected at the time of the Seasat overpass indicate a wind of 6.9 m/s from the north and wave field with a significant wave height of 1.1 meters, a dominant wavelength of 71 meters propagating towards 20°(T).

Figure 14 was collected by Seasat during Rev. 791 (21 August 1978) as it passed over the Anton Dohrn Seamount. The corresponding bathymetry for this imagery is presented in Figure 15. The internal wave signatures collected over the Anton Dohrn Seamount are quite subtle. Three groups of internal waves occur over this seamount (B6 to C6, D/E6 to D/E8, and A8), which is quite steep sided, as can be seen by the narrow spacing of the contour lines in Figure 15.

The sea truth collected at the JASIN test area at the time of Rev. 791 indicates the winds were quite strong, with a speed of 13 m/s out of the southwest. The surface gravity wave field had a significant wave height of 3.3 m, a dominant wavelength of 132 m and was propagating towards 230°(T).

The JPL-optically processed image presented in Figure 16 was collected as Seasat passed over the Faeroe Bank Channel and the edge of the Faeroe Shelf during Rev. 762. The corresponding bathymetric chart for this area is presented in Figure 17. The curved, dark line

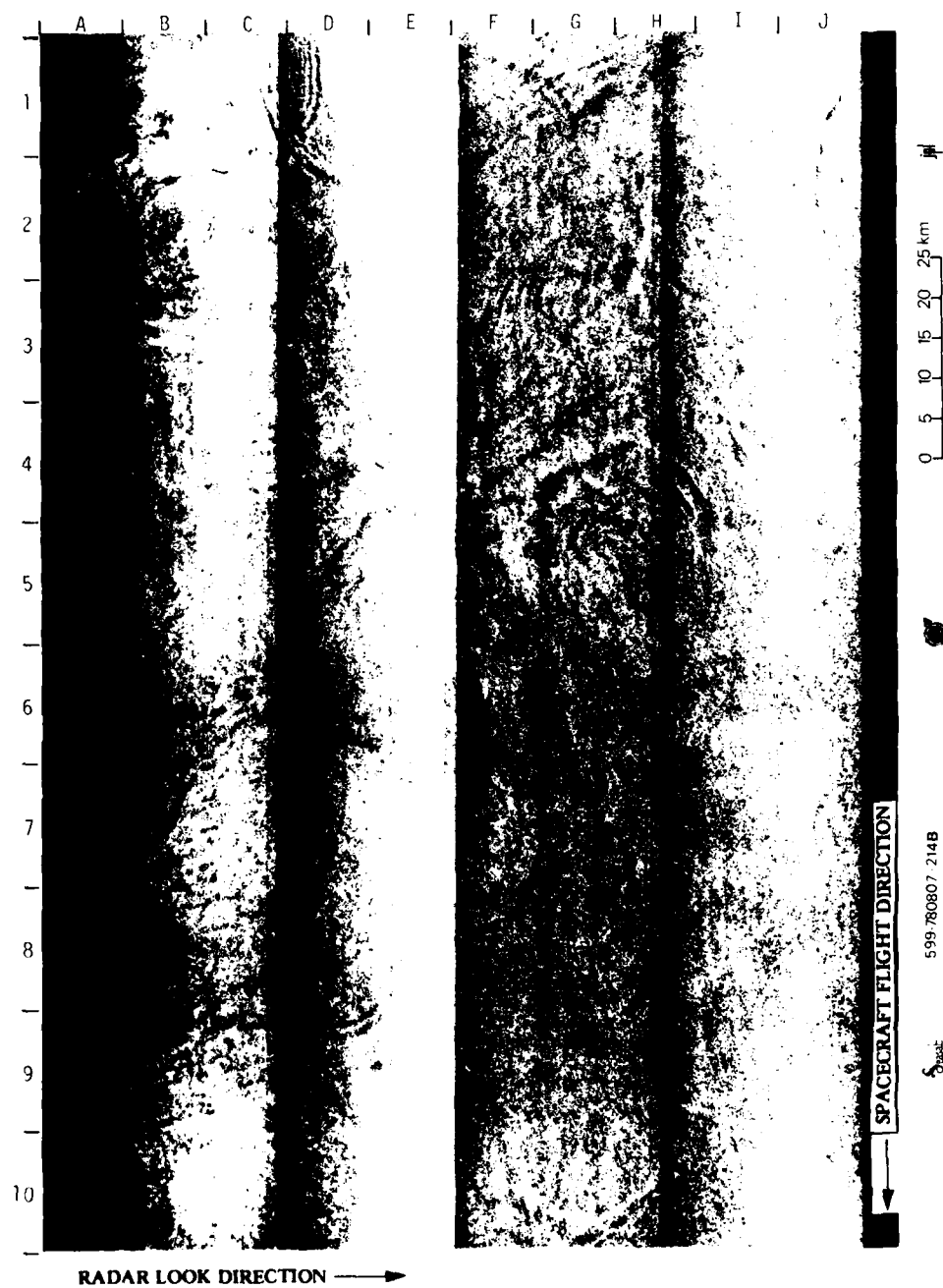


FIGURE 12. SEASAT SAR IMAGERY COLLECTED OVER THE WYVILLE-THOMSON RIDGE DURING REV. 599. (Optically processed imagery courtesy of JPL.)

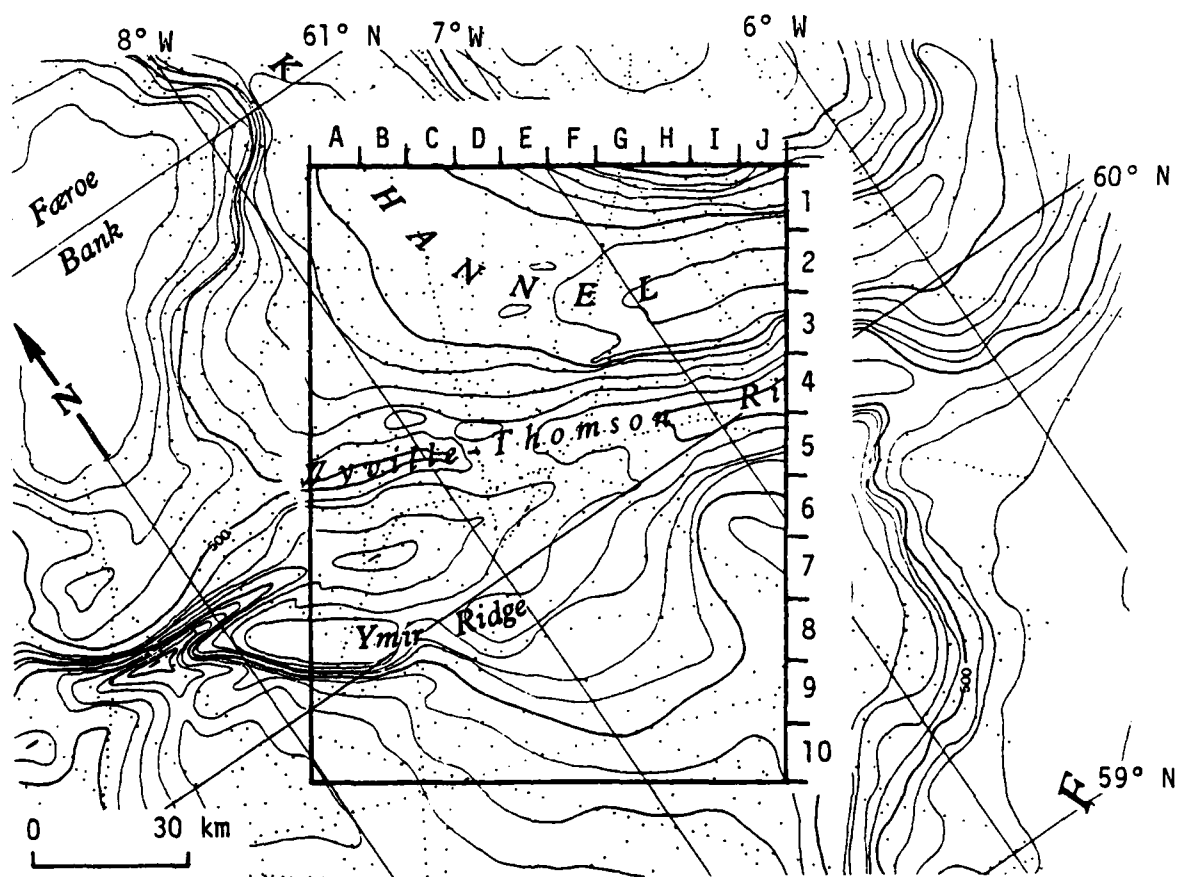


FIGURE 13. GROUND COVERAGE CORRESPONDING TO SEASAT SAR REV. 599.
(After IOS Chart No. C6567, Contour Intervals in
100-Meter Increments.)



FIGURE 14. SEASAT SAR IMAGE COLLECTED OVER ANTON DOHRN SEAMOUNT DURING REV. 791. (Optically processed imagery courtesy of JPL.)

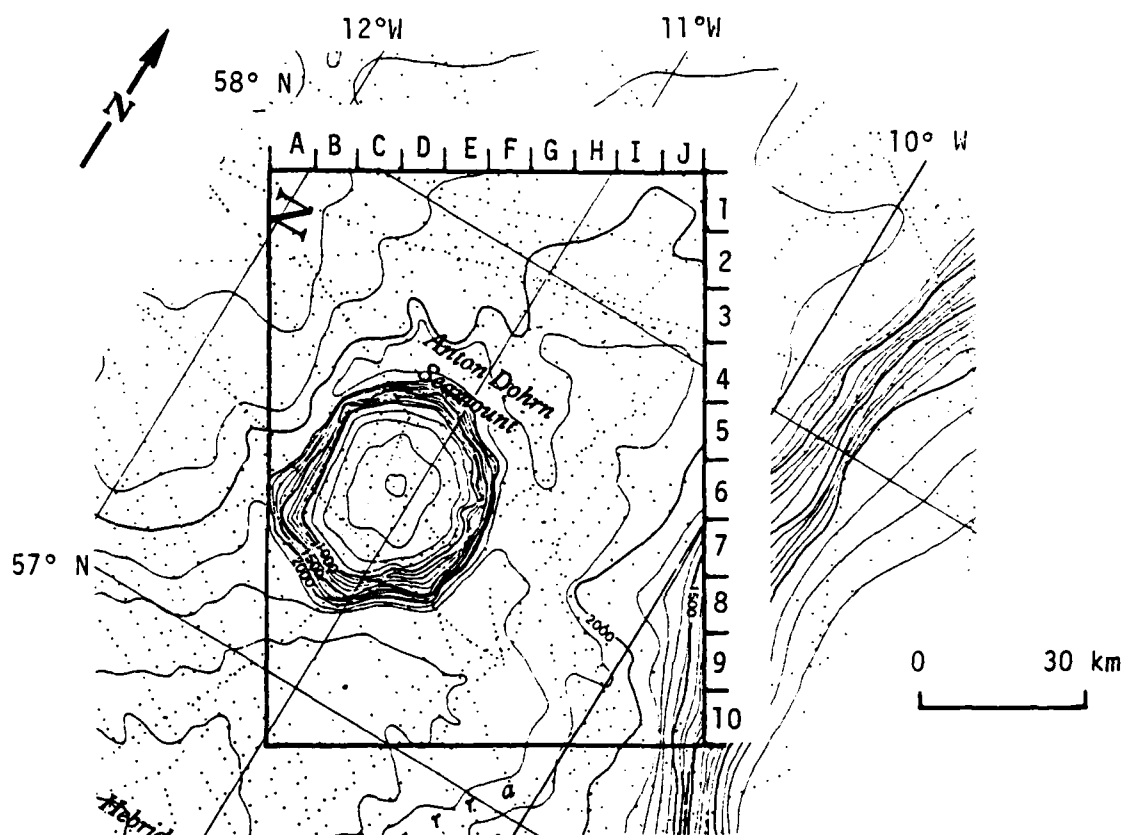


FIGURE 15. GROUND COVERAGE OF REV. 791 OVER ANTON DOHRN SEAMOUNT.
(After IOS Chart No. C6567, Depth Contours in 100-Meter
Increments.)

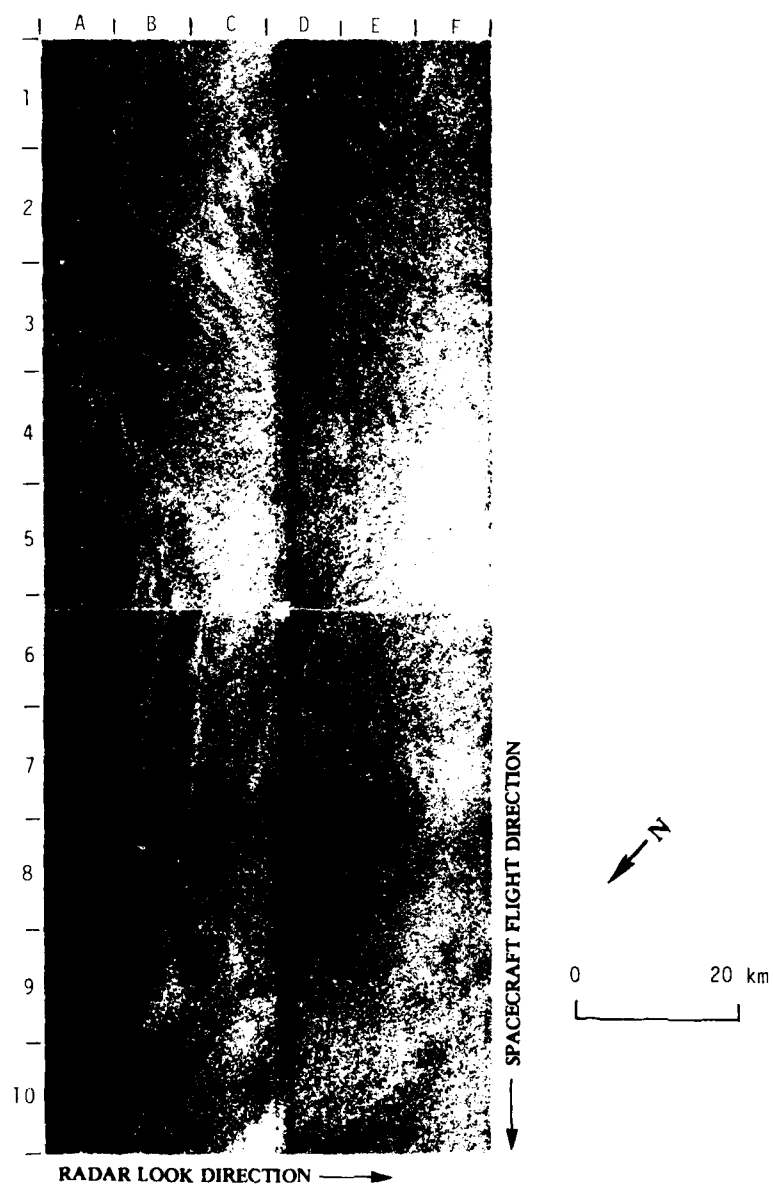


FIGURE 15. SEASAT SAR IMAGE OF A FRONTAL BOUNDARY COLLECTED OVER FAEROE BANK CHANNEL AND FAEROE RIDGE, REV. 762. (Image courtesy of JPL.)

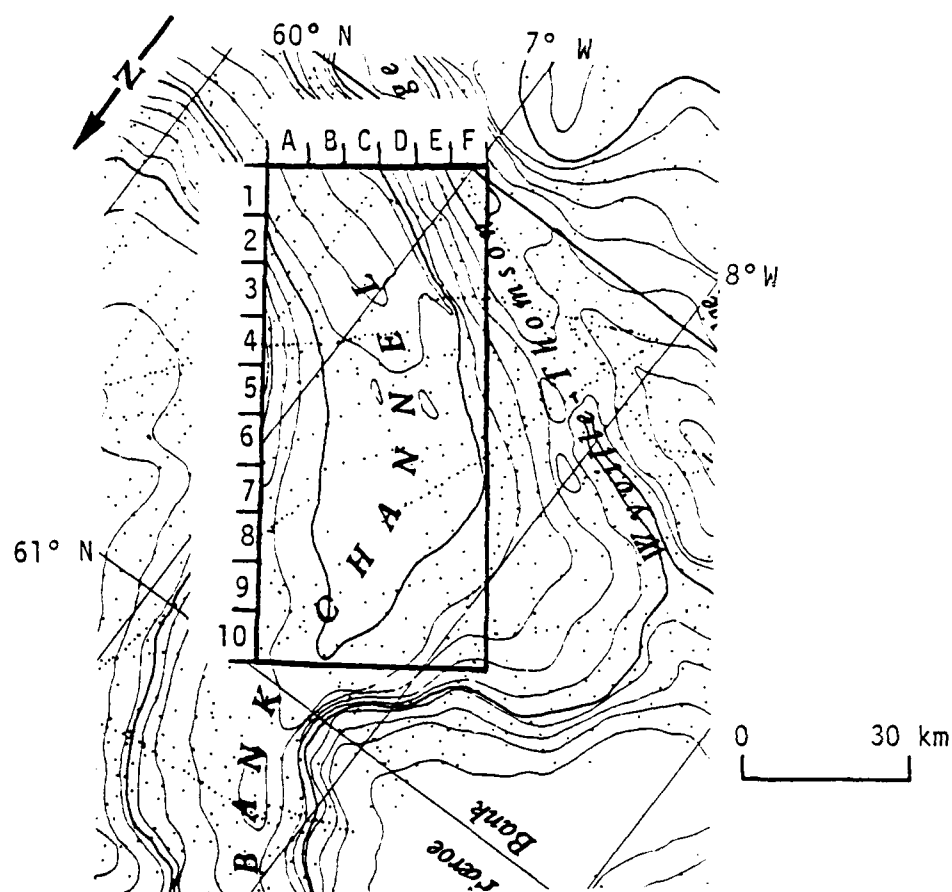


FIGURE 17. GROUND COVERAGE OF SEASAT SAR REV. 762 OVER WYVILLE-THOMSON RIDGE. (After IOS Chart No. C6567, Depth Contours in 100-Meter Increments.)

beginning at A4 and continuing to B9 is believed to be a surface pattern caused by a frontal boundary. Its location appears to be over the edge of the Faeroe Shelf, an area with a water depth between 600 and 1000 meters.

Patterns on the ocean surface caused by meteorological phenomena are quite common on Seasat SAR imagery (see e.g., Beal, et al., 1981; Kasischke, et al., 1982; or Fu and Holt, 1982). Those observed on the JASIN-Seasat imagery appear to be the result of either high or low winds.

High winds can result in a meteorological phenomena known as a windrow or row vortice (LeMone, 1973). Windrows are secondary, crosswind circulations which have a periodic structure in the crosswind direction, i.e., parallel to the wind direction. Their horizontal wavelength is approximately two to four times the thickness of the planetary boundary layer. This periodic variation of the surface wind results in a corresponding alteration of the ocean surface roughness, which in turn can be detected by a SAR. Figure 18 was collected during Rev. 642. Sea truth measurements indicate a wind speed of 12.9 m/sec from 150°(T) was present at this time. As shown in Figure 18, the direction of the wind is parallel to the direction of the periodic structures in the SAR image.

Areas of low velocity surface winds in ocean areas result in dark areas on SAR imagery. This is due to the fact that in these areas, insufficient winds exist to generate the short-period capillary waves responsible for the microwave backscatter from the ocean's surface. Figure 19 presents a SAR image collected during Rev. 556. Although a surface wind of 3.5 m/sec was present in the JASIN area, it is suspected that much lower winds were present in the area of Figure 19, which is located approximately 100 kilometers southeast of the JASIN OIA.

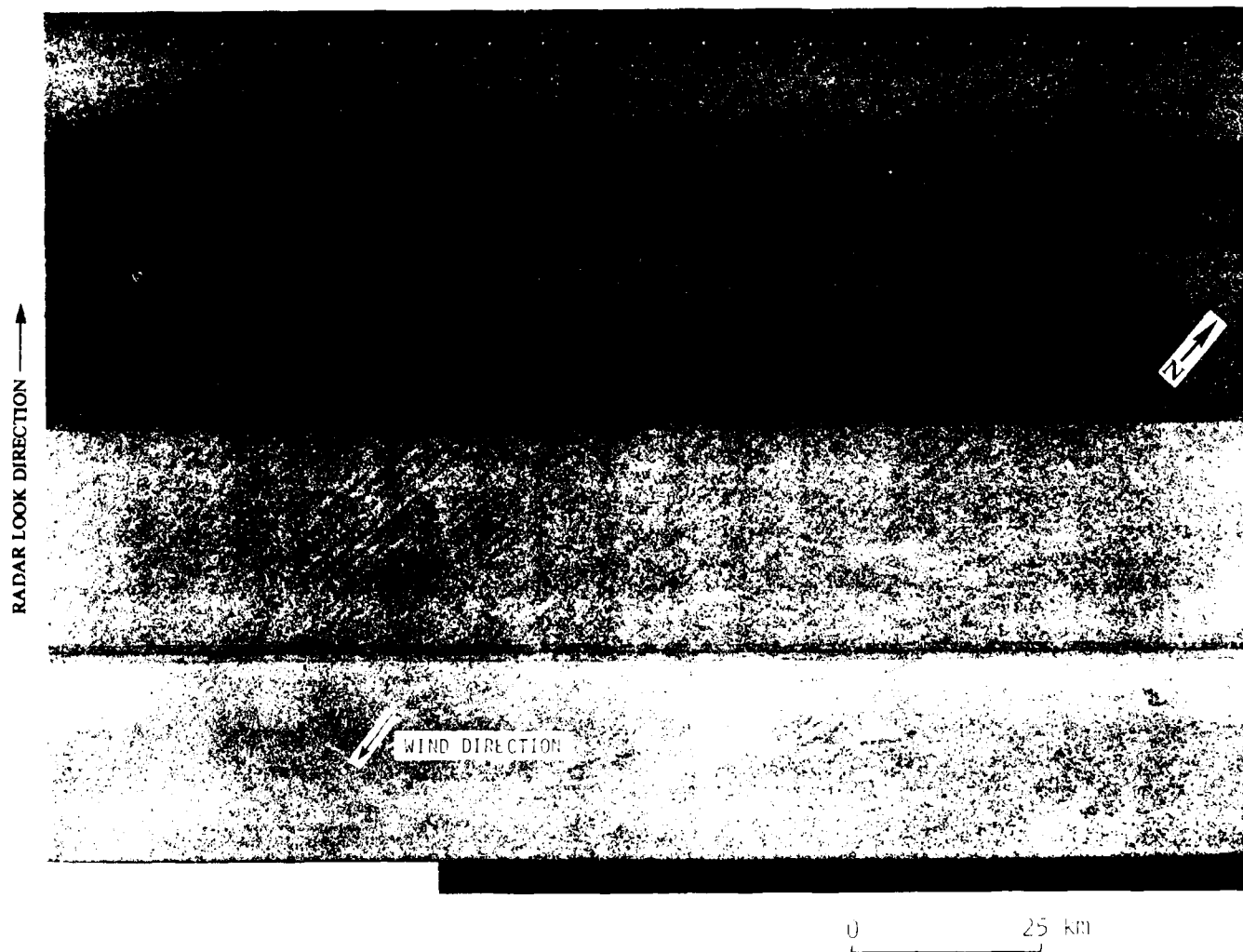


FIGURE 18. WINDROWS IMAGED DURING REV. 642. (JPL Optically Processed Imagery.)

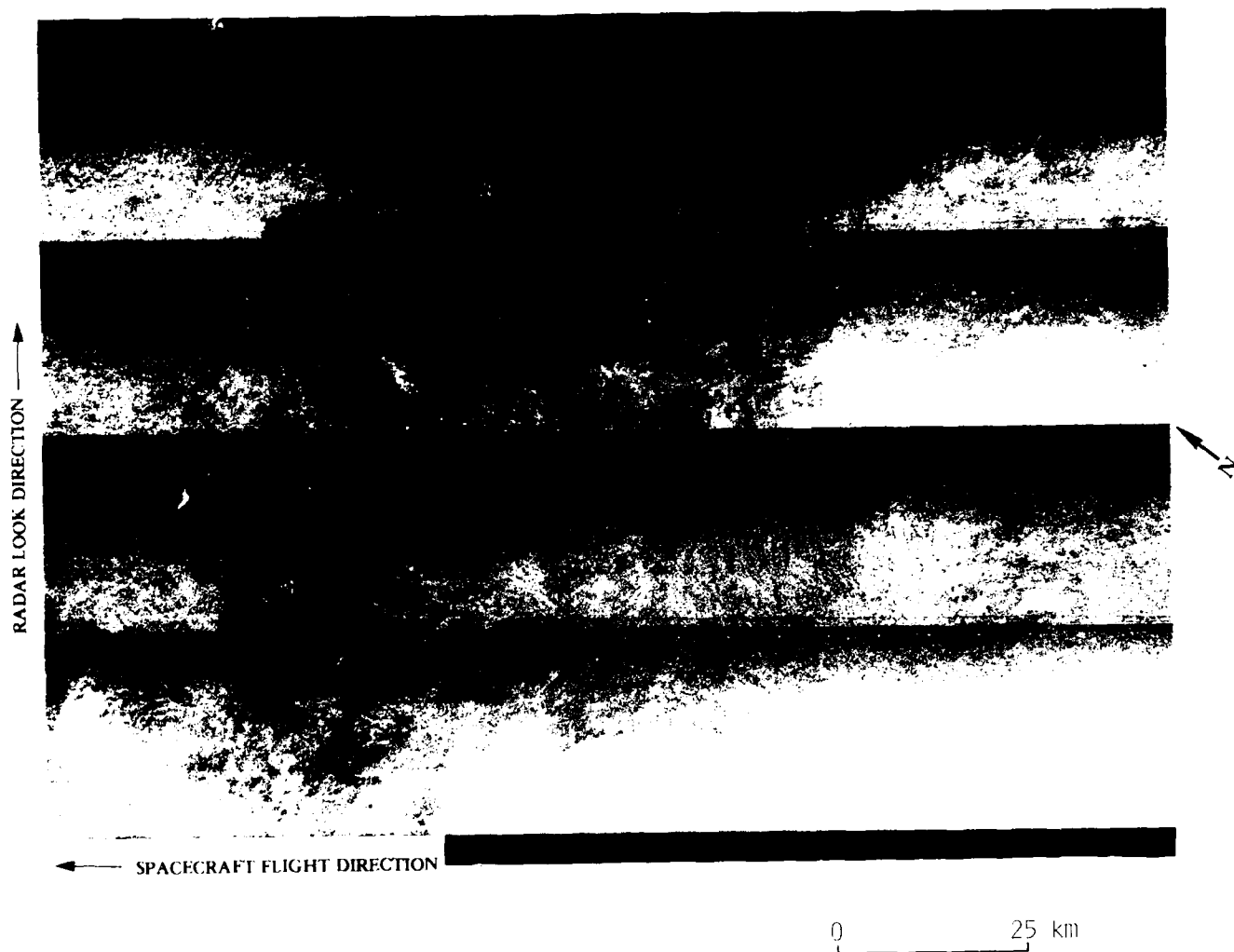


FIGURE 19. AREA OF LOW RADAR IMAGED DURING REV. 547. (JPL Optically Processed Imagery.)

The analysis of the spatial and temporal distribution of internal waves and frontal boundaries on the JASIN-Seasat SAR imagery was supported partially by funding provided by the Naval Research Laboratory (see Kasischke, et al., 1982). The main goal of this effort was to investigate the relationship between these deep-water surface patterns and the seventeen distinct bottom features in the area (see Table 11). Most of the internal waves and frontal boundary patterns occurred quite near these features.

Table 12 summarizes the occurrence of internal wave and frontal boundary patterns on Seasat SAR imagery for each of the seventeen deep water bottom features. Table 13 presents these occurrences for each Seasat revolution. Given in Table 13 are the Seasat revolution number, the total number of deep water bottom features within the ground coverage of a pass, and the total number of times an internal wave or frontal boundary pattern occurred over a bottom feature.

Presented in Figure 20 are the locations of the internal wave features which appeared on the Seasat imagery. The length of the lines indicate the two-dimensional extent of each internal wave packet. The lines with the arrows indicate which direction the crests of the internal waves are traveling. If no direction could be determined, then an arrow was placed at both ends. Plotted on Figure 21 are the locations and extent of the frontal boundaries identified on the JASIN SAR imagery.

From Table 13, we can see that 63 percent of the internal waves and 38 percent of the frontal boundaries were associated with a bottom feature. An interesting result of the multi-temporal, deep water analysis was that at no time did an internal wave pattern occur over a deep water area (i.e., the Rockall Trough, Iceland Basin or Norwegian Basin). These results strongly suggest a correlation between the deep water bottom features and the internal waves and also indicate some relationship may exist between the occurrence of

TABLE 12
SUMMARY OF OCCURRENCES OF BOTTOM-RELATED SURFACE PATTERNS
ON SEASAT SAR IMAGERY

Bottom Feature Covered by Seasat SAR	SAR Revolution Number	SAR Observed Pattern*	
		Internal Wave	Frontal Boundary
Iceland-Faeroe Rise	719	X	
	762	X	X
	958	X	
	1044	X	X
	1087	X	
Bill Bailey's Bank	719	X	X
	757		
	1006		X
	1044		
	1049	X	X
Lousy Bank	1087	X	
	633	X	X
	791		X
	834	X	
	958	X	
Hatton Bank	1006		
	1044	X	X
	1049	X	X
	1087	X	
	547		
George Bligh Bank	791		X
	958		X
	1044	X	
	547	X	
	791		X
Faeroe Bank	958	X	
	1044	X	
	1087	X	
	556		X
	719		X
	757	X	X
	762	X	X

TABLE 12
SUMMARY OF OCCURRENCES OF BOTTOM-RELATED SURFACE PATTERNS
ON SEASAT SAR IMAGERY (Continued)

Bottom Feature Covered by Seasat SAR	SAR Revolution Number	SAR Observed Pattern*	
		Internal Wave	Frontal Boundary
Faeroe Shelf	556		X
	599	X	X
	642	X	X
	757		
	762	X	X
Wyville-Thomson Ridge	556	X	
	599	X	
	642		X
	719	X	
	757		
Ymir Ridge	762	X	X
	556	X	
	599	X	
	642	X	
	719	X	
North Feni Ridge	757	X	
	1049	X	
	547	X	X
	556		X
	633		
Rosemary Bank	757		
	791	X	X
	834		
	1006	X	X
	1049		X
	556	X	
	599	X	
	633	X	X
	757		
	834	X	
	1006	X	X
	1049	X	

TABLE 12
SUMMARY OF OCCURRENCES OF BOTTOM-RELATED SURFACE PATTERNS
ON SEASAT SAR IMAGERY (Concluded)

Bottom Feature Covered by Seasat SAR	SAR Revolution Number	SAR Observed Pattern [*]	
		Internal Wave	Frontal Boundary
Rockall Bank	547	X	
	556		X
	757	X	
	791	X	
	958	X	X
	1044		
	1087		X
Anton Dohrn Seamount	547	X	X
	556	X	
	599	X	
	791	X	
West Shetland Shelf	642	X	
	762	X	
Malin Shelf	547		X
	633	X	
	791	X	
	834		
Hebrides Terrace Seamount	547	X	
	642	X	
	791		
Hebrides Shelf	599		
	633		
	642		
	719		
	762	X	
	834		
	1006		X
	1049		
TOTAL	92	58	35

^{*}An x indicates that surface pattern appeared over the position of the bottom feature during a particular Seasat revolution.

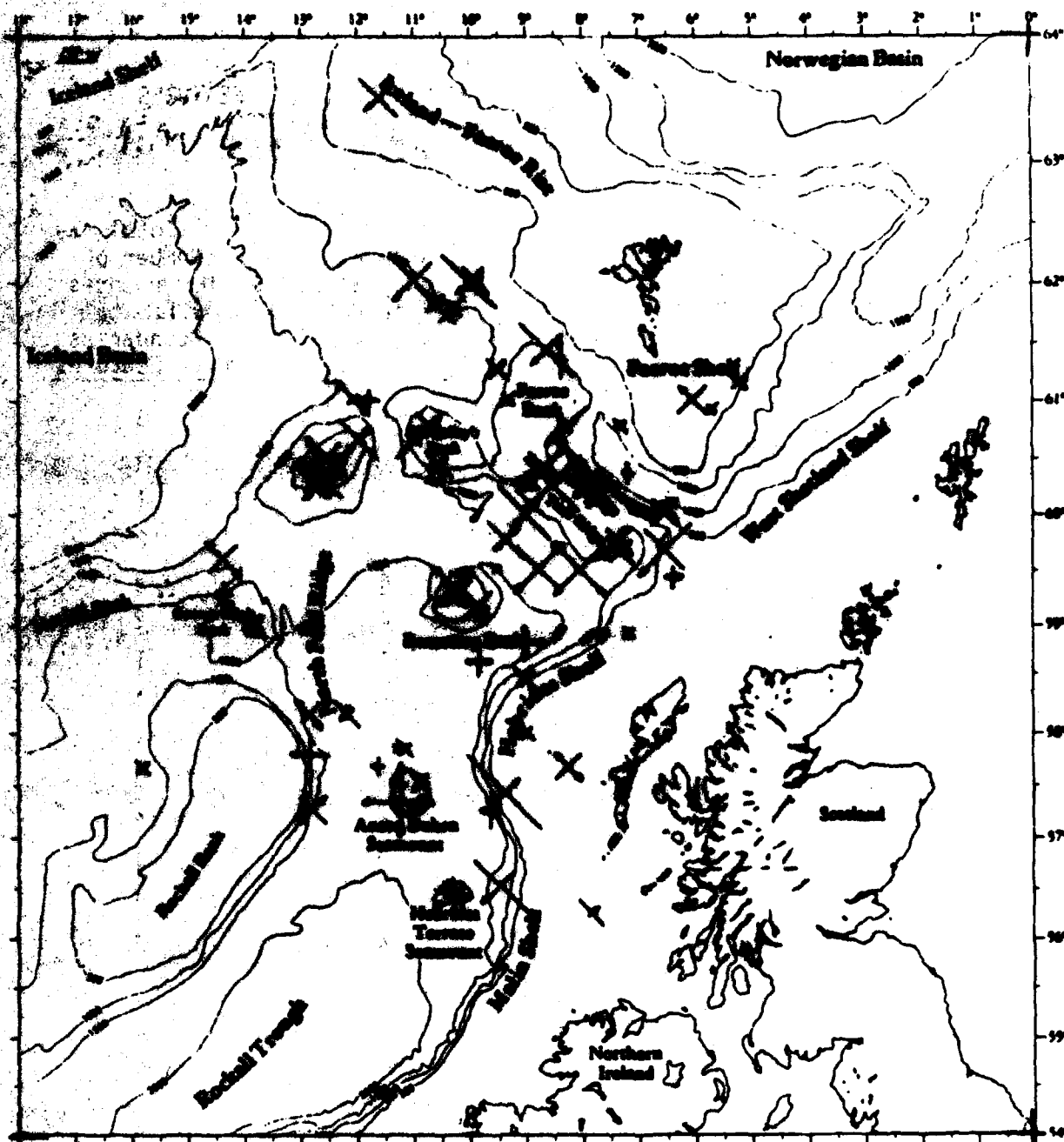
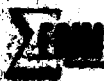


FIGURE 20. LOCATION OF INTERNAL WAVE-LIKE SIGNATURES IDENTIFIED ON SEASAT SAR IMAGES COLLECTED OVER THE JASIN AREA.

TABLE 13
SUMMARY OF DETECTIONS OF DEEP WATER TOPOGRAPHIC FEATURES
BY SEASAT SAR IMAGERY USING DATA COLLECTED
DURING THE JASIN STUDY

<u>Seasat Revolution</u>	<u>Total Number of Deep Water Bottom Features Covered</u>	<u>Total Number of Occurrences of Internal Waves Over Features</u>	<u>Total Number of Occurrences of Frontal Boundaries Over Features</u>
547	7	5	3
556	8	4	4
599	6	5	1
633	5	3	2
642	6	4	3
719	6	4	2
757	8	3	1
762	6	6	4
791	8	4	4
834	5	2	0
958	5	4	2
1006	5	2	4
1044	6	4	2
1049	6	4	2
1087	6	4	1
Total (Percent)	89	58 (63)	35 (38)

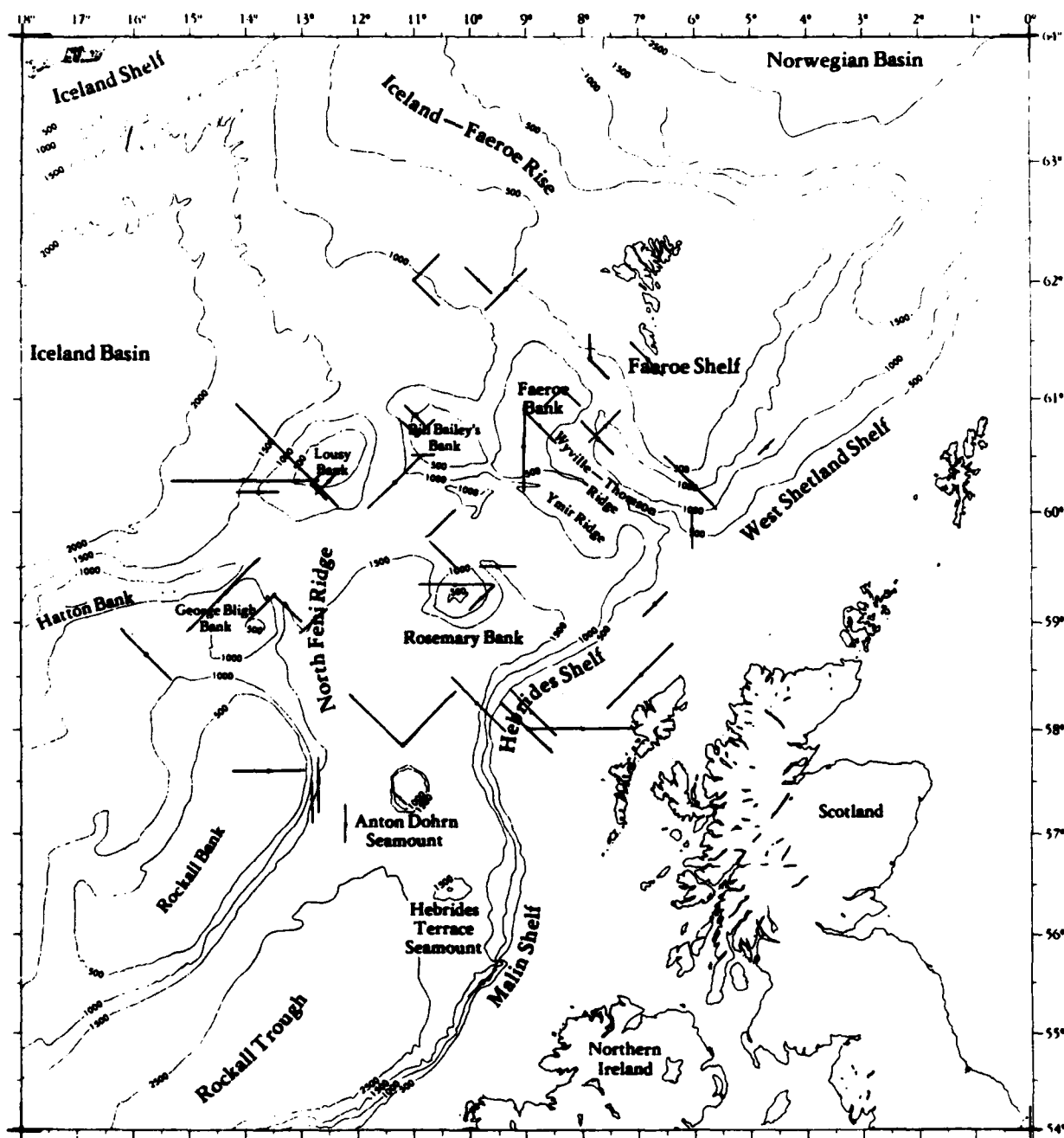


FIGURE 21. LOCATION OF FRONTAL BOUNDARIES IDENTIFIED ON SEASAT SAR IMAGES COLLECTED OVER THE JASIN AREA.

frontal boundaries and deep water features. They also suggest that the dissipation of deep water propagating internal wave pockets is sufficiently high to preclude their detection through successive passes.

Table 14 summarizes the occurrence of windrows and areas of low radar return on the JASIN-Seasat imagery. The patterns were not as widely spread nor as frequent as the frontal boundaries and internal waves. Previous analyses of Seasat SAR imagery have indicated that areas of low radar return collected over water usually indicate areas of low wind (see Beal, et al., 1981). Without any sea truth from the exact areas in Table 14 where dark regions occurred, it is difficult to categorically state that these are low-wind areas also, but it is our belief that they are.

Of the four times windrows were present, on two occasions the windrows were oriented parallel to the wind direction, on one occasion they were oriented 40° to the reported wind direction, and on one occasion no sea-truth was available.

4.3 ANALYSIS OF INTERNAL WAVE AND FRONTAL BOUNDARY PATTERNS

Because of their widespread and frequent appearance, the internal wave and frontal boundary patterns visible on the JASIN/Seasat imagery were further examined.

4.3.1 INTERNAL WAVE SIGNATURES

The surface environmental conditions present at the times of the Seasat overpasses were compared to the occurrence of the internal waves to determine if the absence of patterns could be explained by the theory that adverse surface conditions (i.e., high winds and/or waves) would mask the internal wave patterns. The surface conditions are presented in Table 2.

TABLE 14
SUMMARY OF THE OCCURRENCE OF WINDROWS AND
AREAS OF LOW RADAR RETURN

<u>Seasat Revolution</u>	<u>Windrows</u>	<u>Areas of Low Radar Return</u>
547	No	Yes
556	No	Yes
599	No	No
633	No	Yes
642	Yes	No
714	Yes	No
719	No	No
757	No	No
762	No	No
791	No	No
834	No	No
958	No	Yes
1006	Yes	No
1044	No	Yes
1049	No	Yes
1087	Yes	No

The Seasat Revolutions were divided into two groups for this analysis. Group I contained all those revolutions where the internal wave detection rate was greater than 70 percent. Group II contained all revolutions where the internal wave detection rate was less than 70 percent.

The average wavelength, wave height, wind speed, and direction of wave travel with respect to radar look direction for each group are presented in Table 15. Also presented in Table 15 are the range of these values for each group. Table 15 shows that no strong patterns exist in the data, with the internal waves being detected over a wide variety of environmental conditions, including high surface winds.

It has been suggested that a preferred look direction for viewing internal waves with SARs exists with internal waves whose crest orientations are perpendicular to the radar line-of-sight (i.e., range traveling) being detected more often by SARs than those whose crests are parallel (i.e., azimuth traveling) (Fu and Holt, 1982). Although cases exist where range traveling internal waves have been imaged by SARs (see Vesecky and Stewart, 1982 or Figure 11, this report), these are thought to be the exception rather than the rule.

The orientations with respect to the radar line-of-sight of the crests of the internal waves on the JASIN SAR imagery were determined. Four orientation classifications were used:

1. 0° - 30° : The crests of the internal waves are parallel to the radar line-of-sight (i.e., azimuth traveling).
2. 30° - 60° : The crests of the internal waves are half way between range and azimuth traveling.
3. 60° - 90° : The crests of the internal waves are perpendicular to the radar line-of-sight (i.e., range traveling).
4. 0° - 90° : The crests of the internal waves are oriented in every direction.

TABLE 15
COMPARISON OF INTERNAL WAVE DETECTION GROUPS TO
ENVIRONMENTAL PARAMETERS

<u>Environmental Condition</u>	<u>Group I (Internal Wave Detection >70%)</u>	<u>Group II (Internal Wave Detection <70%)</u>
Wavelength		
Average	169 m	175 m
Minimum	71 m	105 m
Maximum	299 m	256 m
Wave Height		
Average	2.7 m	3.4 m
Minimum	1.1 m	1.5 m
Maximum	5.7 m	5.0 m
Wind Speed		
Average	8.9 m/s	10.3 m/s
Minimum	4.5 m/s	3.6 m/s
Maximum	13.2 m/s	15.2 m/s
Wave Direction with Respect to Radar Look Direction		
Average	60°	47°
Minimum	25°	14°
Maximum	84°	85°

Table 16 summarizes the distribution of the internal wave orientations for both the ascending passes and the descending passes. Also presented in Table 16 are the direction of orientation for the internal waves. A direction of NE-SW, for example, means the crest of the internal wave is oriented from the northeast to the southwest. Note from the data in Table 16, that 44 internal wave packets were observed during the eight ascending orbits and 44 internal wave packets were observed during the seven descending orbits.

If the orientation of the internal waves in the JASIN area were equally distributed in all directions, and the SAR had no bias in the manner it detects internal waves, then we would expect that an equal number of azimuth (0° - 30°) waves and range waves (60° - 90°) would be observed. From Table 16, we can see that well over 50 percent of the detected internal waves had a range orientation. However, we can also see that the majority of the waves were oriented in a northeast to southwest or southeast to northwest direction, indicating the waves were not traveling an equal amount in all directions. It therefore appears more analysis is needed to interpret the meaning of the data presented in Table 16.

Throughout the analysis of the JASIN data, we have referred to a portion of the anomalous deep water surface patterns on the SAR images as internal waves. Although we have yet to develop direct evidence that these surface patterns are internal waves, the circumstantial evidence for this being the case is strong.

The generation mechanisms and sources responsible for internal waves have been extensively researched during recent years (Wunch, 1976; Muller and Olbers, 1975; Bell, 1975; Baines, 1979). Even so, the knowledge of the physical processes for internal wave generation is still very limited because a determination of the sources and sinks of internal waves requires a continuous record of the wave spectra (Garrett and Munk, 1975 and 1979).

TABLE 16
ORIENTATION OF INTERNAL WAVES OBSERVED ON SEASAT SAR IMAGERY
COLLECTED OVER THE JASIN AREA

Seasat Revolution Descending Orbits (Direction of Orientation)	Internal Wave Orientation*				
	0-30	30-60	60-90	0-90	
	NE-SW	E-W N-S	SE-NW	All	
556	1	1	3	0	
599	4	3	2	1	
642	5	3	2	1	
757	0	1	5	0	
958	1	0	3	0	
1044	2	0	2	0	
1087	0	4	0	0	
Subtotal	13	12	17	2	
Ascending Orbits (Direction of Orientation)	SE-NW	E-W N-S	NE-SW	All	
547	0	3	4	1	
633	1	1	5	1	
719	2	0	4	0	
762	0	1	8	0	
791	0	1	4	0	
834	0	0	2	0	
1006	0	0	1	0	
1049	3	0	2	0	
Subtotal	6	6	30	2	
Total	19	18	47	4	
	N-S	E-W	NE-SW	SE-NW	All
Total by Direction of Orientation	4	14	43	23	2

*A 0° orientation indicates the crests of the internal waves are aligned parallel to the radar line-of-sight; a 90° orientation indicates they are aligned perpendicular to the radar line-of-sight.

Several sources for the generation of internal waves have been identified, including surface atmospheric effects, internal (oceanic) effects and topographic effects (Thorpe, 1975). Surface atmospheric effects include traveling atmospheric pressure and stress, buoyancy flux, surface wave interactions and Ekman layer instability. Internal (oceanic) generation can be caused by decay of large scale circulations and breaking baroclinic instability (of which there is very little known). The generation of internal waves due to topographic features is similar to the generation of Lee waves by air flow over irregular surfaces. In the ocean, internal waves can be generated when a current (tidal or otherwise) flows over a deep water feature such as a seamount, guyot, or submarine ridge on the edge of a continental shelf (Wunch, 1975; Bell, 1975; Baines, 1979).

A recent analysis of the JASIN imagery gave further evidence for the occurrence of internal wave signatures on the JASIN Seasat SAR imagery [Liu (1983) and Kasischke, et al. (1983)]. The following discussion is from Liu (1983).

Figure 22 shows the Seasat SAR imagery of deep water features over the Wyville-Thomson Ridge collected during Revolution 762 on 19 August 1978 at approximately 06:45 GMT. Figure 23 combines line drawings of internal waves and a frontal boundary (discussed below) observed in Figure 22 with the corresponding bathymetric chart for this area. From Figure 23, it can be seen that there are numerous internal wave signatures. The internal waves in the middle of the image appear to be generated over the Wyville-Thomson Ridge. Near the lower right corner of the image, three wave packets are visible. It is to be noted that no waves were generated on the north side of the ridge.

The dominant bottom features are a broad, saddle-like valley on the East side of the ridge, and a 90° sector of deep water extending out from the ridge, as shown in Figure 24. The ridge has the

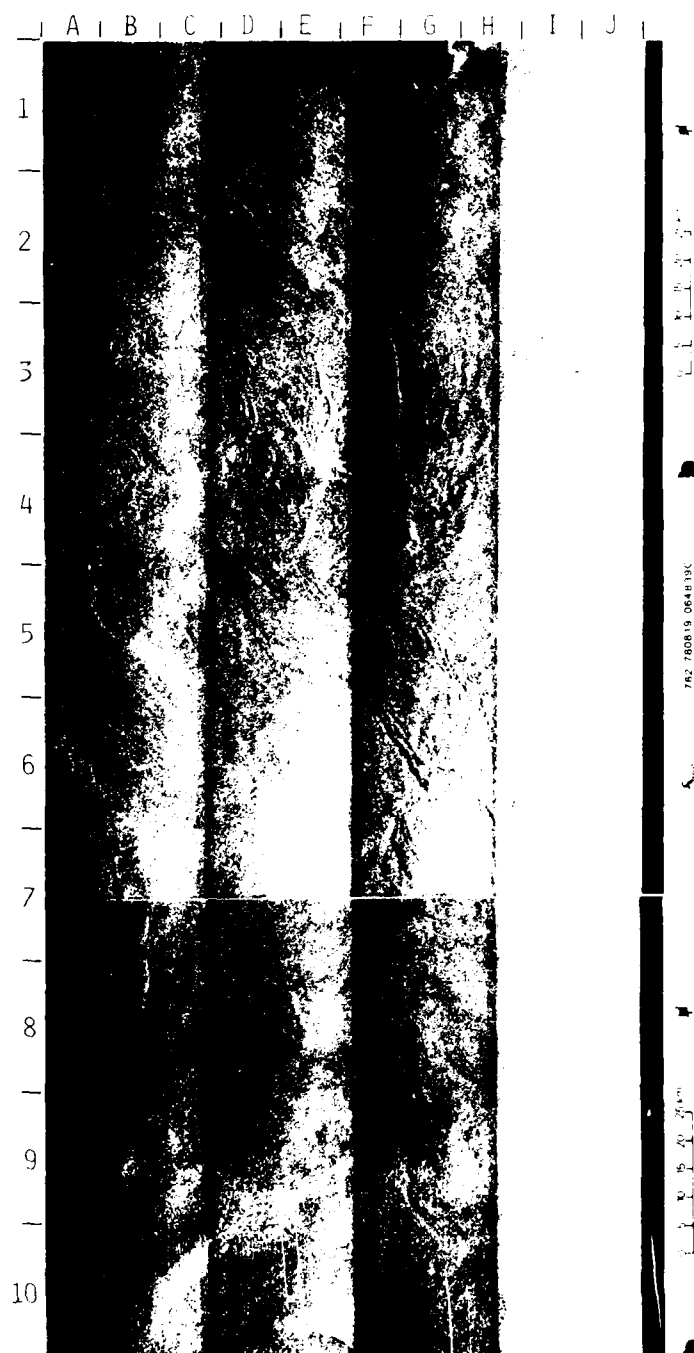


FIGURE 22. SEASAT SAR IMAGERY OF DEEP WATER FEATURES OVER THE WYVILLE-THOMSON RIDGE. REVOLUTION 762 (After Liu, 1983)

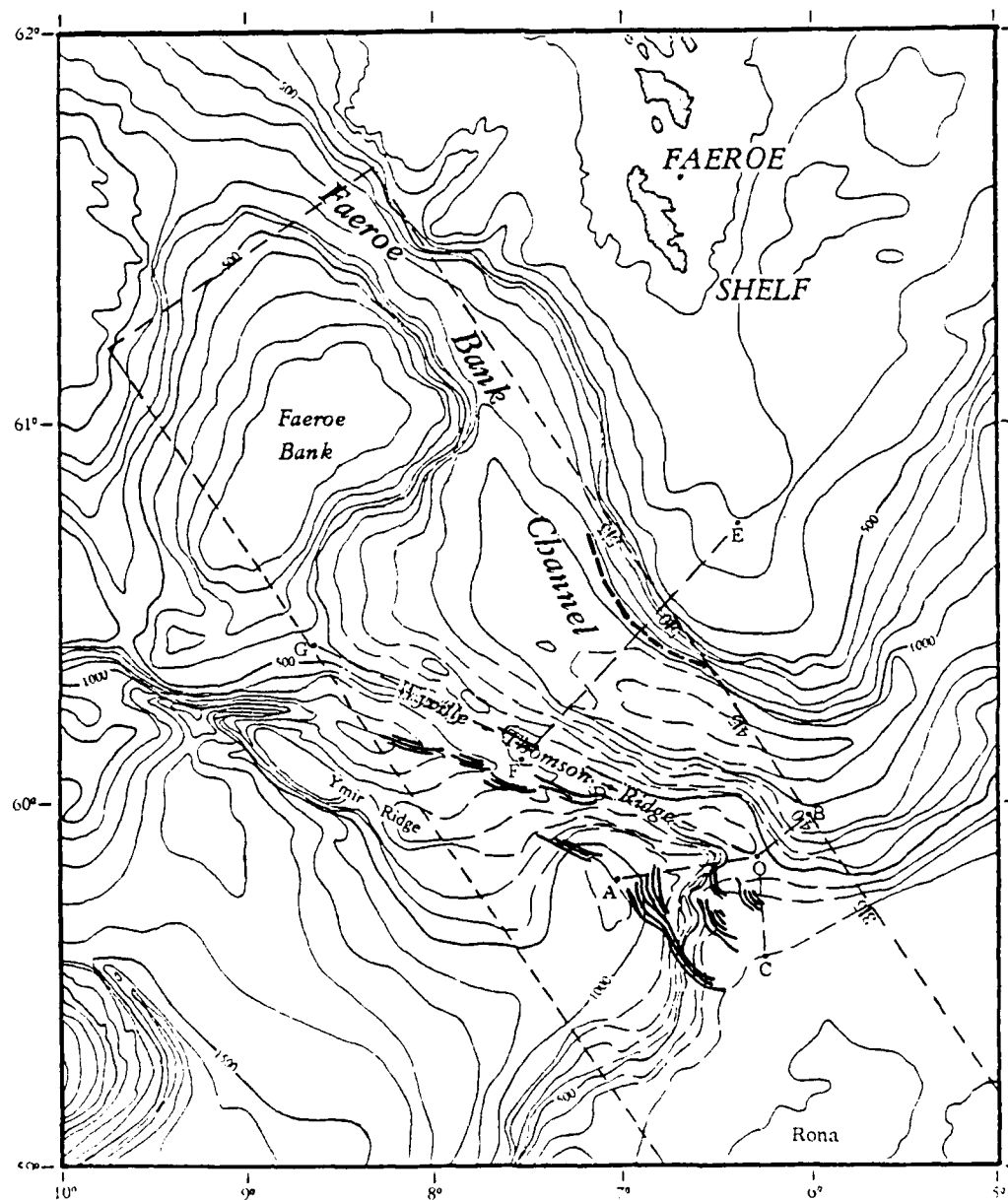


FIGURE 23. LINE DRAWING OF INTERNAL WAVES AND A FRONTAL BOUNDARY OBSERVED IN FIGURE 22 SUPERIMPOSED ON THE HYDROGRAPHIC CHART OF THE NORTHEAST ATLANTIC OCEAN (After Liu, 1983).

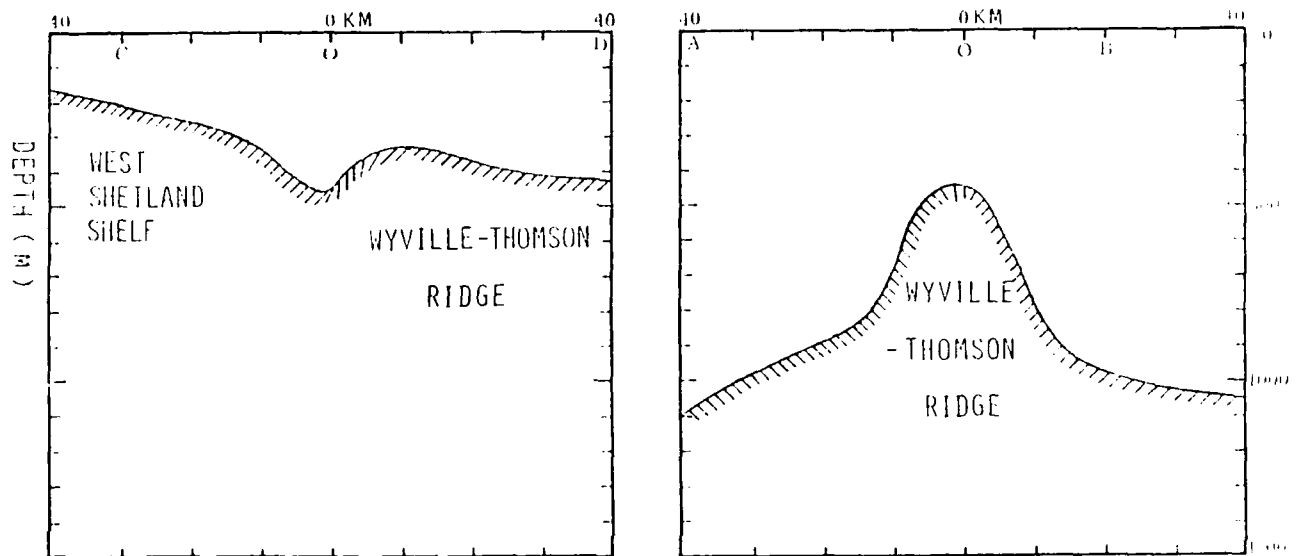


FIGURE 24. LONGITUDINAL AND TRANSVERSE BATHYMETRIC PROFILES ACROSS RIDGE, WITH A SADDLE-LIKE VALLEY AT 0. LOCATIONS OF LETTERS A, B, C, D AND O ARE INDICATED IN FIGURE 10 (After Liu, 1983).

characteristic scales of approximately 10 km in both the longitudinal and transverse direction. The minimax of the bathymetric saddle is at a depth of about 450 m.

Based on the bathymetry, it seems that the wave packets are produced by lee wave formation—a mechanism similar to the undulation of the jet stream as it passes over a mountain ridge. Figure 25 schematically illustrates the stages that are hypothesized during the production of solitary internal wave packets. As the strong semidiurnal tidal current flows north into the Faeroe Bank Channel, an internal lee wave forms on the northern edge of the ridge. As the tidal flow goes to zero six hours later, the lee wave, trying to maintain its group velocity relative to the current, escapes south over the ridge barrier back into the deep water, emerging as a packet of solitary waves. This phenomenon has previously been studied by Holbrook, et al. (1983) in the Sulu Sea. The initial waveform then can be viewed as a localized source that immediately begins to propagate, and evolves into a series of solitary waves while undergoing radial spreading, encountering variable topography and slowly losing energy through dissipation. The disappearance of internal waves on the north side of the ridge is probably because there is no strong tidal current flowing south across the ridge; most of the tidal current may flow along the Faeroe Bank Channel.

Based on the Seasat SAR image, wave packets in deep water over the Wyville-Thomson Ridge have the following properties:

1. Wave packets are separated by distances of the order of 14 km.
2. Wave speed is estimated to be 0.31 m/s based on the assumption of a semidiurnal tidal origin.
3. Wave packets in this region contain about five waves with packet width about 5 km.

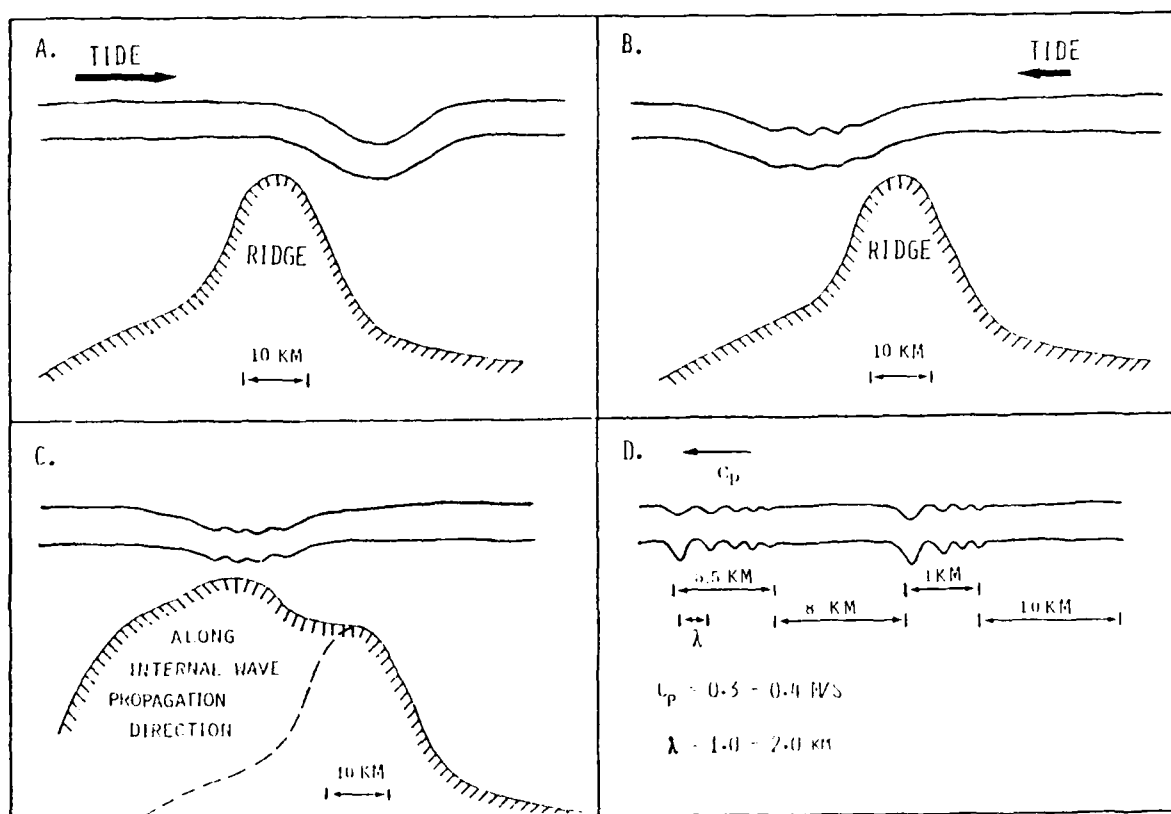


FIGURE 25. SCHEMATIC DIAGRAM SUMMARIZING THE GENERATION AND EVOLUTION OF AN INTERNAL WAVE PACKET OVER THE WYVILLE-THOMON RIDGE (After Liu, 1983).

4. Wavelengths are between 500 m and 1000 m.
5. The crests are curved in a horizontal plane with their convex sides pointed in the direction of propagation.

Although no in situ measurements are available, it is believed this area is dominated by tidal currents with velocities of less than 0.5 m/s at the surface. Figure 26 shows the profiles of potential temperature, salinity and sigma theta generated from data collected over the Iceland-Faeroe Rise during the Atlantic Expedition in August 1972 (Bainbridge, 1980). Station 19 is expected to be the measurement closest to the Wyville-Thomson Ridge area. As evident from Figure 26, a mixed layer of 40 m is dominant in this area during the summer. Based on the two-layer finite depth model, the linear wave speed is given by

$$\left[C_0 \approx \frac{\Delta \rho}{\rho} \frac{g}{k} \frac{1}{\coth kH_1 + \coth kH_2} \right]^{1/2}. \quad (17)$$

Near the Wyville-Thomson Ridge, $\Delta \rho / \rho \approx 0.6 \times 10^{-3}$, $H_1 \approx 40$ m, $H_2 \approx 260$ m, $2\pi/k \approx 500$ m, and thus the wave speed is approximately 0.40 m/s, depending on the water depths. This value is consistent with the estimated wave speed of 0.31 m/s from the SAR image. Based on the wavelength, the wave amplitude is estimated to be between 10 and 15 m. Note that the effect of shear is important in this case, since the wave speed is slow compared with the background current. Also, the bottom topography near the West Shetland Shelf is complex, which influences the evolution of wave packets, as shown in Figure 23. A similar solitary wave theory developed by Liu, et al. (1983) can be applied here. However, due to the limited scope of this investigation, the detailed analysis and calculations will have to wait until sea-truth data are available.

Liu (1983) also modeled the surface strain rate produced by shallow water (coastal) internal waves. He then used this surface strain

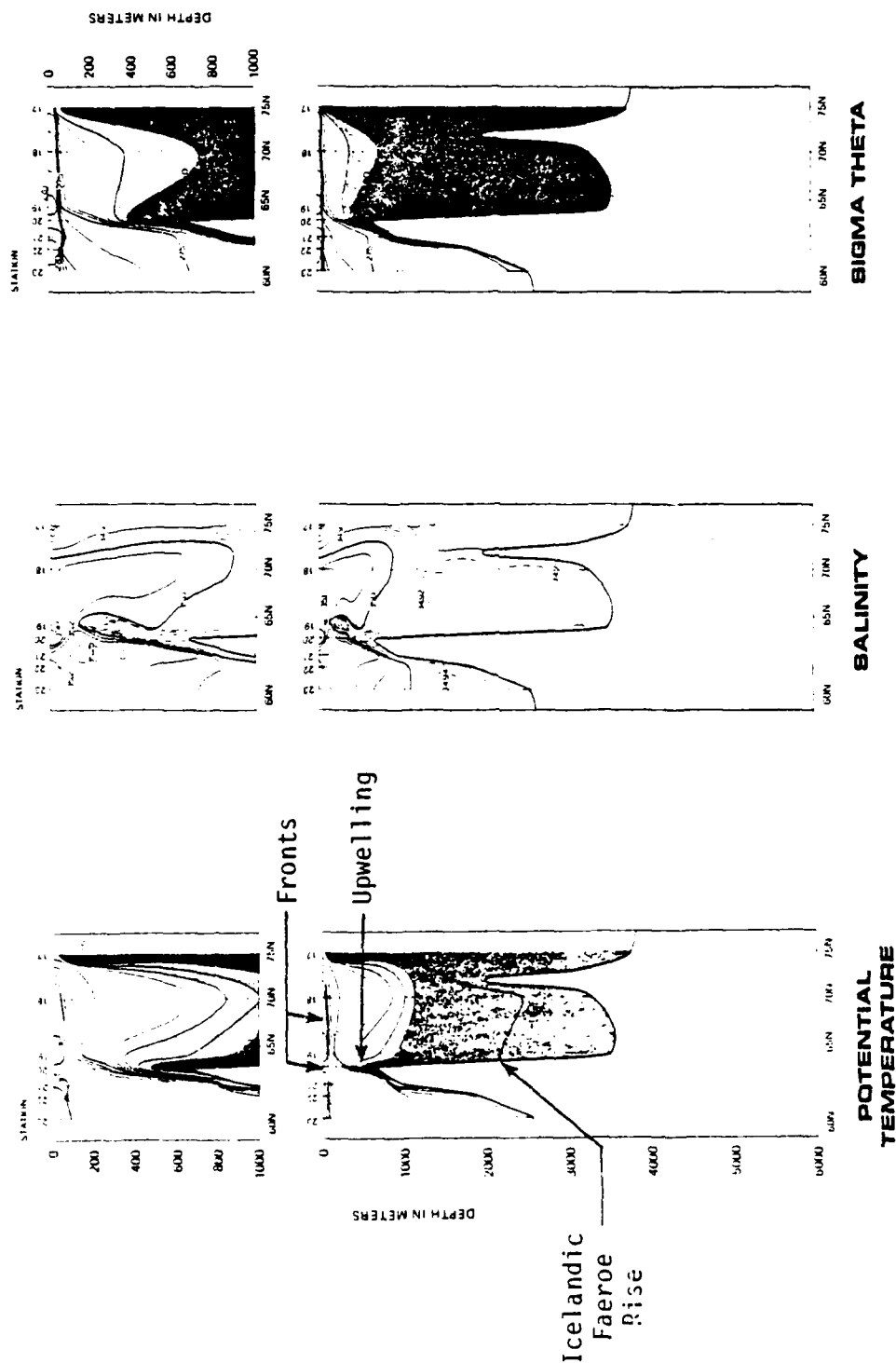


FIGURE 26. PROFILES OF POTENTIAL TEMPERATURE, SALINITY, AND SIGMA THETA FROM DATA COLLECTED OVER THE ICELANDIC-FAEROE RISE ILLUSTRATING DEEP WATER UPWELLING. (After Bainbridge, 1980.)

as an input to an electromagnetic model and simulated a SAR image of the internal wave, which compared favorably to the Seasat image. A similar surface strain is expected to occur for the deep-water internal waves, resulting in the patterns observed on the JASIN imagery.

4.3.2 FRONTAL BOUNDARIES

Even though they were not as prevalent on the JASIN Seasat SAR imagery, the case for frontal boundaries also being related to deep water bottom features is strong.

A front has been described as a convergence zone between two ocean water masses or currents of different velocities. Hence, a frontal boundary detected on SAR imagery is usually characterized by an altered surface roughness caused by the formation of white caps, the bunching of the surface capillary waves due to water velocity differences, or the alteration of capillary waves by surface slicks or foam fronts.

There are four different types of fronts to consider: (1) major ocean currents; (2) mixing of water from estuaries and rivers; (3) coastal upwelling; and (4) deep water upwelling. Fronts at the boundary of major ocean currents can extend over thousands of kilometers. The fronts are associated with the intrusion of either warm, salty water of tropical origin into higher latitudes (e.g., the Gulf Stream) or the intrusion of cold, less saline water into lower latitudes (e.g., the Labrador Current). These currents are generally in quasi-geostrophic balance.

Two smaller scale fronts which are generally restricted to continental or near-continental regions are those found at river or estuary mouths and coastal upwellings, which are the result of an offshore surface Ekman transport due to alongshore wind stresses. These fronts are formed in continental seas and estuaries, and are found around islands, banks, capes, shoals, and generally in the

boundary regions between shallow, wind and tidally mixed near-shore waters and stratified, deeper offshore waters. These fronts are more influenced by local acceleration, bottom stress and interfacial friction than by Coriolis force.

The JASIN area is sufficiently far away from the British Isles to rule out the later two small scale fronts as those observed. Surface measurements of currents made during the JASIN experiment (Tarbell, et al., 1979) and during previous years (Bainbridge, 1980) indicate that no persistent large scale surface currents exist in this region. It is believed this area is dominated by currents with velocities of less than 0.5 m/s at the surface (U.S. Naval Oceanographic Office, 1977). These tidal currents can also generate areas of upwelling. The following discussion of a front observed in the JASIN imagery again follows from Liu (1983).

The cold front that forms the boundary between the two layer system on the off-shore side and the vertically-mixed water in-shore has been observed on Seasat SAR images of the Faeroe Bank Channel. The curved, dark line beginning at 48 and continuing to 55, as indicated in Figure 23, is believed to be a surface pattern caused by a frontal boundary. Its location appears to be over the edge of the Faeroe Shelf, and closely matches the 800 meter bottom contour.

As shown in Figure 26, the deep water upwelling results in a frontal boundary over the Icelandic-Faeroe Rise. The relationship of the front to local upwelling topographic mixing may be described by the following process. Figure 27 shows the cross-section diagram of bottom topography of the Wyville-Thomson Ridge. It appears that the tidal current flowing over the ridge through another saddle-like valley on the west-side of the ridge forces the deep water isotherms up toward the surface. To illustrate this mechanism for frontal boundary generation, a schematic diagram of deep water upwelling over the Faeroe Bank Channel is shown in Figure 28. Therefore, the

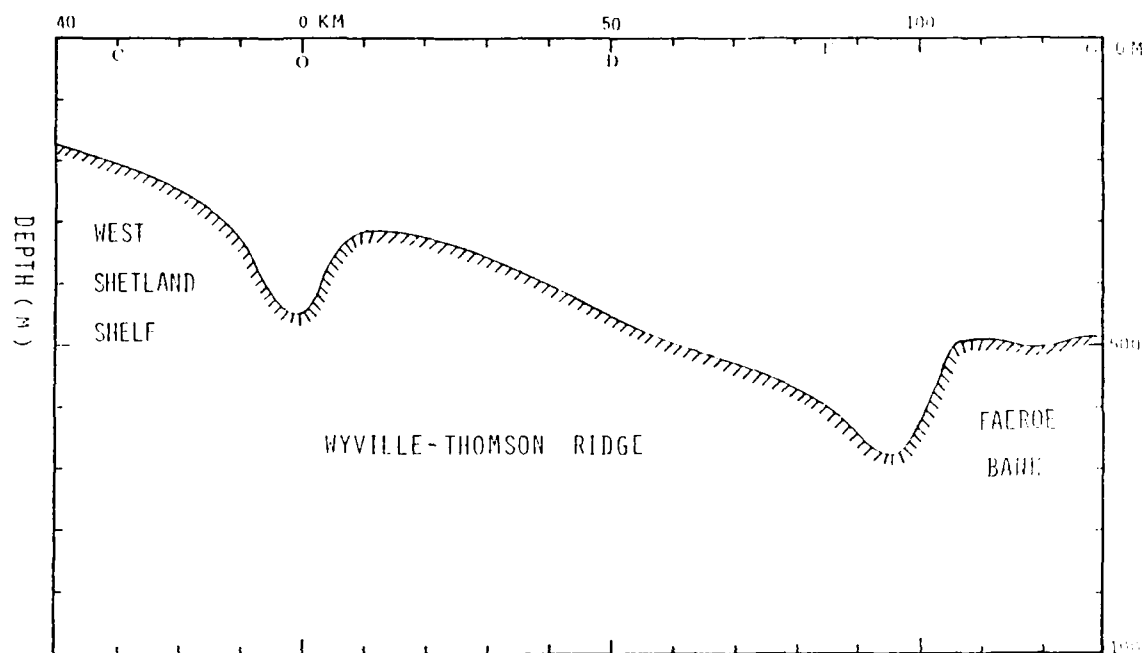


FIGURE 27. CROSS-SECTION DIAGRAM OF BOTTOM TOPOGRAPHY OF THE WYVILLE-THOMSON RIDGE (After Liu, 1983).

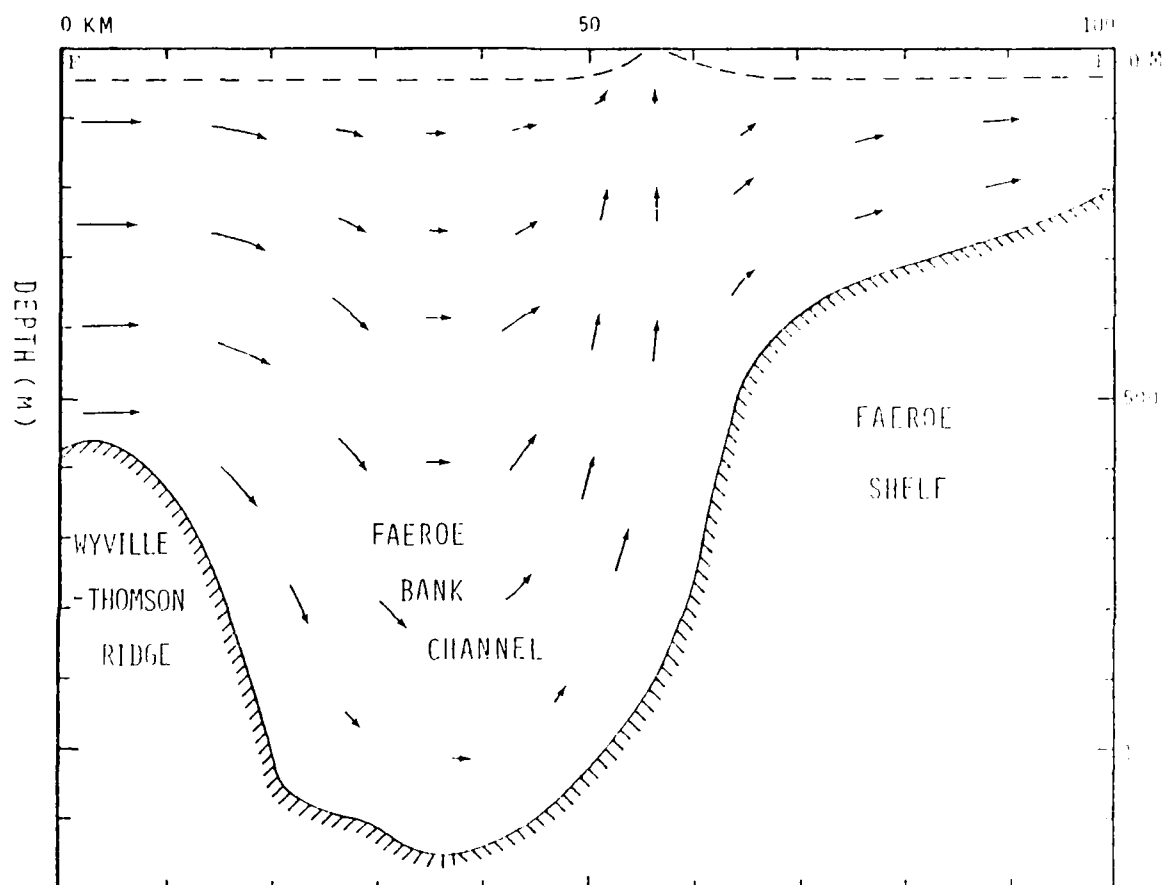


FIGURE 28. SCHEMATIC DIAGRAM ILLUSTRATING DEEP WATER UPWELLING OVER THE FAEROE BANK CHANNEL (After Liu, 1983).

frontal boundary seems to represent simply a surface intersection of the seasonal thermocline. The combination of frontal slope and current shear could yield information on density contrast across the front.

5 SUMMARY

This report further analyzed Seasat SAR imagery collected during the JASIN experiment. Two areas were investigated: SAR detection of gravity waves and SAR detection of large-scale features. Fast Fourier transforms (FFTs) from all 18 JASIN/Seasat orbits were generated. Estimates of dominant wavelength and direction of propagation were obtained from six of the FFTs. The rest did not produce spectra which could be interpreted. Optical Fourier transforms (OFTs) generated interpretable spectra with greater success than Fast Fourier Transformers (FFT). This is most likely due to the larger aperture size used to generate the OFTs.

Comparison of the wave contrast measurement (peak-to-background ratio or PBR) with surface truth measurements revealed a significant statistical relationship between wave contrast and dominant wavelength (λ) and wave height ($H_{1/3}$).

SAR data processing algorithms which compensate for the motion of surface gravity waves were evaluated using Seasat SAR imagery from Revs. 762 and 1087. Both teleshift (azimuth) and telerotation (range) adjustments were tested. It was found that Seasat SAR imagery of gravity waves was not affected using these adjustments. This was true in terms of both wave contrast (i.e., wave visibility) as well as the estimates of dominant wavelength and direction of propagation.

An algorithm by Thomas (1982) which estimates wave height from digital SAR data was evaluated. Although the algorithm showed promise, it raised more questions than it answered. Further evaluations of this technique should include varying the size of the area used to generate the wave height measure and applying the algorithm to a wider range of wave, wind and radar look directions.

AD-A140 584

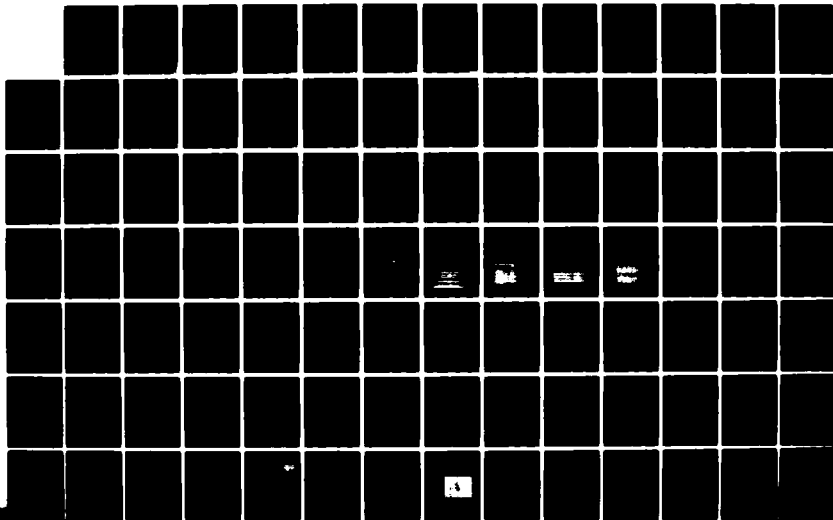
ANALYSIS OF SEASAT SAR IMAGERY COLLECTED DURING THE
JASIN EXPERIMENT(U) ENVIRONMENTAL RESEARCH INST OF
MICHIGAN ANN ARBOR E S KASISCHKE ET AL. MAY 83
ERIM-155900-16-T N00014-81-C-0692

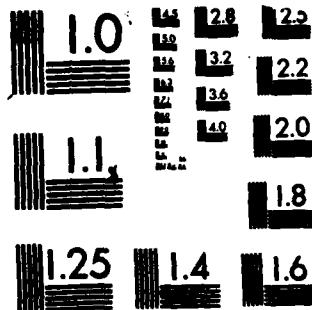
2/3

UNCLASSIFIED

F/G 8/3

NL





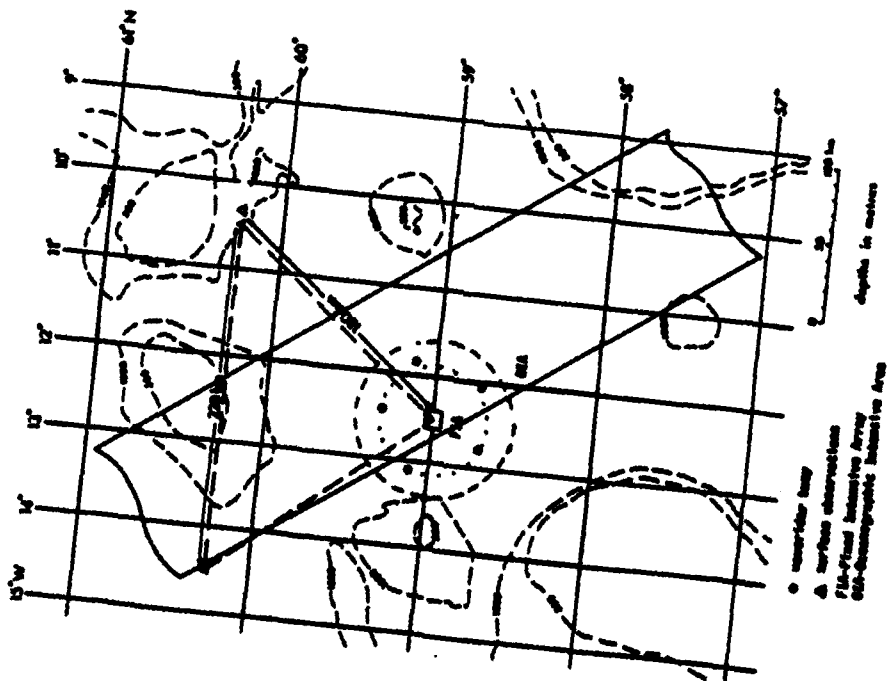
MICROCOPY RESOLUTION TEST CHART
NATIONAL BUREAU OF STANDARDS-1963-A

Mesoscale patterns studied on SAR imagery collected during the JASIN experiment included weather patterns, windrows, frontal boundaries and internal waves. Large areas of low radar return present on Seasat imagery are suggested to be areas of low wind. The location of these areas were compared to the locations of major weather fronts, but no correlation was found. Windrow patterns were detected on Seasat/JASIN imagery and were found to be aligned parallel to the surface truth wind direction.

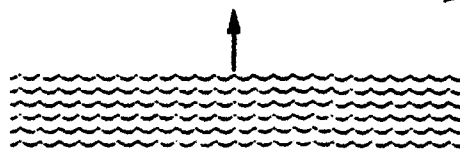
The locations of all frontal boundary and internal wave patterns on JASIN/Seasat images were plotted on a bathymetric chart of the Northeast Atlantic Ocean. These plots revealed that these patterns occurred over or close to a deep water bottom feature, such as a ridge, seamount, bank or shelf. At no time did a pattern occur over a deep water basin. An internal wave pattern appeared in Seasat SAR imagery 63 percent of the time Seasat passed over a deep water feature, while frontal boundary patterns appeared 38 percent of the time. The causes of internal waves and frontal boundaries on the Seasat SAR imagery have been identified as Lee wave generation and deep water upwelling, respectively. Research which combines oceanic, subsurface measures with the Seasat SAR imagery is definitely warranted to further study these patterns.

APPENDIX A SEASAT/JASIN PASSES

Presented in this appendix is a set of figures to assist in the visualization of the Seasat SAR ground track with respect to the oceanographic intensive array of the JASIN experiment. Each JASIN Seasat pass is illustrated in a separate figure. Each figure contains the location of the Seasat ground track superimposed on a map of the JASIN area as well as a schematic diagram of the satellite direction, radar look direction, the surface wave and surface wind fields.



Wind 006°
4.5 m/s

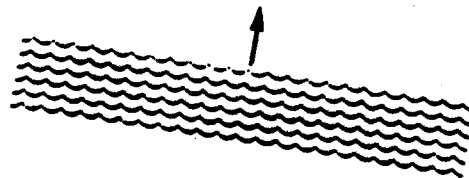


Waves
Direction = 263°
 $\lambda = 169$ m
 $H_{1/2} = 1.7$ m

Sensor (321°)

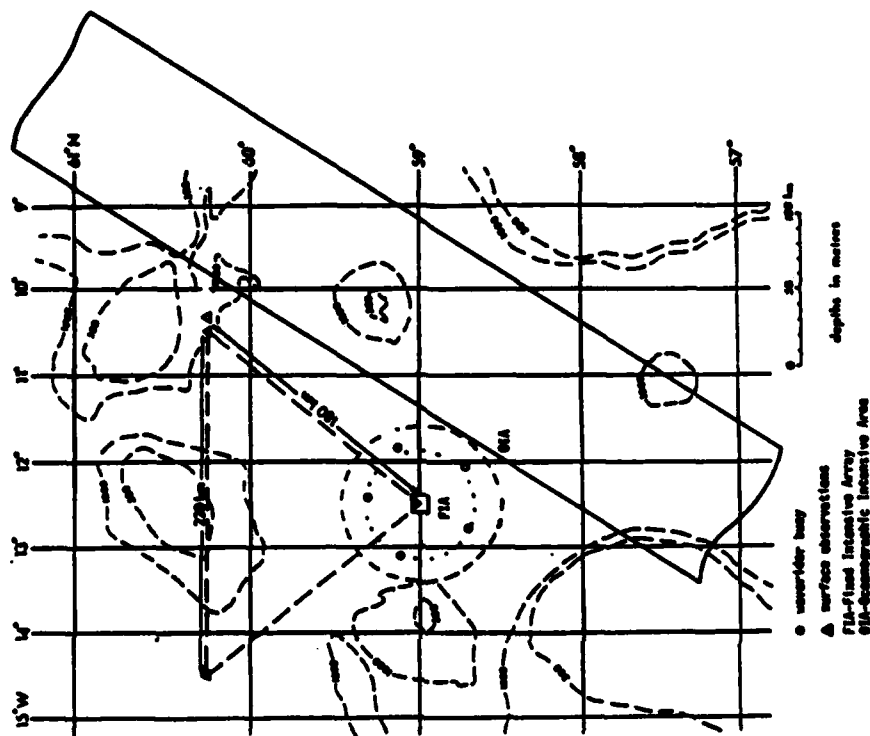
Rev 556

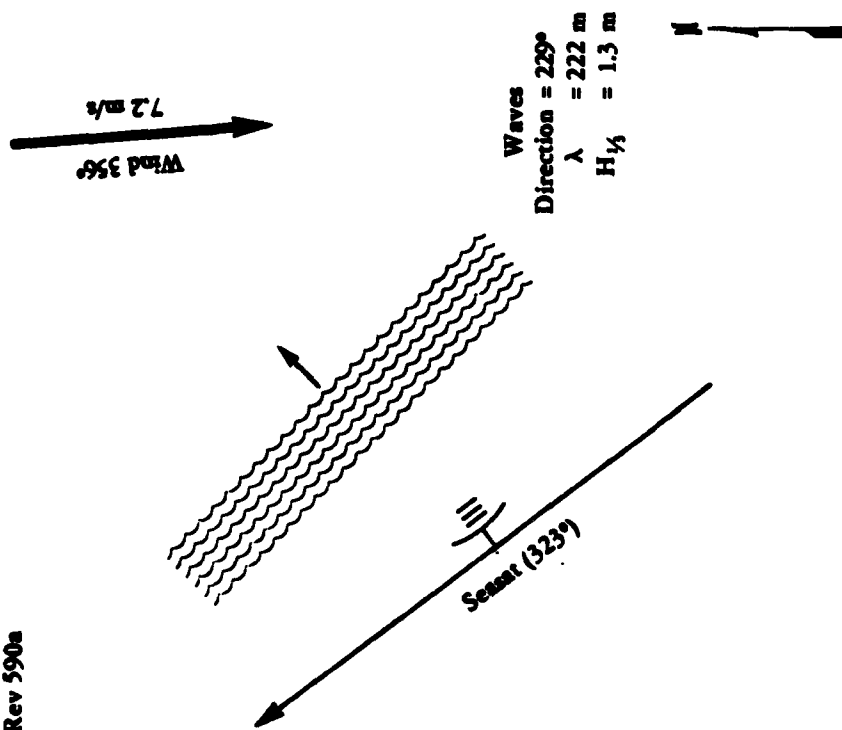
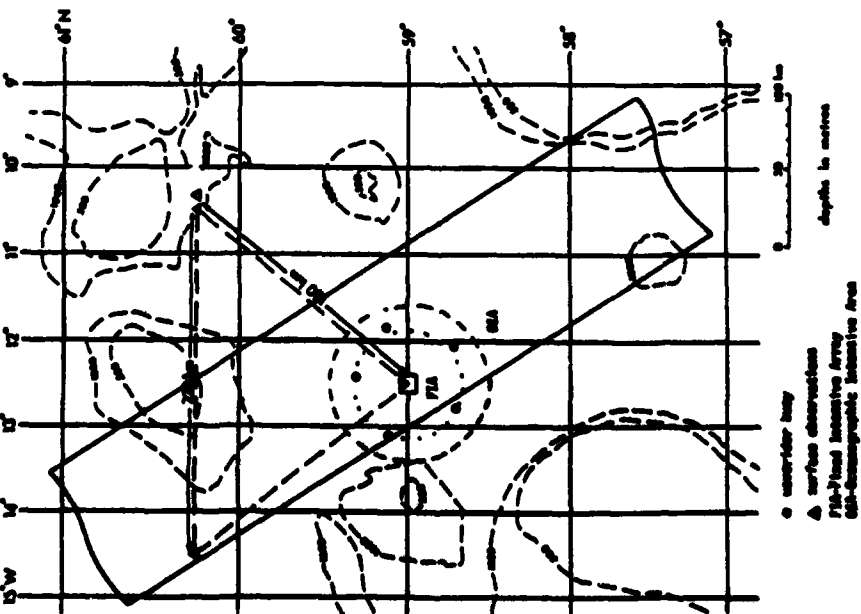
Wind 030°
3.5 m/s



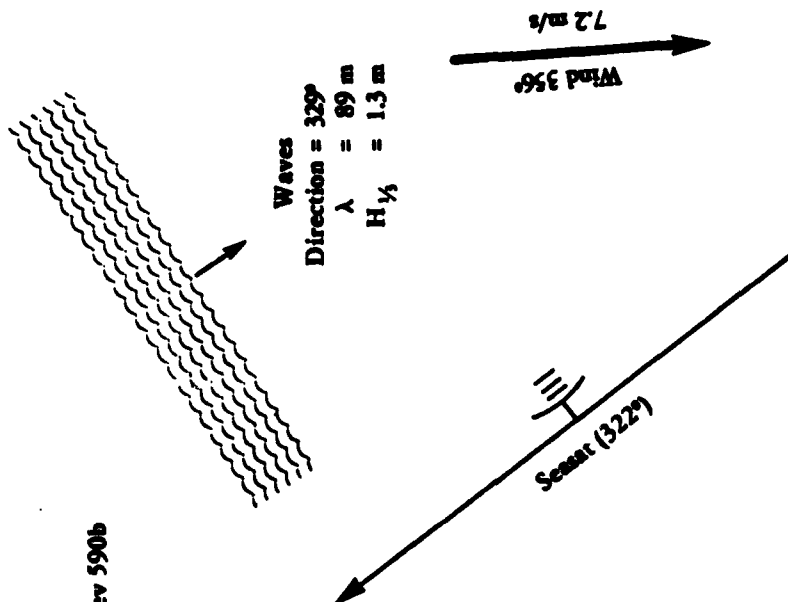
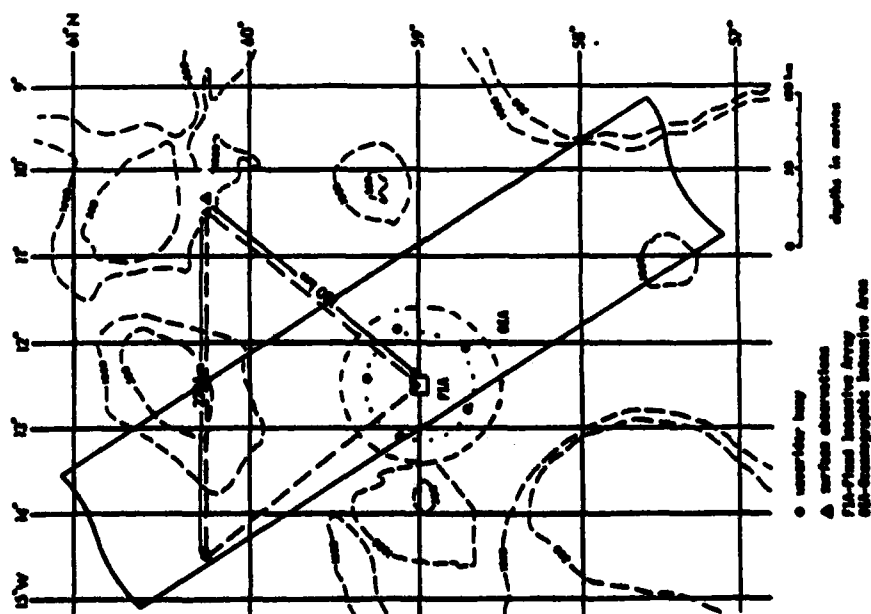
Waves
Direction = 280°
 $\lambda = 149 \text{ m}$
 $H_{1/2} = 1.5 \text{ m}$

Sensor (2169)



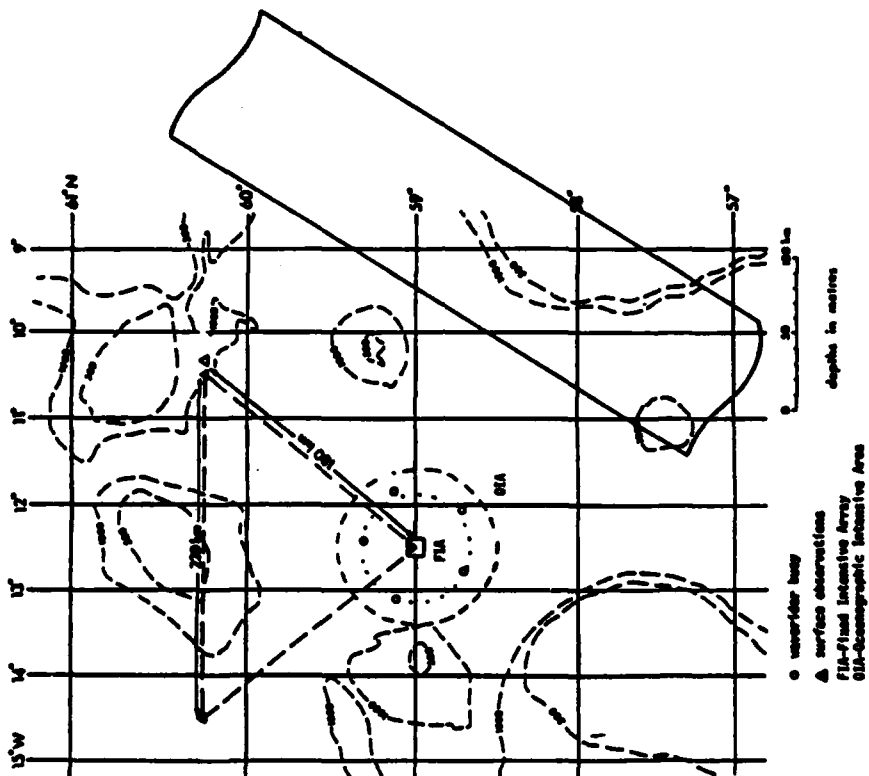
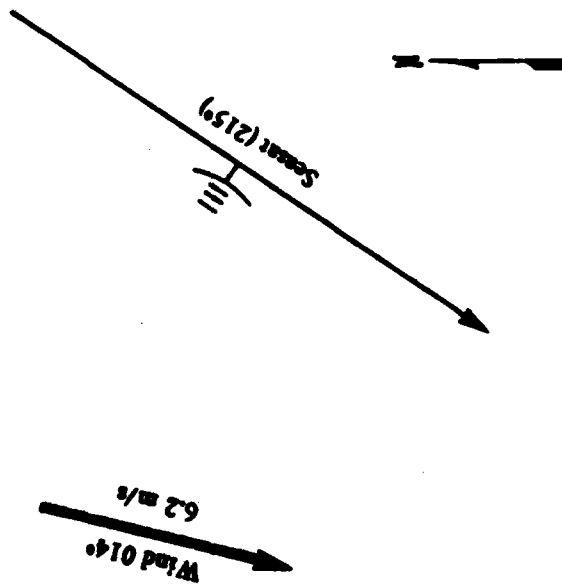


Rev 590b



Waves
 Direction = 20°
 $\lambda = 71 \text{ m}$
 $H_{1/3} = 1.1 \text{ m}$

Rev 599

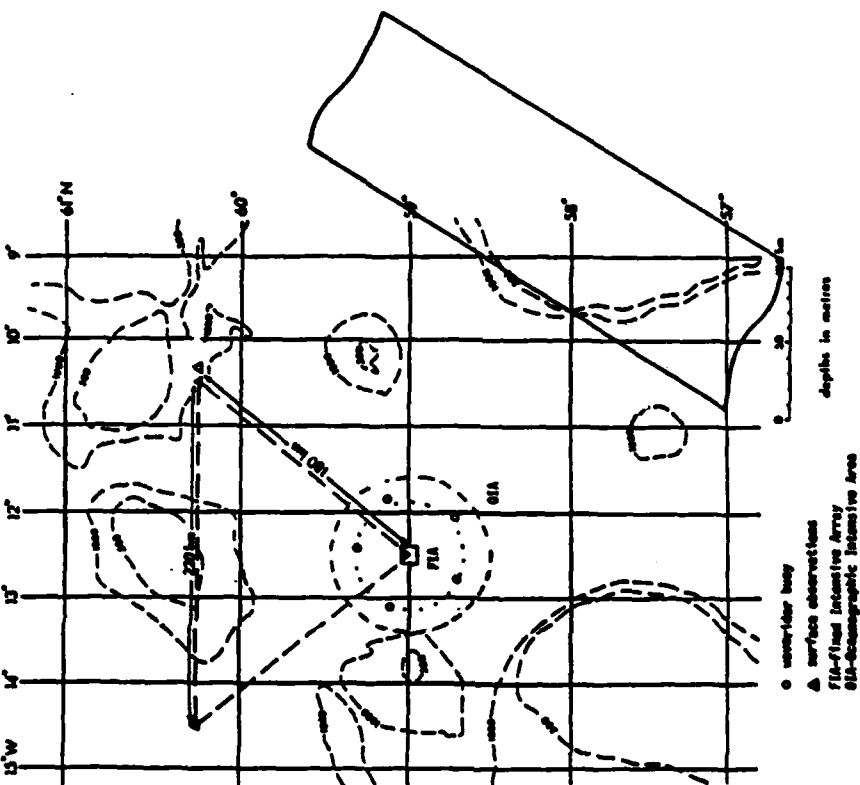


The map displays the study area in the western North Pacific, bounded by 13°N to 15°N latitude and 105°W to 115°W longitude. A grid of 1-degree squares is overlaid. Bathymetry is shown with dashed contour lines for depths of 100, 200, 300, 400, 500, and 600 meters. A solid line indicates the 10°N latitude. A dashed line represents the 110°W longitude. A solid line outlines the FIA-Flux Intensive Array, which is a rectangular area extending from approximately 13.5°N to 14.5°N and 105.5°W to 110.5°W. Within this array, several locations are marked: a solid triangle (▲) at approximately 13.8°N, 106.5°W; a solid square (■) at approximately 14.2°N, 108.5°W; and a solid circle (●) at approximately 14.0°N, 107.5°W. A dashed line labeled '110°W' is also shown. A scale bar at the bottom right indicates distances of 0, 50, and 100 km. A legend at the bottom right identifies the symbols: a solid circle (●) for 'surface buoy', a solid triangle (▲) for 'surface observation', a solid square (■) for 'FIA-Flux Intensive Array', and a dashed line for '600-m bathymetric isobath area'.

Waves
Direction = 220°
 $\lambda = 89 \text{ m}$
 $H_{1/3} = 1.1 \text{ m}$

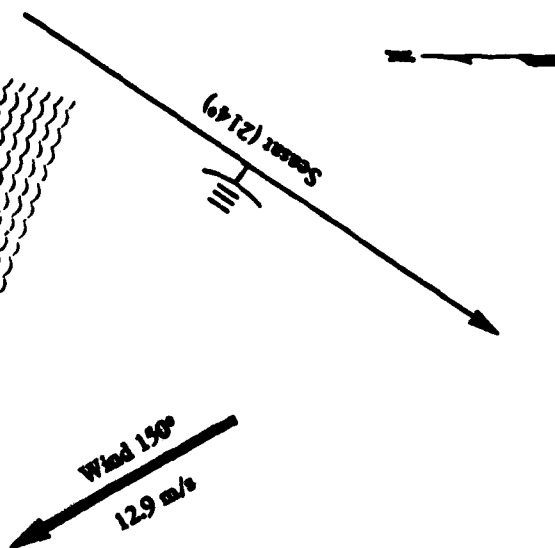
Wind 150°
 7.9 m/s

Senar 3230



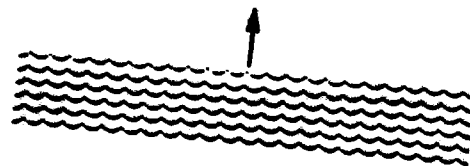
Rev 642

Waves
 Direction = 199°
 $\lambda = 169 \text{ m}$
 $H_{1/3} = 2.9 \text{ m}$

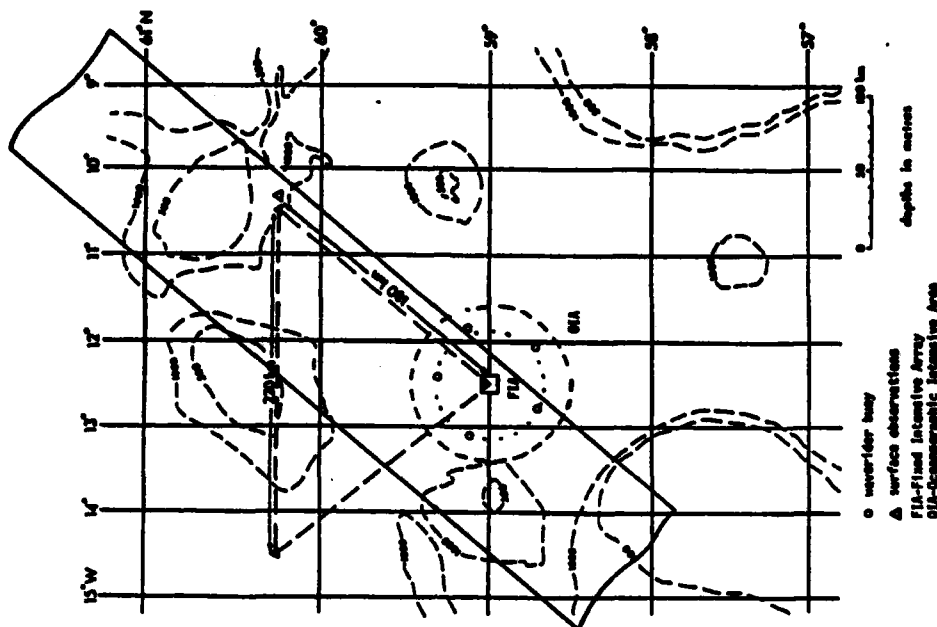


Rev 714

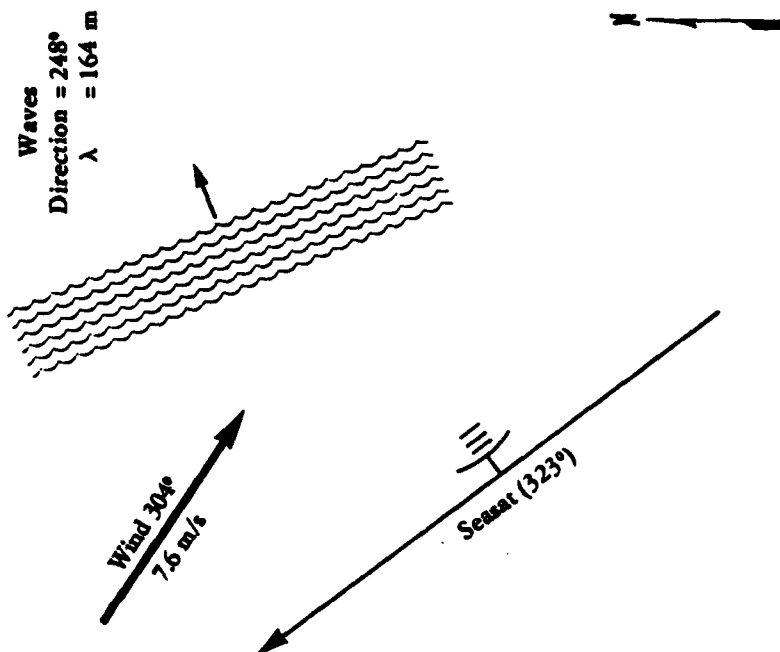
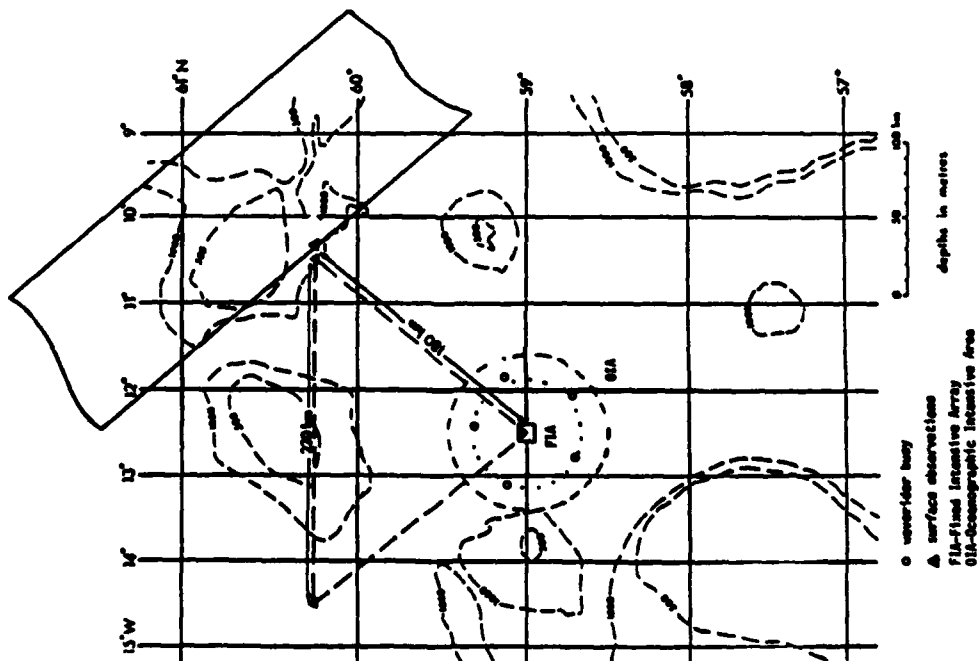
Waves
 Direction = 276°
 $\lambda = 182 \text{ m}$



Source (217°)

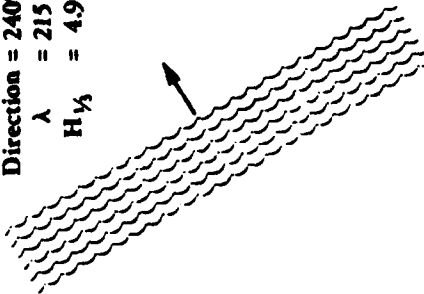


Rev 719



Rev 757

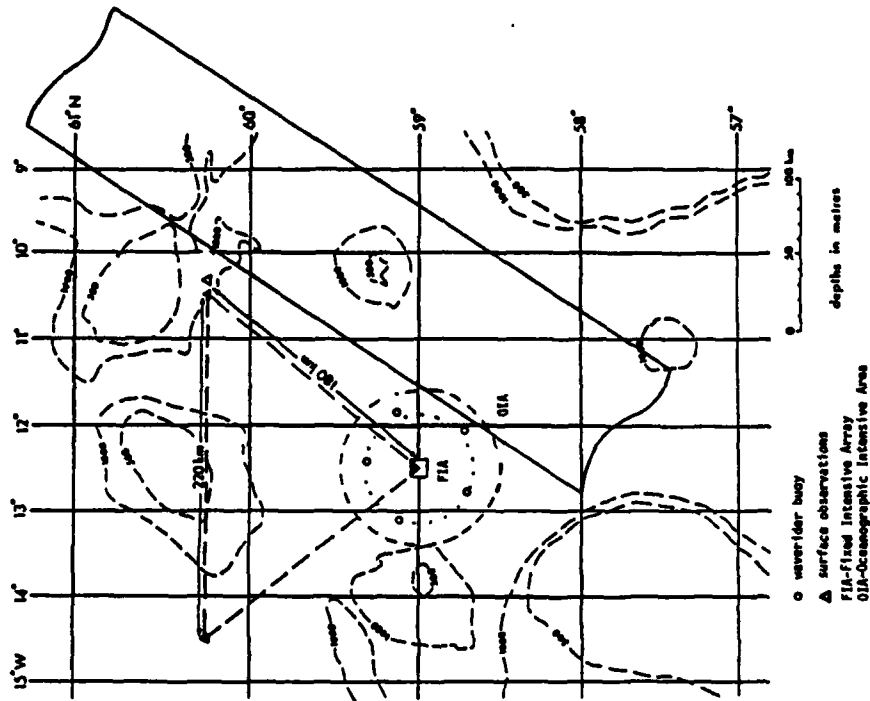
Waves
 Direction = 240°
 $\lambda = 215 \text{ m}$
 $H_{1/3} = 4.9 \text{ m}$

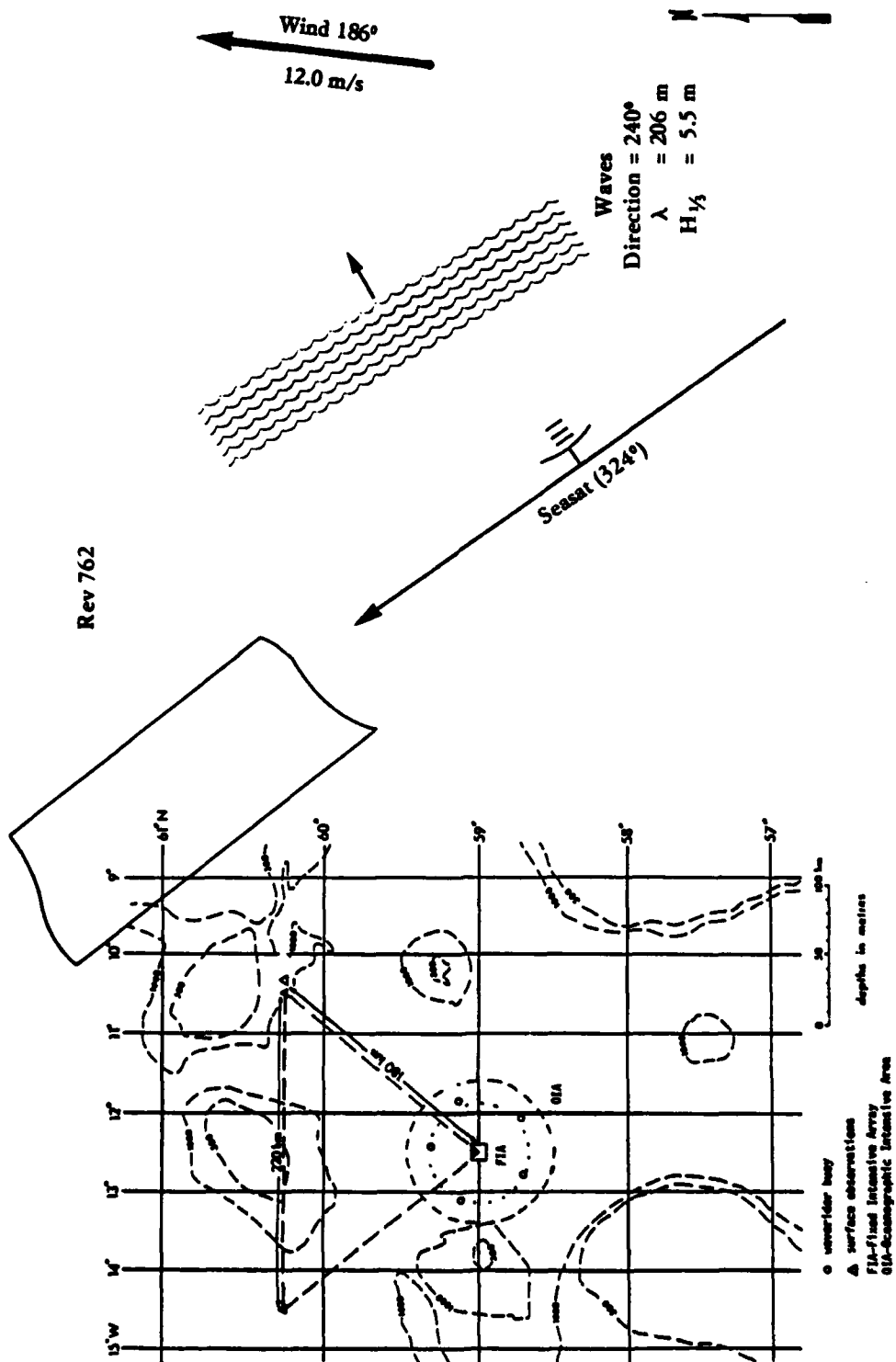


Seamc (2159)



Wind 186°
 15.2 m/s





[illegible]

Waves
Direction = 230°
 $\lambda = 132 \text{ m}$
 $H_{1/3} = 3.3 \text{ m}$

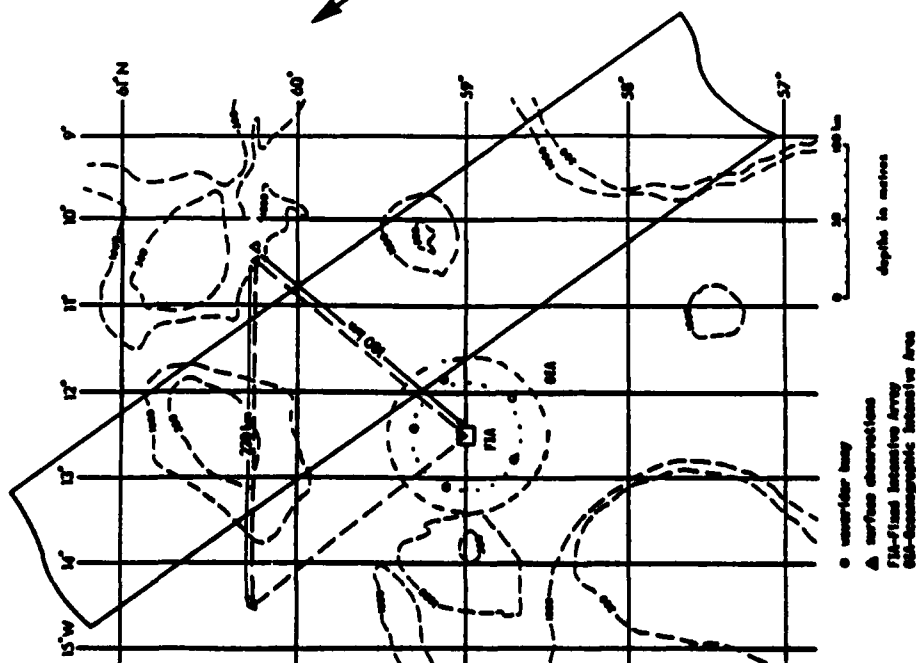
Wind 235°
13.0 m/s

Rev 834

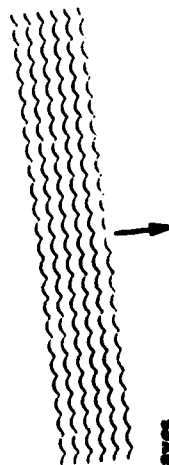
Waves
Direction = 295°
 $\lambda = 149 \text{ m}$
 $H_{1/3} = 2.8 \text{ m}$

Wind 272°
10.2 m/s

Sensor (3249)



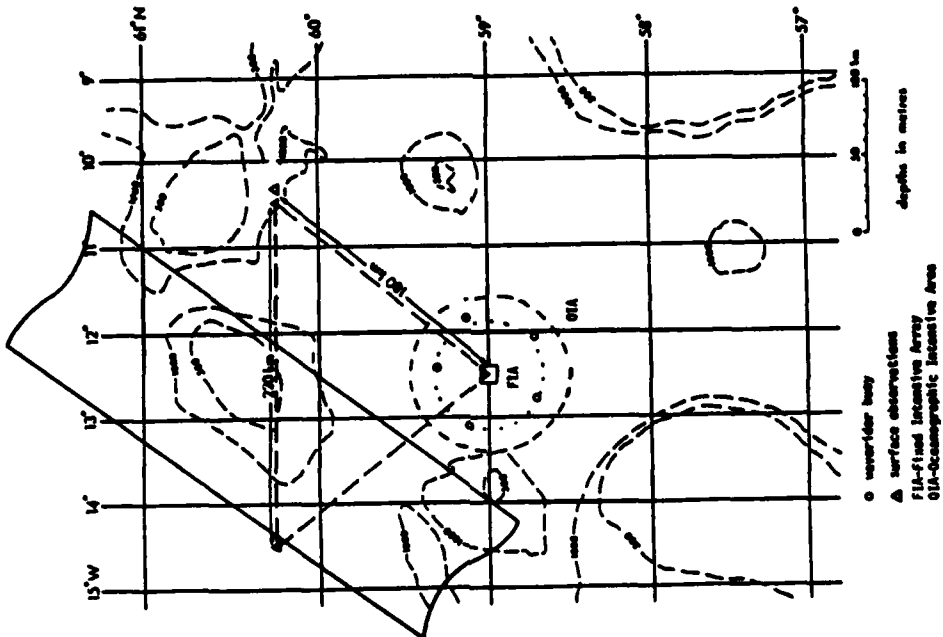
Rev 958



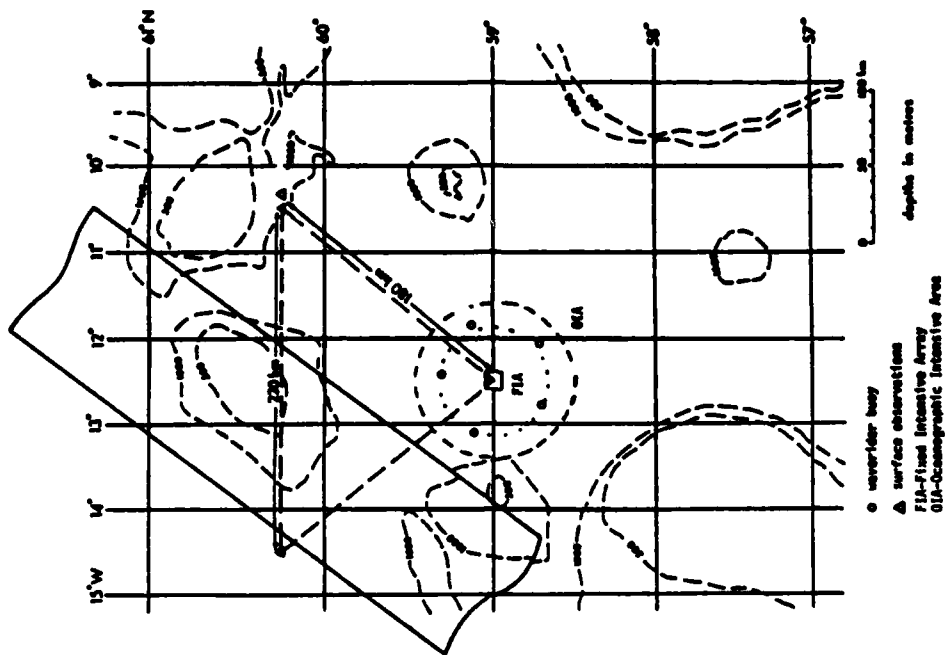
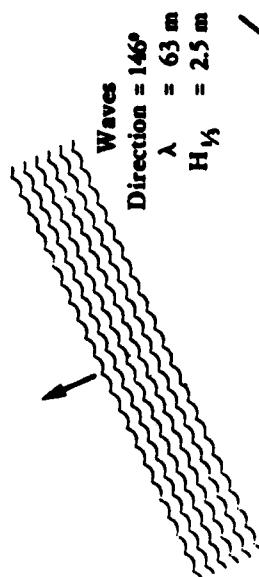
Waves
 Direction = 354°
 $\lambda = 100 \text{ m}$
 $H_{1/3} = 1.3 \text{ m}$

Wind 255°
 7.2 m/s

Seam (2159)



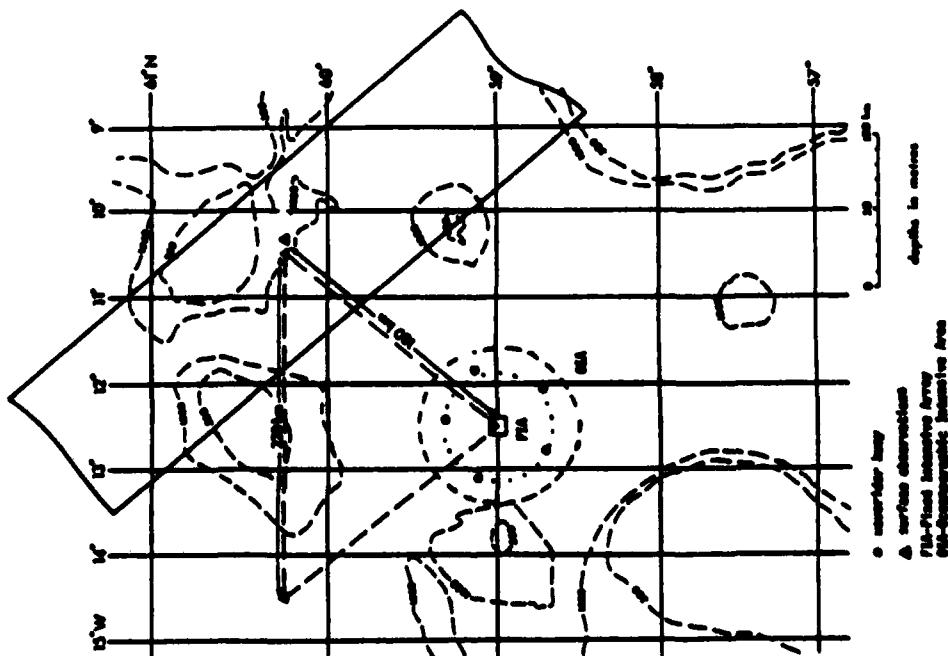
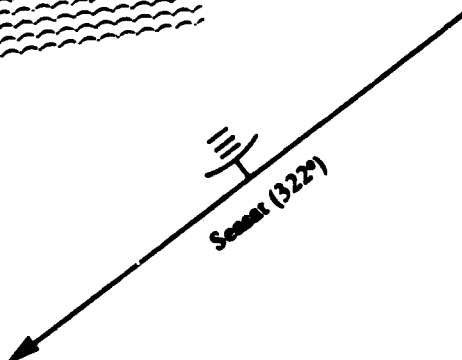
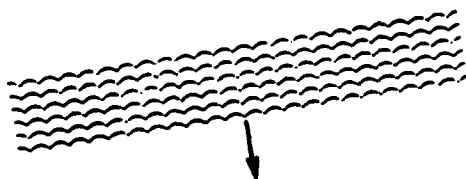
Rev 1001



Rev 1006

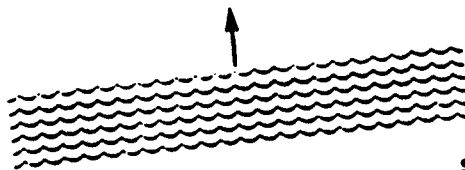
Waves
 Direction = 83°
 $\lambda = 107 \text{ m}$
 $H_{1/3} = 3.6$

Wind 91°
 6.6 m/s



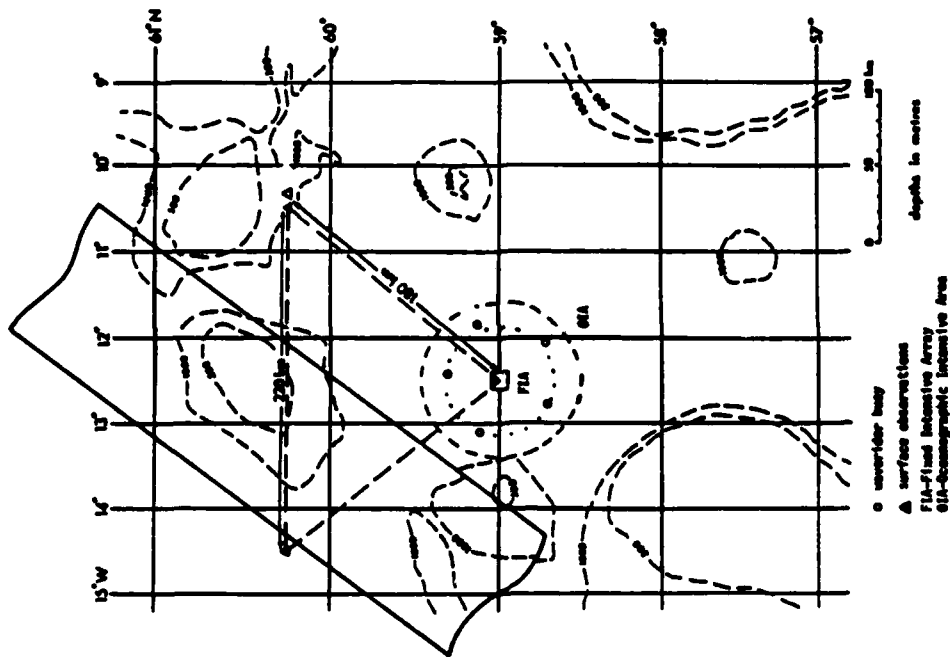
Rev 1044

Waves
 Direction = 264°
 $\lambda = 301 \text{ m}$
 $H_{1/3} = 3.5 \text{ m}$



Seam (220°)

Wind 195°
 11.5 m/s

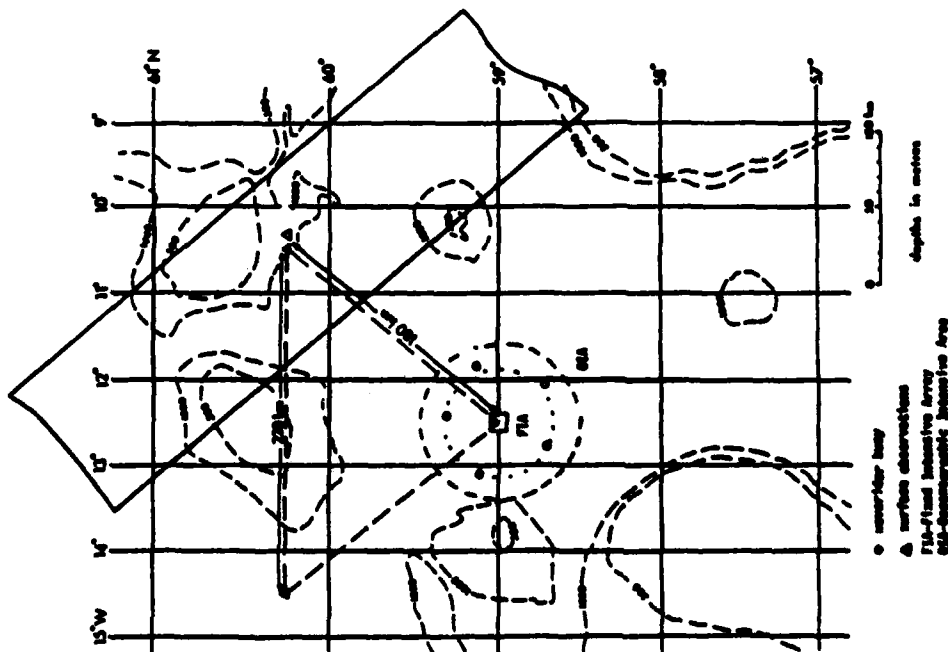


Rev 1049

Waves
 Direction = 264°
 λ = 301 m
 $H_{1/3}$ = 3.5 m

Wind 263°
 6.3 m/s

Seamut (323°)



Wind 046°
13.2 m/s

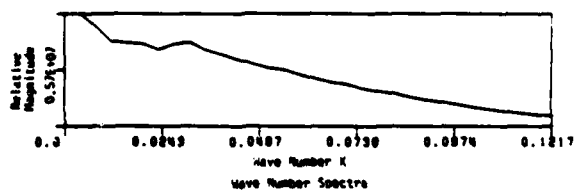
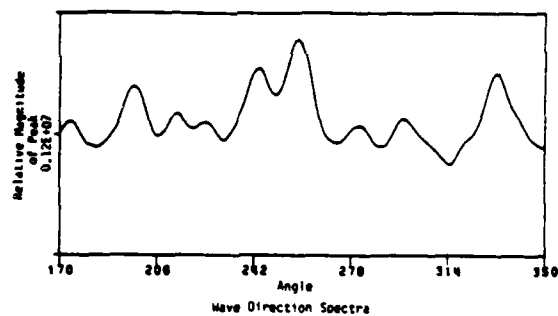
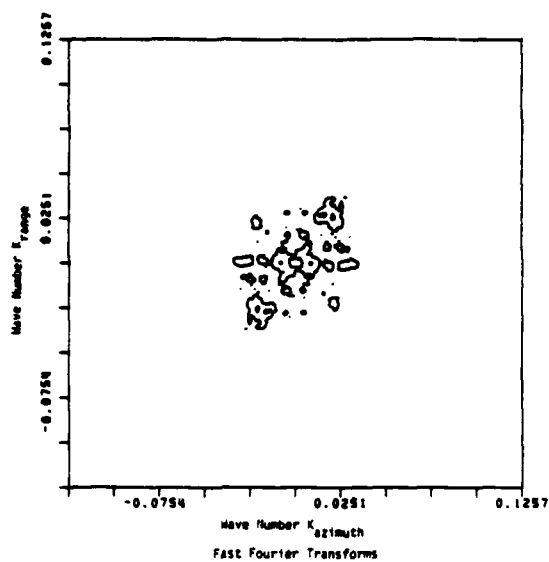
Swell (221°)

Waves
Direction = 253°
 $\lambda = 299$ m

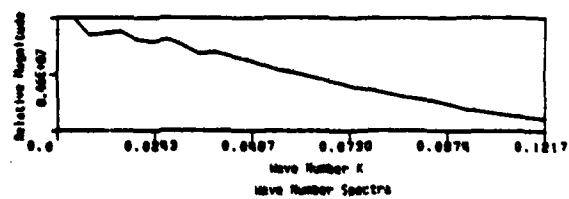
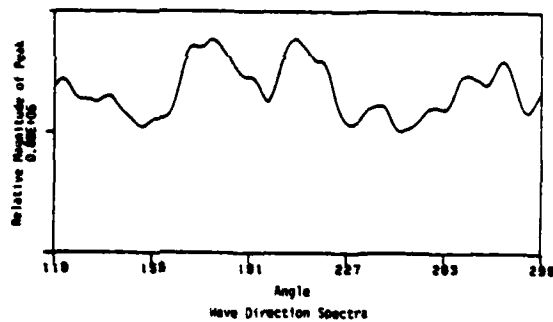
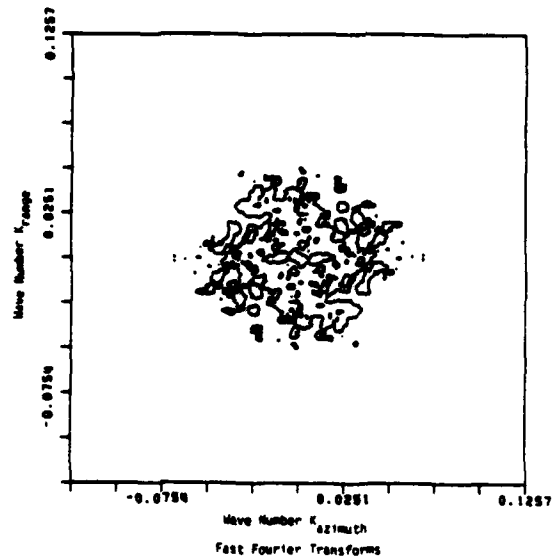


**APPENDIX B
DIGITAL FOURIER TRANSFORMS OF JASIN
SEASAT SAR DATA**

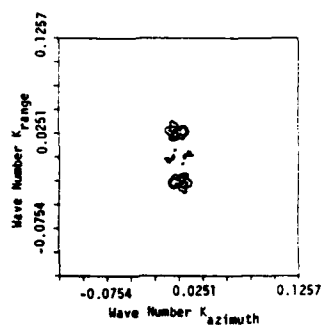
This appendix contains copies of the two-dimensional FFTs and their resultant one-dimensional plots for these passes where interpretable spectra were obtained.



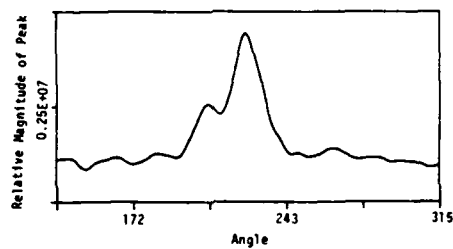
Rev. 547



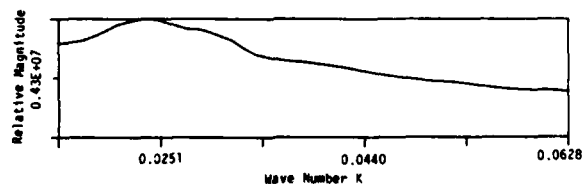
Rev. 556



Fast Fourier Transforms

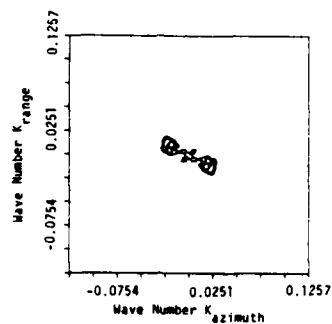


Wave Direction Spectra

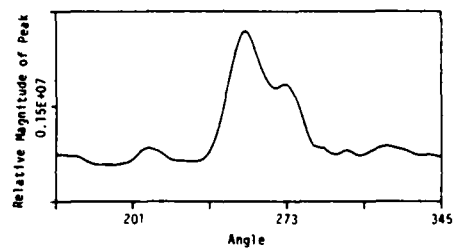


Wave Number Spectra

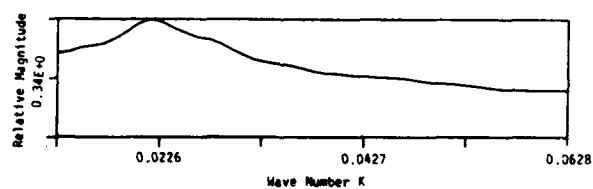
Rev. 762



Fast Fourier Transforms

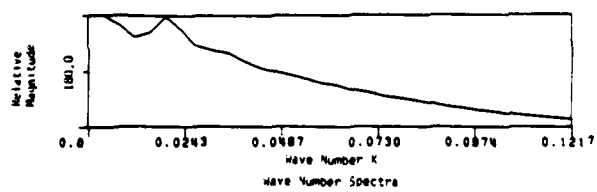
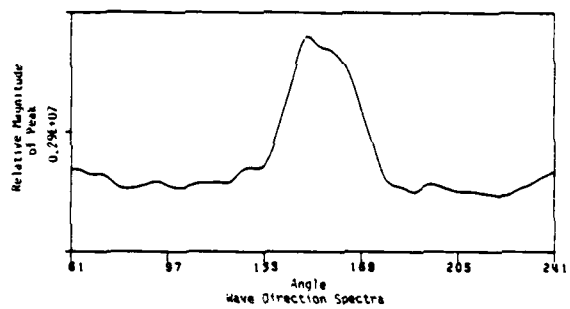
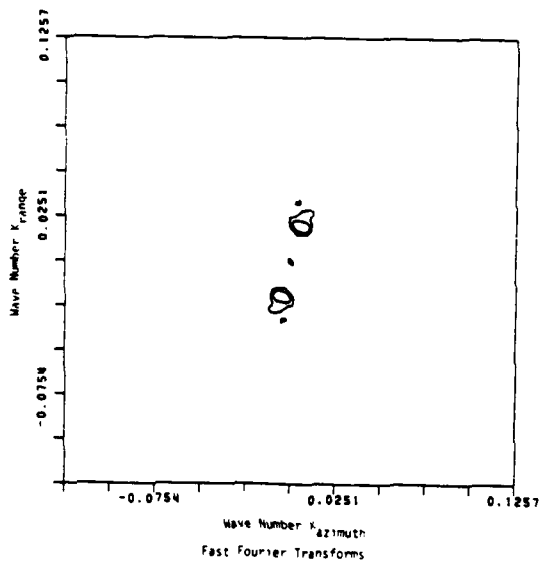


Wave Direction Spectra

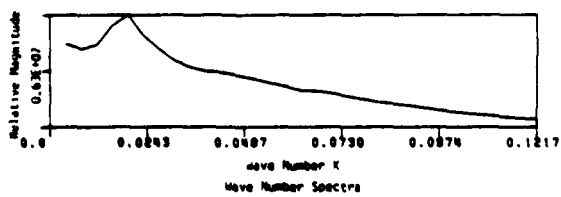
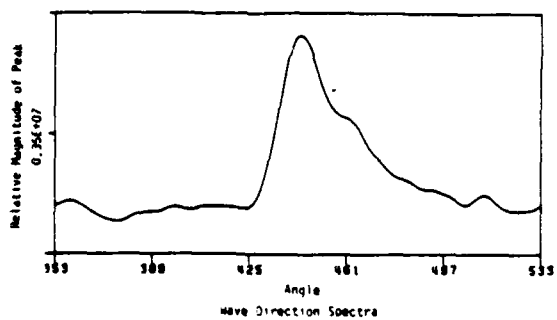
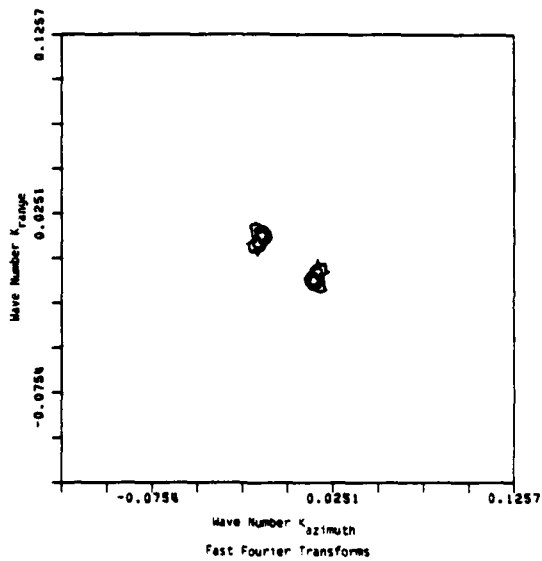


Wave Number Spectra

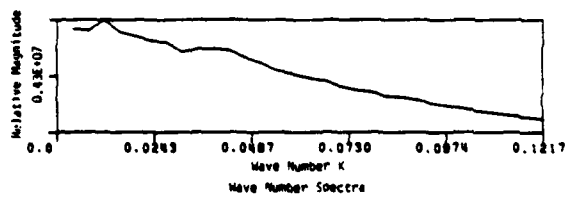
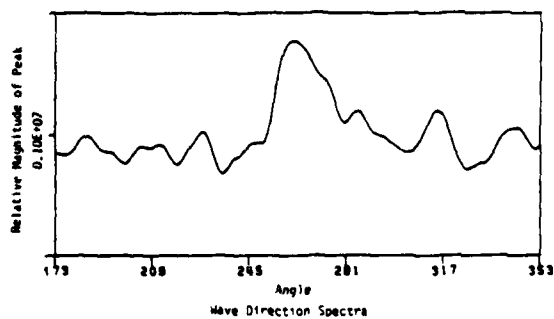
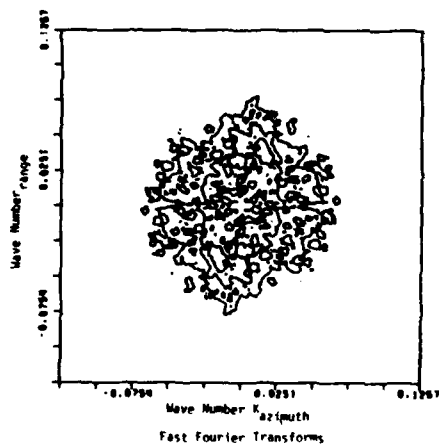
Rev. 1087



Rev. 1049



Rev. 1044



Rev. 792

APPENDIX C
"THE ESTIMATION OF WAVE HEIGHT FROM DIGITALLY
PROCESSED SAR IMAGERY"*

* M.H.B. Thomas, Int. J. Remote Sensing, 3, pp. 63-68, 1982.

The estimation of wave height from digitally processed SAR imagery

M. H. B. THOMAS†

Materials Physics Division, AERE Harwell, Didcot, OX11 0RA, England

(Received 29 June 1981; revision received 3 November 1981)

Abstract. A simple method has been developed for estimating wave height from synthetic aperture radar (SAR) imagery obtained by the Seasat satellite. The method is based on measuring the contrast of the image and the wavelength of the dominant wave. A calculation has been made for two orbits made by the satellite over the North Atlantic in 1978, using digitally processed data supplied by DFVLR in West Germany. Comparison with sea truth measurements shows agreement to within about 20 per cent.

1. Introduction

As part of a programme concerned with the analysis of radar imagery of the sea, it was felt worthwhile to investigate the possibility of obtaining wave height from SAR imagery. Previously, it has been necessary to determine this using a radar altimeter. For satellite applications, this has an obvious disadvantage, because the altimeter views the surface directly under the spacecraft while the SAR looks out to the side. Thus, the wave height is being measured in a totally different area from that where the SAR is acquiring its imagery. Clearly, a method of deriving wave height from the SAR image will be of significant practical value.

2. Theory

The fundamental interaction between radar and the sea surface is Bragg scattering. Three possible mechanisms have been proposed (Alpers *et al.* 1981) for the imaging of waves and these are:

- (a) The lifting and tilting of the Bragg scattering waves by the long-wavelength gravity waves, which create a modulation in the image (*tilt modulation*).
- (b) The asymmetry of capillary waves around a wave crest caused by non-linear wave interactions (*straining*).
- (c) Doppler shifts associated with the wave motion which introduce a modulation into the SAR imagery (sometimes known as *velocity bunching*).

The expected dependence of these mechanisms on wave direction is indicated in figure 1 (Alpers *et al.* 1981). Thus for waves propagating in a direction which is approximately perpendicular to the flight direction, mechanism (c) will have a small effect. Wright *et al.* (1980) suggest that the straining mechanism can be important on the basis of experiments using vertical polarization. However, for horizontal polarization the tilt modulation effect is considerably greater and is dominant for low to moderate sea states (Alpers *et al.* 1981). For the present, we shall assume that the dominant imaging mechanism is (a).

If we denote the surface displacement from the mean level by $f(r, t)$, then the

†Present address: Logica Ltd, 64 Newman Street, London, W1A 4SE.

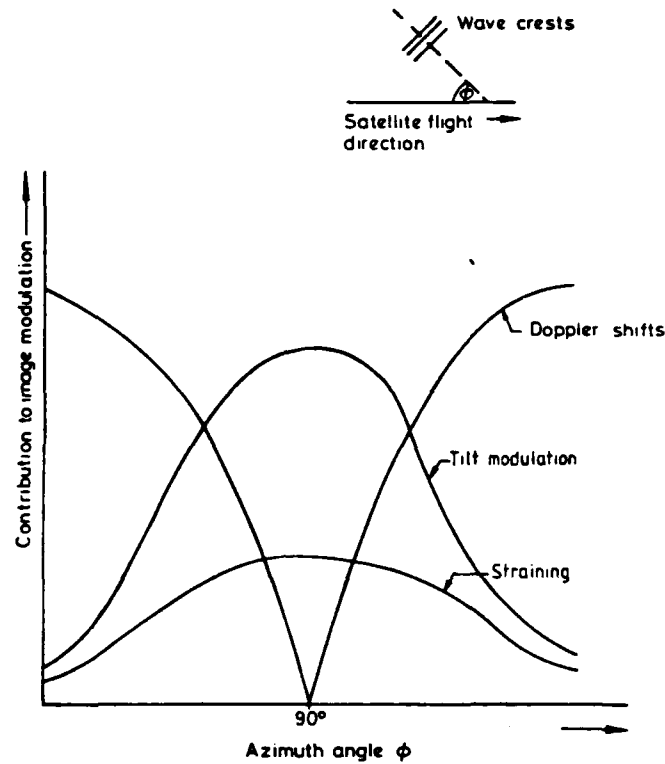


Figure 1. Dependence of wave imaging mechanisms on wave direction (after Alpers *et al.* 1981).

significant wave height, H_s , is defined by

$$H_s = 4 \sqrt{\langle f^2 \rangle}. \quad (1)$$

For a narrow-band swell-wave spectrum centred on wave number k_0 , the r.m.s. slope of the sea surface, $\tan \theta_r$, is given by

$$\frac{\tan \theta_r}{H_s} = \frac{|k_0|}{4} = \frac{\pi}{2\lambda_0}. \quad (2)$$

By rewriting the equation, we can determine H_s if we know $\tan \theta_r$ and λ_0 . From a digital image it is straightforward to determine λ_0 by taking the Fourier transform. The determination of $\tan \theta_r$ is based on the variation of the backscattering cross-section of the sea surface with incidence angle.

Figure 2 shows the theoretical variation of backscatter cross-section for horizontal polarization (which was used by Seasat), given by Valenzuela (1978) at a frequency of 4455 MHz using a composite surface model; a very similar curve is given for 428 MHz. The Seasat frequency of 1275 MHz lies between these values.

The tilt modulation mechanism depends on the change in the local angle of incidence caused by the swell waves, which gives rise to a change in the backscatter cross-section. This intensity modulation then allows the waves to appear in the imagery. A point which should be noted here is that the variation in the local angle of incidence causes a variation in the Bragg scattering wavelength. The backscatter cross-section is

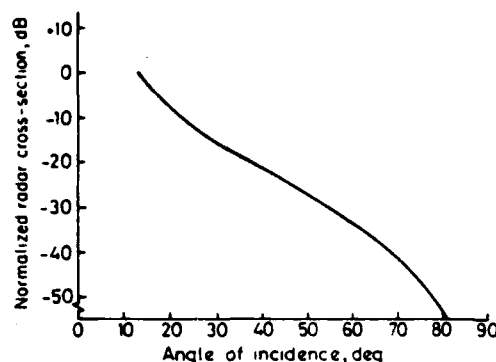


Figure 2. Variation of backscatter cross-section as a function of incidence angle for horizontal polarization at 4455 MHz (Valenzuela 1978).

proportional to the power spectrum at this wavelength and this has been included by Valenzuela by assuming a k^{-4} dependence (Phillips spectrum).

From the curve of figure 2, it is possible to relate a given variation of backscatter to changes in the local angle of incidence at the sea surface. The immediate problem then is to determine the r.m.s. variation in the backscattered power.

This can be determined directly from the image because the pixel intensity in the digital data is proportional to the square root of the backscattered power. In fact, in reading data from tape to our computer disc, the pixel intensities have been squared so that they are now directly proportional to power. The standard deviation of the backscattered power is then readily obtainable. However, the problem is complicated by the presence of speckle in the SAR image. Speckle is characteristic of coherent imaging systems and has been widely studied (Goodman 1975). The intensity distribution of a speckle pattern is a negative exponential distribution and the contrast of the pattern can be defined as the standard deviation of the intensity divided by the mean intensity. For the negative exponential distribution, this is equal to unity. The digital data have been subjected to an averaging process in which four different images have been incoherently averaged, specifically to reduce the speckle. The reduction factor is equal to the square root of the number of separate images, so that the contrast of the speckle will be reduced to 0.5.

When waves are present, the contrast in the image will be increased, so that it should be possible to estimate the variation in backscatter cross-section from the enhanced contrast of the image, provided that the speckle contrast can be accounted for. The local average intensity of the speckle is proportional to the backscatter cross-section at that point in the image, so that the two effects combine in a multiplicative manner (Lee 1981).

We may write

$$I_i = \alpha \mu I_s,$$

where I_i = image intensity, μ = backscatter cross-section, I_s = speckle intensity, and α = a proportionality constant. Therefore

$$\frac{\langle I_i^2 \rangle}{\langle I_i \rangle^2} = \frac{\langle \mu^2 I_s^2 \rangle}{\langle \mu I_s \rangle^2} = \frac{\langle \mu^2 \rangle \langle I_s^2 \rangle}{\langle \mu \rangle^2 \langle I_s \rangle^2}$$

if μ and I_s are independent.

We may use the relationship:

$$\sigma_x^2 = \langle x^2 \rangle - \langle x \rangle^2$$

where x = a measured variable, and σ_x = the standard deviation in x . It now follows that:

$$\frac{\sigma_i^2}{\langle I_i \rangle^2} + 1 = \left[\frac{\sigma_s^2}{\langle I_s \rangle^2} + 1 \right] \times \left[\frac{\sigma_w^2}{\langle I_w \rangle^2} + 1 \right]. \quad (3)$$

where σ_i = standard deviation of the image intensity, $\langle I_i \rangle$ = mean image intensity, σ_s = standard deviation of the speckle in the absence of any waves, $\langle I_s \rangle$ = mean speckle intensity in the absence of any waves, σ_w = standard deviation of image intensity due to waves in the absence of speckle, and $\langle I_w \rangle$ = mean image intensity due to waves in the absence of speckle.

Now we know that $\sigma_s/\langle I_s \rangle$ is equal to 0.5 for a four-look image and we can determine $\sigma_i/\langle I_i \rangle$ directly from the image; so we can write

$$\frac{\sigma_i^2}{\langle I_i \rangle^2} + 1 = 1.25 \left[\frac{\sigma_w^2}{\langle I_w \rangle^2} + 1 \right] \quad (4)$$

from which we can calculate $\sigma_w/\langle I_w \rangle$. From here it is straightforward to obtain the value of the r.m.s. slope using Valenzuela's data and then to determine the significant wave height.

We form the quantity $V = 10 \log_{10}[(\langle I_w \rangle + \sigma_w)/(\langle I_w \rangle - \sigma_w)]$, which expresses the backscatter variation in dB (Valenzuela's curve is logarithmic). This allows the determination of $\tan \theta$, by reference to the curve near an angle of 22.6° , which is the mean angle of incidence at the sea surface for Seasat.

3. Results and discussion

Two Seasat passes have been investigated; these were pass 762 in an area north-west of Scotland and pass 791 over the JASIN area in the Atlantic. In both of these passes, swell waves were observed travelling with an azimuth angle ϕ (see figure 1) approximately equal to 84.5° , i.e. almost perpendicular to the flight direction (see figure 3), so that the Doppler mechanism should be small. The contrast of the image, $\sigma_i/\langle I_i \rangle$, was determined and then $\sigma_w/\langle I_w \rangle$ was calculated from equation (4). This leads directly to the value of $\tan \theta$. The dominant wavelength λ_0 was obtained from a Fourier transform and the significant wave height then calculated from equation (2). Table 1 summarizes these results. The figures for $\tan \theta$, are averages of the values derived from Valenzuela's curves for 428 MHz and 4455 MHz. The value of λ_0 was obtained by calculating the centre of gravity of the swell part of the power spectrum. For pass 762, the sea truth measurement was taken from a shipborne wave recorder on board the *John Murray* (Guymer 1980). For pass 791, wave rider measurements are available from two wave riders (Carlson 1980). The most significant errors in the calculation are associated with the determination of λ_0 and of $\tan \theta$, using

Table 1. Calculation of wave height.

Pass No.	$\sigma_i/\langle I_i \rangle$	$\sigma_w/\langle I_w \rangle$	V , dB	$\tan \theta$	λ_0 , m	H_s , m	Sea truth, m
762	0.798	0.556	5.45	0.0492	217	6.8	5.5
791	0.753	0.503	4.81	0.0434	132	3.7	2.95, 3.25

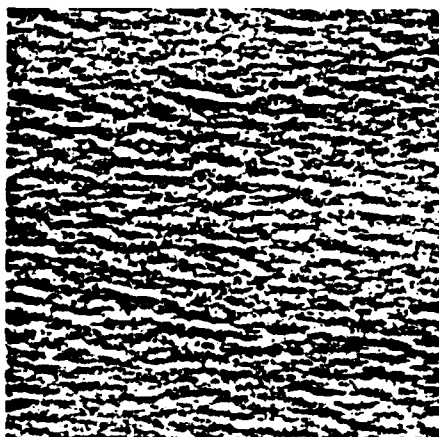


Figure 3. Part of the digitally processed image for Seasat pass 762. The satellite flight path is from left to right.

Valenzuela's curve. The error in λ_0 is estimated to be of the order of 10 per cent, but we have no figure for the error in $\tan \theta_r$. It is unlikely, however, that the overall error is less than 15 per cent.

In both cases, the calculated wave height is rather higher than the measured value: 23 per cent for pass 762 and 18 per cent for pass 791. The similarity of these two errors may indicate some common effect causing the overestimation of wave height. One possibility is that either the straining mechanism or the velocity bunching is making a significant contribution.

An expression for the magnitude of the straining effect's contribution to the modulation transfer function is given by Alpers *et al.* (1981), which contains an unknown parameter μ . No indication of the magnitude of μ is given, but even assuming μ equal to zero, which gives the maximum possible straining effect, this effect is still smaller by a factor of three than the tilt modulation effect. Also, Alpers *et al.* (1981) remark that the tilt modulation is dominant for low to moderate states, and so it is probably safe to neglect it.

The velocity bunching mechanism is linear for a range of azimuth angles about $\phi = 90^\circ$. In this range, Alpers *et al.* (1981) give an expression for the contribution to the modulus of the transfer function $|R_b|$

$$|R_b| = \frac{R}{V} |k| \omega \cos \phi g(\theta, \phi),$$

where R = range to target, V = platform velocity, k = wave number of ocean wave, ω = angular frequency of ocean wave, θ = angle of incidence, and $g(\theta, \phi) = 0.9994$ for Seasat. For Seasat, the range/velocity ratio is 128 s, roughly an order of magnitude greater than for an aircraft. Therefore, as ϕ deviates from 90° , i.e. as the waves acquire an azimuthal velocity component, the bunching mechanism rapidly becomes important. However, the linear regime is very narrow for large values of R/V and is defined by Alpers *et al.* (1981) as the range for which

$$C = |R_b| \times \text{wave amplitude} \leq 0.3.$$

For pass 762, C is equal to 0.5, and so we are well outside the linear regime. For pass

791, C equals 0.64. However, the velocity bunching mechanism is not entirely understood. For example, for Seasat pass 834 over the JASIN area, it is known that waves with a significant wave height of 3.1 m (Guymer 1980) were present, propagating at an azimuth angle ϕ roughly equal to 60° , but no waves are visible on the digitally processed imagery. On the other hand, Alpers *et al.* (1981) refer to passes 308 and 1044 as showing azimuth travelling swell.

Clearly, the position is not fully understood but it seems that, in the two cases analysed in this paper, the tilt modulation mechanism is able to account in large measure for the image modulation. With an airborne SAR, the velocity bunching mechanism would be considerably less than for a satellite system. Indeed, it could be eliminated by flying parallel to the wave crests.

Acknowledgments

Thanks are due to H. Carlson of the Deutsches Hydrographisches Institut for supplying the wave rider data, and also to T. Guymer of the Institute of Oceanographic Sciences (IOS) for the shipborne wave recorder data and for helpful discussions. I should also like to thank K. Ouchi of Imperial College, London, J. Walker and E. Jakeman of RSRE Malvern, and M. Tucker of IOS for useful comments. The work was supported by the Ship and Marine Technology Requirements Board of the Department of Industry.

References

- ALPERS, W. R., ROSS, D. B., and RUFENACH, C. L., 1981, *J. geophys. Res.*, **86**, 6481.
CARLSON, H., 1980 (private communication).
GOODMAN, J. W., 1975, *Laser Speckle and Related Phenomena*, edited by J. C. Dainty (Berlin: Springer-Verlag).
GUYMER, T., 1980, (private communication).
LEE, J-S., 1981, *Comput. Graph. Image Process.*, **17**, 24.
VALENZUELA, G. R., 1978, *Bound. Layer Met.*, **13**, 61.
WRIGHT, J. W., PLANT, J. W., KELLER, W. C., and JONES, W. L., 1980, *J. geophys. Res.*, **85**, 4957.

APPENDIX D
PAPERS PUBLISHED ON JASIN USING RESULTS OF
ONR-SPONSORED RESEARCH

1. Kasischke, E.S., Y.C. Tseng, and G.A. Meadows, Observations of Internal Waves and Frontal Boundaries on Seasat SAR Imagery Collected Over the Eastern North Atlantic Ocean, Proceedings of the Seventeenth International Symposium on Remote Sensing of Environment (In Press), Ann Arbor, MI, 1983.
2. Vesecky, J.F., H.M. Assal, R.H. Stewart, R.A. Shuchman, E.S. Kasischke, and J.D. Lyden, On the Ability of Synthetic Aperture Radar to Measure Ocean Waves, Proceedings of the Symposium on Wave Dynamics and Radio Probing of the Ocean Surface, Miami, FL (In Press), 1984.
3. Vesecky, J.F., H.M. Assal, R.H. Stewart, R.A. Shuchman, E.S. Kasischke, and J.D. Lyden, Seasat-SAR Observations of Surface Waves, Large Scale Surface Features and Ships During the JASIN Experiment, 1982 Int. Geoscience and Remote Sensing Symposium Digest, Munich, Germany, pp. WP-3, 1.1-1.6, 1982.

OBSERVATIONS OF INTERNAL WAVES AND FRONTAL BOUNDARIES ON SEASAT SAR IMAGERY
COLLECTED OVER THE EASTERN NORTH ATLANTIC OCEAN*

E.S. Kasischke

Radar Division
Environmental Research Institute of Michigan
Ann Arbor, Michigan

Y.C. Tseng and G.A. Meadows

Department of Atmospheric and Oceanic Sciences
The University of Michigan
Ann Arbor, Michigan

A.K. Liu

Dynamics Technology, Incorporated
Torrance, California

ABSTRACT

The locations of all frontal boundary and internal wave patterns on 21 passes of Seasat imagery collected over the eastern North Atlantic Ocean were plotted on a bathymetric chart of the region. These plots revealed that the patterns always occurred over or close to a deep water bottom feature, such as a ridge, seamount, bank or shelf. At no time did a pattern occur over a deep water basin. An internal wave pattern appeared in Seasat SAR imagery 67 percent of the time Seasat passed over a deep water feature, while frontal boundary patterns appeared 28 percent of the time. The causes of internal wave and frontal boundary patterns on the Seasat SAR imagery have been identified as Lee wave generation and deep water upwelling, respectively. Research which combines oceanic, subsurface measures with the Seasat SAR imagery is definitely warranted to further study these patterns.

1. INTRODUCTION

The primary mission of the Seasat synthetic aperture radar (SAR) was to image gravity waves, ice and other oceanic surface patterns that are a result of internal waves, currents, frontal boundaries, oil slicks and meteorological occurrences. In collecting over 100 million

*Presented at the Seventeenth International Symposium on Remote Sensing of Environment, Ann Arbor, MI, May 1983.

square kilometers of SAR imagery from space, Seasat provided the oceanographic and remote sensing communities with an abundance of data to examine.

Numerous studies in the past have documented the presence of internal wave and frontal boundary patterns on SAR images in shallow (<100 m), coastal areas. An early Seasat study of imagery collected during Rev. 762 between Scotland and Iceland reported numerous large wave-like patterns in deep-water (>200 m) regions (Shuchman and Kasischke, 1979). Here, we report on the continuation of this earlier study on the appearance of large-scale surface patterns on Seasat SAR imagery collected over the northeast Atlantic Ocean. These large-scale surface patterns have been tentatively identified as surface manifestations of internal waves and regions of upwelling which result in frontal boundaries.

We will first present a background section which contains discussions on the Seasat SAR, SAR imaging of the ocean surface and past investigations on internal wave and frontal boundary patterns on SAR imagery. This is followed by a section which presents examples of deep-water internal wave and frontal boundary patterns observed on the Seasat SAR imagery and discusses the occurrence of these features on the 21 passes of Seasat data examined during this study. Finally, two first-order hydrodynamic models are presented which explain why the observed patterns were detected by the Seasat SAR.

2. BACKGROUND

The data to be presented in this paper were collected by the Seasat satellite. Among the instrumentation carried by Seasat, which was launched during June of 1978, was an imaging synthetic aperture radar (SAR). This satellite collected over 500 passes of SAR data before suffering a catastrophic power loss in October of 1978. The SAR on board Seasat was an L-band (23.5 cm wavelength) radar. It collected 25 x 25 m resolution imagery with a ground swath-width of 100 km and a length of up to 4000 km, and viewed the surface of the earth with an average incidence angle of 20°. For a detailed description of the Seasat SAR system and its mission, see Jordan (1980); Beal, et al. (1981), or Fu and Holt (1982).

An imaging radar such as the Seasat SAR is an active device that senses the environment with short wavelength electromagnetic waves. As an active sensor, the Seasat SAR provided its own illumination in the microwave region of the electromagnetic spectrum and thus was not affected by diurnal changes in emitted or reflected radiation from the earth's surface. Additionally, the 23.5 cm wavelength utilized by the Seasat SAR allowed for imaging the earth's surface through clouds and light rain.

The principle in imaging any ocean surface with a radar is that the backscatter of microwave energy (echo) received by the radar contains information on the roughness characteristics (shapes, dimensions and orientations) of the reflecting area. Parameters that influence the SAR image of the ocean surface include the motion of the scattering surfaces, coherent speckle, system resolution and non-coherent integration as well as the surface roughness. In addition, the orientation of ocean surface patterns with respect to the radar "look" direction can be influencing parameters.

Several scattering models exist that attempt to explain ocean surface image formation with synthetic aperture radars. These models are of two types: static models that depend on instantaneous surface features, and dynamic models that employ surface scatterer velocities.

Three static models have been suggested to describe the radar scattering of energy from large areas on the ocean surface. These three scattering models include: (1) the specular point model which is most appropriate for small incidence angles, (2) the Bragg-Rice scattering model, described below, and (3) a Rayleigh scattering model which is often used in terrestrial earth scattering calculations. There is general consensus within the radio-oceanography scientific community that a Bragg-Rice scattering theory best explains the SAR observed backscatter values obtained from the ocean surface for incidence angles between 20° and 60° (Shuchman, et al., 1981). The Bragg-Rice scattering model is based on a well known phenomena in the study of crystals, grating, and periodic structures. If one considers the random ocean surface to be represented by a combination (i.e., spectrum) of periodic surfaces, then the spectrum region which satisfies the backscatter phase matching condition will be the main contributor to the backscatter cross section. Sometimes in the literature, this phase matching

of the small ocean Bragg waves with the radar electromagnetic energy is termed a resonance phenomenon; more correctly stated, it should be termed a constructive interference between the electromagnetic and ocean waves.

Pioneering theoretical and experimental work by Wright (1966) at the Naval Research Laboratory (NRL) demonstrated the general validity of a Bragg scattering model for an ocean surface imaged by radar. In a series of wave tank measurements using 3 and 25 cm wavelength continuous wave (CW) Doppler radars, Wright demonstrated that Bragg scattering, that is, transmitted radar energy with wave number K , interacts in a resonant or interference fashion with ocean surface waves with wave number K_w , such that

$$K_w = 2K \sin \theta, \quad (1)$$

where $K_w = 2\pi/L$ and $K = 2\pi/\lambda$, (L and λ are the wavelengths of the surface waves and the radar, respectively), and θ is the incidence angle. Shuchman, et al. (1981) showed that a Bragg scattering equation satisfactorily explained the radar backscatter return from SAR using data collected during the Marineland experiment (for a discussion of the Marineland experiment, see Shemdin, 1980). It should be noted that radar data of large ocean areas (1×1 km) were averaged in that analysis. Thus based on the above the principal radar reflectivity mechanism of imaging ocean surfaces is via the capillary and small gravity waves which produce Bragg scattering (Raney and Shuchman, 1978).

Synthetic aperture radars are also sensitive to the motion of scatterers present in the imaged scene (Raney, 1971). Effects of scatterer motion on SAR imagery may include: (1) image displacement, smearing and loss of focus in the azimuth direction, and (2) loss of focus in the range direction. Some of these effects can be removed during processing of the SAR signal histories by making appropriate adjustments to the processor (Shuchman, 1981). Effects which cannot be removed during processing may reduce the detectability of gravity waves, but are not expected to have a large influence on other ocean surface patterns.

A variety of processes can alter the surface Bragg waves, resulting in a distinct pattern on SAR imagery. These include oceanic processes (currents, gravity waves, internal waves, slicks, local water depth variations, water temperature and salinity), climatic processes (wind, rain and air temperature) and man-made phenomena (ships, buoys and oil spills). It is the hydrodynamic interaction between several of oceanic processes and a distinct bottom feature which allows that feature to be detected on SAR imagery. Examples of these bottom-induced, deep-water surface patterns will be presented in this paper. For examples of other surface patterns on Seasat SAR imagery, see Gower (1981); Beal, et al. (1981); or Fu and Holt (1982).

Internal wave patterns have been detected on a variety of remotely-sensed images. They have been detected on aerial and spacecraft photography (Osborne and Burch, 1980; Gower and Hughes, 1979), Landsat MSS imagery (Apel, et al., 1974; 1975; 1975a; 1976) and aircraft and spacecraft SAR imagery (Brown, et al., 1976; Elachi and Apel, 1976; Shuchman and Kasischke, 1979; Gower and Hughes, 1979; Apel, 1981; Fu and Holt, 1982; Ford, et al., 1983; Trask and Briscoe, 1983; Alpers and Salusti, 1983; and Hughes and Gower, 1983). Most of the above studies do not present any direct evidence that the observed patterns are due to internal waves, but the patterns are widely believed to be internal wave surface signatures. An excellent field study by Hughes and Gower (1983; see also Gower and Hughes, 1979) actually measured a tidally-driven internal wave packet as it was being imaged by an aircraft SAR and Seasat. This study verified that SARs can detect surface manifestations of internal wave fields.

An early Seasat study by Shuchman and Kasischke (1979) indicated the presence of internal "wave-like" patterns on Seasat-SAR images in deep-water regions. Since then, deep-water internal wave patterns have been reported on Seasat imagery by Fu and Holt (1982) and SIR-A imagery by Ford, et al. (1983).

There appears to be little question that ocean current or frontal boundaries can frequently be observed on SAR images, although the reason for their appearance is not yet understood. Current boundaries were first noted on aircraft SAR imagery by Moskowitz (1973). Since then, frontal boundaries have been extensively studied by both aircraft SARs (Larson,

et al., 1976; Shuchman, et al., 1977; 1979; Weissman, et al., 1980; Shuchman, et al., 1981) and spaceborne SARs (Hayes, 1981; Shuchman, et al., 1979; Shemdin, et al., 1980a; Mattie, et al., 1980; Cheney, 1981; Lichy, et al., 1981; Shuchman, et al., 1981c). Current velocity gradients (du/dx) on the order of 10^{-3} sec^{-1} appear to be detectable (Larson, et al., 1976), and the sensing of current boundaries apparently occurs for a wide range of wind speeds (3-10 m/s) and air-sea temperature differences ($0.1 - 10^\circ\text{C}$).

The appearance of frontal boundaries on SAR images was at first thought to be due to a Doppler-induced image displacement (Larson, et al., 1976), but this notion has been discounted by the observation of current boundaries at all radar look direction orientations on Seasat data (Hayes, 1981). Although the Doppler mechanism may be a contributing factor in some cases, it is now felt that the main reason for the appearance of current boundaries on SAR imagery is either a stress-induced variation in surface roughness in the area of the shear, or a difference in the surface roughness of the water masses.

3. METHODS

The data set for this analysis was the Seasat SAR imagery collected over the eastern half of the North Atlantic Ocean. These data were available because of the satellite receiving station which was operating at Oak Hangar, England for the European Space Agency. The 21 passes of imagery used in this study are summarized in Table 1.

There were two parts to the present analysis. The first part involved investigating the relationship between the internal wave and frontal boundary patterns and the deep-water bottom features in this region. The second part was to develop a first order, hydrodynamic model as to why the patterns appeared on the Seasat imagery.

In order to study the relationship between surface patterns on Seasat SAR imagery and the deep-water bottom features, the following procedure was used: First, the location of the ground coverage of the Seasat SAR was obtained by consulting the satellite data record (SDR) for each pass. (A SDR contains a series of ground latitude and longitude coordinates for specific times during a Seasat pass. Most of the Seasat SAR images contained annotations of the time the data were collected. Therefore, the location of a particular surface pattern could be identified by noting the time when the pattern occurred during that orbit.) The ground coverage of each pass was then marked on an overlay placed on the chart. Next, the locations of all internal waves and frontal boundaries detected on each pass were noted and then these locations marked on the overlay. Finally, a surface pattern was said to be associated with a bottom feature if its location was within 10 kilometers of that feature.

The bottom morphology of the eastern North Atlantic Ocean is quite well known due to the extensive hydrographic surveys conducted in this region (see e.g., Roberts, et al., 1979). This area contains a large number of submarine ridges, seamounts, banks and shelves. Table 2 lists the major bottom features in this area, along with the shallowest contour interval charted for that feature and the depth of the adjacent deep water.

The second part of the analysis was performed by analyzing the environmental conditions which were most likely present at specific sites for a given set of patterns observed in a single pass of Seasat SAR imagery, and then formulating a first-order hydrodynamic/electromagnetic model which explains the SAR-observed surface pattern.

4. OBSERVATIONS

In this section, we will first present examples of internal wave and frontal boundary patterns from the study area. This will be followed by a summary of the relationship of these patterns to the deep-water bottom features. Figure 1 is a diagram of the positions of the Seasat images presented in this section.

The JPL-optically processed SAR imagery in Figure 2 was collected during Rev. 599 (7 August 1978) as Seasat passed over the Wyville-Thomson Ridge. The corresponding bathymetric chart for this coverage is presented in Figure 3. From Figure 2, it can be seen that there are numerous internal wave signatures. Note on the SAR image that the internal waves are both range (e.g., C/D1 to C/D2) and azimuth (e.g., A9 to D9) traveling. The internal waves in the

lower left corner of the SAR image appear to occur over the Ymir Ridge; the internal waves in the middle of the image appear over the Wyville-Thompson Ridge; and those at the top of the image occur over the Faeroe Bank Channel.

Surface measurements collected at the time of the Seasat overpass indicate a wind of 6.9 m/s from the north, and a wave field with a significant wave height of 1.1 meters, and a dominant wavelength of 71 meters propagating towards 200°(T).

The SAR imagery in Figure 4 was collected during Revolution 958 (1 September 1978) as Seasat passed over the Iceland-Faeroe Rise. The corresponding bathymetric chart for this area is presented in Figure 5. The internal wave patterns in the top half of Figure 4 occur in an area where the water depths are between 600 and 1000 meters. It is in an area where the ocean floor is rising from the deep (>2500 m) Iceland Basin to the relatively shallow (500 m) Iceland-Faeroe Rise. The dark areas of Figure 4 (J7 and D2) are believed to be atmospheric events.

Surface measurements obtained near the test area indicates the gravity wave field present at the time of Revolution 958 had a significant wave height of 1.4 meters, a dominant wavelength of 147 meters and was propagating towards 176°(T). Surface winds had a speed of 7.2 m/s, but no direction was given.

Figure 6 presents Seasat SAR imagery collected during Rev. 762 (19 August 1978). The corresponding bathymetric chart for this region is presented in Figure 7. This image contains both internal wave patterns as well as a frontal boundary pattern. There are two distinct sets of internal wave packets present. One set (F5 to J8) can be seen on the West Shetland Shelf, while the other lies along the southern edge of the Wyville-Thompson Ridge (C3 to H4). The frontal-boundary pattern in this image can be seen to lie along the edge of the Faeroe Shelf (A6 to B9).

Surface measurements obtained near the time of the Seasat overpass indicate a strong wind (12.5 m/s) from the south and a swell with a significant wave height of 3.0 m/s and a wavelength of 210, propagating toward 60°(T) was present.

Not all surface signatures believed to be related to deep-water, bottom topographic features are as clear and distinct as the examples presented previously. Figure 8 was collected by Seasat during Rev. 791 (21 August 1978) as it passed over the Anton Dohrn Seamount. The corresponding bathymetry for this imagery is presented in Figure 9. The internal wave signatures collected over the Anton Dohrn Seamount are quite subtle. Three groups of internal waves (B6 to C6, D/E6 to D/E8, and A8) occur over this seamount, which is quite steep sided, as can be seen by the narrow spacing of the contour lines in Figure 9.

The sea truth collected near the test area indicates the winds were quite strong, with a speed of 13 m/s from the southwest. The surface gravity wave field had a significant wave height of 3.1 m, a dominant wavelength of 151 m and was propagating towards 45°(T).

Table 3 summarizes the occurrences of the internal wave and frontal boundary patterns over the 25 deep-water bottom features in the study area. Table 4 summarizes the number of times each Seasat revolution passed over a deep-water bottom feature and the total number of internal wave and frontal boundary patterns appeared over a bottom feature in that pass.

At no time did an internal wave pattern or frontal boundary pattern appear on the Seasat imagery over a deep-water region without a bottom feature in the immediate vicinity. From Table 3, it can be seen that 67 percent of the time the Seasat SAR imaged the ocean surface over a deep-water bottom feature, an internal wave pattern was present. The corresponding figure for frontal boundary patterns was 28 percent. The figure for internal waves and frontal boundary patterns combined is 82 percent. These figures suggest a strong correlation between the bottom features and the SAR-observed surface patterns. This relationship will be further analyzed in the next section.

5. HYDRODYNAMIC MODELS

The Seasat SAR imagery presented in Figure 6 was used as a base to formulate first-order hydrodynamic models to explain why the internal wave and frontal boundary patterns occur. Figure 10 combines a line drawing of the internal waves and a frontal boundary observed in Figure 6 with the corresponding bathymetric chart for this area. From Figure 10, it can be seen that there are numerous internal wave signatures. The internal waves in the middle of the image appear to be generated over the Wyville-Thomson Ridge. Near the lower right corner of the image, three wave packets are visible. It is to be noted that no waves were generated on the north side of the ridge.

The dominant bottom features in this region are a broad, saddle-like valley on the east side of the ridge, and a 90° sector of deep water extending out from the ridge, as shown in Figure 11. The ridge has the characteristic scales of approximately 10 km in both the longitudinal and transverse direction. The minimax of the bathymetric saddle is at a depth of about 450 m.

Based on the bathymetry, it seems that the wave packets are produced by lee wave formation—a mechanism similar to the undulation of the jet stream as it passes over a mountain ridge. Figure 12 schematically illustrates the stages that are hypothesized during the production of solitary internal wave packets. As the strong semidiurnal tidal current flows north into the Faeroe Bank Channel, an internal lee wave forms on the northern edge of the ridge. As the tidal flow goes to zero six hours later, the lee wave, trying to maintain its group velocity relative to the current, escapes south over the ridge barrier back into the deep water, emerging as a packet of solitary waves. This phenomenon has previously been studied by Holbrook, et al. (1983) in the Sulu Sea. The initial waveform then can be viewed as a localized source that immediately begins to propagate, and evolves into a series of solitary waves while undergoing radial spreading, encountering variable topography and slowly losing energy through dissipation. The disappearance of internal waves on the north side of the ridge is probably because there is no strong tidal current flowing south across the ridge; most of the tidal current may flow along the Faeroe Bank Channel.

Based on the Seasat SAR image, the wave packets in deep water over the Wyville-Thomson Ridge have the following properties:

1. Wave packets are separated by distances of the order of 14 km.
2. Wave speed is estimated to be 0.31 m/s based on the assumption of a semidiurnal tidal origin.
3. Wave packets in this region contain about five waves with packet width about 5 km.
4. Wavelengths are between 500 m and 1000 m.
5. The crests are curved in a horizontal plane with their convex sides pointed in the direction of propagation.

Although no *in situ* measurements are available, it is believed this area is dominated by tidal currents with velocities of less than 0.5 m/s at the surface. Figure 13 shows the profiles of potential temperature, salinity and sigma theta generated from data collected over the Iceland-Faeroe Rise during the Atlantic Expedition in August 1972 (Sainbridge, 1980). Station 19 is the measurement closest to the Wyville-Thomson Ridge area. As evident from Figure 13, a mixed layer of 40 m is dominant in this area during the summer. Based on the two-layer finite depth model, the linear wave speed is given by

$$C_0 = \left[\frac{\Delta \sigma}{\rho} \frac{g}{k} \frac{1}{\coth kH_1 + \coth kH_2} \right]^{1/2} \quad (2)$$

Near the Wyville-Thomson Ridge, $\Delta \sigma / \rho = 0.6 \times 10^{-3}$, $H_1 = 40$ m, $H_2 = 260$ m, $2\pi/k = 500$ m, and thus the wave speed is approximately 0.40 m/s, depending on the water depths. This value is consistent with the estimated wave speed of 0.31 m/s from the SAR image. Based on the

wavelength, the wave amplitude is estimated to be between 10 and 15 m. Note that the effect of shear is important in this case, since the wave speed is slow compared with the background current. Also, the bottom topography near the West Shetland Shelf is complex, which influences the evolution of wave packets, as shown in Figure 10. A similar solitary wave theory developed by Liu, et al. (1983) can be applied here. However, due to the limited scope of this investigation, the detailed analysis and calculations will have to wait until sea-truth data are available.

Liu (1983) also modeled the surface strain rate produced by shallow water (coastal) internal waves. He then used this surface strain as an input to an electromagnetic model and simulated a SAR image of the internal wave, which compared favorably to the Seasat image. A similar surface strain is expected to occur for the deep-water internal waves, resulting in the patterns observed on the JASIN imagery.

The curved, dark line, as indicated by the dashed line in Figure 10, is believed to be a surface pattern caused by a frontal boundary. Its location appears to be over the edge of the Faeroe Shelf, and closely matches the 800 meter bottom contour.

As shown in Figure 13, the deep water upwelling results in a frontal boundary over the Icelandic-Faeroe Rise. The relationship of the front to local upwelling topographic mixing may be described by the following process. Figure 14 shows the cross-section diagram of bottom topography of the Wyville-Thomson Ridge. It appears that the tidal current flowing over the ridge through another saddle-like valley on the west-side of the ridge forces the deep water isotherms up toward the surface. To illustrate this mechanism for frontal boundary generation, a schematic diagram of deep water upwelling over the Faeroe Bank Channel is shown in Figure 15. Therefore, the frontal boundary seems to represent simply a surface intersection of the seasonal thermocline. The combination of frontal slope and current shear could yield information on density contrast across the front.

6. SUMMARY

Twenty-one passes of Seasat SAR imagery collected over the eastern North Atlantic Ocean were examined for the presence of internal wave and frontal boundary patterns. All passes contained such signatures, and the geographic position of all signatures were found to be within 10 kilometers of a deep-water bottom feature, such as a seamount, submarine ridge, bank, or shelf. It was determined that on 67 percent of the occasions the Seasat SAR passed over the geographic location of a deep-water bottom feature, an internal wave pattern was present at that location. The corresponding figure for frontal boundary patterns was 28 percent.

A first-order hydrodynamic model was developed to explain the appearance of the Seasat SAR-observed surface patterns. These models indicate that the internal wave patterns are formed by lee-wave internal waves, which are generated as tidally-driven currents flow over the deep-water bottom features. The frontal boundary patterns were shown to be due to the upwelling of deeper water to intersect the surface layer. This upwelling is generated by tidal currents flowing against a deep-water bottom feature.

7. ACKNOWLEDGEMENTS

The research reported in this paper was supported by the Naval Research Laboratory through NRL Contract Nos. N00014-81-C-2254 and N00014-82-C-2308 and by the Office of Naval Research through ONR Contract No. N00014-81-C-0692. The NRL technical monitor was Mr. Peter Mitchell and the ONR technical monitors were Mr. Hans Dolezalek and Commander Robert Kirk. The authors would like to acknowledge the following individuals for their assistance during this study: Benjamin Holt of the Jet Propulsion Laboratory provided copies of some of the Seasat SAR imagery used in the analysis; Dale Lodge of the Royal Air Force Establishment and the European Space Agency provided the use of the Seasat SAR signal films collected at the Oak Hangar receiving station; and John Vesecky of Stanford University and Robert Stewart of the Scripps Institute of Oceanography provided sea-truth data collected over the North Atlantic at the times of the Seasat overpasses. The authors would like to thank Dr. Robert A. Shuchman of ERIM for his advise throughout this research effort.

8. REFERENCES

- Alpers, W. and E. Salusti, Scylla and Charybdis Observed from Space, J. Geophys. Res., **88**, pp. 1800-1808, 1983.
- Apel, J.R., R.L. Charnell and R.J. Blackwell, Ocean Internal Waves Off the North American and African Coasts from ERTS-1, Proc. Ninth Int. Symp. Remote Sens. Environ., Ann Arbor, MI, pp. 1345-1354, 1974.
- Apel, J.R., H.M. Byrne, J.R. Proni and R.L. Charnell, Observations of Oceanic Internal and Surface Waves from the Earth Resources Technology Satellite, J. Geophys. Res., **80**, pp. 865-881, 1975.
- Apel, J.R., J.R. Proni, H.M. Byrne, and R.L. Sellers, Near-Simultaneous Observations of Intermittent Internal Waves on the Continental Shelf from Ship and Spacecraft, Geophys. Res. Lett., **2**, p. 128, 1975a.
- Apel, J.R., H.M. Byrne, J.R. Proni, and R.L. Sellers, A Study of Oceanic Internal Waves Using Satellite Imagery and Ship Data, Remote Sensing of Environment, **5**, p. 125, 1976.
- Apel, J.R., Non-Linear Features of Internal Waves as Derived from the Seasat Imaging Radar, in Oceanography from Space, ed. by J.F.R. Gower, Plenum Press, New York, pp. 525-533, 1981.
- Bainbridge, A.E., Geosecs Atlantic Expedition - Volume 2: Sections and Profiles, U.S. Government Printing Office, Washington, D.C., 198 pp., 1980.
- Beal, R.C., P.S. DeLeonibus and I. Katz (eds.), Spaceborne Synthetic Aperture Radar for Oceanography, Johns Hopkins Univ. Press, Baltimore, MD, 215 pp., 1981.
- Brown, W.E., Jr., C.E. Elachi and T.W. Thompson, Radar Imaging of Ocean Surface Patterns, J. Geophys. Res., **81**, pp. 2657-2667, 1976.
- Cheney, R.E., A Search for Cold Water Rings with Seasat, in Spaceborne Synthetic Aperture Radar for Oceanography, ed. by R.C. Beal, P.S. DeLeonibus and I. Katz, Johns Hopkins Univ. Press, Baltimore, MD, pp. 161-170, 1981.
- Elachi, C. and J.R. Apel, Internal Wave Observations Made with Airborne Synthetic Aperture Imaging Radar, Geophys. Res. Lett., **3**, p. 647, 1976.
- Ford, J.P., J.B. Cimino, and C. Elachi, Space Shuttle Columbia Views the World with Imaging Radar: The SIR-A Experiment, JPL Publication 82-95, Pasadena, CA, 166 pp., 1983.
- Fu, L. and B. Holt, Seasat Views Oceans and Sea Ice with Synthetic Aperture Radar, JPL Publication No. 81-120, 200 pp., 1982.
- Gower, J.F.R. and B.A. Hughes, Radar and Ship Observations of Coastal Sea Surface Roughness Patterns in the Gulf of Georgia, Proc. Thirteenth Int. Symp. Remote Sens. Environ., Ann Arbor, MI, pp. 103-115, 1979.
- Gower, J.F.R. (ed.), Oceanography from Space, Plenum Press, New York, NY, 977 pp., 1981.
- Hayes, R.M., SAR Detection of the Gulf Stream, in Spaceborne Synthetic Aperture Radar for Oceanography, ed. by R.C. Beal, P.S. DeLeonibus and I. Katz, Johns Hopkins Univ. Press, Baltimore, MD, pp. 146-160, 1981.
- Holbrook, J.R., J.R. Apel, and J. Tsai, The Sulu Sea Internal Soliton Experiment, Part B: Observations and Analysis, J. Phys. Oceanogr. (in press), 1983.
- Hughes, B.A. and J.F.R. Gower, SAR Imagery and Surface Truth Comparisons of Internal Waves in Georgia Strait, British Columbia, Canada, J. Geophys. Res., **88**, pp. 1809-1824, 1983.

- Larson, T.R., L.I. Moskowitz and J.W. Wright, A Note on SAR Imagery of the Ocean, IEEE Trans. Antenna Propag., pp. 393-394, 1976.
- Lichy, D.E., M.G. Mattie and L.J. Mancini, Tracking of a Warm Water Ring Using Synthetic Aperture Radar, in Spaceborne Synthetic Aperture Radar Imagery for Oceanography, ed. by R.C. Beal, P.S. DeLeonibus, and I. Katz, Johns Hopkins Univ. Press, Baltimore, MD, pp. 171-182, 1981.
- Liu, A. K., Detection of Bottom Features on Seasat Synthetic Aperture Radar Imagery, Dynatech Report No. DT-8312-01, Torrance, CA, 45 pp., 1983.
- Liu, A.K., J.R. Apel, and J.R. Holbrook, The Sulu Sea Experiment, Part C: Comparisons with Theory, J. Phys. Oceanogr. (in press), 1983.
- Mattie, M.G., D.E. Lichy and R.C. Beal, Seasat Detection of Waves, Currents and Inlet Discharge, Int. J. Remote Sensing, 1, pp. 377-398, 1980.
- Moskowitz, L.I., The Feasibility of Ocean Current Mapping via Synthetic Aperture Radar Methods, Proc. Amer. Soc. of Photogrammetry, Part II, pp. 760-771, 1973.
- Osborne, A.R. and T.L. Burch, Internal Solitons in the Andaman Sea, Science, 208, pp. 451-460, 1980.
- Raney, R.K., Synthetic Aperture Imaging Radar and Moving Targets, IEEE Trans. Aerospace Elect. Syst., AES-7, pp. 499-505, 1971.
- Raney, R.K. and R.A. Shuchman, SAR Mechanism for Imaging Waves, Proc. Fifth Canadian Symp. on Remote Sensing, Victoria, B.C., 1978.
- Roberts, D.G., P.M. Hunter, and A.S. Laughton, Bathymetry of the Northeast Atlantic: Continental Margin Around the British Isles, Deep-Sea Res., 26A, pp. 417-428, 1979.
- Shemdin, O.H., The Marineland Experiment: An Overview, Trans. Amer. Geophys. Union, 61, No. 38, pp. 625-626, 1980.
- Shemdin, O.H., A. Jain, S.V. Hsiao and L.W. Gatto, Inlet Current Measured with Seasat-1 Synthetic Aperture Radar, Shore and Beach, 48, pp. 35-39, 1980a.
- Shuchman, R.A., Processing Synthetic Aperture Radar Data of Ocean Waves, Oceanography from Space, ed. by J.F.R. Gower, Plenum Press, New York, pp. 477-496, 1981.
- Shuchman, R.A., P.L. Jackson and G.B. Feldkamp, Problems of Imaging Ocean Waves with Synthetic Aperture Radar, ERIM Interim Technical Report No. 124300-1-T, Ann Arbor, MI, 111 pp., 1977.
- Shuchman, R.A. and E.S. Kasischke, The Detection of Oceanic Bottom Topographic Features Using SEASAT Synthetic Aperture Radar Imagery, Proc. Thirteenth Int. Symp. Remote Sens. Environ., pp. 1277-1292, 1979.
- Shuchman, R.A., C.L. Rufenach, F.I. Gonzalez, and A. Klooster, The Feasibility of Measurement of Ocean Surface Currents Using Synthetic Aperture Radar, Proc. Thirteenth Int. Symp. Remote Sens. Environ., Ann Arbor, MI, pp. 93-102, 1979.
- Shuchman, R.A., E.S. Kasischke and G.A. Meadows, Detection of Coastal Zone Environmental Conditions Using Synthetic Aperture Radar, 1981 International Geoscience and Remote Sensing Symposium Digest, Washington, D.C., pp. 756-767, 1981a.
- Shuchman, R.A., A.L. Maffett and A. Klooster, Static Modeling of a SAR Imaged Ocean Scene, IEEE J. Oceanic Eng., OE-6, pp. 41-49, 1981.
- Shuchman, R.A., D.R. Lyzenga, and A. Klooster, Exploitation of SAR Data for Measurement of Ocean Currents and Wave Velocities, ERIM Report No. 137600-1-F, Environmental Research Institute of Michigan, Ann Arbor, 1981c.

Trask, R.P. and M.G. Briscoe, Detection of Massachusetts Bay Internal Waves by the Synthetic Aperture Radar (SAR) on Seasat, *J. Geophys. Res.*, **88**, pp. 1789-1899, 1983.

Weissman, D.E., T.W. Thompson and R. Legeckis, Modulation of Sea Surface Radar Cross Section by Surface Stress: Wind Speed and Temperature Effects Across Gulf Stream, *J. Geophys. Res.*, **85**, pp. 5032-5042, 1980.

Wright, J.W., Backscattering from Capillary Waves with Application to Sea Clutter, *IEEE Trans. Antenna Propagat.*, **AP-14**, pp. 749-754, 1966.

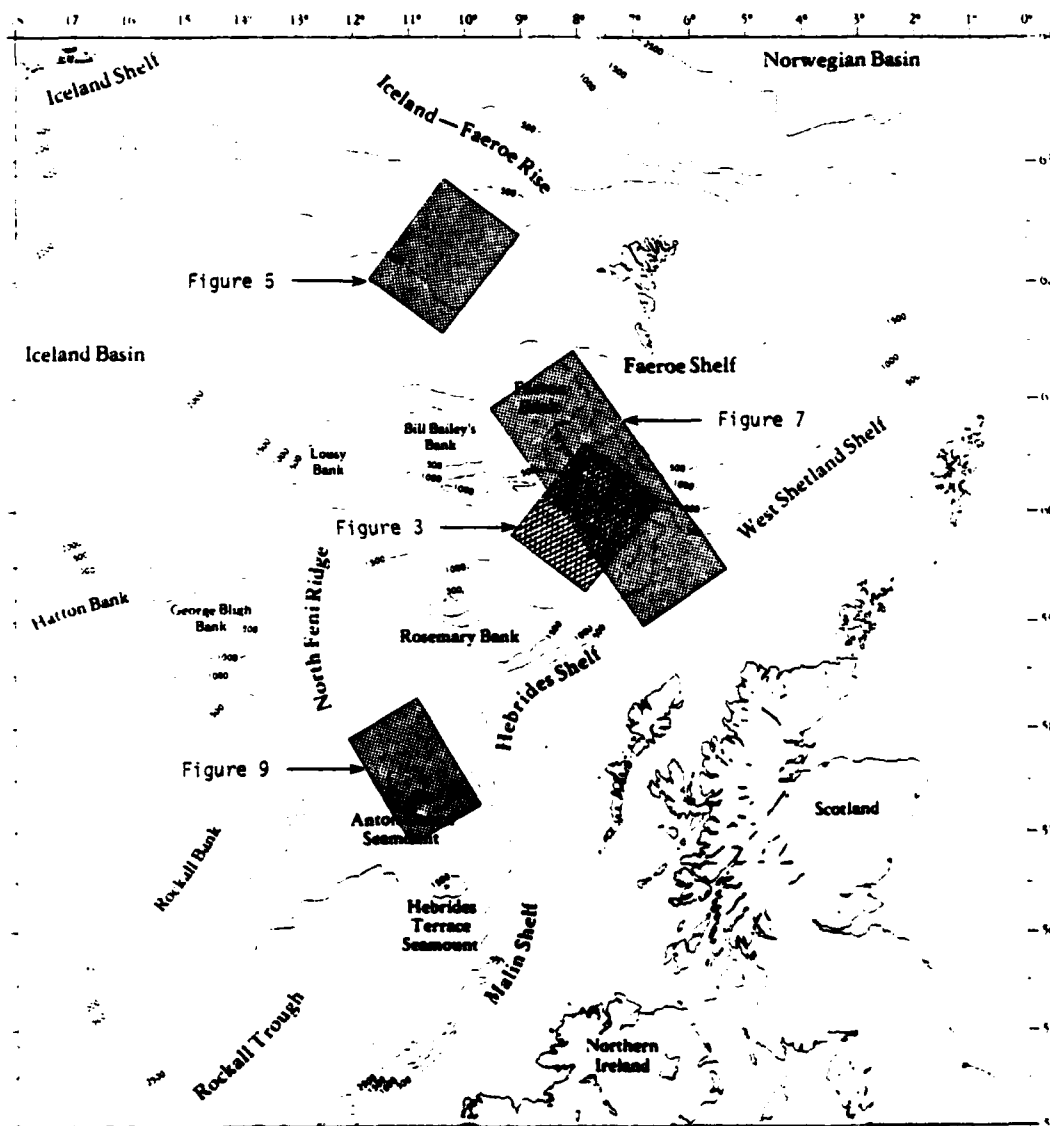


Figure 1. Location of Major Bottom Features in Eastern North Atlantic and Positions of Seasat SAR Images

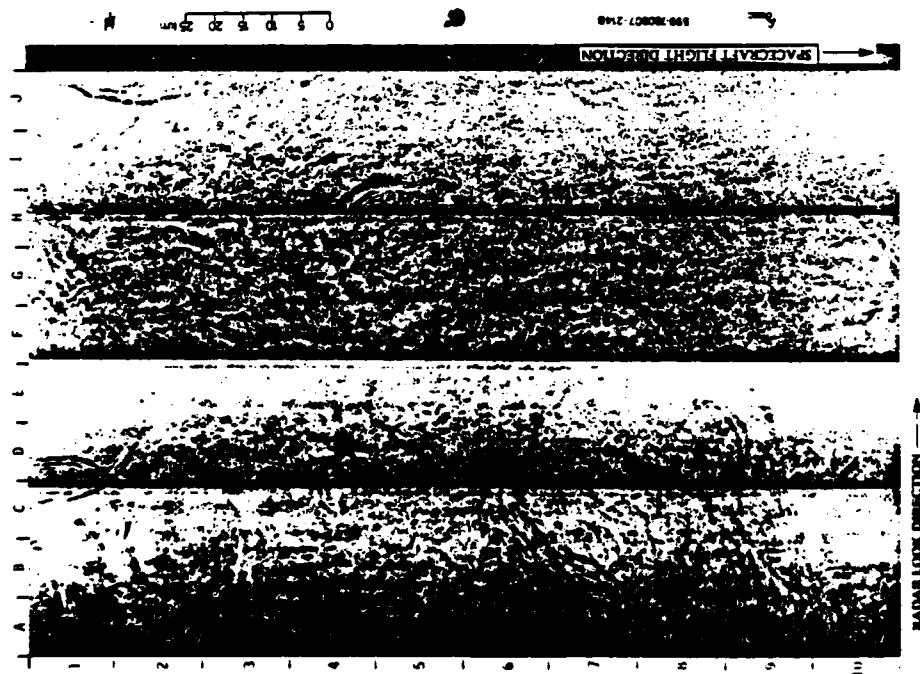


Figure 2. Seasat SAR Imagery Collected Over the Myville-Thomson Ridge During Rev. 599

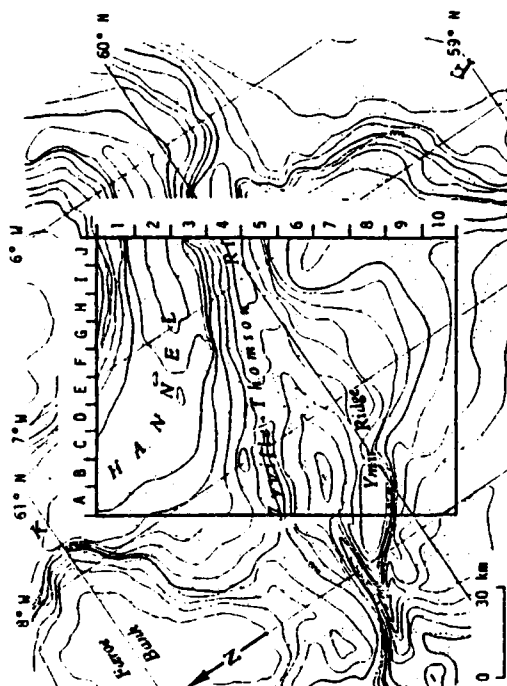


Figure 3. Ground Coverage Corresponding to Seasat SAR Rev. 599. (After IOS Chart No. C6567, Contour Intervals in 100-Meter Increments.)

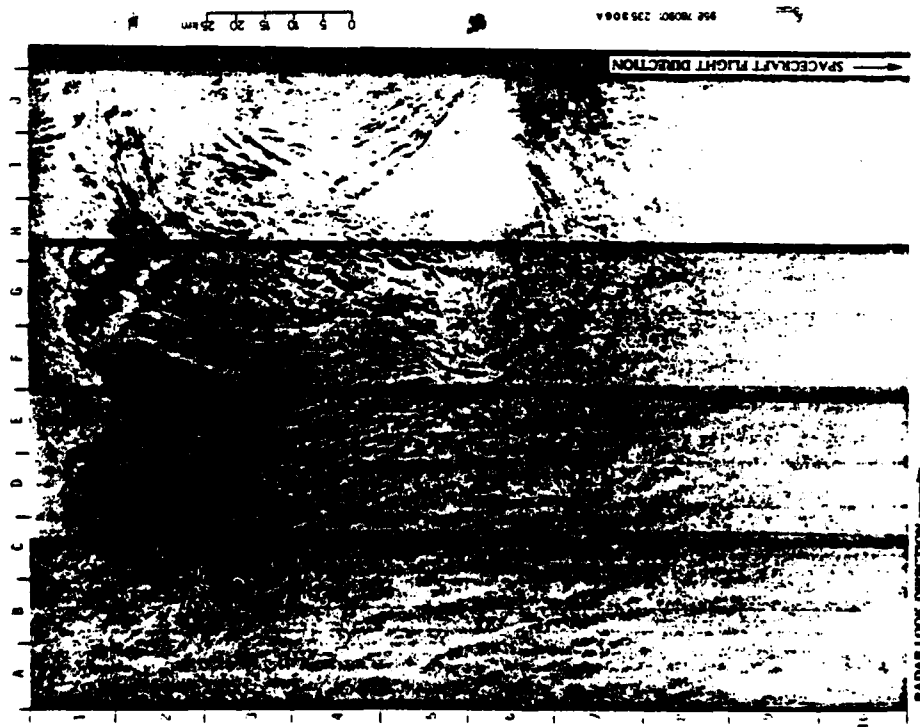


Figure 4. Seasat SAR Imagery Collected Over the Iceland-Faeroe Rise During Rev. 958

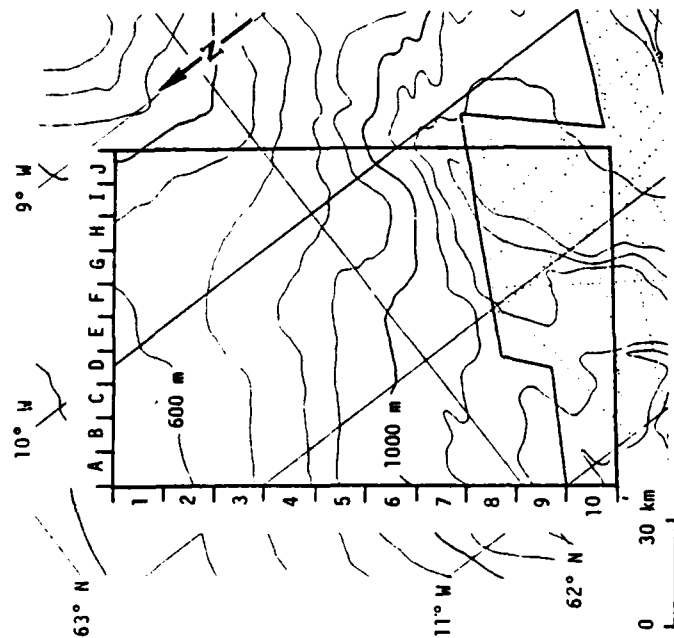


Figure 5. Ground Coverage of Seasat Rev. 958 Over Iceland-Faeroe Rise. (After IODS Chart No. C6567, Depth Contours in 100-Meter Increments.)

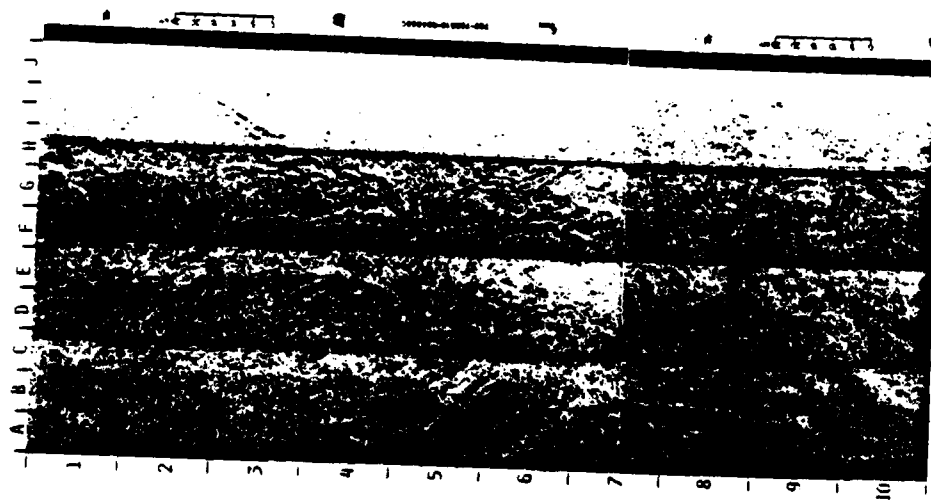


Figure 6. Seasat SAR Imagery Collected Over Myville-Thomson Ridge During Rev. 762

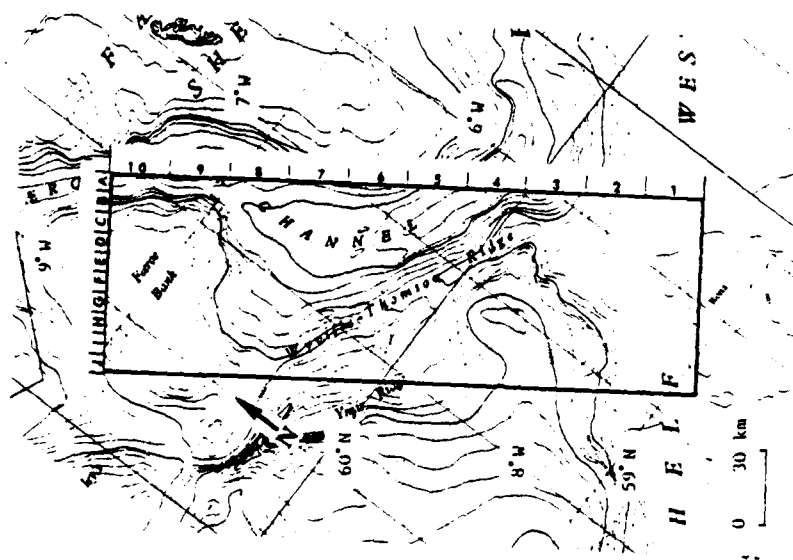


Figure 7. Ground Coverage of Rev. 762 Over Myville-Thomson Ridge. (After IOS Chart No. C6567, Depth Contours in Meters.)

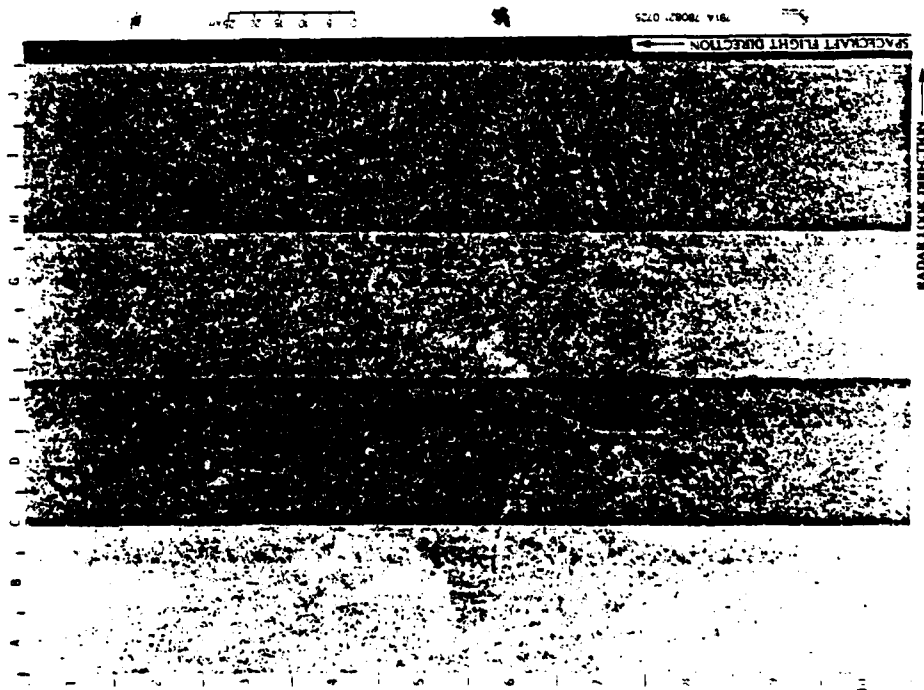


Figure 8. Seasat SAR Imagery Collected Over Anton Dohrn Seamount During Rev. 791

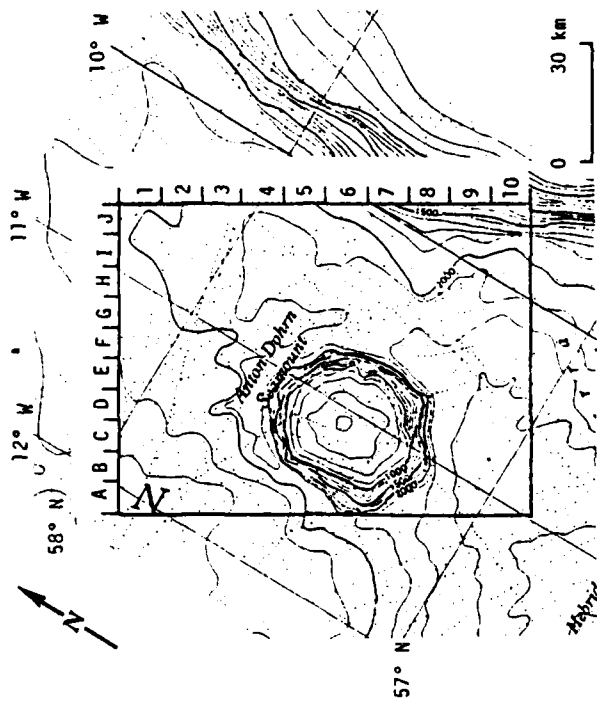


Figure 9. Ground Coverage of Rev. 791 Over Anton Dohrn Seamount. (After IOS Chart No. C6567, Depth Contours in 100-Meter Increments.)

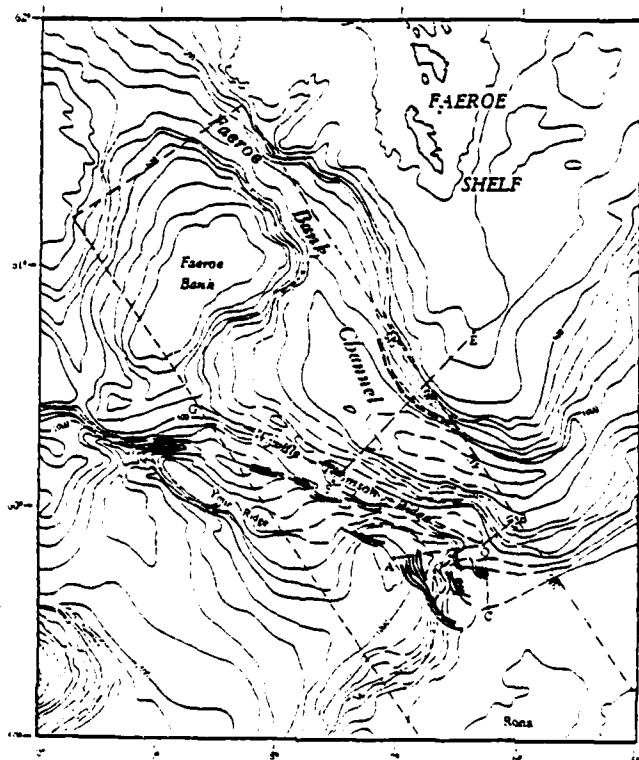


Figure 10. Line Drawings of Internal Waves and a Frontal Boundary Observed in Figure 6 Superimposed on the Hydrographic Chart of the Northeast Atlantic Ocean

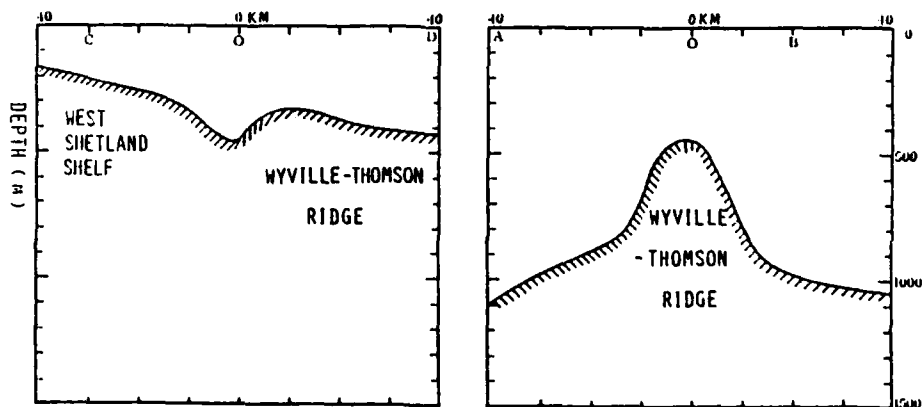


Figure 11. Longitudinal and Transverse Bathymetric Profiles Across Ridge, with a Saddle-Like Valley at O. Locations of Letters A, B, C, D and O are Indicated in Figure 10.

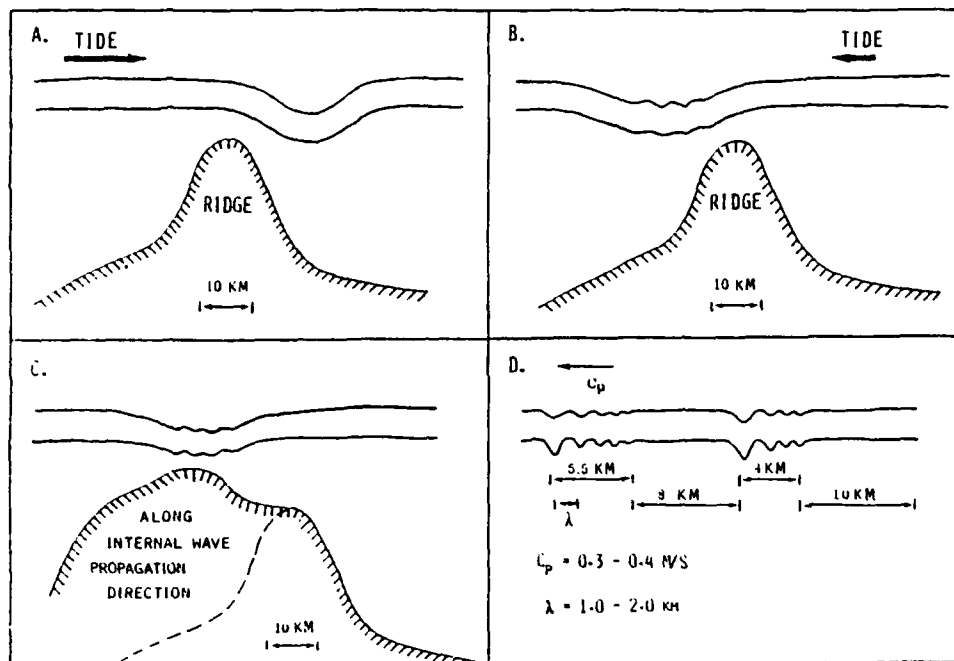


Figure 12. Schematic Diagram Summarizing the Generation and Evolution of an Internal Wave Packet Over the Wyville-Thomson Ridge

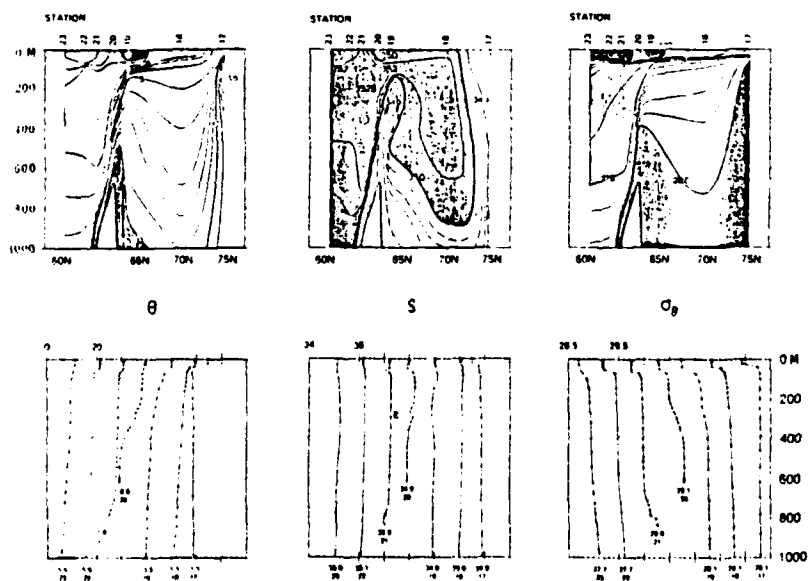


Figure 13. Profiles of Potential Temperature, Salinity and Sigma Theta From Data Collected Over the Icelandic-Faeroe Rise. (From Bainbridge, 1980)

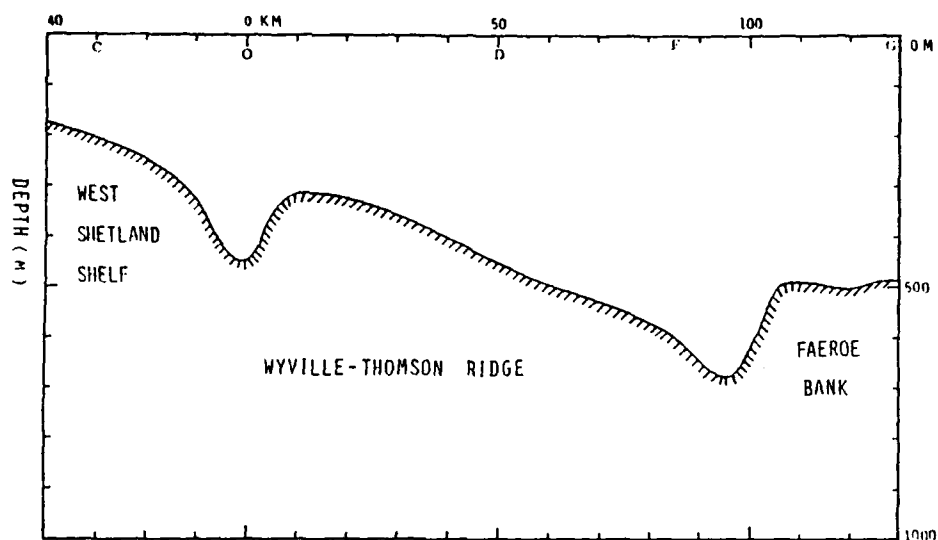


Figure 14. Cross-Section Diagram of Bottom Topography of the Wyville-Thomson Ridge

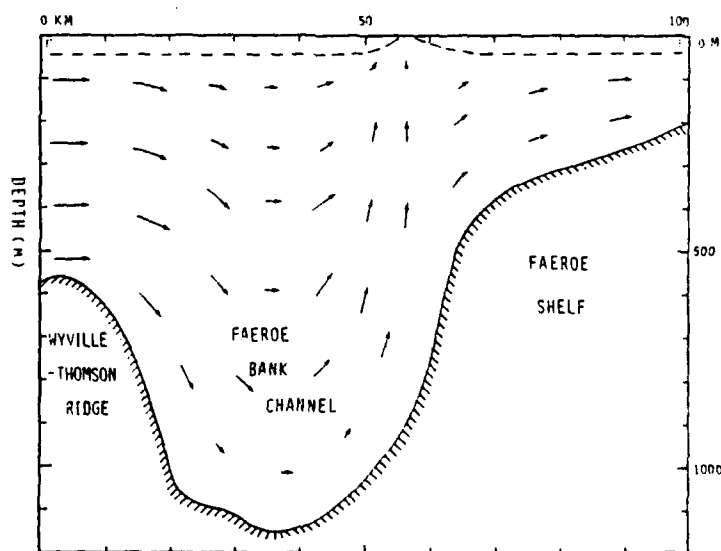


Figure 15. Schematic Diagram Illustrating Deep Water Upwelling Over the Faeroe Bank Channel

TABLE 1
SUMMARY OF SEASAT SAR PASSES COLLECTED OVER EASTERN NORTH ATLANTIC OCEAN

<u>Seasat Revolution</u>	<u>Date</u>	<u>Time (GMT)</u>
547	4 August 1978	06:15
556	4 August 1978	21:35
590	7 August 1978	06:20
599	7 August 1978	21:45
633	10 August 1978	06:30
642	10 August 1978	21:50
714	15 August 1978	22:35
719	16 August 1978	06:40
757	18 August 1978	22:40
762	19 August 1978	06:45
785	20 August 1978	21:40
791	21 August 1978	07:25
834	24 August 1978	07:30
958	1 September 1978	23:53
1006	5 September 1978	08:15
1044	8 September 1978	00:18
1049	8 September 1978	08:27
1087	10 September 1978	00:30
1149	15 September 1978	08:20
1307	26 September 1978	09:45
1359	30 September 1978	01:15

TABLE 2
BOTTOM TOPOGRAPHIC FEATURES IN THE NORTHEASTERN ATLANTIC

<u>Bottom Feature</u>	<u>Shallowest Point (m)</u>	<u>Depth of Deep Water Adjacent (m)</u>
Iceland-Faeroe Rise	300	1000
Bill Bailey's Bank	100	1200
Lousy Bank	300	1500
Hatton Bank	500	2000
George Bligh Bank	500	1100
Faeroe Bank	100	1000
Faeroe Shelf	300	1000
Wyville-Thomson Ridge	400	1200
Ymir Ridge	600	1500
North Feni Ridge	1200	2000
Rosemary Bank	500	2000
Rockall Bank	300	2300
Anton Dohrn Seamount	600	2100
West Shetland Shelf	300	1000
Malin Shelf	200	2000
Hebrides Terrace Seamount	1000	2400
Hebrides Shelf	200	1500
Iceland Continental Shelf	200	2000
Norway Continental Shelf	200	600
Ormonde Seamount	100	2500
Gettysburg Seamount	100	2500
Coral Patch Seamount	500	2500
Ampere Seamount	100	2500
Porcupine Bank	300	3000
Mid-Atlantic Ridge	700	1500
South Feni Ridge	2300	3000

TABLE 3. SUMMARY OF OCCURRENCES OF BOTTOM-RELATED SURFACE PATTERNS
ON SEASAT SAR IMAGERY COLLECTED OVER THE NORTHEAST ATLANTIC

Bottom Feature Covered by Seasat SAR	SAR Revolution Number	SAR-Observed Pattern	
		Internal Edge	Frontal Boundary
Rockall Bank	547	X	
	556		X
	714	X	
	757	X	
	791	X	
	958	X	X
	1044		
Anton Dohrn Seamount	1087		X
	547	X	X
	556	X	
	599	X	
West Shetland Shelf	791		
	642	X	
	762	X	
Malin Shelf	1359	X	
	547		X
	633	X	
	791	X	
Hebrides Terrace Seamount	834		
	547	X	
	642	X	
	791		
Hebrides Shelf	590	X	
	599		
	633		
	642		
	719		
	762	X	
	834		X
	1006		X
Iceland-Faeroe Rise	1049		
	1307		
	719	X	
	762	X	X
	958	X	
	1044	X	X
	1087	X	
Bill Bailey's Bank	1149	X	
	719	X	X
	757		
	1006		X
	1044		
	1049	X	X
	1087	X	
Lousy Bank	1307		
	533	X	X
	590	X	
	791		X
	834	X	
	958	X	
	1006		
	1044	X	X
Hatton Bank	1049	X	X
	1087	X	
	547		
	791		X
George Bligh Bank	958		X
	1044	X	
	547	X	
	791	X	
Faeroe Bank	958	X	
	1044	X	
	1087	X	
	556		X
Faeroe Shelf	719		X
	757	X	
	762	X	
	791	X	
Auvville-Thomson Ridge	1149	X	
	556		
	599	X	
	642		X
	719	X	
Auvville Ridge	757		
	762	X	X
	556		
	599	X	
	442	X	
Auvville Ridge	719	X	
	757	X	
	1049	X	
	1307	X	

27:SARabil1t2

ON THE ABILITY OF SYNTHETIC APERTURE RADAR
TO MEASURE OCEAN WAVES

J. F. Vesecky¹, R. H. Stewart², R. A. Shuchman³,
H. M. Assal¹, E. R. Kasischke³, and J. D. Lyden³

Revised Manuscript for the Proceedings of the IUCRM Symposium
on Wave Dynamics and Radio Probing of the Ocean Surface,
Prof. O. M. Phillips, editor

September, 1982

¹Stanford Center for Radar Astronomy, Stanford, CA 94305

²Scripps Institution of Oceanography, La Jolla, CA 92093 and Jet Propulsion
Laboratory, Pasadena, CA 91103

³Environmental Research Institute of Michigan, Ann Arbor, MI 22217

ABSTRACT

The SEASAT satellite system, using an onboard 23 cm wavelength synthetic aperture radar (SAR), collected ~ 25 to 40 m resolution radar images of the ocean in 100 km wide swaths ranging in length from ~ 300 to 3000 km. Here we report results from the 18 SEASAT SAR passes during the Joint Air-Sea Interaction (JASIN) experiment conducted off the west coast of Scotland in summer, 1978. These many SAR images; when coupled with the intensive ship, buoy and aircraft measurements of the JASIN experiment; provide a unique opportunity to assess the ability of satellite SAR to measure ocean surface phenomena, particularly surface wave fields. In this study we use only optically processed SAR images. Although gravity waves of length ~ 80 to 300 m are often seen in SAR imagery, they are not always seen. We find that SAR resolution and waveheight are important criteria for determining wave visibility and suggest that wind velocity is also. Comparisons between SAR and buoy estimates of dominant wavelength and direction (including data from several other experiments) agree to within about $\pm 13\%$ ¹⁴ and $\pm 10^\circ$ respectively. We use a focus sharpness algorithm to resolve the 180° directional ambiguity of SAR image directional estimates. Correlation of buoy measurements of significant waveheight ($H_{1/3}$) with peak signal to noise ratio in Fourier transforms of SAR images ($r = 0.7$), suggests that $H_{1/3}$ can be estimated to an accuracy of about ± 1 m. However, a similar, but weaker, correlation exists between signal to noise and wavelength, i.e. $H_{1/3}$ and wavelength are correlated in the JASIN data set. SAR image power spectra are in rough agreement with buoy measurements of omnidirectional ocean waveheight spectra $\Psi(K)$ and correspond less closely with ocean wave slope spectra $\Psi'(K)$. However, the dominant wavenumber (K_{peak}) in SAR spectra typically falls below the dominant wavenumber of corresponding buoy spectra. Further, the slope of

SAR spectra for $K < K_{\text{peak}}$ is typically steeper than corresponding buoy measurements of $\Psi(K)$ while the slope of SAR spectra for $K > K_{\text{peak}}$ is typically less steep than corresponding buoy spectra $\Psi(K)$. These differences between SAR spectra and buoy measurements of $\Psi(K)$ form qualitative support for the imaging mechanisms developed by Alpers, Ross and Rufenach. Analysis algorithms based on this theory, but including empirical modifications, should substantially improve estimates of $\Psi(K, \theta)$ using SAR images.

I. INTRODUCTION

Our primary objective in this paper is to assemble a number of comparison sets of ocean gravity wave measurements based on both synthetic aperture radar (SAR) and surface buoys. These comparison sets are then used to comment upon the ability of synthetic aperture radar to measure ocean gravity waves in the period range from about 7 to 19 s. Comparisons are made with respect to dominant wavelength and direction of the wave field, significant wave height $H_{1/3}$ and the directional wavenumber spectrum of waveheight variance $\psi(\vec{k})$. SAR imagery collected by the SEASAT satellite over the Joint Air Sea Interaction (JASIN) experiment area, west of Scotland provides an excellent opportunity to make the desired comparisons. During the SEASAT-JASIN experiment (August-September, 1978) observations of many air and sea parameters were made by ships, buoys and aircraft including the wind and waves which are of most interest here (Pollard, 1979). Swaths of four of the 18 SEASAT SAR passes over the JASIN area are shown in Fig. 1.

The 23 cm wavelength SAR carried aboard the SEASAT satellite collected ≈ 25 to 40 m resolution radar images of the ocean in 100 km wide swaths ranging in length from ≈ 300 to 3000 km along, but displaced to the right of, the subsatellite track. The SEASAT SAR is unique, being the only scientific SAR ever carried aboard a satellite. During the short lifetime of SEASAT (June-September 1978) some 10^8 km² (equivalent to about 20% of the Earth's surface) were imaged. A description of the instrument is given by Jordan (1980) and preliminary results from all SEASAT instruments were given in the June 29, 1979 issue of Science. Beal et al. (1981) and Gower (1981) report further SEASAT SAR results and Vesecky and Stewart (1982) assess and review the ability of SEASAT SAR to sense ocean surface phenomena. Here we report results of SEASAT SAR observations during the JASIN experiment.

SAR images collected by SEASAT are basically high resolution maps of the radar reflectance (backscatter) of the ocean surface modified by surface motion effects. Because the dielectric properties of the ocean surface are relatively uniform, variations in reflectance are due primarily to variations in surface roughness. In particular the reflectance is due to resonant backscatter of the $\lambda = 23$ cm radar waves from ocean surface waves of length $\Delta = \lambda/2 \sin \theta \approx 30$ cm, the angle of incidence θ being about 19 to 26°. The resonant mechanism is typical of radiation scattered from a lattice and is often called Bragg scatter (Bragg, 1933). Because SAR uses the phase of the radar echo to achieve high azimuthal resolution in the image (i.e. to correctly locate the origin on a given echo) motion of the ocean surface, which introduces a phase shift in the scattered signal, causes points in the image to be displaced from their true position. Such misplacement is aptly illustrated by moving ships being displaced from their wakes (e.g. see Vesecky et al., 1982 or Vesecky and Stewart, 1982). Spatial modulation of surface roughness and surface motion (giving rise to Doppler shifts) produce the majority of ocean surface features in SAR imagery. Phillips (1981) describes a number of ways in which wind, waves and current can modulate decimeter scale surface roughness. Often the difficulty in interpreting SAR imagery of the ocean is to discover which of the several candidates is really the underlying cause of the surface roughness modulation sensed by the radar. Ocean gravity waves are easily recognized when they are highly coherent and present an easily recognized large scale pattern as shown in Fig. 2.

The radar echo signal as received on the SEASAT satellite and relayed to a ground station can be processed into an image using any one of a number of different algorithms. Further these algorithms can be implemented using either optical (analogue) or digital processing apparatus. The relative

merits of optical and digital processing are discussed by Vesecky and Stewart (1982). In general optical processing can be done more quickly and at less expense, while digital processing allows a better quality image to be produced. The SAR images used in this study have all been processed optically either at Jet Propulsion Laboratory (JPL) or at Environmental Research Institute of Michigan (ERIM).

II. THE SEASAT-JASIN EXPERIMENT

The SEASAT-JASIN experiment was conducted some four hundred km off the west coast of Scotland during the summer of 1978. As shown in Fig. 1 this area of open ocean is generally deep with numerous banks and sea mounts rising to depths of $\lesssim 500$ m. The oceanic intensive area (OIA), where the majority of buoy measurements were made, has a depth of greater than 1000 m so bottom topography does not modify the deep-water dispersion relation for ocean gravity waves. Moderate seas prevailed during the SEASAT-JASIN experiment period with significant wave heights ($H_{1/3}$) ranging from about 1 to 5 m. Winds were also moderate, ranging from about 3 to 15 ms^{-1} . Locations of wave rider buoys in the OIA are shown in Fig. 1 along with the FIA area, where most of the pitch-roll buoy measurements were made. Further details are given in both Fig. 1 and Table I.

Both pitch-roll and wave rider buoys were used to make wave measurements. Pitch-roll buoys were deployed from both the R.V. Atlantis II (Woods Hole Oceanographic Institution) and the M.V. Discovery (Institution of Oceanographic Sciences) on 8 and 2 occasions respectively. These buoys provide measurements of the omnidirectional waveheight variance spectrum $\Psi(\omega)$ as well as estimates of the dominant wave direction and beam width. The Atlantis II buoy is described by Stewart (1977). Wave rider buoys

were moored by the Deutsches Hydrographisches Institut at a number of locations as shown in Fig. 1. These buoys measured only $\psi(\omega)$ and provided no directional information. The SAR data collected over the JASIN area and used in this study was optically processed into images at both the Jet Propulsion Laboratory (JPL) and the Environmental Research Institute of Michigan (ERIM). The JPL images were the standard SEASAT SAR data product having a resolution of 25 to 40 m. The ERIM images were specially processed to obtain focus information as described below and to achieve consistent 25 m resolution. An example of JPL imagery is shown in Fig. 2 where a field of about 170 m waves is present. Examples of ERIM imagery are given by Kasischke et al. (1982).

During the experiment period (4 August to 11 September, 1978) 18 SEASAT SAR passes were made over various portions of the JASIN area. Table I summarizes the data collected during these passes. On 16 of the passes concurrent or nearly concurrent buoy measurements were made. On three occasions a buoy was within the SAR swath. The distances between the SAR swaths and buoy locations in the other cases are noted in Table I. Wind measurements were also made concurrent with most of the SEASAT SAR passes as noted in Table I. The wind speeds are averages of observations by 3 to 5 surface instruments within the OIA area of Fig. 1 and hence near the wave buoy locations.

III. VISIBILITY OF OCEAN WAVES IN SAR IMAGES

Although ocean gravity waves of length ~ 80 to 300 m are often seen in SAR images, they are not always seen. Wave visibility is not simply a case of insufficient wave height. For example, one notes from Table I that waves with $H_{1/3} \sim 3.6$ m in a 6.6 ms^{-1} wind were not seen in SAR images from orbit 1006. Why is this so?

We suggest that three criteria are important in determining wave visibility:

1. SAR resolution (including the degrading effects of wave orbital motion) must be sufficiently good that the Nyquist sampling criterion, i.e. at least two resolution cells per projected ocean wavelength, be satisfied in both the azimuth direction (parallel to the SAR flight path) and the range direction (perpendicular to the SAR flight path).
2. $H_{1/3}$ greater than about 1 m.
3. Wind speed greater than a few ms^{-1} .

In this study we have used only SAR images processed optically at the Jet Propulsion Laboratory (JPL) and the Environmental Research Institute of Michigan (ERIM).

Alpers, Ross and Rufenach (1981) point out that orbital velocities associated with surface gravity waves produce a smearing effect on SAR imagery degrading resolution, especially along the azimuth (y) direction. They also note that the ocean surface coherence time (τ_s) affects resolution (Raney, 1980) as do adjustments (ΔV) in the azimuthal focus relative to the nominal focus for land. Alpers et al. (1981) argue that the coherence (τ_s) term can usually be neglected and we do so here. If Δy is the land (unsmear) azimuth resolution (~ 25 to 40 m for SEASAT SAR), then the degraded azimuth resolution Δy^* for N looks is given by

$$\Delta y^* = N \Delta y \{ 1 + N^{-2} [\frac{\pi T^2}{\lambda} (-A \omega^2 g(\theta, \psi) \cos(\vec{k} \cdot \vec{r} + \alpha')) + (2V \Delta V / R)]^2 + (\frac{T}{\tau_s})^2 \}^{1/2} \quad (1)$$

where T is the one-look, full bandwidth integration time (≈ 2.3 s for SEASAT SAR), λ is radar wavelength, \vec{r} the location of the target in the (x,y) plane, $\alpha' = \tan^{-1}(\tan\theta \sin\phi)$ and A , ω , and \vec{K} are the amplitude, radian frequency and vector wavenumber of the dominant ocean wave. V is the satellite velocity relative to the Earth and ΔV is an azimuthal focus adjustment parameter which we take to be zero here since no focus adjustment was made in imaging the data used here. The function

$g(\theta, \phi) = (\sin^2\theta \sin^2\phi + \cos^2\theta)^{1/2}$; other variables are defined in Fig. 3. In our calculation of Δy^* we have taken $1/\pi$ as the typical value of the cosine term. Knowing Δy^* and the dominant ocean wavelength along the y -direction $\Delta_y = \Delta/\cos\phi$, the number of SAR resolution elements or samples n_y along the azimuth direction can be estimated. The Nyquist sampling criterion (Bracewell, 1979) demands $n_y > 2$ for the waves to be adequately sampled. Jain (1978) and Vesecky et al. (1981) have developed wave visibility criteria along these lines. While an analagous criterion $n_x > 2$ must also be met along the range direction, resolution degradation along the x -direction is much less severe and we have neglected it here.

Because of the roles played by waveheight and/or slope in wave imaging mechanisms (Alpers et al., 1981) one expects wave visibility to decrease with decreasing waveheight $H_{1/3}$ and indeed we find waves are seldom imaged for $H_{1/3} \lesssim 1$ m. This waveheight criterion is probably set by the influence of slopes on the wave imaging mechanism, i.e. on the spatial modulation of the normalized radar cross section σ_0 . If slopes are the dominant mechanism modulating σ_0 , and if slopes are small, then so too is $\Delta\sigma_0$. If $\Delta\sigma_0$ is less than the noise fluctuations of σ_0 in the image, the waves are invisible. Interestingly, theory implies that there may be both a minimum $H_{1/3}$ below which waves are invisible and a maximum $H_{1/3}$ above which waves traveling near

the azimuth direction are not imaged because azimuthal resolution is severely degraded by large wave orbital velocities. The two criteria

$n_y \geq 2$ and $H_{1/3} \geq 1$ m are applied to the SEASAT-JASIN data set in Fig. 4. In calculating n_y N was set at four and Δy at 6.25 m corresponding to 4 look optical processing. Where possible ocean wave data are drawn from buoy measurements given in Table 1. Cases where SAR estimates were used for Φ are noted in Fig. 4.

Since surface winds raise the ~ 30 cm ocean waves to which the radar is sensitive, we expect wave images to disappear when wind speed falls below a few ms^{-1} , and the sea becomes calm. A wind speed of 3.5 ms^{-1} is typical of speeds required to maintain a saturated spectrum of gravity waves for $\lambda \lesssim 30$ cm (Vesecky and Stewart, 1982). A SAR image of a calm region containing no visible waves is given by Beal (1981). During the SEASAT-JASIN experiment waves were detectable over a range of wind speeds of from 3.5 to 15.2 ms^{-1} while for wind speeds of from 6.6 to 12.9 ms^{-1} waves were not detected. Thus wind speed was apparently not a factor during the SEASAT-JASIN experiment mainly because wind speeds were always above 3.5 ms^{-1} .

IV. SAR IMAGE ANALYSIS METHODS

SAR image analysis done here is tied to a very simple assumption, namely, that SAR image intensity fluctuations δI are proportional to ocean surface height fluctuations δh . This assumption implies that the Fourier power spectrum of the image intensity distribution $|F_I(K, \theta)|^2 = |F\{I(x, y)\}|^2$ is proportional to the directional waveheight spectrum $\Psi(K, \theta)$ of the ocean surface corresponding to the image. As will become evident, the truth is not so simple. However, this assumption is not far wrong and provides a convenient working hypothesis. Using the assumption dominant wavelength and

direction can be estimated simply by noting the values of K and θ where $|F(K,\theta)|^2$ peaks. We discuss below in section VI how the constant of proportionality can be estimated and thus $\Psi(K,\theta)$ estimated.

Several complicating factors which qualify the simple assumption can be summarized in the following equation where these factors enter as linear transfer functions:

$$|F_I(K,\theta)|^2 = |H|^2 \cdot |B|^2 \cdot |R|^2 \cdot \Psi(K,\theta) . \quad (2)$$

These transfer functions H , B and R are related to the point response of the SAR system, background (non-wave-related) fluctuations in the image and the radar wave-ocean wave interaction (imaging) mechanism respectively. The magnitude signs are used since the transfer functions are in general complex.

As with all measurements, the response of the measuring instrument is not perfect. Thus the SAR image of a point target is spread over some region of the image characterized in size by the resolution cell dimensions (Δx and Δy) and in shape by the point spread function. To preserve details SAR images are digitized at sampling intervals small compared to Δx and Δy . When an image is Fourier transformed and the energy spectrum calculated, one expects the spectral power level to decrease significantly (roll off) as K increases approaching $2\pi/2\Delta x$. Here we take $\Delta x = \Delta y$ since SAR imaging schemes usually strive toward this condition. The transfer function $H(K,\theta)$ can be used to characterize the effects of the point spread function in the wavenumber domain (for reference see Bracewell, 1979 or Champeney, 1973).

Perusal of SAR images of the ocean quickly reveals that there are numerous features on all size scales resolved. Many of these features are clearly not related to ocean gravity waves and hence constitute a background against which the wave images are viewed. It is well known that the radar-backscatter-reflectance of a uniform rough surface is dependent on angle of

incidence. This fact along with the effects of antenna pattern and automatic gain control (AGC) introduce a large scale trend in image brightness perpendicular to the SAR flight path and hence a low K background component in the image transform. Although some compensation for this variation can be introduced in the data processing, some effects remain, especially in optically processed images, e.g. see Vesecky and Stewart (1982). We lump all effects related to background, i.e. non-wave-related, fluctuations in a single transfer function $B(K, \theta)$. Clearly this is a crude model for these effects, but it proves to be useful.

The physical mechanism(s) which allow ocean gravity waves to be imaged are discussed by a number of authors and summarized by Alpers, Ross and Rufenach (1981) and Vesecky and Stewart (1982). The three principal mechanisms considered are as follows:

- 1) tilt mechanism (R_t) in which the change in large scale surface slope along the length ($\Delta \sim 10$'s to 100 's of m) of a gravity wave changes the angle of incidence at which the short ($\Delta \sim 30$ cm) radar-resonant waves are viewed by the radar and hence spatially modulates the radar reflectance as a function of position along the wave

- 2) hydrodynamic mechanism (R_h) in which the variation in acceleration with position along a long gravity wave, i.e. along the direction of wave travel, induces a change in energy density of the radar-resonant waves and again spatially modulates the radar echo strength as a function of position along the wave

- 3) velocity bunching mechanism (R_b) in which the variation in wave orbital velocity with position along a long gravity wave causes the SAR imaging process (which assumes a stationary land surface) to systematically misplace image brightness along the azimuth direction thus spatially

modulating SAR image brightness in a manner corresponding to the variation in wave orbital velocity.

Assuming these imaging mechanisms to be linear we can write

$|R(K, \theta)|^2 = |R_t|^2 |R_h|^2 |R_b|^2$. As pointed out by Alpers, Ross and Rufenach (1981) we can expect the tilt and hydrodynamic mechanisms to be modeled reasonably well by linear transfer functions, but the velocity bunching mechanism is linear only over a small range of directions nearly perpendicular to the SAR flight path. Alpers, Ross and Rufenach have estimated the K dependence of $|R_t|^2$, $|R_h|^2$ and $|R_b|^2$ to be $|R_t|^2 \sim K^2$; $|R_h|^2 \sim K^2$ to $(\omega/\mu)^2 K^2$ for μ , the relation time constant, increasing from 0 to $\mu > \omega$ and $|R_b|^2 \sim (K\omega)^2$ where ω is the ocean wave radian frequency. On the basis of these transfer functions alone we would expect $|F_I|^2 \sim K^{\alpha}$ where $\alpha = 2$ to 3. This K dependence of R_b applies only to the range of wave directions near $\psi = 90^\circ$ where the velocity bunching mechanism is thought to be linear.

The transfer function H can be estimated analytically by knowing the radar system and image processing parameters as done by Beal (1981). In this study we have taken an empirical approach using the variance spectrum of a given SAR image to estimate the product of H and B. Our technique is to first consider the raw image spectrum $|F_I(K, \theta)|^2$ finding the range(s) of θ where wave energy is present. If we further assume that H and B are isotropic, then $|F_I(K, \theta)|^2$ averaged over directions away from the dominant wave direction(s) represents background fluctuations B modified by the SAR image response H and we can thus estimate $|H|^2 \cdot |B|^2$ via

$$|H|^2 \cdot |B|^2 \approx \langle |F_I(K, \theta)|^2 \rangle \quad (3)$$

where the average is taken over θ away from dominant wave directions. Having estimated $|H|^2$ times $|B|^2$ we can remove their effect to obtain the corrected

or rectified image K spectrum $|F_R(K, \theta)|^2 = |F_I(K, \theta)|^2 / |H|^2 \cdot |B|^2$. Because radar system and processing parameters may change from scene to scene we estimate $|H|^2 \cdot |B|^2$ separately for each image.

The omnidirectional spectra presented in this paper (Figs. 7 and 11) were obtained by using the rectified spectrum $|F_R|^2$ averaged over directions near (within about $\pm 15^\circ$) the dominant wave direction(s). Thus these spectra are not truly omnidirectional. However, to have included background fluctuations from directions well away from the dominant wave direction would only have added noise. We consider $|F_R|^2$ as shown in Fig. 7 to be our best present estimate of $\Psi(K)$ for comparison with buoy estimates of this quantity. Note that we have not made any adjustments for the wave imaging mechanism $|R|^2$ since we feel it is not sufficiently well known at this time. Rather we hope that comparisons of $|F_R|^2$ with buoy measurements of $\Psi(K)$ will help clarify which if any of the proposed SAR imaging mechanisms correspond to reality.

We consider results from SEASAT orbit 547 (see Fig. 1) to illustrate several techniques of SAR image analysis as well as methods for displaying the results. In Fig. 5 we show an optical Fourier transform (OFT) produced at ERIM. In this method the coherent optical image, formed by a normal SAR processing optical train, is run through a converging lens to obtain the two-dimensional Fourier transform and a piece of film in the focal plane records the intensity spectrum which corresponds to $|F_I|^2$ discussed above. Practice has shown that weakly imaged waves are often more easily detected in a photographic display such as Fig. 5.

Digital Fourier transforms (DFT's) of SAR images are generated by first digitizing a SAR image and then performing the Fourier transform using the fast Fourier transform algorithm on a digital computer. Generally only the magnitude squared or variance spectrum $|F_I(K, \theta)|^2$ or $|F_R(K, \theta)|^2$ is

examined. In Fig. 6 we see a contour plot of $|F_I(K_x, K_y)|^2$ performed digitally at ERIM using SEASAT data from orbit 547 (see Fig. 1). Fig. 7 shows another method of displaying DFT results, which have been corrected as discussed above, i.e. $|F_R|^2$ is displayed. Generally OFT's have been used for quick-look analysis and to detect weakly imaged waves while DFT's have been used for more quantitative analysis.

Practice thus far indicates that the threshold for detecting waves in SAR images, i.e. estimating dominant wavelength and direction, differs between the OFT and DFT techniques. However, this difference is not fundamental and does not always hold. OFT's, optically displayed as in Fig. 5, are apparently more sensitive because they include data from a relatively large image area. (DFT's usually use a relatively small image area to avoid excessive computation.) Also the photographically displayed OFT allows the eye and brain to perform the pattern recognition. The $|H|^2 \cdot |B|^2$ correction technique, described above, aids in detecting weakly imaged waves in DFT's, i.e. waves not detected in displays of $|F_I|^2$ are evident in displays of $|F_R|^2$. Waves not detectable in an $|F_I|^2$ plot of orbit 599 data were detected when $|F_R|^2$ was computed and plotted.

An important measurement which is derived from OFT or DFT data is the peak signal to noise (S/N) or peak to background ratio (PBR) for a given image. We shall use (S/N) to denote the peak signal to background noise level of $|F_R|^2$ as shown in Fig. 7. The PBR ratio refers to OFT results displayed photographically and denotes the ratio of film density at the peak point (corresponding to the dominant wavelength and direction) to the film density at a specific background location in the OFT display, e.g. near the upper lefthand corner of Fig. 5.

V. COMPARISON OF SAR ESTIMATES WITH BUOY MEASUREMENTS FOR THE WAVELENGTH, DIRECTION AND BEAMWIDTH OF THE DOMINANT WAVES

Comparisons of SAR estimates of ocean waveheight spectra with buoy measurements of the same quantity serve two purposes. First, they allow one to judge the usefulness of SAR observations in making wave measurements. Second, the comparisons shed light on the physical mechanisms which allow waves to be imaged by a SAR. Better understanding of the imaging mechanism should lead to more accurate SAR estimates through improvement of the analysis algorithms, i.e. progress beyond the simple assumption discussed above. Table 1 summarizes the experiment parameters and many of the results of the SEASAT-JASIN experiment.

It is clear that buoy and SAR measurements are fundamentally different in that the SAR measurements are largely spatial averages at a point in time while buoy measurements are mainly temporal averages at a point in space. To compare the two we assume that the ocean surface is statistically homogeneous and stationary over scales of ~ 20 km in space and ~ 0.5 hr in time so that spatial and temporal averages are statistically equivalent, i.e.

$\Psi(\omega, \theta) d\omega = \Psi(K, \theta) K dK$ The omnidirectional slope spectrum $\Psi'(K)$ is derived from the wave height spectrum simply by multiplication by K^2 , i.e.

$$\Psi'(K) = K^2 \Psi(K) \text{ (Kinsman, 1965).}$$

Estimates of dominant wavelength and direction are obtained simply by noting the (K, θ) location of the wave-related maximum in $|F_I|^2$ or $|F_R|^2$. Two estimates of K_{\max} and θ_{\max} were made; one using ERIM OFT data corresponding to $|F_I|^2$ and one using Stanford DFT data corresponding to $|F_R|^2$. In making comparisons of dominant wavelength and direction we have simply averaged these two SAR estimates. As one would expect for random errors, in the two estimates, the average of the OFT and DFT estimates

compares more favorably with buoy measurements than either SAR estimate taken alone. This leads one to conclude that the corrections introduced to produce $|F_R|^2$ do not make emphatic improvements in SAR estimates of K_{\max} and θ_{\max} . However, K spectra, such as those in Figs. 7 & 11, were substantially improved by these corrections especially in terms of distinguishing between the ocean-wave-related component and the background.

Fig. 8 shows dominant wavelength comparisons for the SEASAT-JASIN experiment and includes 2 similar comparisons from the DUCK EX experiment and 10 from GOASEX (Gonzalez, et al., 1981). Using all these data we find SAR estimates agree with buoy estimates within an average error of about $\pm 14\%$. We also note that the SAR estimates of wavelength are biased high by about 10%. The reason for this bias is discussed below. A simple scaling error does not appear to be the cause since the same bias is found in data imaged and analyzed independently by three different research groups -- ERIM and Stanford (this paper) and Gonzalez et al. (1981).

In Fig. 9 we compare SAR estimates of wave direction with buoy estimates. Results from GOASEX and DUCK EX are included as in Fig. 8. The SAR measurements show no significant bias and the mean difference between the two estimates is $\pm 10^\circ$. In this error calculation approximate buoy measurements (marked * in Table 1 and shown by diamonds in Fig. 9) were excluded and hence only 4 JASIN cases were used.

SAR estimates of wave direction based on the simple assumption discussed above contain a 180° ambiguity, i.e. one cannot distinguish between waves traveling along $\hat{\phi}$ and those traveling along $(\hat{\phi} + 180^\circ)$. Shuchman and Zalenka (1978) have shown that this ambiguity can be resolved using SAR data alone by special focusing of a SAR image during the imaging process. The difference in the point of sharp focus for waves relative to the sharp focus

point for land reveals the direction of wave travel, either toward or away from the radar. By applying this procedure to the JASIN data set, we are freed from relying on ad hoc assumptions (such as waves always traveling toward coasts or down wind) to resolve the 180° ambiguity in dominant wave direction.

As shown in Fig. 6 SAR images yield information on the wave directional distribution. Beside the dominant wave direction discussed above a "beamwidth" for the distribution can also be calculated by noting the full width at half maximum in a SAR image directional distribution such as shown by Vesecky et al. (1981 and 1982). The SAR directional distribution is calculated by averaging $|F_R(K, \theta)|^2$ over an octave range of K centered on the dominant wavenumber. The SAR estimates of beamwidth are remarkably close to the pitch-roll buoy estimates in four cases -- average difference between the two is ~ 4°. A fifth case (orbit 834) was difficult to interpret since the peak SAR response was only a factor of two above the noise level. We note here that SAR directional distributions often show considerable structure. Vesecky et al. (1980) provide evidence that at least some of this structure is physically real. Hence SAR measurements of wave directional distributions having multiple maxima could be useful in locations where wave sensor arrays are impractical.

VI. SAR ESTIMATES OF SIGNIFICANT WAVEHEIGHT

As discussed above and illustrated in Fig. 7, the signal to noise ratio S/N (at the peak of the wave K spectrum) can be calculated from digital transforms of SAR data. This ratio corresponds to the peak to background ratio (PBR) obtained from optically transformed SAR data as shown in Fig. 5. Nine cases during the SEASAT-JASIN experiment contain both SAR (S/N) and buoy

$H_{1/3}$ estimates. In Fig. 10 we plot these nine cases and note a clear correlation between (S/N) and $H_{1/3}$ --correlation coefficient $r = 0.7$. A linear least mean squares fit to these data points yields $(S/N) = 0.02 + 1.64 H_{1/3}$ with a coefficient of determination $R^2 = 0.53$. Based on this data set the linear fit estimates the value of $H_{1/3}$ with a mean error of about ± 1 m. The ± 1 m error compares well with the accuracy of waveheights determined from SAR data using observations of speckle diversity (Jain, Medlin and Wu, 1982). Further, the correlation of (S/N) and $H_{1/3}$ could be used to produce SAR estimates of $\Psi(K)$ which yield absolute values along the ordinates as well as the abscissae of Figs. 7 and 11, i.e. no normalization along the ordinates would be required. However, we note that in the JASIN data set $H_{1/3}$ and Δ are themselves correlated ^{and hence (S/N) and Δ} though less strongly ($R^2 = 0.40$) than (S/N) and $H_{1/3}$.

VII. COMPARISON OF SAR IMAGE SPECTRA WITH WAVEHEIGHT AND WAVE SLOPE SPECTRA MEASURED BY BUOYS

In Fig. 11 we show six cases in which SAR images from SEASAT and concurrent buoy spectra were collected during the SEASAT-JASIN experiment. An additional case is shown in Fig. 7. The SAR spectrum in each case corresponds to $|F_R|^2$, i.e. the correction discussed above is included. In several cases the buoy was located within the SAR image while in other cases the two are displaced as noted in Table 1. The omnidirectional waveheight spectrum $M_{00}(K)$, which is equivalent to $\Psi(K)$, is shown by the dotted line and corresponds to the calibration on the ordinate. These values of $M_{00}(K)$ were measured by either waverider or pitch-roll buoys as noted in Table 1. To represent the shape of the wave slope spectra $\Psi'(K)$ we have simply multiplied the $M_{00}(K)$ curve by K^2 and normalized the result to the peak level of the M_{00} curve. The SAR spectra are normalized along the ordinate to the

peak level of M_{00} . No normalization was done along the abscissa. As discussed above it should be possible to make a direct comparison of the SAR and buoy estimates of M_{00} without any normalization by using the (S/N) vs $H_{1/3}$ correlation.

One of the most salient features of the comparisons is that the peak of the SAR spectrum is often displaced (toward lower K) from the peaks of M_{00} or $K^2 M_{00}$ as measured by buoys. This bias of SAR spectra toward longer wavelengths is also evident in Fig. 8. Although there is only a small range of K above the peak value of K we can make a rough estimate of the slope of a power law fit (K^β) to $|F_R|^2$ for $K > K_{peak}$. For the cases shown in Figs. 7 and 11 the average slope in this region is $\langle \beta \rangle \sim -2.9$. For the same cases the average slope of $\Psi(K)$ or M_{00} for $K > K_{peak}$ is $\langle \beta \rangle \sim -3.7$. For wave slope spectra the slope is of course 2 larger than for wave height spectra, i.e.

$\langle \beta \rangle \sim -1.7$. Thus the SAR spectral slope for $K > K_{peak}$ is approximately midway between the average slopes for waveheight and wave slope spectra. Overall the SAR spectra correspond slightly better with the waveheight spectra than with the waveslope spectra.

Both of the spectral features described above can be explained, at least qualitatively, by noting that in equation (2) there is a transfer function $|R|^2$ related to the radar wave - ocean wave interaction (imaging) mechanism. Work by Alpers, Ross and Rufenach (1981), discussed in section IV above, indicated that we can expect $|R|^2$ to be proportional to K^2 to K^3 . Consider the curves for $\Psi(K)$, or M_{00} in Figs. 7 and 11. If one were to apply the transfer function $|R|^2$ to these curves (as indicated by eq. 2), we would expect the slope of the resulting SAR spectrum to be relatively more steep on the low wavenumber side of the peak ($K < K_{peak}$) and relatively less steep on the high wavenumber side of the peak ($K > K_{peak}$) and this is indeed what we

generally find in the SEASAT-JASIN data of Figs. 7 and 11. Further the changes in slope from $\Psi(K)$ to $|F_R|^2$ induced by $|R|^2$ could cause the peak wave number to be shifted toward relatively lower wavenumber in SAR spectra as is observed. However, the change in slope from $\Psi(K)$ to $|F_R(K)|^2$ is not as dramatic as one would expect from $|R|^2 \sim K^2$ or K^3 . Thus we conclude that the theory of Alpers, Ross and Rufenach is qualitatively, though not quantitatively, supported by the JASIN data set. Since the transfer functions derived by Alpers, et al. are linear and apply rigorously only to monochromatic waves, quantitative agreement is not necessarily expected for a spectrum of real ocean waves in which non-linear phenomena may play an important role. Further theoretical development along the lines pursued by Alpers, Ross and Rufenach together with empirical modifications where necessary should lead to better algorithms for estimating $\Psi(K, \theta)$ from SAR imagery.

VIII. SUMMARY AND CONCLUSIONS

The principal results and conclusions of the SEASAT-JASIN experiment are summarized below. The results are based on optically processed SAR imagery collected by the SEASAT satellite and surface measurements collected by buoys, ships and aircraft.

1. Wave Visibility in SAR Images: Waves observed by surface buoys are sometimes, but not always, imaged by the SEASAT SAR. Three factors appear to be of primary importance for waves to be visible:

- a. SAR system resolution should be good enough to resolve at least two SAR pixels per ocean wavelength along either the along track (azimuthal) or cross track (range) directions. SAR resolution is adversely affected by ocean wave motion, especially resolution along the azimuth direction.

b. Significant waveheight $H_{1/3}$ should be above some threshold. The data examined here are insufficient to determine this threshold, but suggest it is less than or approximately equal to 1 m.

c. Wind speed should be above some threshold. In the data examined here wind speeds do not fall below 3.5 ms^{-1} and in the 3.5 ms^{-1} case waves were visible in the SAR image. Thus the threshold must be below 3.5 ms^{-1} , probably a few ms^{-1} .

2. SAR Based Estimates of Dominant Wavelength and Direction: Unadjusted SAR estimates of dominant wavelength and direction for the SEASAT-JASIN experiment are accurate to about $\pm 13\%$ and $\pm 10^\circ$ respectively. In computing the latter figure approximate buoy measurements (marked * in Table 1) were excluded and thus only 4 JASIN cases were used. The SAR estimates of dominant wavelength (for the JASIN experiment alone) are biased high by about 10%. If this bias were to be removed by a linear least mean squares fit the dominant wavelength could be estimated to about $\pm 10\%$ using SAR data. The 180° ambiguity usually present in SAR estimates of wave direction can be resolved by focussing tests during the imaging process. These tests remove the need for ad hoc assumptions such as waves always traveling downwind or toward coasts.

3. Estimates of $H_{1/3}$ Using SAR Images: The signal to noise ration (S/N) or peak to background ratio (PBR) at the dominant wavenumber of a SAR image K spectrum is correlated with the significant wave height $H_{1/3}$ ($R^2 = 0.53$). On the basis of the data reported here we suggest that $H_{1/3}$ can be measured to an average accuracy of about $\pm 1 \text{ m}$ using Fourier spectra of SAR images. We note, however, that in the JASIN data set wavelength is also correlated to (S/N), though less strongly ($R^2 = 0.40$).

4. Estimates of Directional Waveheight Spectra Using SAR Image

Spectra: SAR image spectra are in rough agreement with buoy measurements of omnidirectional ocean waveheight spectra $\Psi(K)$ and correspond less closely with ocean wave slope spectra $\Psi'(K)$. However, the dominant wavenumber in a SAR spectrum typically falls below the dominant wavenumber of a buoy spectrum. Further, the typical slope of the SAR spectra on the high wavenumber side of the peak ($K > K_{\text{peak}}$) is $\sim K^{-2.9}$ while the corresponding slopes for buoy spectra are $\sim K^{-3.7}$ and $\sim K^{-1.7}$ for waveheight and wave slope respectively. These differences between SAR and buoy spectra are in qualitative agreement with the theory of Alpers, Ross and Rufenach (1981). Analysis algorithms based on this theory, but including empirical modifications should substantially improve estimates of $\Psi(K, \theta)$ using SAR images.

ACKNOWLEDGEMENTS

We gratefully acknowledge Herbert Carlson of the Deutsches Hydrographisches Institut and Trevor Guymer and David Webb of the Institution of Oceanographic Sciences (IOS) U.K. for supplying wind and wave data collected during the JASIN experiment. Kurt Graf, Dennis Douglas and Dennis Tremain at SRI International provided valuable help in digitizing the JPL imagery. We also thank Harriet Smith, Martha Smith and Sara Zientek for help in preparing the manuscript. The authors gratefully acknowledge financial support from the Office of Naval Research (Physical Oceanography Branch), the National Oceanic and Atmospheric Administration (Ocean Sciences Branch) and the National Aeronautics and Space Administration.

REFERENCES

- Alpers, W.R., Ross, D.B., and Rufenach, C.L. 1981 On the detectability of ocean surface waves by real and synthetic aperture radar, J. Geophys. Res. 86, 6481-6498.
- Beal, R.C. 1981 Spatial evolution of ocean wave spectra in Beal, DeLeonibus and Katz (1981), 110-127.
- Beal, R.C., DeLeonibus, P.S. and Katz, I. (eds.) 1981 Spaceborne Synthetic Aperture Radar for Oceanography, Johns Hopkins University Press.
- Bracewell, R.N. 1979 The Fourier Transform and its Applications, McGraw-Hill.
- Bragg, W.L. 1933 A General Survey, vol. 1 of The Crystalline State, (Sir L. Bragg, ed.) Bell and Sons.
- Champeney, D.C. 1973 Fourier Transforms and their Physical Applications, Academic Press.
- Gonzalez, R.I., Shuchman, R.A., Ross, D.B., Rufenach, C.L. and Gower, G.F.R. 1981 Synthetic aperture radar observations during Goasex in Gower (1981), 459-467.
- Gower, G.F.R. (ed.) 1981 Oceanography from Space, Plenum.

Jain, A. 1978 Focusing effects in synthetic aperture radar imaging of ocean waves, Appl. Phys. 15, 323-333.

Jain, A., Medlin, G., and Wu, C. 1982 Ocean wave height measurement with SEASAT SAR using speckle diversity, IEEE J. Oceanic Engr. OE-7, 103-107.

Jordan, R.L. 1980 The SEASAT-A synthetic aperture radar system. IEEE J. Oceanic Eng. OE-1, 154-163.

Kasischke, E.S., Shuchman, R.A., Lyden, J.D., Stewart, R.H., Vesecky, J.F. and Assal, H.M. 1982 SEASAT observations of ocean gravity waves during the JASIN experiment, J. Geophys. Res. (submitted).

Kinsman, B. 1965 Wind Waves, Prentice Hall.

Phillips, O.M. 1981 The structure of short gravity waves on the ocean surface in Beal, DeLeonibus and Katz (1981), 24-31.

Pollard, R.T. (coordinator). 1979 Air-sea interaction project: summary of the 1978 field experiment. The Royal Society.

Schuchman, R.A. and Zalenka, J.S. 1978 Processing of ocean wave data from a synthetic aperture radar. Boundary-Layer Meteorology 13, 181-191.

Stewart, R.H. 1977 A discus-hulled wave measuring buoy. Ocean Engng. 4, 101-107.

Vesecky, J.F. and Stewart, R.H. 1982 Observations of ocean surface phenomena by the SEASAT synthetic aperture radar--an assessment. J. Geophys. Res. 87, 3397-3430.

Vesecky, J.F., Assal, H.M. and Stewart, R.H. 1981 Remote sensing of the ocean wave height spectrum using synthetic-aperture-radar images in Gower (1981), 449-458.

Vesecky, J.F., Hsiao, H.V., Teague, C.C., Shemdin, O.H. and Pawka, S.S. 1980 Radar observations of waves in the vicinity of islands, J. Geophys. Res. 85, 4977-4986.

Vesecky, J.F., Stewart, R.H., Shuchman, R.A., Assal, H.M., Kasischke, E.S., and Lyden, J.D. 1982 Gravity waves, large-scale surface features and ships observed by SEASAT synthetic aperture radar during the 1978 JASIN experiment. submitted to Boundary Layer Meteorology.

Table 1.

DATE (UT)	TIME (UT)	ORBIT NUMBER	*SURFACE BUOY	SEPARA- TION(km)	DOMINANT		**DOMINANT WAVE		WAVE BEAM-		WAVE VISI-		ϕ^{***} (DEG)	$H_{1/3}$ (m)	U (ms ⁻¹)
					WAVELENGTH (m)	SAR ^{††}	SURFACE	DIRECTION (°T)	WIDTH (deg)	SURFACE	PDR	S/N			
4 AUG.	0615	547	a	0	198	169	263	266	≥ 32(S)	32	3.6	5.3	116	1.7	4.5
4 AUG.	2136	556	a	63	148	149	280	274	≥ 40(S)	54	1.8	1.8	248	1.5	3.5
7 AUG.	0622	590	a	0	--	222/89	229/329	--	--	83/77	0	0	83/183	1.3/1.3	7.2
7 AUG.	2144	599	b(C2)	119	67(S)	71	--	322(S)	≥ 146(S)	--	0	1.1	289†††	1.1	6.9
10 AUG.	0629	633	a	56	--	89/58	220/220	--	--	70/40	0	0	74/74	1.1/1.1	9.2
10 AUG.	2151	642	a	204	--	169	199	--	--	29	0	0	167	2.9	12.9
15 AUG.	2235	714	none	--	182(E)	--	--	276(E)	--	--	1.8	0	242†††	--	--
16 AUG.	0643	719	none	--	160	--	--	275	120(S)	--	1.5	1.6	130†††	--	7.6
18 AUG.	2241	757	b(C4)	0	275(E)	215	--	253(E)	--	--	2.9	0	221†††	4.9	15.2
19 AUG.	0649	762	b(C6)	256	265	206	--	245	33(S)	--	5.1	5.1	100†††	4.4	12.0
	0649	762	b(C2)	266	258	199	--	239	46(S)	--	--	8.4	94†††	4.3	12.0
21 AUG.	0725	791	b(C2)	25	168	132	--	251	75(S)	--	3.4	4.3	104†††	3.0	13.0
24 AUG.	0730	834	a	53	188	149	295	266	76	35	1.8	1.9	149	2.8	10.2
1 SEPT.	2354	958	b(C4)	83	120(E)	108	--	296(E)	--	68	1.6	0	260†††	1.3	7.2
5 SEPT.	0006	1001	a	76	81(E)	63	--	125(E)	--	62	2.5	0	110	2.5	12.6
5 SEPT.	0015	1006	a	120	--	107	--	83	--	61	0	0	299	3.6	6.6
8 SEPT.	0019†	1044	c†	22†	333	301	264	256	25	19	6.0	6.7	229	3.5	11.5
8 SEPT.	0028	1049	c	138	316	301	264	250	21	19	5.2	8.0	117	3.5	6.3
11 SEPT.	0031	1087	none	--	312	--	--	259	48(S)	--	4.2	3.8	224†††	--	13.2

Notes:

a, Atlantic II pitch roll buoy; b, III Wave rider buoys moored in OIA--see Fig. 1; c, Discovery Pitch roll buoy.

triangles use only buoy data, while the solid triangles indicate that a SAR estimate for Φ was used in the absence of buoy data.

Fig. 5. Optical Fourier transform (OFT) of an ocean wave field from orbit 547 near the FIA area of Fig. 1. The photographic display is in the form of a polar plot with wavenumber K measured linearly from the bright central spot. The angular coordinate in the display corresponds to wave direction. Note the 180° ambiguity in direction and the two directional components. The bright radial lines are due to the rectangular aperture used with the lens system.

Fig. 6. Digital Fourier transform (DFT) of an ocean wave field from orbit 547 near the FIA area of Fig. 1. The contour plot is in polar coordinates with the K_x and K_y axes corresponding to the directions shown in Fig. 3. This DFT was computed from a portion of the same image used to form the OFT in Fig. 5. Note the two directional components and the 180° directional ambiguity.

Fig. 7. Comparison of SAR image spectrum (corrected for background fluctuations and SAR point response) $|F_R(K)|^2$ with omnidirectional waveheight and waveslope spectra $\Psi(K)$ and $\Psi'(K)$ as measured by pitch-roll buoy. Both $|F_R(K)|^2$ and $\Psi'(K)$ have been normalized along the ordinate to the peak of $\Psi(K)$.

Fig. 8. Comparison of dominant ocean wavelength as measured by SEASAT SAR and surface buoys. The SAR measurements are biased slightly high with respect to the surface measurements. The average percent difference between the two techniques is 14%.

Fig. 9. Comparison of dominant ocean wave direction as measured by SEASAT SAR and surface pitch-roll buoys. The SAR measurements show no significant bias with respect to the surface measurements. The mean difference between the two measurements is $\pm 12^\circ$. If two JASIN cases involving approximate buoy measurements (labeled * in Table 1) are omitted, the mean difference is reduced to $\pm 10^\circ$.

Fig. 10. Comparison of SEASAT SAR image (S/N) at the peak of the K spectrum with buoy measurements of $H_{1/3}$. The two quantities are correlated with a determination coefficient $R^2 = 0.54$. A linear least mean squares fit to the data is shown by the dotted line. Using the linear fit $H_{1/3}$ could be measured to within ± 1 m using SAR image data. Note, however, that wavelength also correlates with (S/N), though less strongly ($R^2 = 0.40$).

Fig. 11. Comparisons of SAR image spectra (corrected for background fluctuations and SAR point response) $|F_R(K)|^2$ with omnidirectional waveheight and waveslope spectra $\Psi(K)$ (or M_{00}) and $\Psi'(K)$ (or $K^2 M_{00}$) as measured by pitch-roll buoys. Both $|F_R(K)|^2$ and $\Psi'(K)$ have been normalized along the ordinate at the peak of $\Psi(K)$. Note that the peak of $|F_R(K)|^2$ is typically displaced toward smaller K relative to the peak of $\Psi(K)$. Further notice that the slope of $|F_R(K)|^2$ below the peak (smaller K) is typically more steep than the slope of $\Psi(K)$ and that the slope of $|F_R(K)|^2$ above the peak (larger K) is typically less steep than the slope of $\Psi(K)$. These six comparisons are from orbits 556 (a), 762 (b) & (c), 791 (d), 1044 (e), 1049 (f). Further details are given in Table 1. For orbit 762 (b) refers to the upper entry and (c) to the lower entry in Table 1.

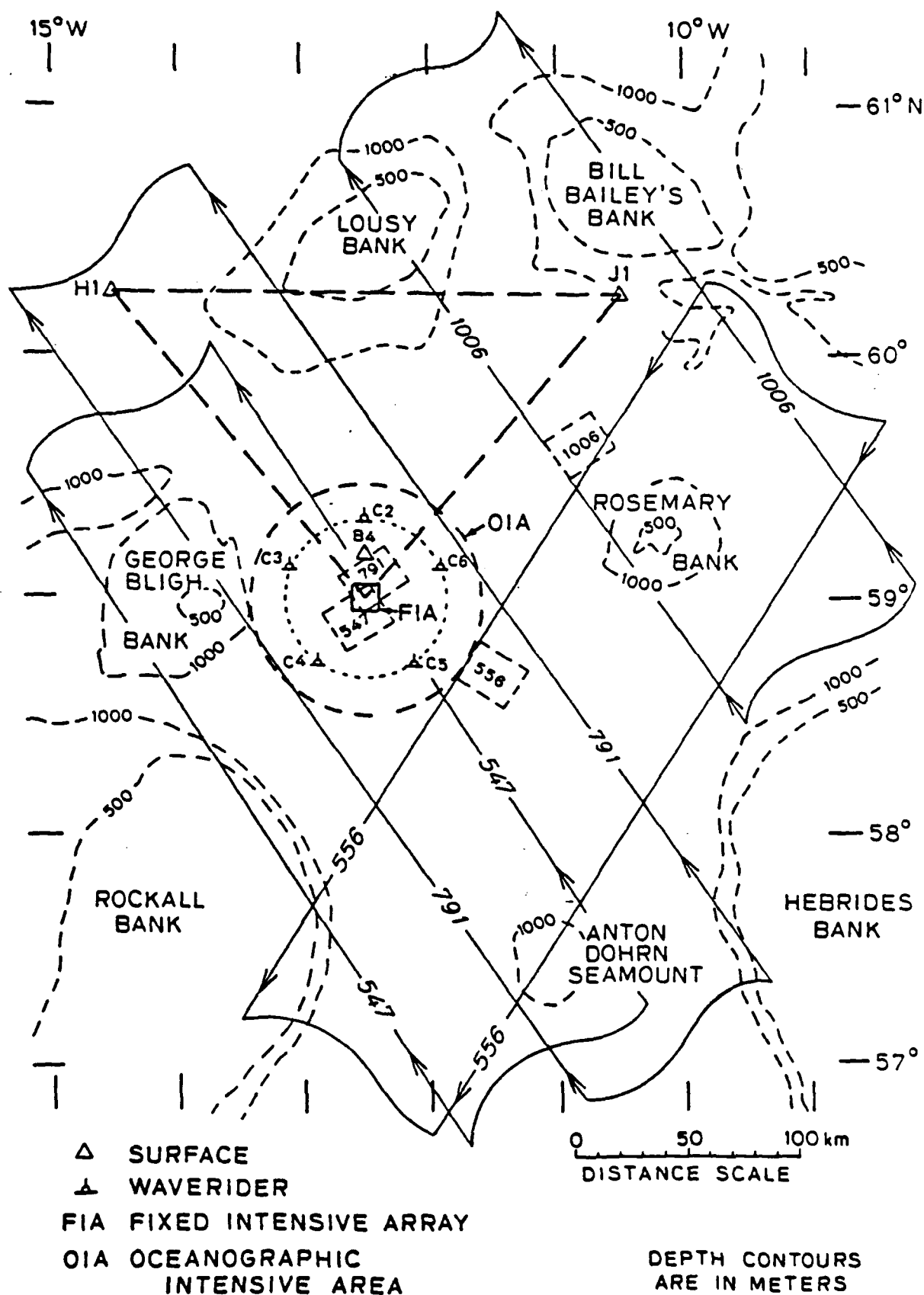


Fig. 1

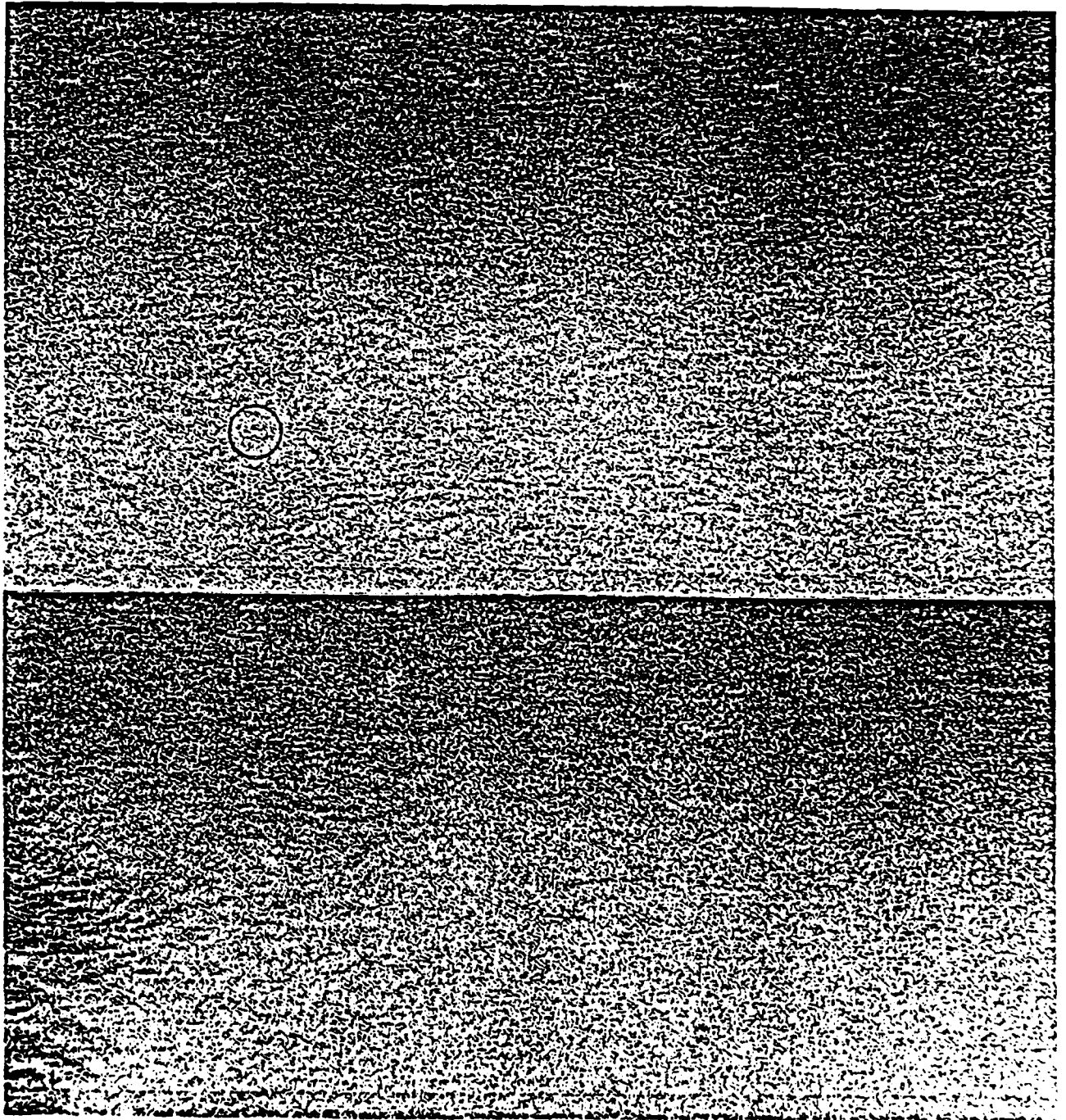


Fig. 2

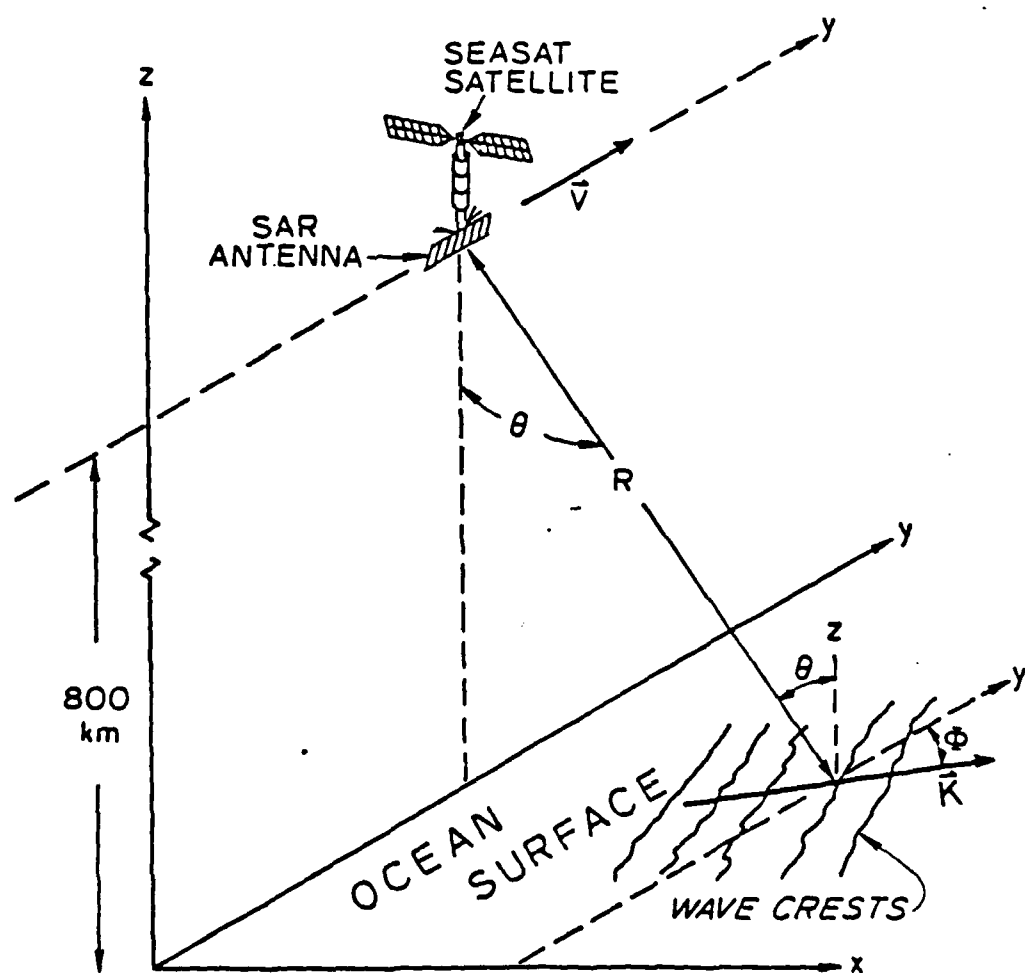


Fig. 3

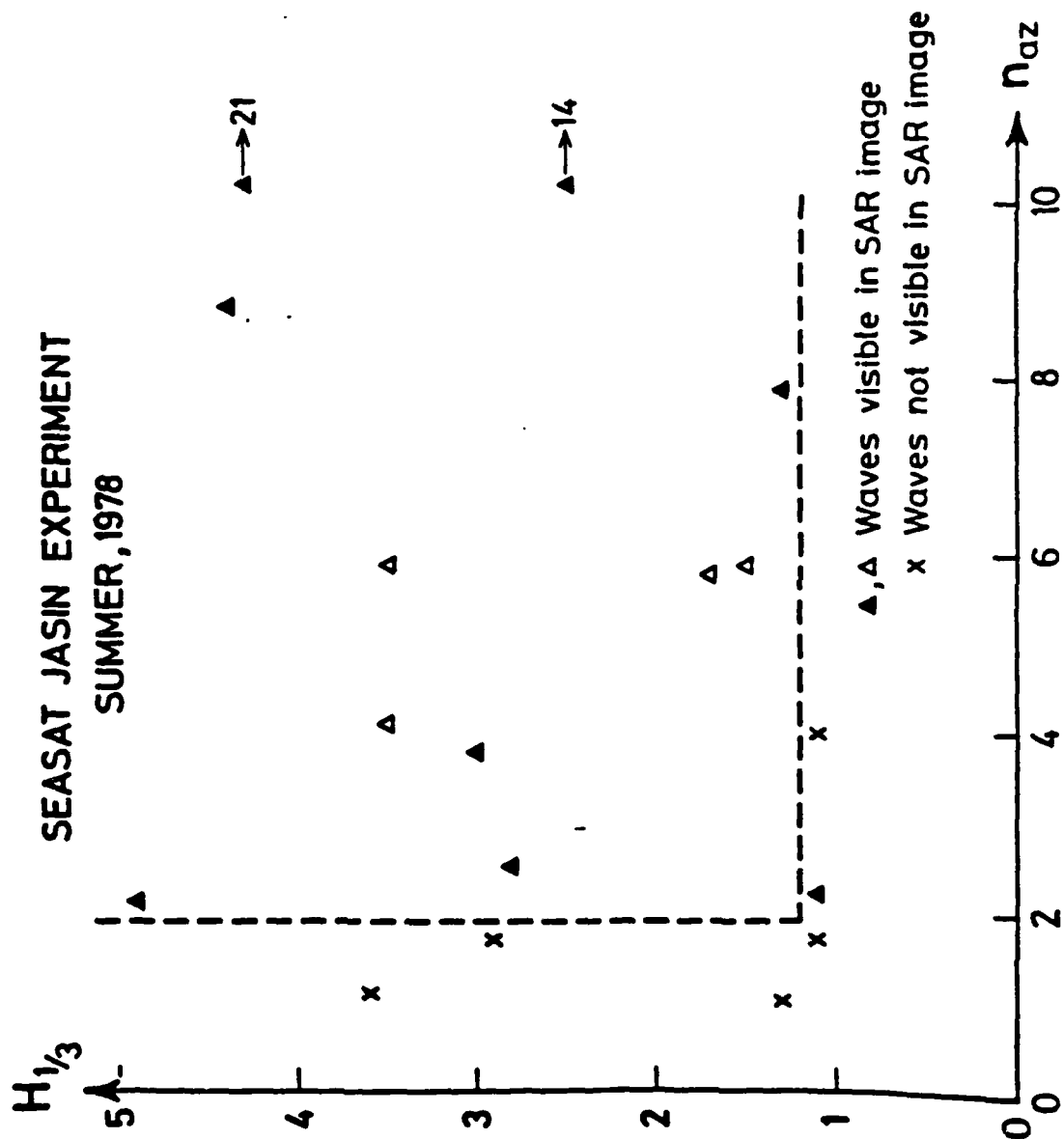
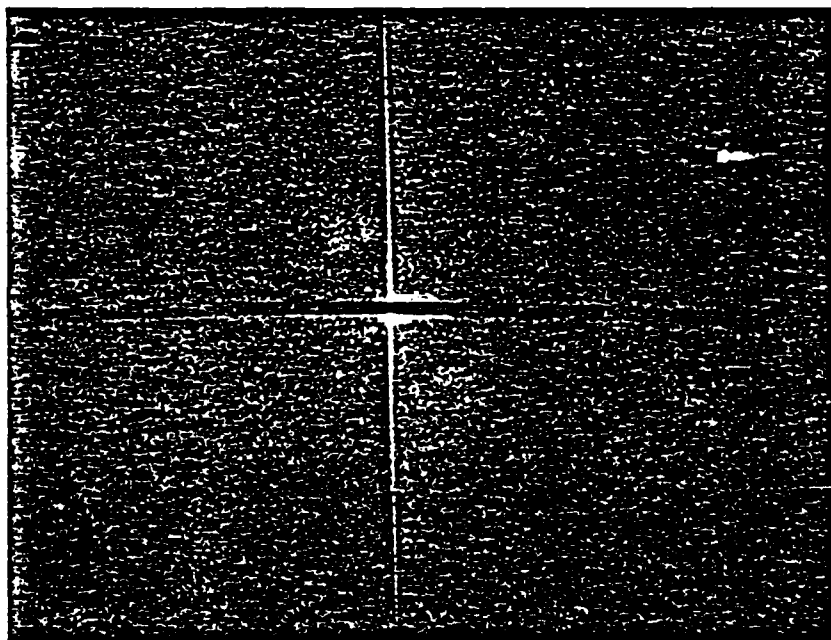


Fig. 4



74344 547 0215 1 sec

Fig. 5

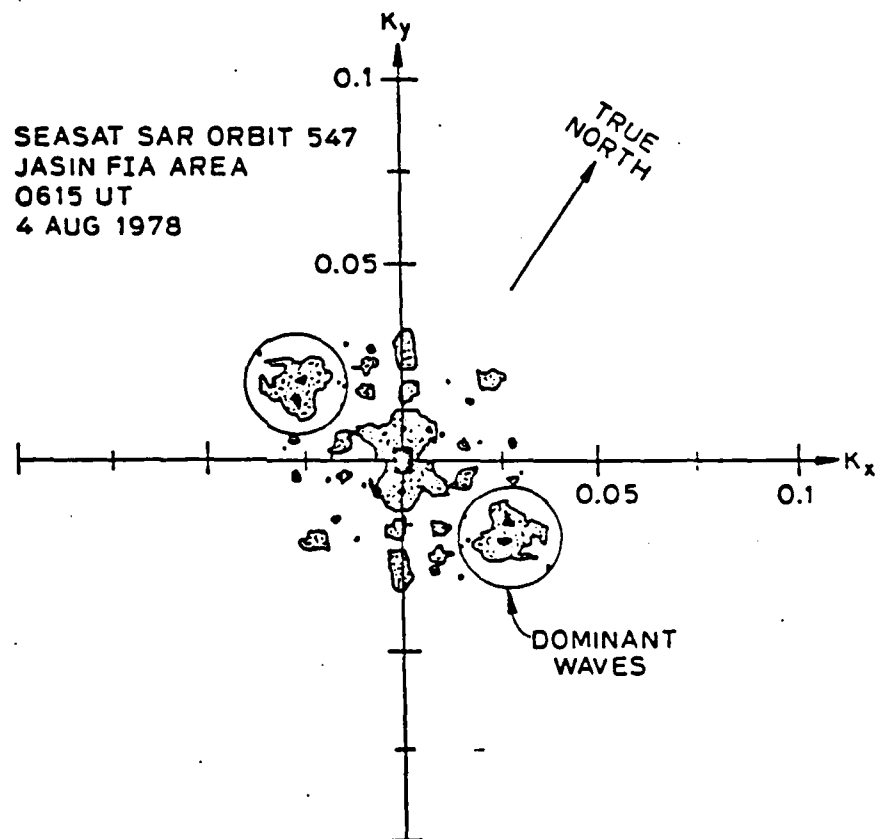


Fig. 6
181

OMNIDIRECTIONAL WAVEHEIGHT
VARIANCE SPECTRUM — m^{-4}

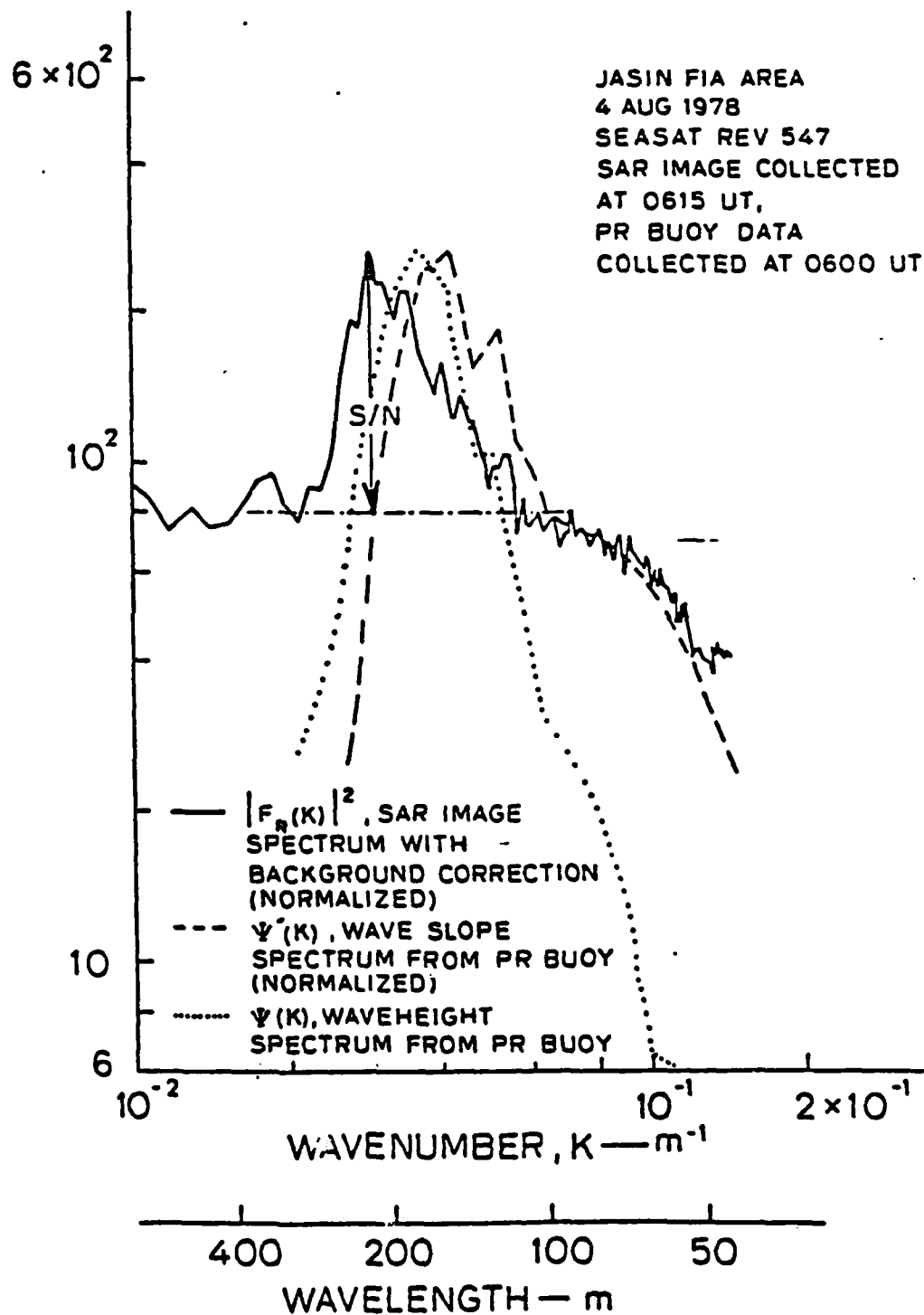


Fig. 7

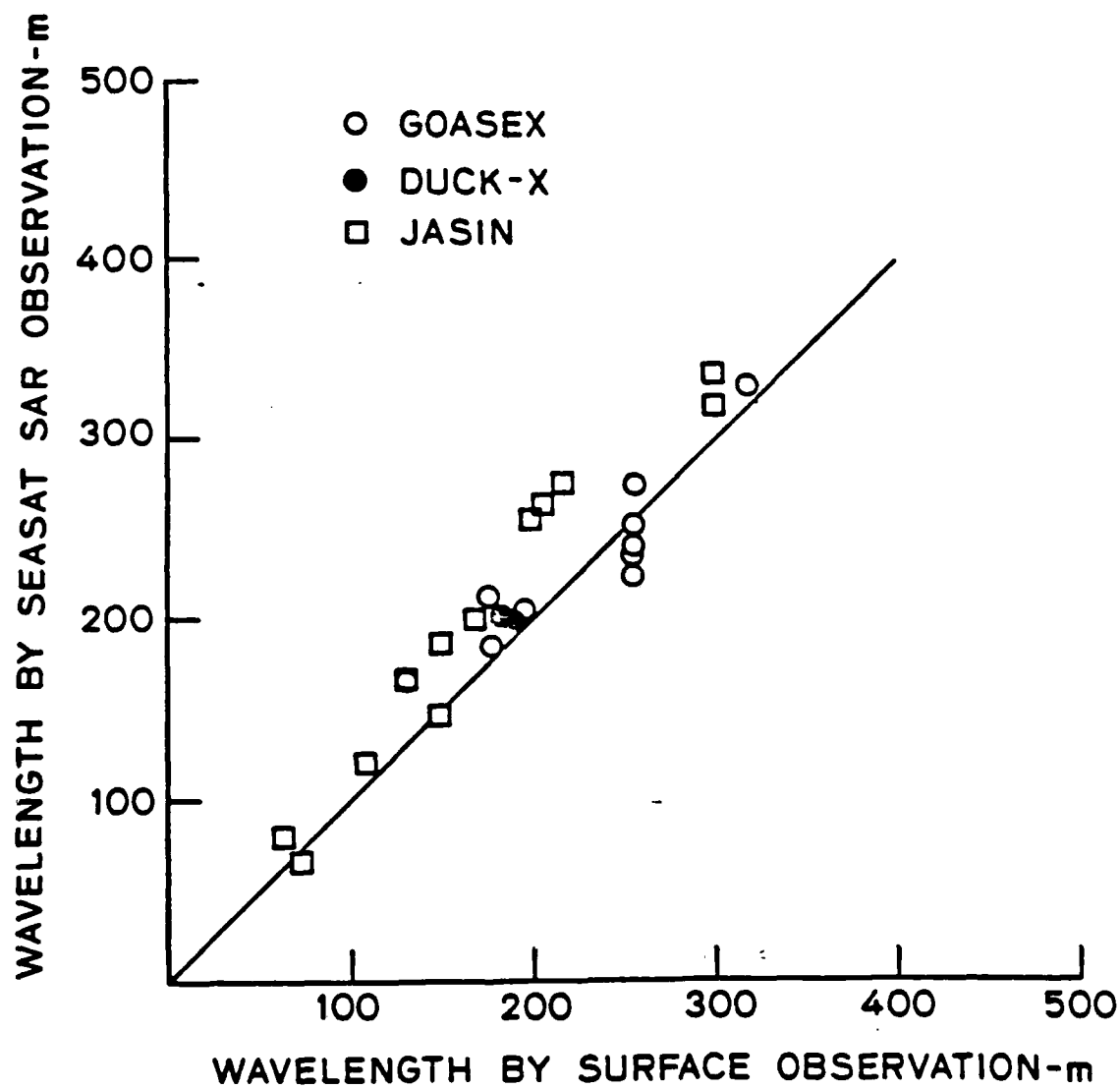
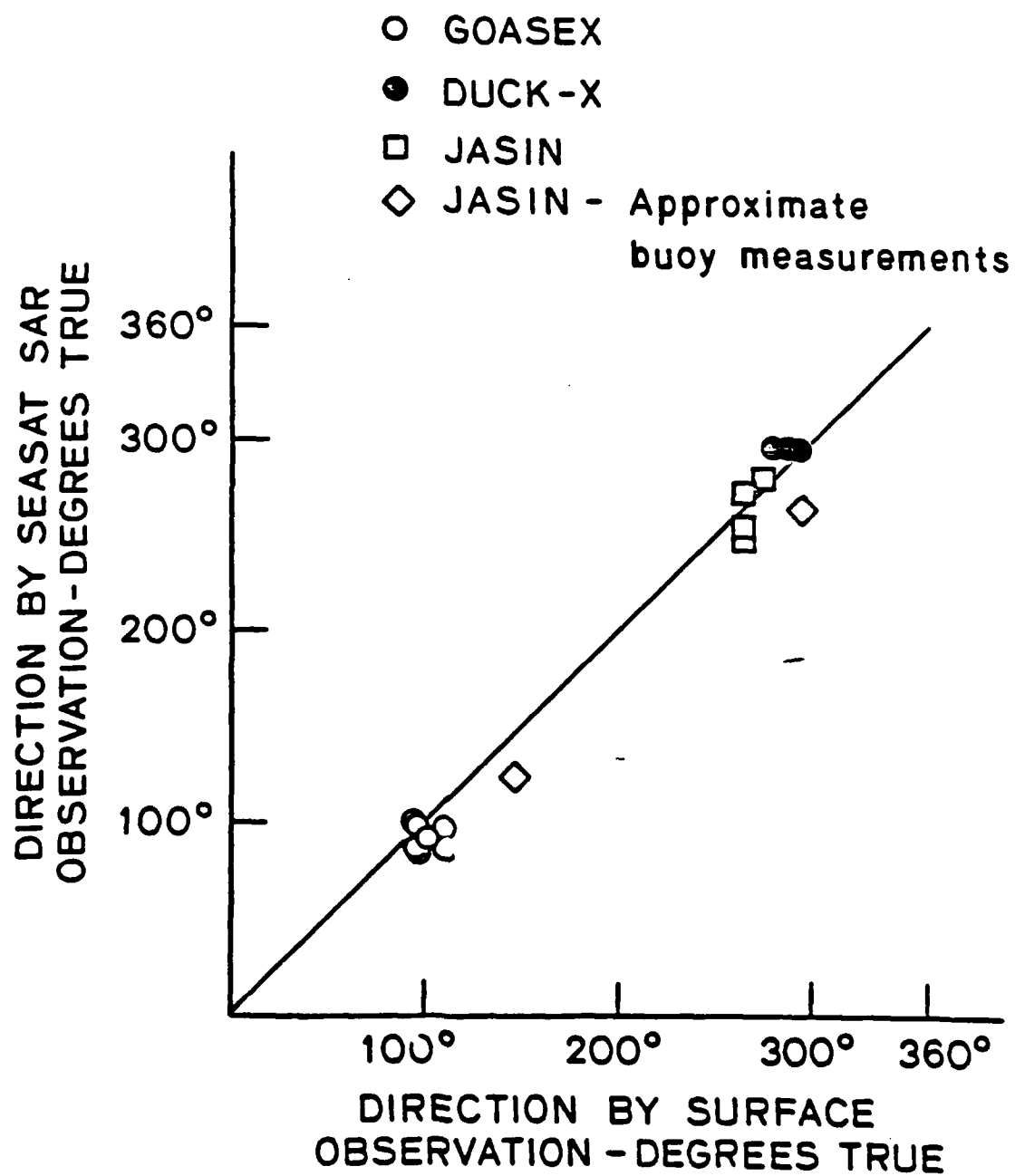


Fig. 8



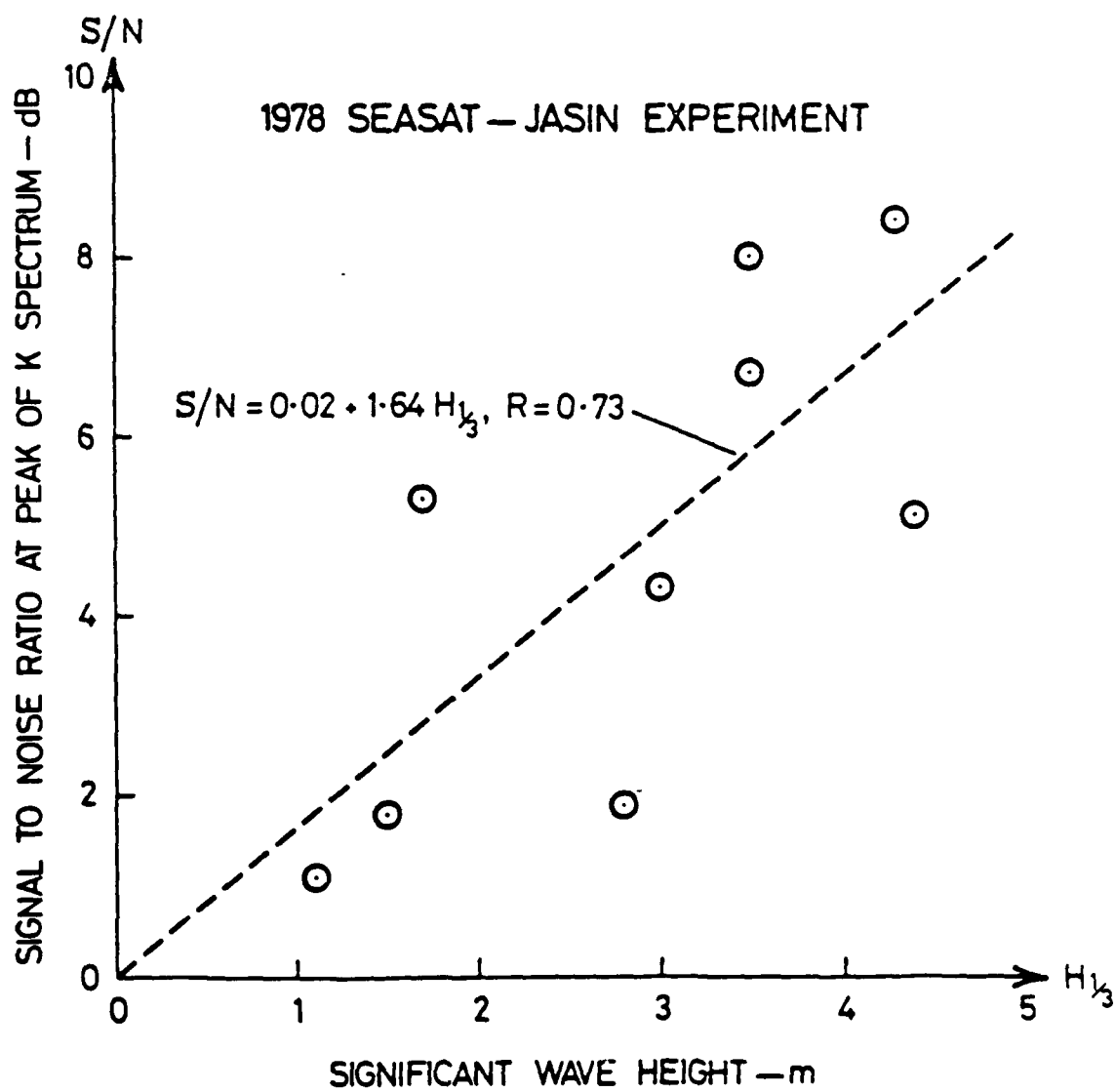


Fig. 10

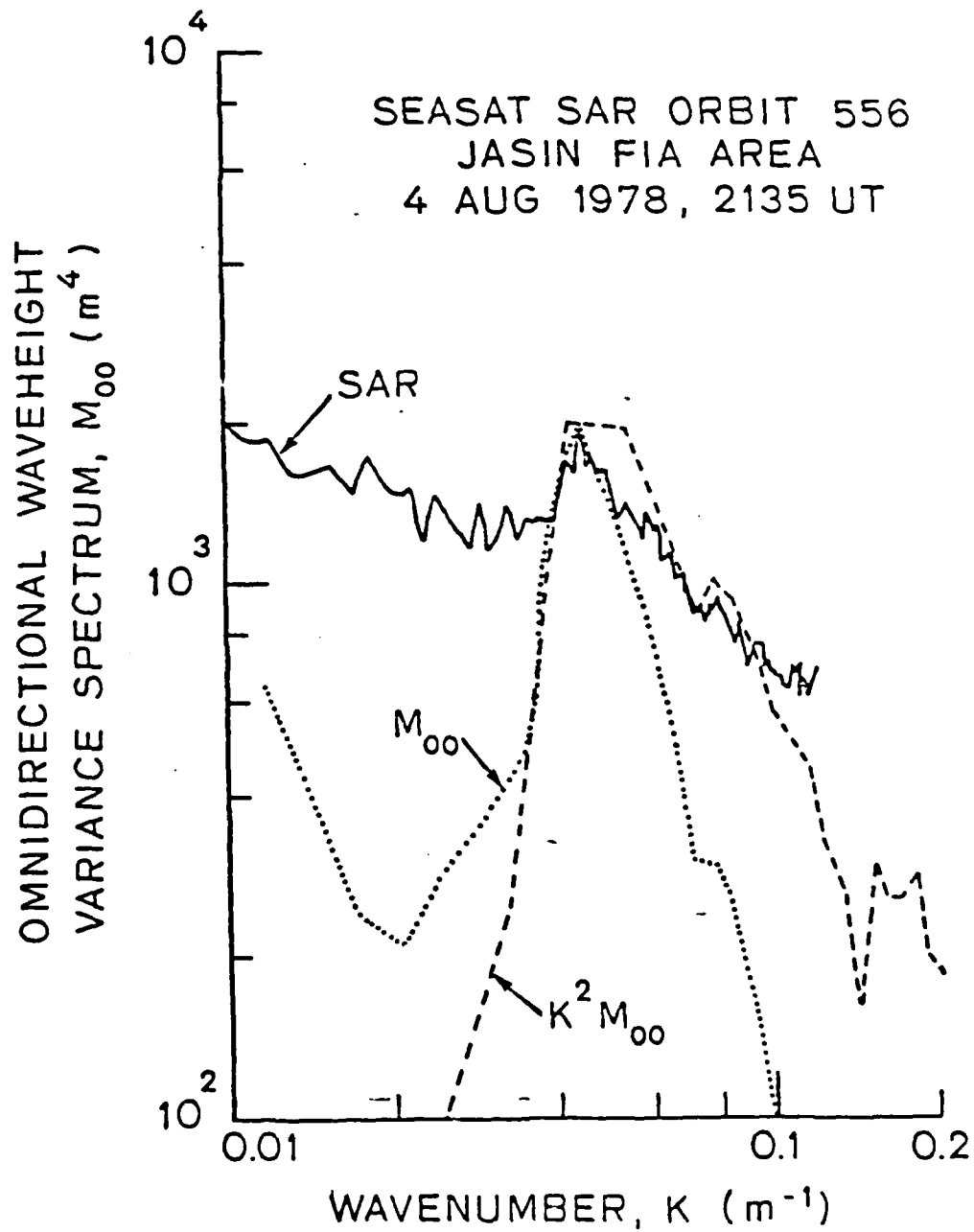


Fig. 11(a)

AD-A140 584

ANALYSIS OF SEASAT SAR IMAGERY COLLECTED DURING THE
JASIN EXPERIMENT(U) ENVIRONMENTAL RESEARCH INST OF
MICHIGAN ANN ARBOR E S KASISCHKE ET AL. MAY 83

3/3

UNCLASSIFIED

ERIM-155900-16-T N00014-81-C-0692

F/G 8/3

NL

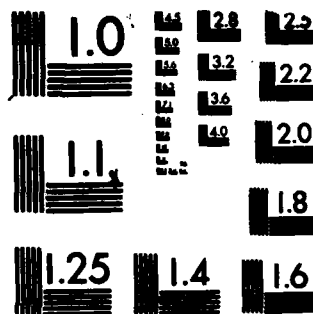


END

DATE

FORMED

0101



MICROCOPY RESOLUTION TEST CHART
NATIONAL BUREAU OF STANDARDS-1963-A

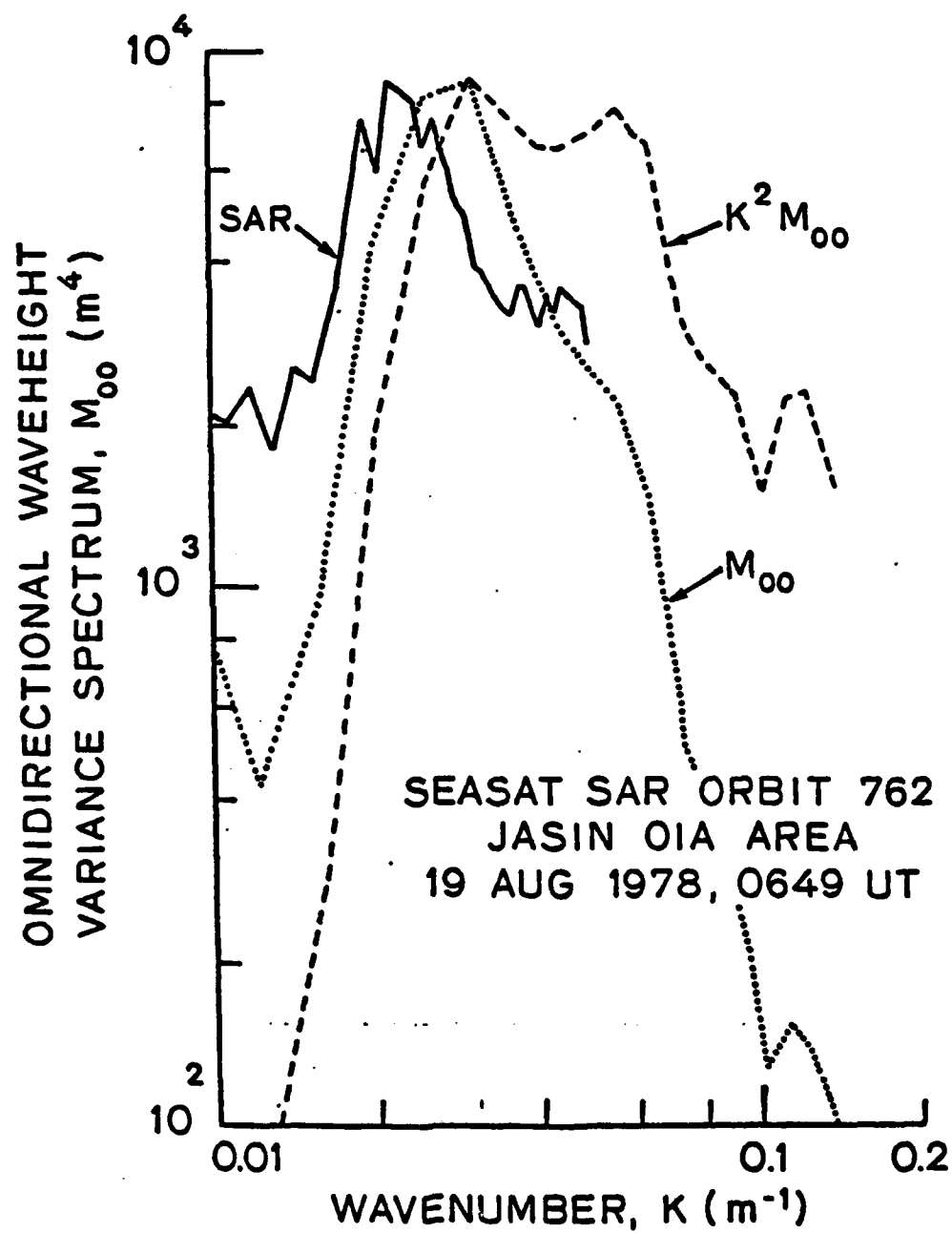


Fig. 11(b)
187

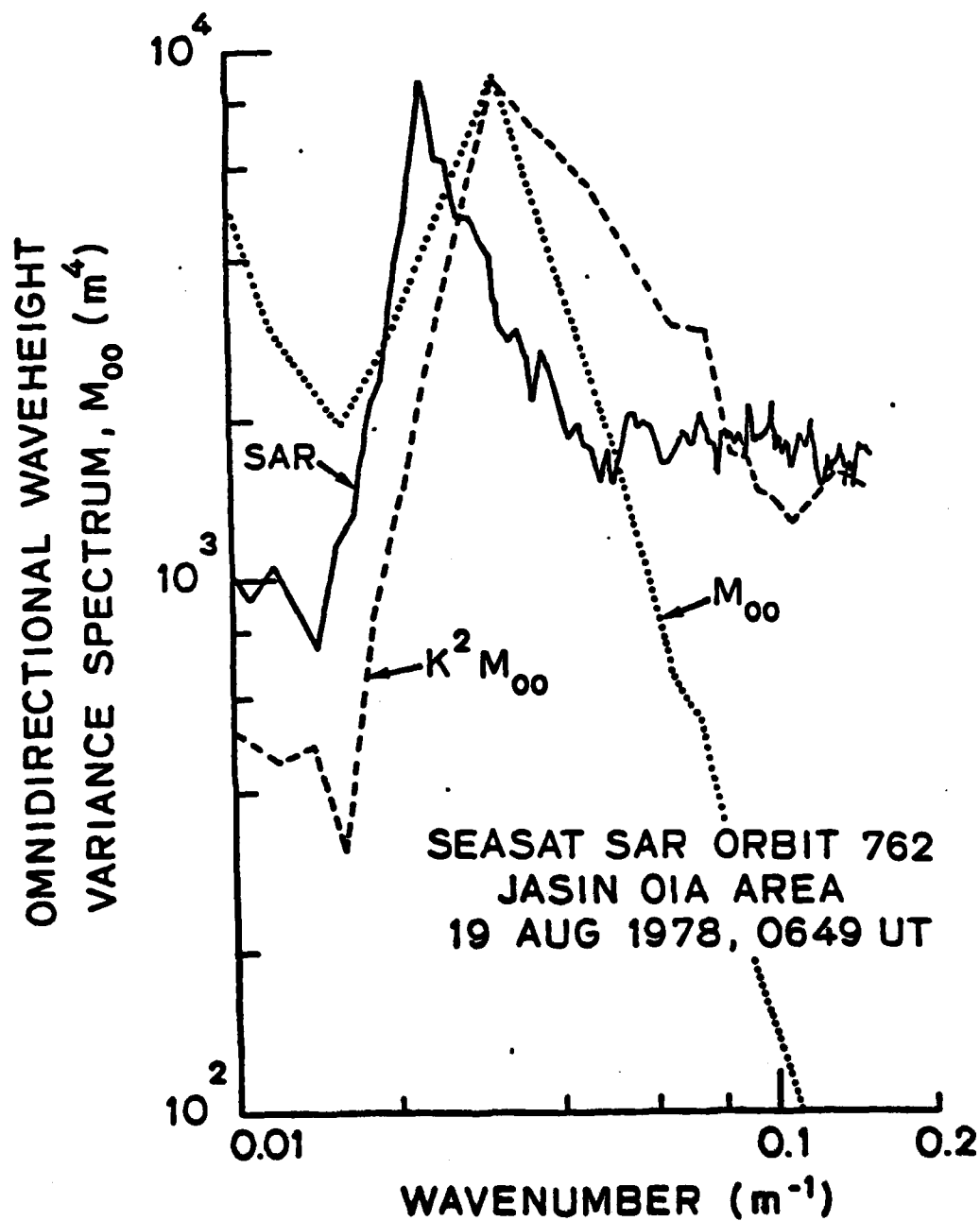


Fig. 11(c)

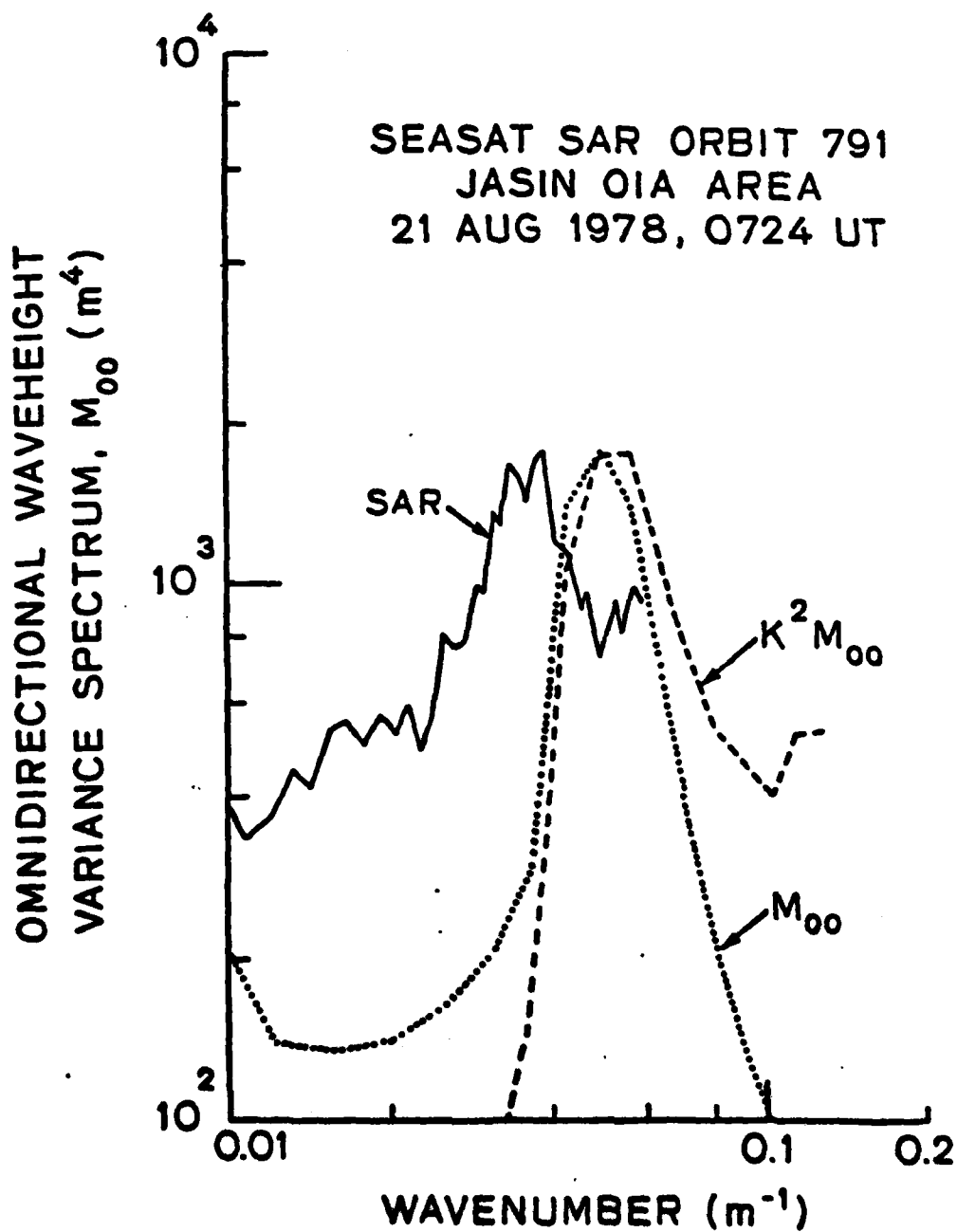


Fig. 11(d)

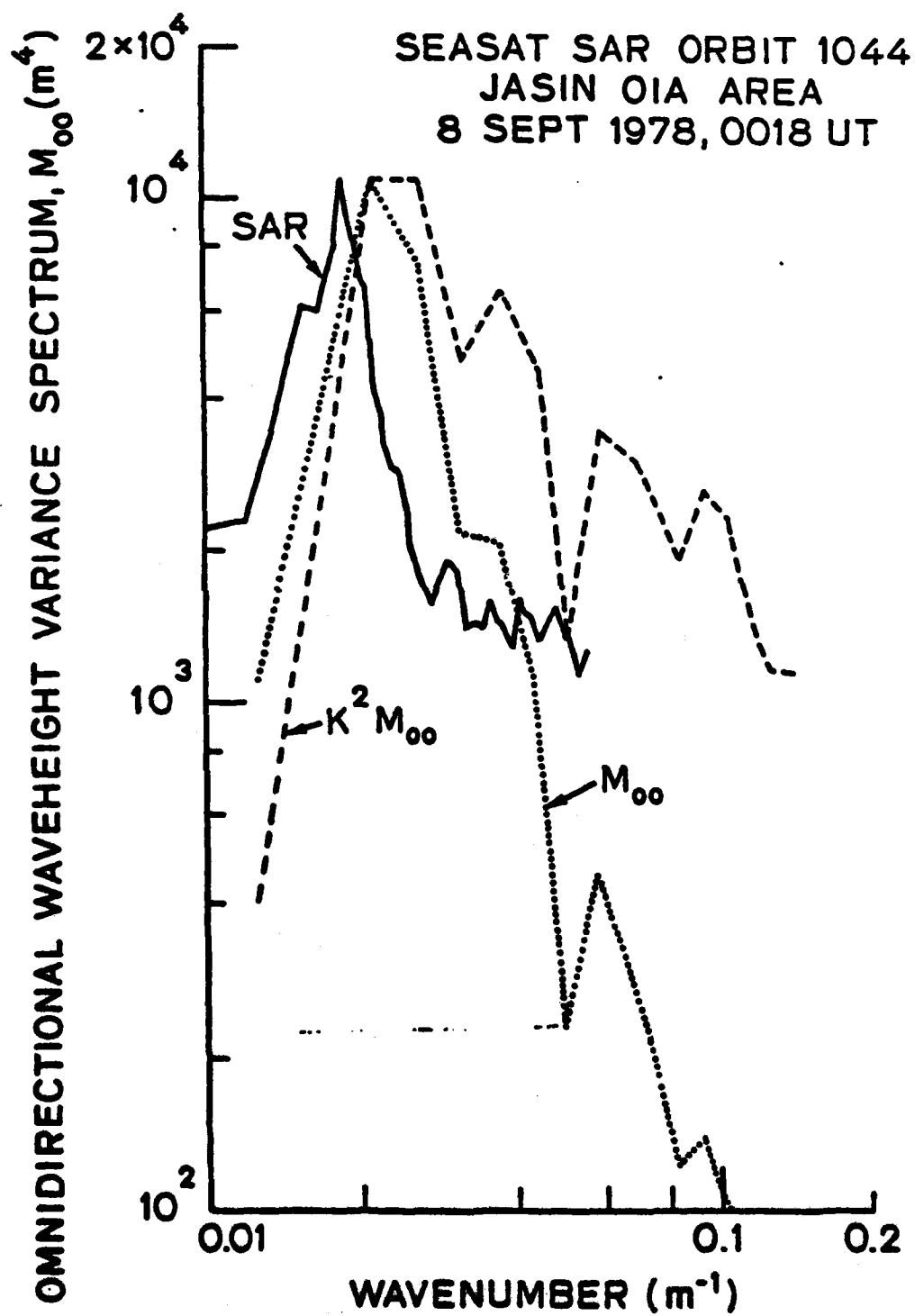


Fig. 11(e)
190

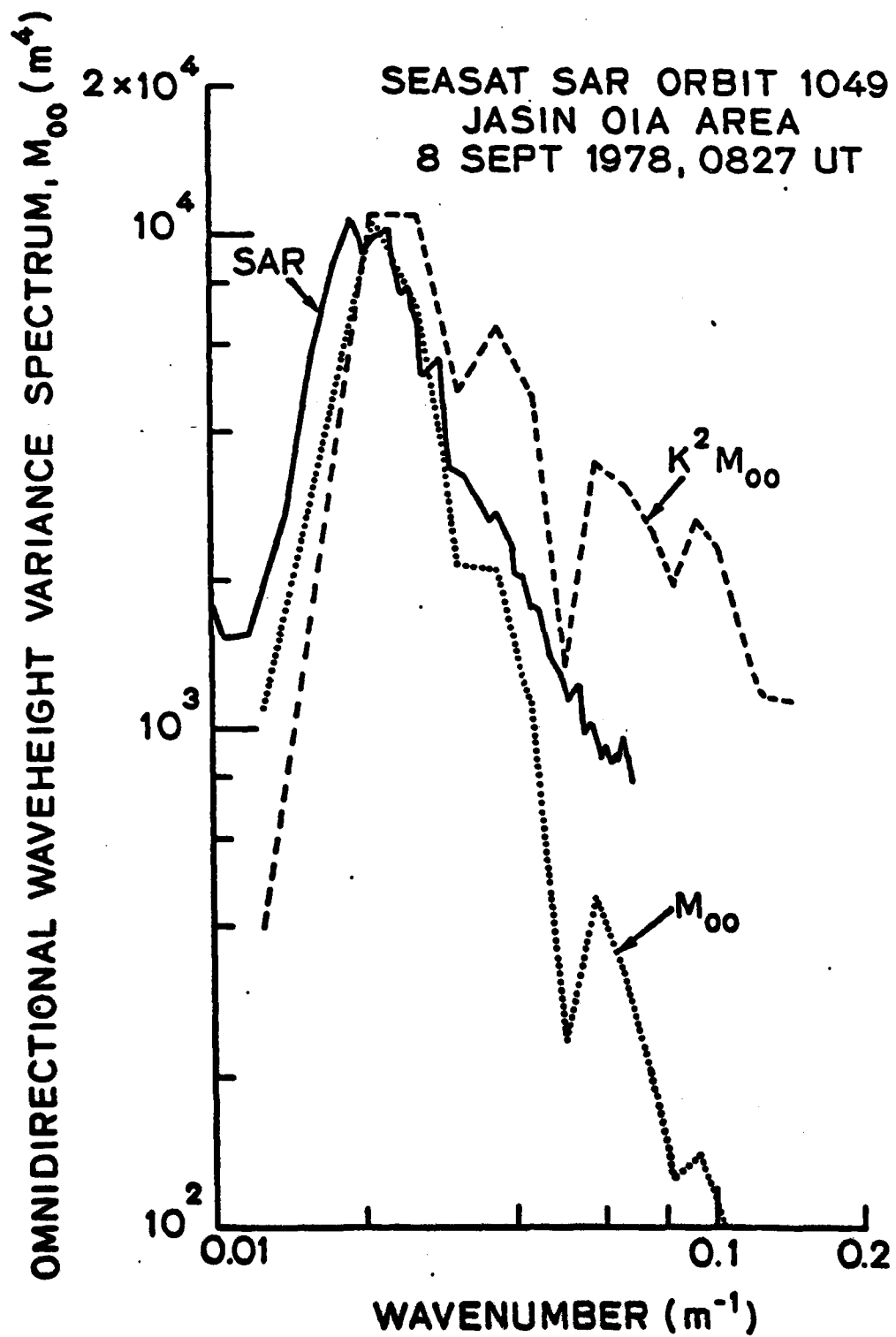


TABLE 3. SUMMARY OF OCCURRENCES OF BOTTOM-RELATED SURFACE PATTERNS ON SEASAT SAR IMAGERY COLLECTED OVER THE NORTHEAST ATLANTIC (CONTINUED)

Bottom Feature Covered by Seasat SAR	SAR Revolution Number	SAR-Observed Pattern	
		Internal Line	Frontal Boundary
North Feni Ridge	547	X	X
	556		X
	990	X	
	633		
	757		
	791	X	X
	834		
	1006	X	X
	1049		X
South Feni Ridge	556	X	
Rosemary Bank	556	X	
	999	X	
	633	X	X
	757		
	834	X	
	1006	X	X
	1049	X	
Iceland Continental Shelf	547		
	990	X	
	633	X	
	719	X	
	762	X	
	791	X	
	834		
Norway Continental Shelf	556	X	
	999		
	757	X	
Oranien Seamount	785	X	
Gettysburg Seamount	738	X	
Anders Seamount	785		
Coral Patch Seamount	785	X	
Porcupine Bank	999	X	
Mid-Atlantic Ridge	642	X	
	556	X	
	999	X	
	642	X	
	714	X	
	757	X	

TABLE 4. SUMMARY OF DETECTIONS OF DEEP WATER TOPOGRAPHIC FEATURES BY SEASAT SAR IMAGERY USING DATA COLLECTED OVER THE NORTHEAST ATLANTIC

Seasat Revolution	Total Number of Deep-Water Bottom Features Covered	Total Number of Occurrences of Internal Lines Over Features	Total Number of Occurrences of Frontal Boundaries Over Features
547	8	6	3
556	11	7	4
990	4	4	0
999	9	6	1
633	6	4	2
642	8	6	3
714	3	3	0
719	7	5	2
757	10	5	1
762	7	7	4
791	4	2	0
791	9	5	4
834	6	3	0
990	5	4	2
1006	5	2	4
1049	6	4	2
1049	6	4	2
1057	8	4	1
1149	2	2	0
1387	3	0	0
1399	1	1	0
Total	120	94	38
Percent		67%	29%

SEASAT-SAR OBSERVATIONS OF SURFACE WAVES, LARGE-SCALE SURFACE FEATURES AND SHIPS DURING THE JASIN EXPERIMENT

J. F. Vesceky and H. M. Assal
Stanford Center for Radar Astronomy, Stanford, CA 94305

R. M. Stewart
Scripps Institution of Oceanography, La Jolla, CA 92038
Jet Propulsion Laboratory, Pasadena, CA 91103

R. M. Shuchman, E. S. Kasischke and J. N. Lyden
Environmental Research Institute of Michigan, Ann Arbor, MI 48107

The SEASAT satellite system, using an onboard 23 cm wavelength synthetic aperture radar (SAR), collected ~ 25 to 40 m resolution radar images of land and ocean. We summarize results from 18 SEASAT SAR passes during the Joint Air-Sea Interaction (JASIN) experiment conducted off the west coast of Scotland in summer 1978. Gravity waves of length ~ 80 to 300 m are often seen in SAR images; however, existing waves are not always seen. We find that waveheight, SAR resolution and wind velocity are important criteria for determining wave visibility. Buoy measurements of $H_{1/3}$ correlate with peak signal to noise ratio in Fourier transforms of SAR images. Although there are significant differences, SAR estimates of omnidirectional waveheight spectra are in rough agreement with buoy spectra. Features resembling internal wave patterns are almost always found over seamounts and at the edge of the continental shelf. Ships and their wakes are often, but not always, detectable in SEASAT SAR images.

Keywords: Radio Oceanography, Remote Sensing, Gravity Waves, Ships, Wakes

1. INTRODUCTION

The synthetic aperture radar (SAR) carried aboard the SEASAT satellite collected radar images of the ocean in 100 km wide swaths ranging in length from about 300 to 3000 km. During the JASIN experiment (June-September, 1978) surface observations of many air and sea parameters were made by ships, buoys and aircraft, e.g. the wind and wave conditions which are of most interest here (Ref.1). During August and September, 1978, 18 SEASAT passes produced SAR imagery of the JASIN area. Examples of such passes are illustrated in Fig. 1. These multiple SEASAT observations coupled with intensive surface measurements provide a unique opportunity to assess the ocean measurement capabilities of satellite synthetic aperture radar.

SAR imagery is capable (under suitable conditions) of sensing a large variety of ocean surface phenomena including long gravity waves (with wavelength, λ , greater than about twice the SAR resolution), winds, surface currents, internal waves, ocean fronts, underwater topography, slicks, and ships and their wakes (Refs. 2,3). The SAR image is basically a high resolution map of the radar

reflecting properties of the ocean surface modified by surface motion effects. Since the dielectric properties of the ocean surface are relatively uniform, variations in surface roughness are primarily responsible for changes in the radar backscatter strength. In particular "resonant" ocean waves with $\lambda \sim 30$ cm interacting with the 23 cm radar waves via a Bragg scatter mechanism produce the dominant radar echo. Because SAR

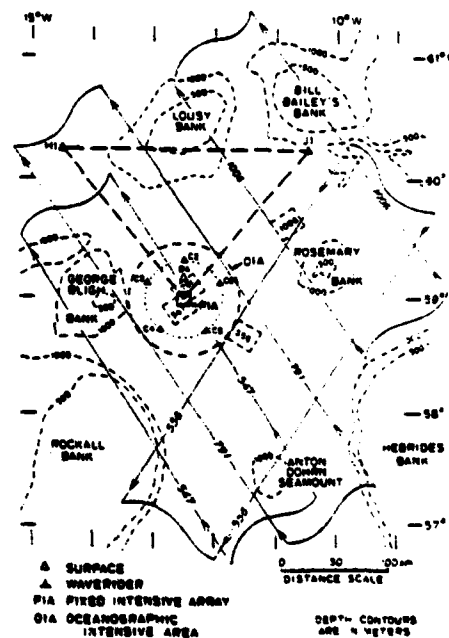


Fig. 1. Joint Air-Sea Interaction (JASIN) experiment area showing typical SEASAT SAR image swaths and sections of images used for wave analysis. Wave rider buoys are denoted by C2, C3, etc. Pitch-roll buoys were generally deployed in the FIA area.

utilizes the phase of the radar echo to achieve high resolution in the direction parallel to the flight path, i.e. to correctly locate the origin of a given echo, motion of the ocean surface can cause echo energy to be misplaced in the image. This misplacement is illustrated in Fig. 4 where a moving ship is displaced from its wake. Spatial modulation of surface roughness and motion (giving rise to Doppler shifts) produces the majority of ocean surface features in SAR imagery. Phillips (4) describes a number of ways in which wind, wave and current variations can modulate decimeter scale surface roughness.

2. GRAVITY WAVE OBSERVATIONS

2.1 Wave Visibility in SAR Images

Although gravity waves of length ~ 80 to 300 m are often seen in SAR imagery, we find that waves observed by surface buoys are not always visible. In our study we have used only imagery optically processed at Jet Propulsion Laboratory (JPL) and Environmental Research Institute of Michigan (ERIM). Study of JASIN data indicates three criteria are important in determining wave visibility: wave height, SAR resolution and wind velocity. Alpers, Ross and Rufenach (5) point out that the orbital velocities associated with surface waves produce a smearing effect on SAR imagery increasing resolution cell size especially along the azimuth direction. (parallel to the SAR flight path). An expression for the degraded resolution cell length Δy^* along the azimuth direction is given in Ref. 5. Knowing Δy^* and the ocean wavelength along the azimuth direction $\lambda_y = \lambda / \cos \theta$, the number of samples per wavelength n_y along the azimuth direction can be calculated. Here θ is the angle between the spacecraft velocity vector V and the ocean wave vector K . The Nyquist sampling criterion demands $n_y > 2$ in order that the waves be adequately sampled. Jain (6) and Vescey et al. (7) have developed wave visibility criteria along these lines. Because of the roles played by waveheight and/or slope in wave imaging mechanisms (Ref. 5) one expects wave visibility to decrease with decreasing significant waveheight $H_{1/3}$ and indeed we find waves are seldom imaged for $H_{1/3} \leq 1$ m. Applying these two criteria $n_y \geq 2$ and $H_{1/3} \geq 1$ m to the JASIN data set we found only one case out of 15 in which these criteria did not work--nine cases where waves were visible in SAR images and six when waves were not observed in SAR images. All ocean wave data were drawn from buoy measurements.

Since wind raises the 35 cm ocean waves which the radar senses, one expects reduced wave visibility at low wind speeds. During the SEASAT-JASIN experiment waves were detectable over a range of wind speeds of from 3.5 to 15.2 m/s while for wind speeds of from 6.6 to 12.9 m/s waves were not detected. It is thus apparent that wind speed was not a factor during the SEASAT-JASIN experiment mainly because wind speeds were always above 3.5 m/s.

2.2 Comparisons of SAR and Buoy Estimates of Wave Characteristics

2.2.1 Wave Measurement Method. The wave measurements from SAR imagery made here are based on a simple assumption, to wit, that fluctuations in SAR image intensity $I(x,y)$ are proportional to ocean wave height fluctuations. The (x,y) plane

is the plane of the average ocean surface. Under this assumption the directional ocean waveheight spectrum $\eta(K,\theta)$ is simply proportional to the magnitude squared of the two-dimensional Fourier transform of the intensity fluctuations, namely $|F\{I(x,y)\}|^2$. Here K is 2π divided by the ocean wavelength and θ is direction in the (x,y) plane (θ is usually degrees clockwise from true north). As will become clear below, this assumption is not precisely correct. However, it is apparently not far wrong (Ref. 8) and provides a convenient working hypothesis. Although this algorithm is straight-forward, there are numerous variations to its implementation. Here we have used optically imaged data produced at the Jet Propulsion Laboratory (JPL) and at the Environmental Research Institute of Michigan (ERIM). Once the imagery is Fourier transformed, estimates of the dominant wavelength and direction can be made on the basis of our assumption by simply finding the peak of $|F\{I\}|^2$ and noting the location in terms of wave-number K and direction θ . The 180° ambiguity in θ can be resolved by special focussing measurements during the optical imaging process. Vescey et al. (7) note that the peak signal to noise power ratio (S/N) in the Fourier transform of a SAR image is correlated ($r = 0.8$) with significant waveheight $H_{1/3}$. Peak S/N is estimated in Fig. 2 by noting the level regions in $|F\{I\}|^2$ at very low ($K \leq 0.015 \text{ m}^{-1}$) and very high ($K \geq 0.05 \text{ m}^{-1}$) wave-numbers and averaging the two levels to obtain a background noise level. With this method $H_{1/3}$ can probably be measured to $\pm 3/4$ m using this correlation.

2.2.2 SAR and Buoy Estimates of Dominant Wavelength and Direction. Eleven estimates by SAR and surface buoys during the JASIN experiment were compared. The average distance between the center of the SAR image and the buoy was ~ 67 km with a range of 0 to 146 km. The average percent difference in wavelength was 15% with a consistent bias of SAR estimates toward longer wavelengths by about 10%. Six SAR and buoy estimates of dominant wave direction were compared with an average error of 13° . However, two pitch-roll buoy estimates were only approximate due to compass problems. If we exclude these two approximate estimates, the average error was only 7° . There was no bias relative to the range direction, i.e. perpendicular to the subsatellite track.

2.2.3 SAR and Buoy Estimates of Omnidirectional Waveheight Spectrum. During the JASIN experiment estimates of the omnidirectional wave height spectrum M_{00} from buoys and from SAR images were compared in seven cases. Fig. 2 shows a typical example of these comparisons. The buoy estimates were computed by standard methods (Ref. 9) while the SAR estimates are simply $|F\{I\}|^2 = |F(K,\theta)|^2$ averaged over a 30° angular sector around the dominant wave direction and normalized along the ordinate to the peak of M_{00} from buoy measurements. No normalization was done along the abscissa. Since in these cases there is only a single dominant wave direction, data from directions away from the dominant wave direction contains only background fluctuations; its inclusion would only serve to raise the noise level in the SAR estimate of M_{00} .

2.2.4 Differences Between SAR and Buoy Estimates of M_{00} and their Explanation by Image Formation Theory. Fig. 7 illustrates a number of features which are typical of comparisons between SAR image intensity spectra $|F(K)|^2$ and buoy measurements of ocean wave height and wave slope spectra, $K^4 M_{00}$. The peak of the SAR spectrum is ~ 3 times the background indicated by the horizontal line. Typically this would correspond to $M_{00}/3 \sim 3$ m. The peak of $|F(K)|^2$ corresponds to a wavelength some 10% above the wavelength of the peak M_{00} and 20% above the wavelength of the peak $K^4 M_{00}$ measured by surface buoys. The shape of the SAR spectrum corresponds most closely with the waveheight spectrum. However, at wavenumbers above the peak, the slope of the SAR spectrum $\sim K^{-2.3}$ is closer to the slope of the wave slope spectrum $\sim K^{-1.7}$ than to that of the waveheight spectrum $\sim K^{-3.7}$. This behavior of the slope corresponds roughly to the

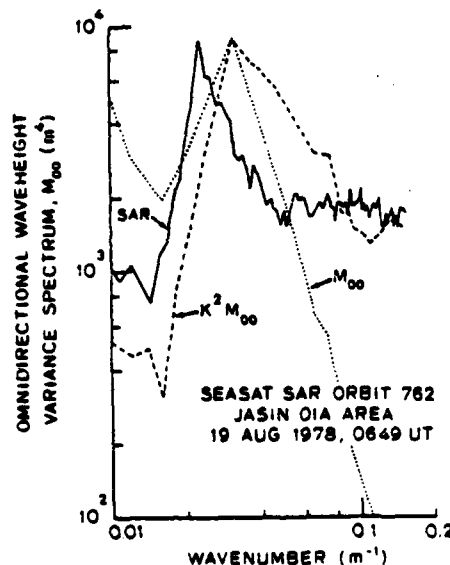


Fig. 7. Comparison of SAR image spectra (corrected for background fluctuations and SAR point response) with omnidirectional waveheight and wave slope spectra ($M_{00}(K)$ and $K^4 M_{00}$ respectively) measured by moored wave rider buoy C2 in Fig. 1. Both the SAR spectrum and $K^4 M_{00}$ have been normalized along the ordinate at the peak of M_{00} . The SAR and buoy measurements were separated by some 260 km along the surface and some 8 hours in time, but under stable conditions (Aug. 18 and 19, 1978). This comparison is used here because it illustrates typical features in well. Note that the peak of the SAR spectrum is displaced toward smaller K with respect to the peaks of both M_{00} and $K^4 M_{00}$. Further notice that the slope of the SAR spectrum below the peak (smaller K) is more steep than the slope of M_{00} and that the slope of the SAR spectrum above the peak (larger K) is less steep than the slope of M_{00} .

theory discussed by Albers et al. (6) where they predict that the SAR spectrum slope should be $\sim K^{-1.7}$ to $K^{-1.9}$ where the waveheight spectrum slope is $\sim K^{-3.7}$. This theory also predicts the bias of the SAR estimate of the peak of M_{00} toward longer wavelengths which we observe.

3. LARGE-SCALE FEATURES DURING THE SEASAT-JASIN EXPERIMENT

3.1 Persistence of Large-Scale Features

One of the great advantages of SAR imagery as a remote sensing tool is that surface morphology can be examined over large areas (100's to 1000's of km) in virtually a snap shot fashion. SAR images of the ocean often show features, 1 to 50 km in extent which appear to be internal waves, oceanic fronts, slicks and spatial variability (mottiness) of wind speed. Various examples off the U.S. east coast are given by Real et al. (7). Visual examination of SEASAT SAR imagery (1:1,000,000 scale) collected over the JASIN experiment area revealed a number of interesting characteristics.

When the same area was imaged twice within a relatively short period, no bold large scale features were found to persist over time scales of 8 hours (4 image pairs) and 15 hours (3 image pairs). Since the image pairs could not be precisely aligned, small weak features could have persisted, but been overlooked. In four cases land at some point could be used to register the images to within a few kilometers. In the other three no land was present in the imagery and superposition was less accurate. The 4 orbits which produced these pairs of images did not have parallel ground tracks and so the boundaries of the image swaths intersect with angles of about 110°. Fig. 1 contains an example involving orbits 547 & 556. Thus the viewing geometry differs considerably between the two images in a pair. From these observations we conclude that either the features were not persistent and hence not oceanic in origin or that the conditions for sensing the phenomenon did not persist.

3.2 Internal Wave Features

Features resembling the internal wave patterns of LANDSAT visual imagery (Ref. 10) were almost always found over seamounts and at the edge of the continental shelf. The patterns are ephemeral probably depending on the stage of the tide. Fig. 3 illustrates such patterns occurring over the steep bathymetric gradients associated with the Wyville-Thomson Ridge near 60° 20' N, 25° W. Depths range from ~ 100 to 500 m in this region.

3.3 Wind Poll Vortices

In imagery from orbit 1006, rows of streaks separated by either 1.2 or 2.6 km are seen over an area of at least 100 x 200 km. These streaks are aligned along the wind direction where the wind speed was approximately 12 m/s. Assuming that these changes in SAR image brightness over a large area were due to changes in wind velocity a reasonable assumption, viz. Ref. 11 we conclude that this is the first clear observation of poll vortices in the surface boundary layer over the ocean.

Copy available to DTIC does not permit fully legible reproduction

3.4 Damping of 30 cm Surface Waves by Rain

On orbit 556 an area roughly 50 km in size appeared very dark (very low radar reflectivity). Several sources of data including ship logs, infrared satellite imagery and weather synopses indicated that thunderstorms were likely. We conclude that rain in this area probably smoothed the sea on scale sizes of ~30 cm (to which the radar signal is sensitive) thus causing the dark feature seen in the imagery.

4. SHIPS

A perusal of SEASAT SAR imagery (e.g. see Ref. 2 or Fig. 4) reveals many images of stationary ships as well as moving ships with their attendant wakes, which can extend ~20 km. In only a few cases have searches been made for ships with known positions. We have searched for oceanographic ships involved in the JASIN experiment on orbits 547 and 590 using imagery which was optically processed at JPL. The ships involved and their approximate lengths are: R.V. Atlantis II (66 m), M.V. Gardline Endurer (53 m), R.V. Meteor (82 m) and H.R. M.S. Tydeman (89 m). The ship locations in latitude and longitude at the times

of SEASAT SAR imagery are known to an accuracy of a few km or less. Without special processing we are usually able to locate points in SEASAT imagery to within about 5 km. Allowing an additional 10 km for unknown systematic error, we expect to find ship images within 15 km of their estimated position in the imagery.

On orbit 547 only the Atlantis II was within the SAR swath and a ship image was found 12 km from the estimated position of the image. None of the other JASIN ships mentioned above were within the SAR swath and no other ship images were found within ± 100 km along the same 25 km wide sub-swath. Near the Atlantis II position the dominant swell was of wavelength $\lambda \sim 170$ m out of 25° true with $H_{1/3} \sim 1.6$ m while the wind was out of 15° at 3.6 m/s.

On orbit 590 all four ships were within the SAR swath. However, only the largest ship (H.R. M.S. Tydeman) can even be tentatively identified -- a weak target some 7 km from the estimated position. Near the positions of all the ships, save the Gardline Endurer, the dominant swell was $\lambda \sim 222$ m out of 250° true with $H_{1/3} \sim 1.2$ m while the wind was out of 10° at 6.6 m/s. At the position of the Gardline Endurer some 180 km to the NW the wave conditions were approximately the same while the wind speed was 5.2 m/s.

This evidence, taken with an unsuccessful search for the R.V. Oceanographer during the GOASFX experiment, leads us to conclude that images of stationary or slowly moving ships (no significant wakes) are difficult or impossible to trace in SEASAT imagery (optically processed at JPL) for moderate seas and wind velocities greater than about 3.5 m/s. Thus such SAR imagery cannot be routinely used to determine ship positions as an aid to performing research at sea. We emphasize that the imagery used in these searches was the standard 'production run' data product. Improvements in resolution and focussing by either specialized optical or digital imaging would presumably improve detection performance. Fig. 3 is an example of high quality digitally processed imagery. Many ships are evident. The wakes of faster moving ships make them more evident. It is interesting to note that a group of four ships just to the lower right of center are imaged to the left of their wakes. Vesceky and Stewart (12) point out that this displacement (which is simply a result of ship movement relative to the average ocean surface) can be used to measure ship velocity. A ship having a velocity component v_x perpendicular to the satellite ground track causes the ship to be displaced a distance $d = v_x/V$ parallel to the satellite velocity vector V , but in an opposite direction, where x is the perpendicular distance from the satellite surface track to the ship location. In Fig. 4 the satellite surface track is parallel to the top of the image and runs left to right some 240 km above the top of the image. Knowing $V = 7180$ m/s, $d = 330$ m and $x = 272,000$ m for the ship nearest the bottom in the group to the lower right of center we find $v_x = 8.7$ m/s. From the ship's wake we see that it is moving very nearly along the x-direction so that its speed is ~18 kts--a reasonable value.

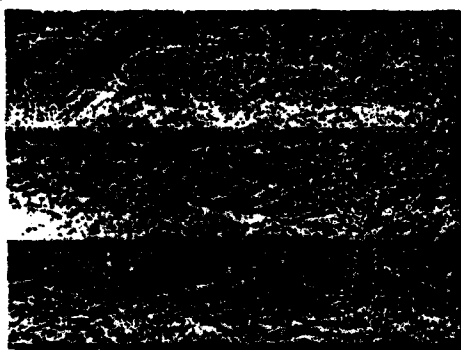


Fig. 3. SEASAT SAR image from orbit 782 near 0648:39 UT on Aug. 19, 1978. The small white dots are about 7.2 km apart. We interpret the wave packets, most prominent at center and lower left center, as surface roughness modulation associated with the surface current divergence produced by internal waves. The region imaged is centered over the steep bathymetric gradients of the Myville-Thomson Ridge near $40^\circ 20' N$ and $8^\circ 15' W$. Lengths are ~100 km.

The small white dots are the result of the bathymetric gradient below. The arrow below the image indicates true north and the image was optically processed at the Jet Propulsion Laboratory.



Fig. 4. SEASAT SAR image from orbit 762 near 0646 UT on Aug. 19, 1978. Vertically upward in the figure is along direction 241° true. The coast line shown extends from Calais (bright region at top left) to Dunkerque (bright region along coast at lower left). Surface roughness variations associated with bathymetric features in the Straits of Dover cause linear and curved features in the SAR image especially at lower left and upwards along the coast. At lower right center a group of several ships and their wakes are visible. Note that the ships are displaced from their wakes during the SAR imaging process because of the ship velocity (~ 10 m/s) with respect to the average surface. This image was digitally processed at the Norwegian Defense Research Establishment.

ACKNOWLEDGEMENTS

We gratefully acknowledge Herbert Carlson of the Deutsches Hydrographisches Institut and Trevor Guymer and David Webb of the Institution of Oceanographic Sciences (IOOS), U.K., for supplying wind and wave data collected during the JASIN experiment. Bernhard Gravdal of the Norwegian Defense Research Establishment kindly provided the digitally processed image of Fig. 4. Kurt Graf, Dennis Douglas and Dennis Tremaine at SRI International provided valuable help by digitizing the JPL imagery. We also thank Harriet Smith, Martha Smith and Sara Zientek for help in preparing the manuscript. The authors gratefully acknowledge financial support from the Office of Naval Research (Physical Oceanography Branch), the National Oceanic and Atmospheric Administration (Ocean Sciences Branch) and the National Aeronautics and Space Administration.

REFERENCES

1. Pollard, R. T. (Coordinator) 1979. Air-Sea Interaction Project: Summary of the 1979 Field Experiment. London, The Royal Society.
2. Real, P. C. et al. (Eds) 1991. Spaceborne Synthetic Aperture Radar for Oceanography. Baltimore, Johns Hopkins University Press.
3. Gower, G. F. R. (Ed) 1991. Oceanography from Space. NY, Plenum.
4. Phillips, G. W. 1981. The structure of short gravity waves on the ocean surface. In (Ref. 2), 24-31.
5. Alpers, W. R. et al. 1981. On the detectability of ocean surface waves by real and synthetic aperture radar. J. Geophys. Res., 86, 6421-6437.
6. Jain, I. 1978. Focusing effects in the synthetic aperture radar imaging of ocean waves. Appl. Phys., 15, 323-332.
7. Vesecky, J. F. et al. 1992. On the ability of synthetic aperture radar to measure ocean waves. accepted for publication in Proceedings of the 110th Symposium on Wave Dynamics and Radio Probing of the Ocean (G. W. Phillips, ed.), NY, Plenum Press.
8. Vesecky, J. F. et al. 1991. Remote sensing of the ocean waveheight spectrum using synthetic aperture-radar images. Oceanography from Space (G. F. R. Gower, ed.), NY, Plenum, 329-337.
9. Longuet-Higgins, M. S. et al. 1963. Observation of the directional spectrum of sea waves using the motion of a floating buoy. Conference on Ocean Wave Spectra, NY, Prentice Hall, 111-132.
10. Joel, J. R. et al. 1975. Observations of oceanic internal and surface waves from the Earth Resource Technology Satellite. J. Geophys. Res., 80, 666-681.
11. Valenzuela, G. R. 1979. Theories for the interaction of electromagnetic and ocean waves -- a review. Boundary-Layer Meteorology, 12, 61-86.
12. Vesecky, J. F. & Stewart, P. W. 1992. The observation of ocean surface phenomena using imagery from the SEASAT synthetic aperture radar -- an assessment. J. Geophys. Res., in press.

Copy available to DTIC does not permit fully legible reproduction

REFERENCES

- Allan, T.D. and T.H. Guymer, Seasat and JASIN, Int. J. Remote Sensing, 1, pp. 261-267, 1980.
- Alpers, W.R. and C.L. Rufenach, The Effect of Orbit Motions on Synthetic Aperture Radar Imagery of Ocean Waves, IEEE Trans. Antennas Propagat., AP-27, pp. 685-690, 1979.
- Ausherman, D.A., Digital Versus Optical Techniques in Synthetic Aperture Radar (SAR) Data Processing, Optical Eng., 19, pp. 157-167, 1980.
- Ausherman, D.A., W.D. Hall, J.N. Latta and J.S. Zelenka, Radar Data Processing and Exploitation Facility, Proceedings IEEE International Radar Conference, Washington, D.C., 1975.
- Bainbridge, A.E., Geosecs Atlantic Expedition - Volume 2: Sections and Profiles, U.S. Government Printing Office, Washington, D.C., 198 pp., 1980.
- Baines, P.G., Observations of Stratified Flow Over Two-Dimensional Obstacles in Fluid of Finite Depth, Tellus, 31, pp. 351-371, 1979.
- Beal, R.C., P.S. DeLeonibus and I. Katz (eds.), Spaceborne Synthetic Aperture Radar for Oceanography, Johns Hopkins Univ. Press, Baltimore, MD, 215 pp., 1981.
- Bell, T.H., Jr., Topographically Generated Internal Waves in the Open Ocean, J. Geophys. Res., 80, pp. 320-327, 1975.
- Brown, W.M. and L. Porcello, An Introduction to Synthetic Aperture Radar, IEEE Spectrum, 6, pp. 52-66, 1969.
- Draper, N.R. and H. Smith, Applied Regression Analysis, John Wiley and Sons, Inc., New York, 407 pp., 1966.
- Elachi, C. and W.E. Brown, Models of Radar Imaging of the Ocean Surface Waves, IEEE Trans. Antenna Propagat., AP-25, pp. 84-95, 1977.
- Fu, L. and B. Holt, Seasat Views Oceans and Sea Ice with Synthetic Aperture Radar, JPL Publication No. 81-120, 200 pp., 1982.
- Garrett, C. and W. Munk, Space-Time Scales of Internal Waves: A Progress Report, J. Geophys. Res., 80, pp. 291-297, 1975.
- Garrett, C. and W. Munk, Internal Waves in the Ocean, Ann. Rev. Fluid Mech., 11, pp. 339-369, 1979.
- Harger, R.O., Synthetic Aperture Radar Systems, Academic Press, New York, NY, 240 pp., 1970.
- Holbrook, J.R., J.R. Apel, and J. Tsai, The Sulu Sea Internal Soliton Experiment, Part B: Observations and Analysis, J. Phys. Oceanogr. (in press), 1983.

- Kasischke, E.S., Extraction of Gravity Wave Information from Synthetic Aperture Radar Data, Univ. of Mich. M.S. Thesis, 108 pp., 1980.
- Kasischke, E.S., A. Klooster and R.A. Shuchman, Verification of Synthetic Aperture Radar Focusing Algorithms, Proc. Thirteenth Int. Symp. Remote Sens. Environ., Ann Arbor, MI, pp. 1077-1092, 1979.
- Kasischke, E.S. and R.A. Shuchman, The Use of Wave Contrast Measurements in the Evaluation of SAR/Gravity Wave Models, Proc. Fifteenth Int. Symp. Remote Sens. Environ., pp. 1187-1206, 1981.
- Kasischke, E.S., D.R. Lyzenga, R.A. Shuchman, Y.S. Tseng, B.S. Termaat, B.A. Burns, and G.A. Meadows, The Use of Synthetic Aperture Radar to Detect and Chart Submerged Navigation Hazards, ERIM Final Report No. 155200-1-F, Ann Arbor, MI, 232 pp., 1982.
- Kasischke, E.S., D.R. Lyzenga, J.D. Lyden, G.A. Meadows, R.A. Shuchman, and S.C. Crane, The Use of Satellite and Aircraft SAR to Detect and Chart Submerged Navigation Hazards, ERIM Final Report No. 163000-1-F, Ann Arbor, MI (in press), 1983.
- Kinsman, B., Wind Waves - Their Generation and Propagation on the Ocean Surface, Prentice-Hall, Englewood Cliffs, N.J., 676 pp., 1965.
- Kozma, A., E.N. Leith and N.G. Massey, Tilted Plane Optical Processor, Applied Optics, 11, pp. 1766-1777, 1972.
- Lee, J., Speckle Analysis and Smoothing of Synthetic Aperture Radar Images, Computer Graphics and Image Processing, 17, pp. 24-32, 1981.
- LeMone, M.A., The Structure and Dynamics of Horizontal Roll Vertices in the Planetary Boundary Layer, J. Atmos. Sci., 30, pp. 1077-1091, 1973.
- Liu, A. K., Detection of Bottom Features on Seasat Synthetic Aperture Radar Imagery, Dynatech Report No. DT-8312-01, Torrance, CA, 45 pp., 1983.
- Liu, A.K., J.R. Apel, and J.R. Holbrook, The Sulu Sea Internal Soliton Experiment, Part C: Comparisons with Theory, J. Phys. Oceanogr. (in press), 1983.
- Lyden, J.D., D.R. Lyzenga, R.A. Shuchman, and A.L. Maffett, SAR Detection of Ocean Surface Winds, ERIM Informal Information Report No. 155900 (in press), Ann Arbor, MI, 1983.
- Muller, P. and D.J. Olbers, On the Dynamics of Internal Waves in the Deep Ocean, J. Geophys. Res., 80, pp. 3848-3860, 1975.
- Phillips, O.M., The Structure of Short Gravity Waves on the Ocean Surface, in Spaceborne Synthetic Aperture Radar for Oceanography, ed. by R.C. Beal, P.S. DeLeonibus, and I. Katz, Johns Hopkins Univ. Press, Baltimore, MD, pp. 24-31, 1981.

Porcello, L.W., N.G. Massey, R.B. Innes, and J.M. Marks, Speckle Reduction in Synthetic Aperture Radars, J. Opt. Soc. Am., 66, pp. 1305-1311, 1976.

Raney, R.K., Synthetic Aperture Imaging Radar and Moving Targets, IEEE Trans. Aerospace Elect. Syst., AES-7, pp. 499-505, 1971.

Roberts, D.G., P.M. Hunter, and A.S. Laughton, Bathymetry of the Northeast Atlantic: Continental Margin Around the British Isles, Deep-Sea Res., 26A, pp. 417-428, 1979.

Royal Society, Air-Sea Interaction Project: Summary of the 1978 Field Experiment, The Royal Society, London, England, 139 pp., 1979.

Shuchman, R.A., Processing Synthetic Aperture Radar Data of Ocean Waves, Oceanography from Space, ed. by J.F.R. Gower, Plenum Press, New York, pp. 477-496, 1981.

Shuchman, R.A. and J.S. Zelenka, Processing of Ocean Wave Data from a Synthetic Aperture Radar, Boundary-Layer Meteorol., 13, pp. 181-191, 1978.

Shuchman, R.A., K.H. Knorr, J.C. Dwyer, P.L. Jackson, A. Klooster and A.L. Maffett, Imaging Ocean Waves with SAR - A SAR Ocean Wave Algorithm Development, ERIM Interim Technical Report No. 124300-5-T, Ann Arbor, MI, 123 pp., 1979.

Shuchman, R.A., A.L. Maffett and A. Klooster, Static Modeling of a SAR Imaged Ocean Scene, IEEE J. Oceanic Eng., OE-6, pp. 41-49, 1981.

Shuchman, R.A., E.S. Kasischke, G.A. Meadows, J.D. Lyden, D.R. Lyzenga, P.L. Jackson, A.L. Maffett, and A. Klooster, Jr., The Utility of SAR to Monitor Ocean Processes, ERIM Final Report 124300-11-F, 133 pp., 1981.

Shuchman, R.A., E.S. Kasischke, J.D. Lyden, A. Klooster, and W. Rosenthal, Analysis of MARSEN Synthetic Aperture Radar Wave Imagery, 1982 Int. Geoscience and Remote Sensing Symposium Digest, Munich, Germany, pp. WP-3, 3.1-3.7, 1982.

Stewart, R.H., A Discus-Hulled Wave Measuring Buoy, Ocean Eng., 4, pp. 101-107, 1977.

Tarbell, S., M.G. Briscoe, and R.A. Wellar, A Compilation of Moored Current Meter and Wind Recorder Data - Volume XVIII (JASIN 1978, Mooring, 651-653), Woods Hole Oceanographic Institute Technical Report No. WHOI-79-65, Woods Hole, MA, 200 pp., 1979.

Thomas, M.H.B., The Estimation of Wave Height from Digitally Processed SAR Imagery, Int. J. Remote Sensing, pp. 63-68, 1982.

Thorpe, S.A., The Excitation, Dissipation, and Interaction of Internal Waves in the Deep Ocean, J. Geophys. Res., 80, pp. 328-338, 1975.

U.S. Naval Oceanographic Office, Oceanography of the North Atlantic, Section I - Tides and Currents, Washington, D.C., 1977.

Valenzuela, G.R., Theories for the Interaction of Electromagnetic and Oceanic Waves — A Review, Boundary Layer Meteorology, 13, pp. 61-85, 1978.

Vesecky, J.F. and R.H. Stewart, The Observation of Ocean Surface Phenomena Using Imagery from the Seasat Synthetic Aperture Radar - An Assessment, J. Geophys. Res., 87, pp. 3397-3430, 1982.

Vesecky, J.F., H.M. Assal and R.H. Stewart, Remote Sensing of Ocean Waveheight Spectrum Using Synthetic-Aperture-Radar Images, in Oceanography from Space, ed. by J.F.R. Gower, Plenum Press, New York, pp. 449-457, 1981.

Vesecky, J.F., H.M. Assal, R.H. Stewart, R.A. Shuchman, E.S. Kasischke and J.D. Lyden, On the Ability of Synthetic Aperture Radar to Measure Ocean Waves, Proceedings of the Symposium on Wave Dynamics and Radio Probing of the Ocean Surface, Miami, Florida (in Press), 1982.

Vesecky, J.F., H.M. Assal, R.H. Stewart, R.A. Shuchman, E.S. Kasischke, and J.D. Lyden, Seasat-SAR Observations of Surface Waves, Large Scale Surface Features and Ships During the JASIN Experiment, 1982 Int. Geoscience and Remote Sensing Symposium Digest, Munich, Germany, pp. WP-3, 1.1-1.6, 1982a.

Wu, C., A Derivation of the Statistical Characteristics of SAR Imagery Data, Proc. 3rd ESA SAR Image Quality Workshop, Frascati, Italy, 1980.

Wunch, C., Geographical Variability of the Internal Wave Field: A Search for Sources and Sinks, J. Phys. Ocean., 6, pp. 471-485, 1976.

E

D

FILE

6

D

